Measurements and Simulations of Impedance Reduction Techniques in Particle Accelerators

A thesis submitted to the University of Manchester for the degree of

Doctor of Philosophy

in the Faculty of Engineering and Physical Sciences

2013

Hugo Alistair Day

School of Physics and Astronomy

Contents

Abstract **32**

Declaration **33**

Copyright **34**

The Author **35**

Acknowledgements **36**

1 Introduction **38**

1.1 The CERN Accelerator Complex 38

1.2 The LHC 38

1.3 Operational Figure of Merit for a Collider - Luminosity 40

1.3.1 Integrated Luminosity 41

1.4 Beam Dynamics 42

1.4.1 Transverse Beam Emittance 44

1.5 Structure of Thesis 45

2 Wakefields and Impedances **47**

2.1 Wakefields 47

2.1.1 The Electromagnetic Fields of a Moving Charged Particle in Free Space 48

2.1.2 Longitudinal Wakefields of a Bunch 50

2.1.3 Transverse Wakefields 51
2.1.4 Panofsky-Wenzel Theorem 51
2.2 Impedances 53
2.2.1 Beam Coupling Impedance 53
2.2.2 Transverse Impedances 54
2.2.3 Geometric Impedance 54
2.2.4 Resistive Wall Impedance 58
2.3 Example of the Effects of Wakefields 60
2.3.1 Beam Induced Heating 61
2.3.2 Beam Instabilities 75
2.4 Conclusion 81

3 Beam Based Measurements of Beam Coupling Impedance 82
3.1 Longitudinal Beam Impedance Measurements 82
3.1.1 Potential Well Distortion with Bunch Intensity 82
3.1.2 Synchronous Phase Shift 84
3.2 Transverse Beam Impedance Measurements 85
3.2.1 Tune shift change with bunch intensity 86
3.2.2 Growth time change with chromaticity 87
3.3 Conclusion 87

4 Bench Top Measurements of Beam Coupling Impedance 88
4.1 Low Q-factor Impedances 88
4.1.1 Classical Coaxial Wire Method 89
4.1.2 Resonator Coaxial Wire Method 93
4.1.3 Transverse Impedance Measurements 96
4.1.4 Measurements on Example Geometries 104
4.2 High Q-factor Impedances 118
4.3 Conclusion 118

5 Computational Simulations of Beam Coupling Impedance **121**

5.1 Time Domain Simulations 122

5.1.1 Direct Simulation of a Particle Beam 122

5.2 Frequency Domain Simulations 123

5.2.1 Eigenmode Simulations 123

5.2.2 The Coaxial Wire Method by Simulation 125

5.2.3 Simulation of the particle beam 125

5.3 Conclusion 125

6 Beam Coupling Impedance Reduction Techniques **126**

6.1 Tapering of Step Transitions 127

6.2 Transition Pieces 127

6.3 Conductive Coatings 130

6.4 Beam screens in Kicker Magnets 132

6.5 Serigraphy on Kicker Magnets 133

6.6 Use of damping materials to de-Q resonant cavities 134

6.6.1 Heat Loads on the Damping Material 137

6.7 Conclusion 145

7 LHC Collimation Upgrades **148**

7.1 Introduction 148

7.2 LHC Phase 2 Secondary Collimator Jaw Material 153

7.2.1 Impedance Studies and Analysis 154

7.3 TCTP Impedance Studies 159

7.3.1 TCTP Collimator - Design and Geometry 160

7.3.2 Impedance Simulations and Results 161

7.3.3 Beam-Induced Heating 162

7.4 Conclusion 170

8 LHC Injection Kicker Magnets **172**

8.1 LHC Injection Kicker Magnets 173

8.1.1 Development of the LHC-MKI Beam Screen 176

8.1.2 Observations of heating during 2011 and 2012 until Technical Stop 3 (23.09.2012 - 27.09.2012) 178

8.2 Simulations and Measurements of the MKI with 15 Screen Conductors . . 181

8.2.1 Beam Induced Heating Estimates for 15 Screen Conductors . . . 186

8.3 Other Concerns for the MKI Operation and Temperature Reduction . . . 188

8.4 Simulations and Measurements of the MKI with 19 Screen Conductors . . 189

8.4.1 Temperature of MKI8d after Technical Stop 3 192

8.5 The Dependence of the Beam Coupling Impedance on the Kicker Components 193

8.5.1 The Impedance of the MKI - Effects of the Inclusion of the Beam Screen 195

8.5.2 How Screening Changes with the Number of Screen Conductors . 198

8.5.3 Dependence of the Impedance on the Beam Screen Dimensions . 201

8.6 New Beam Screen Designs 207

8.7 Upgrade Plans for Long Shutdown 1 and Beyond 213

8.8 Conclusion 218

9 Summary and Conclusions **219**

9.1 Summary 219

9.2 Future Directions 220

Bibliography **222**

A Beam Dynamics **236**

A.1 Longitudinal Beam Dynamics 236

A.1.1 Longitudinal Equations of Motion 238

A.1.2 RF Acceptance and Longitudinal Emittance 240

A.2 Linear Transverse Dynamics 241

B TCTP Eigenmode Simulations - No Ferrite 248

C TCTP Eigenmode Simulations - With Ferrite 254

D Cavity Parameters and the Calculation of Eigenmode Properties 258

D.1 Longitudinal R_s/Q 260

D.2 Transverse R_s/Q 260

E Ferrite Properties 262

E.1 TT2-111R 262

E.2 4S60 263

E.3 4A4 263

E.4 4E2 263

F Heat Transfer in Vacuum 266

F.1 Convection 266

F.2 Conduction 267

F.3 Radiation 267

F.3.1 Near-field radiation 268

G Analytical Models of Resistive Wall Impedance 270

G.1 Tsutsui Model 270

G.2 Zannini Model 272

G.3 Mounet Model 272

Total word count: 37872

List of Tables

6.1 Comparison of the power loss on the surface of a pillbox cavity by both direct calculation and internal calculation by HFSS (in units normalised to 1 V/m maximum electric field). 141

6.2 Comparison of the power loss in the volume of a pillbox cavity by both direct calculation and internal calculation by HFSS (in units normalised to 1 V/m maximum electric field). 141

7.1 The electrical conductivity of the different jaw materials proposed for use in the phase 2 design. All results are given for measurements at room temperature (20^oC) 154

7.2 The impedance budgets (both transverse and longitudinal) for LHC at injection and collisions. Taken from the LHC Design Report [72]. 160

7.3 The LHC operational parameters considered for heating estimates for the TCTP. Operational parameters include the nominal LHC parameters for 25 ns bunch spacing, the peak operational intensity for 50 ns bunch spacing used in 2012, and the two possible HL-LHC operational schemes, using both 25 ns and 50 ns bunch spacing. Here the bunch length is assumed to encompass the 4σ Gaussian width. 166

7.4 The power loss of a the TCTP collimator with ferrite for a number of operational modes in the LHC and HL-LHC assuming each cavity mode falls upon a beam harmonic. All losses are in Watts using the parameters found in Tab. 7.3 166

7.5 The power loss of a TCTP collimator without the ferrite damping tiles for a number of operational modes in the LHC and HL-LHC assuming each cavity mode falls upon a beam harmonic. All losses are in Watts using the parameters found in Tab. 7.3 167
7.6 The power loss of a TCTP collimator with ferrite for a number of operational modes in the LHC and HL-LHC assuming beam harmonics spaced at the reciprocal of the bunch spacing. All losses are in Watts using the parameters found in Tab. 7.3 167
7.7 The power loss of a TCTP collimator without ferrite for a number of operational modes in the LHC and HL-LHC assuming beam harmonics spaced at the reciprocal of the bunch spacing. All losses are in Watts using the parameters found in Tab. 7.3 168
7.8 The percentage of power loss lost in thermally sensitive components in the TCTP. 169
7.9 The power loss in the ferrite of the TCTP collimator. The most pessimistic of the losses estimated in Tab. 7.4 and Tab. 7.6 for the 1.0 ns case. All losses are in Watts using the parameters found in Tab. 7.3 169

8.1 MKI operational parameters 174
8.2 The upper 2012 LHC operational parameters used for estimating the power loss in the MKI with 15 screen conductors. 187
8.3 Power loss estimates for the LHC-MKI with 15 screen conductors in the beam screen (in Watts) for a number of different bunch lengths and profiles ($4\sigma_z$ for the Gaussian profile). 187

8.4 The power loss due to the impedance calculated for the MKI with 15 (most common configuration) and 19 (as for the new MKI8d) screen conductors. Estimates are given assuming a beam with 1380 bunches, seperated by 50 ns, with each bunch containing 1.7×10^{11} particles. Estimates of the power loss assuming a Gaussian, a parabolic and a $\cos^2$ longitudinal bunch profile are calculated (in Watts), and a range given for the lowest (typically the Gaussian distribution) and highest (typically the $\cos^2$ distribution due to the large high frequency lobes) values calculated ($4\sigma_z$ for Gaussian profile). 193

8.5 The beam induced heating calculated for a number of beam screen designs with 24 screen conductors with equal thickness of ceramic tube (thickness of 7mm) with different effective overlaps assuming 50 ns bunch spacing LHC conditions (1380 bunches, 1.7×10^{11}ppb with a bunch length of 1 ns assuming a Gaussian bunch profile (length is $4\sigma_z$ value)). It can be seen that the broadband heating component is relatively constant for the change in overlap, whilst the resonant component only significantly changes with a large increase in the effective overlap. 205

8.6 The beam induced heating calculated for a number of beam screen designs with 24 screen conductors of equal length (overlap of 100mm) with different tube thicknesses assuming 50 ns bunch spacing LHC conditions (1380 bunches, 1.7×10^{11}ppb with a bunch length of 1 ns). It can be seen that the change in broadband heating component does not strongly correlate with the change in tube thickness, whilst the resonant component can increase drastically due to the increasing peak impedance as a result of increasing the tube thickness. 206

8.7 The power loss expected due to beam-wakefield interactions in the MKIs for a number of proposed beam screen designs. Estimates are given for 50 ns and 25 ns bunch spacing in the LHC (1380 bunches, 1.7×10^{11} particles per bunch for 50 ns, 2808 bunches, 1.15×10^{11} particles per bunch for 25 ns) assuming a $\cos^2$ bunch distribution with a bunch length $t_b = 1\ ns$. 216

8.8 Possible HL-LHC bunch parameters and the estimated heating for the LHC beam screen to be installed during LS1. Here the bunch length is assumed to encompass the 4σ Gaussian width. 217

E.1 A selection of the physical properties of TT2-111R 263

E.2 A selection of the physical properties of 4S60 264

E.3 A selection of the physical properties of 4A4 264

E.4 A selection of the physical properties of 4E2 265

List of Figures

1.1 The CERN accelerator complex, showing both the proton and heavy ion (lead) accelerator chains from LINACs 2 and 3 up to the LHC. Different experimental uses are highlighted in the diagram. 39

1.2 The representation of the coordinate system of a circular accelerator, and additionally the co-moving reference frame of a circulating particle. . . . 43

1.3 An illustration of betatron oscillations around the ideal orbit of a circular accelerator. These oscillations occur in both the horizontal and vertical planes. 43

2.1 The relative displacements and velocities of the source (S) and test (T) particles. 48

2.2 The relative displacements of the source particle and witness particle in the horizontal and vertical planes that identify the dipolar/driving and quadrupolar/detuning impedances. 55

2.3 Cross section of a cylindrical pillbox cavity with an attached beam pipe. . 56

2.4 The equivalent RLC parallel circuit for a cavity resonance, driven by a current i_b, in this case the beam current. 57

2.5 The geometry of the Tsutsui resistive wall formalism. 59

2.6 Examples of the longitudinal (a) and transverse (b) resistive wall impedance per unit length of a beam pipe of aperture $a = 2\ cm$ made of of either copper ($\sigma = 6 \times 10^7\ Sm^{-1}$) or graphite ($\sigma = 7 \times 10^4\ Sm^{-1}$). 61

2.7 A comparison of (a) a measured beam power spectrum and a Gaussian bunch of the same bunch length in the frequency domain and (b) the resulting time domain beam profile. The Gaussian has a bunch length ($4\sigma_z$ = 1.2 ns). Measured spectrum taken by P. Baundrenghien et al [32]. Time domain fit taken from E. Metral [33]. 64

2.8 The longitudinal bunch profile of a number of bunch distributions. Note that all of these are normalised to have a peak bunch current of 1. For the Gaussian distribution the bunch length is the 4σ value. The bunch length $t_b = 1.2\ ns$. 66

2.9 The frequency domain (a) current spectrum and (b) power spectrum for a number of different bunch profiles with a bunch length $\tau_b = 1.2\ ns$. . . . 66

2.10 (a) The longitudinal profile and the (b) associated bunch power spectrum for a number of bunch lengths assuming a Gaussian bunch profile. 67

2.11 (a) The longitudinal profile and the (b) associated bunch power spectrum for a number of bunch lengths assuming a parabolic bunch profile. 67

2.12 A comparison of a measured beam power spectrum and a number of analytical bunch profiles assuming a bunch length of 1.2 ns. 68

2.13 The beam harmonics of a beam with a bunch spacing of 25ns overlayed on the real component of the longitudinal impedance an example of a low Q impedance ($R_s = 10\ \omega$, Q = 10, $f_{res} = 1\ GHz$). The blue lines represent the frequency of a beam harmonic, not necessarily the magnitude of the power spectrum at that point. Note that a number of beam harmonics overlay non-zero impedance values. 69

2.14 The beam harmonics of a beam with a bunch spacing of 25 ns overlayed on the real component of the longitudinal impedance of a sample of a high Q impedance ($R_s = 10\ \Omega$, Q = 1000, $f_{res} = 1\ GHz$). The blue lines represent the frequency of a beam harmonic, not necessarily the magnitude of the power spectrum at that point. Note that only a single beam harmonic overlays a non-zero impedance values. 70

2.15 The change in power loss due to a narrow band resonance characterised by $\omega_0 = 2\ GHz$, $R_s = 100\ \Omega$, $Q = 1000$ with a Gaussian bunch distrbution of different lengths. 72

2.16 (a) The change in power loss due to a narrow band resonance characterised by $\omega_0 = 2\ GHz$, $R_s = 100\ \Omega$, $Q = 1000$ interacting with a $\cos^2$ bunch distribution with different bunch lengths. The impedance and the beam power spectrum are shown in (b) to illustrate how this relates to the power loss. 73

2.17 (a) The change in power loss due to a narrow band resonance characterised by $\omega_0 = 2\ GHz$, $R_s = 100\ \Omega$, $Q = 1$ interacting with a $\cos^2$ bunch distribution with different bunch lengths. The impedance and the beam power spectrum are shown in (b) to illustrate how this relates to the power loss. 74

2.18 A tune diagram illustrating the unperturbed tune of a machine, and the resulting perturbed tune and the tune spread as a result of direct space charge interactions on a bunch. Note that the tune spread has caused some particles to lie upon a major resonance harmonic. Taken from K. Schindl [42]. 77

2.19 The change in the bunch length of a proton beam in the SPS due to the effects of a broadband resonator impedance ($f_{res} = 1\ GHz$, $R_s = 10\ \Omega$, $Q = 1$) without space charge. Note that the bunch length increases when the beam is above transition, and decreases below transition, as the bunch intensity is increased. 78

2.20 Examples of a number of modes of headtail oscillations without 2.20(a) and with 2.20(b) chromaticity. Note that radial and azimuthal modes may occur, as may coupled modes, in which the motion of the horizontal and vertical planes is coupled. Images courtesy of G. Rumolo [43]. 80

4.1 Comparison of the electromagnetic field profile of a moving charged particle and a short time pulse propagating along a coaxial wire. 89

4.2 The resistive networks for matching a DUT to the attached measuring network (VNA and connecting cables). (a) shows series resistive matching and (b) shows a two way matching network. 90
4.3 Experimental setup for a measurement of the beam coupling impedance using the classical coaxial wire method. 91
4.4 An example of a reflection measurement made with and without matching resistors. The faded line (lower trace) is the measurement with matching, the bold line (upper trace) that without. The reduction in the reflection can be seen due to the flatter line after the initial reflection. 91
4.5 An example of the resonance pattern seen whilst performing measurements using the resonant method. Each peak corresponds to one data point in the final measurements. Taken from measurements of the LHC injection kicker magnets. 95
4.6 Measurement setup for measurements of the dipolar beam coupling impedance using the two wire setup for the classical coaxial wire method. 98
4.7 The geometries used for coaxial wire measurement simulations. For the geometry with top/bottom, left/right symmetry we use the Tsutsui model ((a)) using two parallel plates. For the asymmetric structure we use the Zannini-model for a C-core ferrite kicker magnet ((b)), which generates a constant term and a noticeable asymmetric term. 106
4.8 The complex permeability of 4A4 ferrite. 107
4.9 An example of the simulation model used for coaxial wire simulations. In this case a displaced single wire between two parallel plates. The wire is highlighted in purple. 107
4.10 The longitudinal impedance of two parallel ferrite plates simulated using a longitudinal coaxial wire. Presented is the impedance as measured in the horizontal plane ((a)) and in the vertical plane (b). 109

4.11 The dipolar impedance of two parallel ferrite plates simulated using two longitudinal coaxial wires. Presented are the impedances as measured in the horizontal plane ((a)) and in the vertical plane (b). 109
4.12 The quadrupolar impedance of two parallel ferrite plates simulated using a combination of displaced single wire simulated measurements and two wire simulated measurements. Presented is the impedance as measured in the horizontal plane ((a)) and in the vertical plane (b). 110
4.13 The longitudinal impedance of two parallel graphite plates as measured by taking the constant term of a quadratic equation fitted to a series of displaced single wire simulated measurements. Shown are simulated measurements acquired from fitting displacements in (a) horizontal axis and in (b) the vertical axis. 113
4.14 The dipolar impedance of two parallel graphite plates measured using two longitudinal coaxial wires. Presented is the impedance as measured in the horizontal plane ((a)) and in the vertical plane (b). 114
4.15 The quadrupolar impedance of two parallel graphite plates measured using a combination of displaced single wire measurements and two wire mesurements. 114
4.16 The impedance of the C-core ferrite kicker as acquired by simulating the classical coaxial wire method in HFSS. Shown is the (a) longitudinal impedance, (b) the dipolar impedance, (c) the quadrupolar impedance and (d) the constant transverse impedance. 117
4.17 Comparison of the geometries of a cavity and attached beampipes (a) without and (b) with the coaxial wire in place. Note the dimensions and that the dashed line in (a) and the solid line in (b) represent the rotational plane of symmetry 119

4.18 A comparison of the transmission parameters through a pillbox cavity with and without a coaxial wire. A displaced coaxial wire is also shown to illustrate the possibility of exciting dipolar modes also. It can be seen that the transmission signals are drastically changed depending on the presence or not of the wire. 119

5.1 An illusration of the (a) source signal and witness integration in a time domain code. Here a sample from the UA9 goniometer is shown. The source signal and the resulting wakefield are shown in (b). 124

6.1 An example pillbox structure with and without a tapered transition region (a), in this case with the taper of 15°. The resulting imaginary component of the longitudinal impedances are shown in (b), with Z/n shown in (c), as these are the most significant for beam stability. 128

6.2 Example of RF fingers (in this case for the PIMS (Plug In ModuleS) module, placed between cryo-modules in the LHC). 129

6.3 The layout of the RF fingers in the VMTSA both in (a) the fully operational configuration and (b) when some RF fingers lose contact. (c) shows the transmission parameter S_{21} for the VMTSA module with and without good electrical contact between the fingers and the beam pipe as acquired by coaxial wire measurements. Photos and measurements courtesy of J.L. Nougaret. 131

6.4 An example of serigraphy in the SPS Extraction Kicker Magnets (SPS-MKE). The layout of the interleaved fingers is shown in (a) and the actual serigraphed ferrites in (b). A comparison of the measured real component of the longitudinal beam coupling impedance with and without the serigraphy is shown in (c). 135

6.5 The complex permeability of a sample ferrite of the sort used for damping. In this case 8C11. In usage a high Curie temperature (T_c) ferrite is recommended, such as TT2-111R. 136

6.6 Two sample geometries used to examine the effects of ferrite damping material on cavity resonances. (a) shows a cavity with the ferrite unshielded, and (b) shows a more realistic case in which the ferrite is shielded from directly seeing the traversing beam. 139

6.7 The real component of the longitudinal beam coupling impedance of a cavity without and with a damping material with $\epsilon^{'} = 10$, $\mu^{'} = 10$ and $\mu^{''}/\mu^{'}$ is varied. The non-damped cavity is shown for comparison. The change in resonanct frequency and shunt impedance is due to the increased $\epsilon^{'}$ of the damping material. 142

6.8 (a) The reduction in the Q of the cavity resonance with the increasing loss tangent of the ferrite damping, showing a strong decrease of the resonant Q with a small increase in loss tangent. (b) The percentage of the power loss in the ferrite as the resonant Q decreases. This can be seen to tend towards 100% as the Q approaches 0. 143

6.9 The power loss due to a beam with 1.15×10^{11} particles per bunch, 288 bunches, a ring circumference 6911 m and a bunch length $4\sigma = 0.04$ m assuming a Gaussian bunch distribution in the unscreened cavity. 144

6.10 The real component of the longitudinal beam coupling impedance of a cavity without and with shielded damping material with $\epsilon^{'} = 10$, $\mu^{'} = 10$ and $\mu^{''}/\mu^{'}$ is varied. The non-damped cavity is shown for comparison. The change in resonance frequency and shunt impedance impedance is due to the increased $\epsilon^{'}$ of the damping material. 145

6.11 (a) The reduction in the Q of the cavity resonance with the increasing loss tangent of the ferrite damping, showing a strong decrease of the resonant Q with a small increase in loss tangent. (b) The percentage of the power loss in the ferrite as the resonant Q decreases. This can be seen to tend towards 100% as the Q approaches 0. 146

6.12 The power loss due to a beam with 1.15×10^{11} particles per bunch, 288 bunches, a ring circumference 6911 m and a bunch length $4\sigma = 0.04$ m assuming a Gaussian bunch distribution in the screened cavity. 147

7.1 The processes by which the collimation system in the LHC acts to clean the beam and manage losses in a controllable way. Taken from [78]. . . . 150

7.2 Different components of impedance reduction measures in the phase 1 collimator design. (a) shows the longitudinal RF fingers, ensuring a good conducting path for the beam image currents, and (b) shows the sliding RF contacts on the collimators jaw. These are intended to minimise the volume seen by the beam, thus confining any cavity modes that may be excited by the beam to very high frequencies where the beam power spectrum is very small. 151

7.3 The RF system for use in the phase 2 collimation system. The sliding RF contacts of the phase 1 design are replaced with a ferrite damping system. The RF contacts are removed, allowing the beam to see the entire RF cavity, causing resonances at lower frequencies. The Q of these resonances are decreased by the use of ferrite damping tiles (see Sec. 6.6). The location of the beam is shown in green. 152

7.4 A number of the proposed jaw designs for the phase 2 secondary collimators. (a) shows the jaw made entirely from molybdenum. Glidcop maybe substituted for molybdenum in this design. (b) shows the jaw made from a mixture of molybdenum diamond composite with a 2 mm coating of pure molybdenum on the surface. The composite ensures a mechanically strong jaw, whilst the coating screens the higher resistivity composite and provides a smooth surface on the beam-facing part of the jaw. In this case the composite maybe substituted with copper diamond composite, and likewise the coating may be replaced with GlidCop. 155

7.5 The physical model of the Mounet model of parallel plate impedance. Note that the two sides of the structure do not have to be symmetric. The materials maybe any material provided it's frequency dependent properties are well defined. 155
7.6 The impedances of different jaw materials for the phase 2 secondary collimators. (a) The longitudinal impedance, (b) the horizontal dipolar impedance, (c), the vertical dipolar impedance per unit length. 156
7.7 The impedances of different jaw materials for the phase 2 secondary collimators. (a) the horizontal quadrupolar impedance and (b) the vertical quadrupolar impedance per unit length. 157
7.8 The real component of the vertical dipolar impedance of the various collimator jaw materials assuming a 2mm half gap. 158
7.9 The TCTP collimator has a number of important impedance reduction techniques present in its design. Ferrite tiles replace the sliding transverse RF contacts of the phase 1 design, shown in (a) (ferrite tiles shown in black) to reduce the resonant Q of the structure. The longitudinal RF fingers, shown in (b), provide a good conducting path for the beam image current in the transition from the beam pipe to the collimator jaw. 160
7.10 The different RF systems considered for the TCTP collimator. (a) shows an RF system similar to the phase 1 RF system. In these simulations the sliding RF contacts are replaced by a perfect connection - for frequencies lower than 2-3 GHz this is a good approximation and greatly simplifies the simulation model. (b) shows the RF circuit complete with ferrite. Two further variants may be considered, where the ferrite is replaced by either vacuum (to indentify how the ferrite damps the otherwise present modes) and replacing the ferrite with PEC (to see whether it is the ferrite or the small aperture that reduces the coupling of the beam to the surrounding vacuum tank). 162

7.11 The longitudinal impedance of the TCTP collimator for a number of different configurations. Shown is the system using the ferrite damping system (ferrite being 8C11 in this case), RF fingers as in phase 1, and the RF system with the ferrite replaced by PEC. The real (a) and imaginary (b) components are shown. 163
7.12 The real component of the longitudinal impedance for the TCTP collimator as simulated in the frequency domain for the case with and without ferrite damping tiles. The strong resonances present in the case without ferrite can be seen to be strongly damped when the ferrite tiles are added. However a substantial broadband component occurs in addition due to the broadened resonance peaks. 165
7.13 The different thermally sensitive components of the TCTP collimator highlighted in purple. (a) shows the ferrite tiles, and (b) the longitudinal RF fingers. 168
7.14 The temperature increase of the ferrite damping tiles in the TCTP collimator under a number of beam operating conditions and for a number of different jaw support materials. Plot taken from [89]. 170

8.1 An example layout of a injection system for an accelerator with the timing of the kicker field with an injected bunch train. Taken from [91]. 172
8.2 The location of the LHC injection systems in the LHC ring, with the layout of an injection line. 174
8.3 Cross sections of the MKI parallel to (a) and perpendicular to (b) the direction of travel of the beam. Ferrite is indicated in red and the beam path in green. 175
8.4 (a) An MKI out of its tank, showing the internal components. (b) MKIs in the LHC tunnel connected together in the complete injection line. . . . 176

8.5 Cross sections of the beam screen perpendicular to (a) and parallel to (b) the direction of beam travel. The screen conductors removed from the majority of the MKIs during the original construction phase are highlighted in red. 178
8.6 The measured temperature of the MKIs at (a) IP2 and (b) IP8 during 2011 in the LHC. Note MKI8b and MKI8d show significantly higher measured temperatures than the other MKIs. 180
8.7 The measurement setup for the two wire measurement setup. 183
8.8 The simulation model of the LHC injection kickers implemented in CST Particle Studio. 183
8.9 The real component of the longitudinal impedance of the LHC MKI acquired by measurements using the resonant coaxial wire method and time domain simulations using CST Particle Studio. (15 tapered screen conductors). 184
8.10 The real component of the dipolar impedances of the LHC MKI acquired by measurements using the resonant coaxial wire method and time domain simulations using CST Particle Studio. (a) shows the real component of the horizontal dipolar impedance, and (b) the real component of the vertical dipolar impedance. (15 tapered screen conductors). 184
8.11 The real component of the quadrupolar impedances of the LHC MKI acquired by measurements using the resonant coaxial wire method and time domain simulations using CST Particle Studio. (15 tapered screen conductors). 185
8.12 The real component of the constant transverse impedances of the LHC MKI acquired by measurements using the resonant coaxial wire method and time domain simulations using CST Particle Studio. The simulated results from taking the displaced source signal and the displaced witness signal lie on top of one another. (15 tapered screen conductors). 185

8.13 The additional screen conductors and the elongated spheres place in MKI8d to reduce both beam coupling impedance and the electric field. 191
8.14 The real component of the longitudinal beam coupling impedance of the replacement MKI8d with 19 screen conductors from both simulations and measurements. The corresponding impedance for an MKI with 15 screen conductors is shown for comparison. 192
8.15 The temperature profile of the IP8 injection kicker magnets during the time period before and after technical stop 3 (TS3), when the MKI8d was changed from a kicker magnet with 15 screen conductors to one with 19 screen conductors. It can be seen this magnet (solid red trace) goes from being the magnet with the highest measured temperature to the magnet with the lowest measured temperature after TS3 (17/09/2012 - 27/09/2012). 194
8.16 The geometries simulated for the various components in the LHC-MKI. These are c-core ferrite only (a), c-core ferrite and the ceramic tube (b), c-core ferrite with the ceramic tube containing 24 screen conductors (c) and finally the complete MKI magnet (without vacuum tank for clarity) (d). 196
8.17 The (a) real component and the (b) imaginary components of the LHC MKI kicker magnet impedances for different components in the magnet. . 197
8.18 Beam screens with different numbers of screen conductors removed from the design quantity of 24. Models of 15 (a), 19 (b) and 24 (c) screen conductors are considered for the impedance simulations. Conductors surrounded by the boxes are removed in this case. 198
8.19 Beam screens with different numbers of screen conductors removed from the design quantity of 24. Models of 17 (a), 19 (b), 20 (c) and 24 (d) screen conductors are considered for the impedance simulations. Conductors that are coloured red are the removed in each case. 199
8.20 The longitudinal impedance of the MKIs with different numbers of screen conductors included in the beam screen. Shown is the real component (a) and the imaginary component (b) of the longitudinal impedance. 200

8.21 The cut down simulation model used for simulations of the MKI beam screen with 24 screen conductors. 202
8.22 A comparison of the mesh that may be generated in CST Particle Studio using both the full model (a) and the cutdown model (b). Note the greatly increased mesh density in the important overlap region between the screen conductors and external metallization. The simulation time for the first is on the order a of day, for the second 30 minutes. 202
8.23 (a) The simulated real component of the longitudinal beam coupling impedance for different lengths of the overlap, and (b) a zoomed in plot of the first resonances of all the overlaps with the calculated resonance frequency (shown as vertical lines) for each based on the effective length. For each the thickness of the ceramic tube is 7 mm. 204
8.24 The simulated impedance of the beam screen with 24 screen conductors with an overlap $L_{overlap} = 100\ mm$ and the predicted resonance frequencies from Eqn. 8.1 shown as vertical lines. 205
8.25 The variance of the real beam coupling impedance with the tube thickness. External diameters of 50, 53 and 56mm correspond to tube thicknesses of 4, 5.5 and 7mm respectively. The physical overlap is 100mm in all cases. 207
8.26 A MKI beam screen design with alternating lengths of screen conductors - with a difference in length b. 210
8.27 A MKI beam screen design with tapered lengths of screen conductors. The taper may be altered to acquire the desired combination of impedance and surface electric field on the ceramic tube. 210
8.28 A MKI beam screen design with a combination of tapered and alternating screen conductors. The degree of alternating and tapering may change dependent of the desired impedance and surface electric field associated with the screen conductors. The alternating length conductors are closest to the return busbar (those with the lowest induced voltage). 211

8.29 A MKI beam screen design with enclosed slots (shown in comparison to the usual beam screen design with open slots) for the screen conductors. . 211
8.30 A MKI beam screen design using an alternative screen conductor layout in which 2 (cross section shown here) conductors are connected to ground at one end of the screen, and all conductors are connected together at the other end. Both ends have capacitive coupling. 212
8.31 A MKI beam screen design implementing a replacement of some of the external metallization with a metallic cylinder so as to remove the ground plane closest to the ends of the screen conductors from the outer surface of the ceramic tube. 212
8.32 The proposed final MKI design. A combination of alternating and tapered screen conductors is used, along with a step out of the external metallization to a metal cylinder. The outline of the step out is shown by the red-dashed line. 213
8.33 The real component of the beam coupling impedance for a number of the proposed beam screen designs (a). In addition the imaginary component of the longitudinal impedance is shown for completeness (b). In all cases the outside diameter of the ceramic tube is 56mm. 214
8.34 The variation of the predicted beam induced power loss with bunch length for a number of screen designs. The variation for 25 ns (a) and 50 ns (b) machine settings. 215
8.35 The maximum steady-state temperature reached by the ferrite yoke in the MKI depending on the power load in the ferrite yoke as calculated using a 2D cross section of the MKI assuming different tank emissivities and rates of convection outside of the tank (alfa). P_{yoke} is the power lost in the ferrite yoke and T the maximum steady state temperature of the ferrite yoke. Provided by M. Garlasche et al [118]. The worst case scenario is for alfa=1.9 W/(m^2 K). 217

A.1 The focusing synchronous phase positions for a particle below (P_1) and above (P_2) transition. The synchronous phase is chosen for a given particle energy and desired behaviour, and an off-momentum particle will be longitudinally focused to the synchronous phase by the RF system if the correct phase is chosen. This occurs due to balance of increased velocity with an increased size of orbit as a particle is accelerated by the RF electric field. Taken from [122]. 240

A.2 The seperatrix for different synchronous phase values. Note that the acceptance decreases as $\phi_s \rightarrow \pi/2$. Taken from [121]. 242

D.1 The equivalent circuit model for a cavity mode with no coupling to neighbouring cavities. 259

E.1 The permeability (a) and penetration depth (b) for TT2-111R. 264

E.2 The permeability (a) and penetration depth (b) for 4S60. 264

E.3 The permeability (a) and penetration depth (b) for 4A4. 265

E.4 The permeability (a) and penetration depth (b) for 4E2. 265

F.1 The power transfer between two surfaces by radiative heat transfer as a function of emissitivity of the absorbing component and the ratio of the visible surface areas of the components. K_A is the ratio of the surface of the absorbing component and the emitting component. Figure produced by Garlasche et al [125]. 268

F.2 An illustration of the change between the two regimes of thermal transfer by radiation and by conduction as the distance between two surfaces is reduced. It can be seen that there is a period between radiation and the beginning of transfer by contact where-in the rate of thermal transfer greatly increases. This is due to an effect known as radiative tunnelling [126]. . . 269

G.1 The geometry treated by the Tsutsui model of resistive wall impedance. . 271

G.2 The geometry treated by the Zannini model of resistive wall impedance. . 273

G.3 The geometry treated by the Mounet model of resistive wall impedance. . 273

List of Notations

(ρ, θ, z) Coordinate system of an ideal on-momentum particle

(x, y, z) Coordinate system comoving with the on-momentum particle

(x_1, y_1, z_1) The coordinates of the source or inducing particle of a wakefield

(x_2, y_2, z_2) The coordinates of the test or witness particle of a wakefield

β Particle velocity normalised by the speed of light

$\beta_{x/y}(s)$ The horizontal/vertical betatron function

δ The skin depth of a material

$\epsilon^{'}$ The real component of the complex permitivitty of a material

ϵ_0 The permitivitty of free space

ϵ_l Longitudinal beam emittance

ϵ_r The relative permitivitty of a material

$\epsilon_{x/y}$ The horizontal/vertical beam emittance

γ Relativistic factor

$\Im m$ The imaginary component of a number or function

$\lambda(f)$ Frequency domain longitudinal distribution

λ Wavelength

$\mathbf{B} = (B_x, B_y, B_z)$ The magnetic induction (referred to as the magnetic field in the text due to convention) components relative to the coordinate system following the on momentum particle

$\mathbf{B}_\perp$ The perpendicular components of a magnetic field

$\mathbf{E} = (E_x, E_y, E_z)$ The electric field components relative to the coordinate system following the on-momentum particle

$\mathbf{E}_\perp$ The perpendicular components of an electric field

$\mathbf{F}_\perp$ The perpendicular components of a force

$\mathbf{v}$ Particle velocity

$\mathcal{L}$ Luminosity at a collision point

$\mu^{'}$ The real component of the complex permeability of a material

μ_0 The permeability of free space

μ_r The relative permeability of a material

ω Angular velocity or angular frequency

ω_{res} The resonant angular frequency of a resonant impedance

$\Re e$ The real component of a number or function

$\rho(t)$ Time domain longitudinal distribution

ρ The resistivity of a material

σ The conductivity of a material

σ_p Production cross section for a particle reaction

$\sigma_{x,y}$ Gaussian bunch sigma for the transverse cross-section in the horizontal and vertical planes

σ_z The bunch length in distance (4σ length for Gaussian distributions)

τ The time between the source and witness particle in the comoving reference frame

$B_\parallel$ The longitudinal component of a magnetic field

C The capacitance of an RLC circuit

c Speed of light in vacuum(=299792458 m/s)

e Charge of an electron

$E_\parallel$ The longitudinal component of an electric field

$F_\parallel$ The longitudinal component of a force

f_{res} The resonant frequency of a resonant impedance

f_{rev} Revolution frequency of the accelerator

I_b DC beam current

j imaginary number ($\sqrt{-1}$)

k Wave number

k_f Focal strength of a quadrupole magnet

k_{loss} The loss factor of a single particle wakefield

L The inductance of an RLC circuit

m Particle Mass

N_b Bunch population. b replaced by 1 or 2 for the case of colliding beams

n_b The number of bunches in the accelerator. In the case of colliding beams it it the number of colliding bunches

p Particle momentum

P_{loss} The power lost by a beam due to interaction with a beam impedance

P_{surf} The power loss due to ohmic losses on the surface of a cavity

Q The quality factor of a resonant impedance

q Charge of a particle

Q_0 Unperturbed betatron tune

q_1 Charge of the source or inducing particle of a wakefield

q_1 Charge of the test or witness particle of a wakefield

Q_{pert} Part of the betatron tune caused by a perturbing force

R_s The shunt impedance of a resonant impedance

$S_{21,DUT}$ The transmission parameter through a device under test

S_{21} The transmission parameter for an RF system

t_b The bunch length in time (4σ length for Gaussian distributions)

T_c Curie temperature of a ferrite

V_{acc} The voltage experienced by a witness particle traversing a cavity

W The energy stored in a cavity due to a given cavity mode

$W_\parallel$ The longitudinal wake function of a bunch or wakepotential

$w_\parallel$ The longitudinal wake function

$W_\perp$ The transverse wake function of a bunch or trasnverse wakepotential

$w_\perp$ The transverse wake function

Z_0 Impedance of free space

$Z_\parallel$ The total longitudinal impedance

$Z_{\perp}$ The total transverse impedance

$Z_{const,x}$ or $Z_{constant,x}$ The horizontal constant impedance

$Z_{const,y}$ or $Z_{constant,y}$ The vertical constant impedance

$Z_{dip,x}$ or $Z_{dipolar,x}$ The horizontal dipolar or driving impedance

$Z_{dip,y}$ or $Z_{dipolar,y}$ The vertical dipolar or driving impedance

$Z_{quad,x}$ or $Z_{quadrupolar,x}$ The horizontal quadrupolar or detuning impedance

$Z_{quad,y}$ or $Z_{quadrupolar,y}$ The vertical quadrupolar or detuning impedance

Abstract

Wakefields and the corresponding frequency-domain phenomenon beam coupling impedance have been well studied for a number of years as a source of beam instabilities within particle accelerators. With the development of the Large Hadron Collider (LHC) and the large beam currents stored in the LHC during fills for physics production, wakefield driven instabilities and strong beam induced heating have become a limiting factors in luminosity production due to both instantaneous luminousity and the available time for collisions.

In this thesis is presented an in depth study of the beam coupling impedance of two important (from an impedance and operational point of view) devices in the LHC; the collimation system and the injection kicker magnets (MKIs). These systems have both been sources of concern for the beam impedance of the LHC, the collimators due to their large transverse impedance and the MKIs due to the strong heating observed during the increased of beam current during operation in 2011 and 2012. The source of the heating for the MKIs is studied in depth, found to be power lost by the beam to wakefields in the MKIs. Simulations and measurements are used to characterise the impedance and localise the areas responsible for the high impedance, here the beam screen and ferrite yoke of the magnet; improvements are proposed to better screen the ferrite yoke and verified. A new RF damping system using ferrite for the collimation system is studied and compared to the existing RF damping system, focusing on the heating of the damping system. Highlights include a new method for measuring the quadrupolar and constant transverse impedances of an asymmetric structure using a coaxial wire technique is proposed and verified using computational simulations, and a study of the heat loss in a ferrite damped cavity, focusing on the location of the power loss for cavities being damped to varying degrees.

Declaration

No portion of the work referred to in this thesis has been submitted in support of an application for another degree or qualification of this or any other university or other institute of learning.

Hugo Alistair Day
School of Physics and Astronomy
University of Manchester
Oxford Road
Manchester
M13 9PL
May 2013

Copyright

The author of this thesis (including any appendices and/or schedules to this thesis) owns certain copyright or related rights in it (the "Copyright") and s/he has given The University of Manchester certain rights to use such Copyright, including for administrative purposes.

Copies of this thesis, either in full or in extracts and whether in hard or electronic copy, may be made only in accordance with the Copyright, Designs and Patents Act 1988 (as amended) and regulations issued under it or, where appropriate, in accordance with licensing agreements which the University has from time to time. This page must form part of any such copies made.

The ownership of certain Copyright, patents, designs, trade marks and other intellectual property (the "Intellectual Property") and any reproductions of copyright works in the thesis, for example graphs and tables ("Reproductions"), which may be described in this thesis, may not be owned by the author and may be owned by third parties. Such Intellectual Property and Reproductions cannot and must not be made available for use without the prior written permission of the owner(s) of the relevant Intellectual Property and/or Reproductions.

Further information on the conditions under which disclosure, publication and commercialisation of this thesis, the Copyright and any Intellectual Property and/or Reproductions described in it may take place is available in the University IP Policy (see http://documents.manchester.ac.uk/DocuInfo.aspx?DocID=487), in any relevant Thesis restriction declarations deposited in the University Library, The University Library's regulations (see http://www.manchester.ac.uk/library/aboutus/regulations) and in The University's policy on Presentation of Theses.

The Author

The author grew up in the south of the UK, leaving King Edward VI Grammar School in 2005 to read physics at the University of Southampton. In 2008 he was lucky enough to be selected for a summer studentship at CERN studying particle behaviour in the spectrometer of the 3MeV test bed for the Linac4 H- source. After graduating from Southampton in 2009 with an MPhys in Physics he went north to study for a PhD in the School of Physics and Astronomy at the University of Manchester. He was able to acquire a Doctoral Studentship from the CERN Doctoral Student Programme and subsequently spent three exceptional years at CERN, Switzerland.

Acknowledgements

Alles hat ein Ende, nur die Wurst hat zwei.

First and foremost thanks to my supervisors, Elias Metral and Roger Jones. You've provided, in your own ways, insight and guidance that helped get this work on the road and ultimately to it's destination. Particular thanks to Elias for being willing to answer my questions, no matter how basic, convoluted, badly explained or even entirely relevant they may be. An additional thanks should go to my "not-supervisor" supervisor Fritz Caspers. Fritz, CERN's persistent bastion of wisdom. Your tenacity, even if... especially if delivered with your usual flair is always refreshing, even if it requires twice the work to satisfy. To my friends at work, both near and far. I've bothered you with questions, queries and inane banter for 3 years and you still haven't lynched me! Nicolas, Niccolo, Carlo, Serena, Olav, Jean-Luc many thanks to all of you for your assistance. Thanks to Adina and James "Oh god that beard is immense" M. in Manchester for listening to the frequent rant I'd have. And to all the members in the MEW group, past and present, for an abundance of technical support and advice. Especially to Ian for being an immense Dude! Further thanks to Prof. Vitorrio Vacarro, Alexej Grudiev and Alexey Burov. Your collective wisdom on all things RF and impedance has pulled me out of more holes than I can count by this point. And one final thanks to the Commisar of the Impedance Team - Benoit Salvant. A little hint, consistent questioning and the occassional boot to the posterior have been much appreciated over the years.

To my family, either by blood or by choice. The gamers (Southampton and CERN) for incessantly dragging me away from reality into a strange dark place far from here, filled

with demons, heroes and cake. The library crew for unintentionally providing me an outlet during those long times of writing amongst the books. Piotr, Ruben, Steffen, Joni and a number of others for dragging me up into the mountains and ensuring we all got back down intact. Penny, Jan, Nic, Victor, Joe, Steffen, Suzanne and Thiago for providing somewhere I'm happy to return home to. The Random Trip Club for providing sugar and insanity in relatively equal portions. LHCz collaboration for getting me started on helping to make films, and the Zurichians for helping continue the path. Sharman and Oscar - whether intentionally or not you've both provided the means and motive to jump onto the adventure over the years. Hopefully it's been worth it. Continue being awesome you all.

So here we are again, it's been such a pleasure,

We typed and we wrote and plotted it all,

Off it is sent, as the final measure,

It's menace leaves one a gibbering thrall,

Dreaming of a splendid, magnificant hall.

Rakkatakka \m/

Chapter 1

Introduction

1.1 The CERN Accelerator Complex

CERN (Organisation europeene pour la recherche nucleaire) is a particle physics laboratory near Geneva, Switzerland crossing the Franco-Swiss border between the Swiss commune of Meyrin and French town of Saint-Genis Pouilly. It was founded in 1952 with the creation of the Conseil Européen pour la Recherche Nucléaire, which became the Organisation in 1954. It houses an accelerator complex (shown in Fig. 1.1) ranging in energies from hundreds of MeV (extraction energy for Linac2) to energies of 7 TeV (for the LHC), delivering proton bunches to various experiments (fixed target, colliding and beam) at all energy levels. These experiments have a variety of aims, varying from neutrino physics [1], neutron physics [2] antimatter experiments [3–5] as well as radio isotope [6] and hadron therapy [7] research. The Large Hadron Collider (LHC), the largest accelerator at CERN, is at the forefront of high-energy physics designed to push the energy frontier of knowledge of particle physics.

1.2 The LHC

The LHC is a synchrotron built to collide counter rotating beams of hadrons at an centre of mass energy of 14 TeV for protons and 2.76 TeV per nucleon for lead ions. It uses 1,232

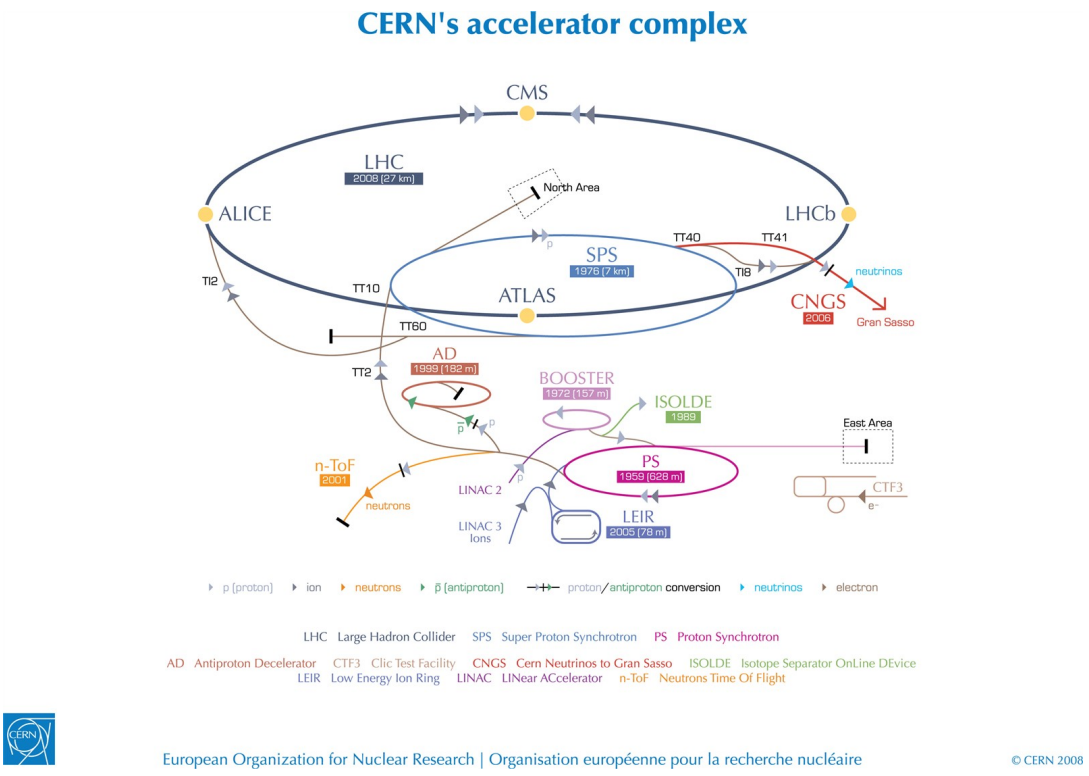

Figure 1.1: The CERN accelerator complex, showing both the proton and heavy ion (lead) accelerator chains from LINACs 2 and 3 up to the LHC. Different experimental uses are highlighted in the diagram.

superconducting dipole magnets to bend the hadron beams on a circular orbit around the beam line, in addition to using 392 quadrupole magnets for focusing in the transverse plane to maintain the bunch cross section and carry out final focusing for the 4 detector experiments in the LHC. Four detector experments are operated at the LHC; two general purpose detectors ATLAS and CMS, used for searches of new physics beyond the current energy frontier [8, 9]; LHCb, a forward detector specialised in the analysis of B-physics [10] and ALICE, a detector specialised in heavy ion collisions with the intent of observing the physics of quark-gluon plasma [11]. Three further experiments are in place in the LHC, LHCf (an experiment related to the effects of high-energy cosmic rays), TOTEM (measuring the total cross-section of the proton via elastic scattering processes at the collision points) and MoEDAL (an experiment searching for magnetic monopoles and stable massive particles): these three complete the experiments provided with data by collisions using LHC delivered protons.

1.3 Operational Figure of Merit for a Collider - Luminosity

One of the key figures of merit for the operation of the LHC (along with the centre of mass energy) is the luminosity at the colliding interaction regions (IRs). This is a figure which denotes the total rate of production of new (in the sense of produced during interactions during collisions between protons) particles in collider experiments. It can be thought of as the factor of proportionality between the cross section of a reaction scheme, σ_p and the number of interactions per second $\mathcal{L}$

$$\frac{dR}{dt} = \mathcal{L} \times \sigma_p \tag{1.1}$$

where $\frac{dR}{dt}$ is the interaction rate. For two colliding bunches, each with a gaussian transverse distribution, the peak luminosity $\mathcal{L}_{peak}$ can be given in a simplified form by

$$\mathcal{L} = \frac{N_1 N_2 f_{rev} n_b}{4\pi\sigma_x\sigma_y} \tag{1.2}$$

where σ_x, σ_y are the RMS beam sizes in the horizontal and vertical directions, $N_{1/2}$ are the bunch populations in beam 1 and 2, n_b is the number of bunches in the machine and f_{rev} is the revolution frequency of the machine. Bunch populations $N_{1/2}$, the revolution frequency f_{rev} and the number of bunches n_b also contribute towards the DC beam current in the machine $I_b = N_1 f_{rev} e n_b$. As will be seen in Sec. 2.3.1 the expected power loss due to beam-equipment interactions is proportional to the I_b^2, thus it can be seen that increasing the luminosity will increase the power loss experienced by equipment in a linear to quadratic fashion (the non-quadratic behaviour being due to other effects on the heating mechanism due to the changing beam current, explained more in Sec. 2.3.1).

1.3.1 Integrated Luminosity

Following from the peak luminosity, the determinant of the quantity of experimental data is the integrated luminosity $\mathcal{L}_{int}$ which is given by

$$\mathcal{L}_{int} = \int_0^T \mathcal{L}\,(t)\,dt \tag{1.3}$$

where T is the integrated collision time and $\mathcal{L}(t)$ is the time varying luminosity (typically decaying exponentially over the lifetime of any given fill of the collider [12]), varying due to changing beam conditions (emittance growth) and bunch population depletion due to collisions and particle losses. The integrated luminosity is significant as the number of a given particle production schema observed by the experiments n_{event} is given by

$$n_{event} = \mathcal{L}_{int} \times \sigma_p. \tag{1.4}$$

It can thus be seen that in addition to increasing the luminosity, maximising the available time for collisions is important to maximising data collection. This requires a high level of availability of the machine, minimising failures of key systems and the down time experienced by the machine. In particular, unavoidable waiting periods between fills are

to be eliminated or reduced. As is shown in Chapter 8, long cool down times (on the order of hours, similar in magnitude to the length of the average LHC fill) for equipment that requires a specific maximum temperature to operate correctly are thus unacceptable during ideal operation and should be reduced to a minimum. These and other sources of reduction of the running time and luminosity (due to both beam coupling impedance and other sources of instabilities and interlock trips due to hardware mishaps) must thus be carefully studied and controlled by the technical and operations teams.

1.4 Beam Dynamics

To introduce the terms and coordinate systems used in later chapters we shall briefly introduce some of the commonly used coordinate systems used to describe the motion of particles in circular accelerators. Typically an ideal orbit is defined for an on momentum particle. In addition a reference frame placed upon the orbit of an ideal on-momentum particle is defined shown in Fig. 1.2. Here ρ and θ determine the location around the centre point of the circular accelerator, whilst (x, y, z) denote a reference frame co-moving with the on-momentum particle on the ideal orbit.

The use of charged particles within an accelerator is controlled by the use of both magnetic and electrical elements in the machine, leading to the particles being acted upon by the Lorentz force

$$\mathbf{F} = q\left(\mathbf{E} + \mathbf{v} \times \mathbf{B}\right). \tag{1.5}$$

In high energy particle accelerators the magnetic and electric fields are typically seperated in location, with the magnetic fields of the beam optics only having a transverse component, being of the form

$$\mathbf{B} = \hat{\mathbf{x}}B_x + \hat{\mathbf{y}}B_y \tag{1.6}$$

Due to the cross product between the velocity ($\mathbf{v} = \hat{\mathbf{z}}v$), it can be seen that there is no component of the force from the magnetic field in the z-direction. In addition the electric

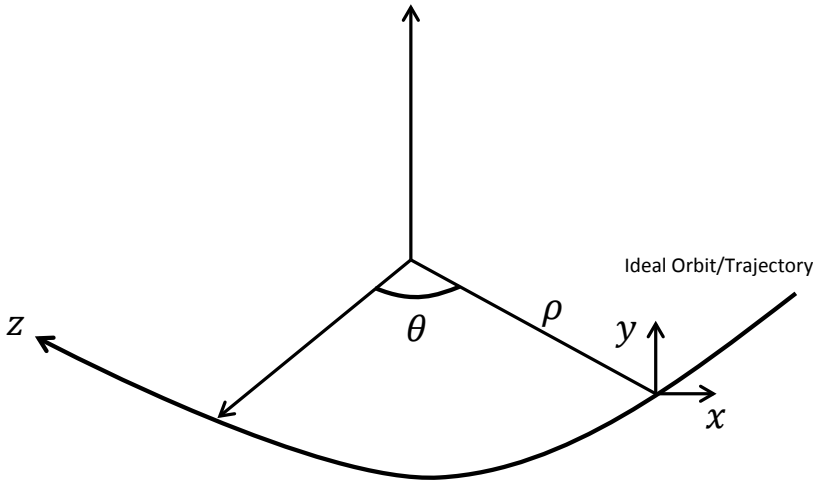

Figure 1.2: The representation of the coordinate system of a circular accelerator, and additionally the co-moving reference frame of a circulating particle.

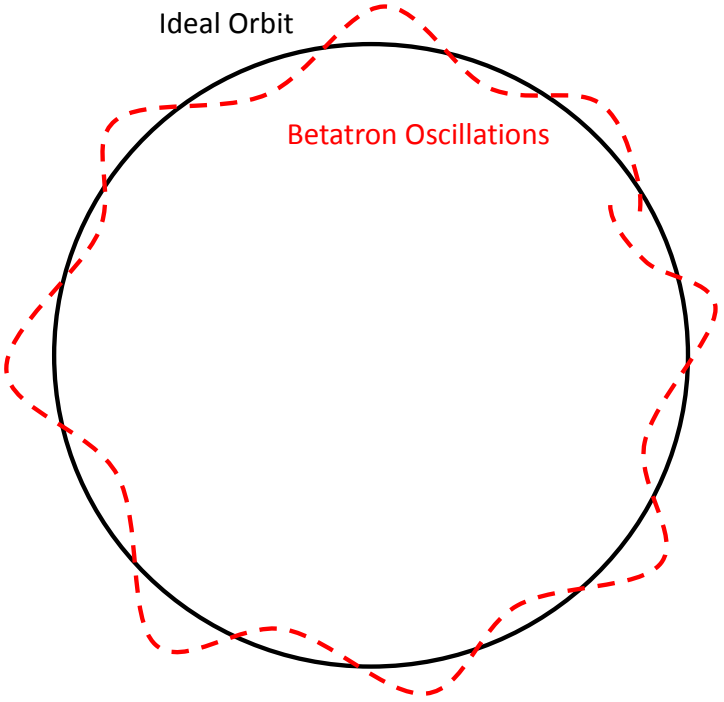

Figure 1.3: An illustration of betatron oscillations around the ideal orbit of a circular accelerator. These oscillations occur in both the horizontal and vertical planes.

field usually only has a longitudinal component such that $\mathbf{E} = \hat{\mathbf{z}}E_z$. This results in the seperation of transverse and longitudinal motion such that

$$F_{\parallel} = qE \tag{1.7}$$

$$\mathbf{F}_{\perp} = q\left(vB_y\hat{\mathbf{x}} - vB_x\hat{\mathbf{y}}\right). \tag{1.8}$$

Subsequently the transverse and longitudinal motion may both be treated independently of one another. This is discussed in detail in App. A.

1.4.1 Transverse Beam Emittance

In this section we shall briefly discuss the role of transverse beam emittance in determining luminousity at a collision point. The transverse beam emittance ϵ is related to the transverse offset x with respect to the design orbit and the beta function of a particle, $\beta(s)$, by

$$x\left(s\right) = \sqrt{\epsilon}\sqrt{\beta\left(s\right)}cos\left(\psi\left(s\right) + \phi\right), \tag{1.9}$$

explained in more detail in App. A. ϕ is an integration constant, ψ the phase advance of the oscillation and s the distance long the ideal circular path. ϵ can be shown to be a constant of integration for a given starting area in phase space, in this case a property of the starting conditions of the bunch. $\beta(s)$ can be shown to be a function solely of the machine, thereby showing that to maximise the luminousity at an interaction point for a given machine setting (i.e. $\beta(s_{IP}) = constant$) it is necessary to have an injector chain that produces bunches with a low emittance, and can preserve the low emittance during acceleration and transfer so as to have the optimal value of $\sigma_{x/y}$ at the collision point such that Eqn. 1.2 is ideal for the experimental conditions. Emittance dilution may occur due to transfer procedures (extraction/injection of the beam between machines and transfer lines) and due to beam instabilities (space charge, wakefields, IBS etc.) making the characterisation of equipment throughout the accelerator chain key in permitting the exploitation of the full range of possible collision parameters.

1.5 Structure of Thesis

In this thesis are studied in detail the beam coupling impedance and beam induced heating of two important devices in the LHC - the injection kicker magnets and the collimation systems, using computational simulation tools and bench-top measurement methods, and the subsequent steps taken to reduce the beam coupling impedance to reduce the heat loads on these devices. The thesis progresses as follows; we have begun by introducing the dangers of beam induced heating from the mechnical point of view, in addition to the operational figures of merit that may be limited by equipment that requires a cool down time between fills to be operated. To understand the nature of beam-induced heating, it is necessary to introduce wakefields and beam coupling impedances which are the power source for the heating. In this section we cover in some detail the beam parameters upon which beam-induced heating is dependent.

In the next chapters we introduce the tools which can be used to evaluate a structures beam coupling impedance, beam-based measurements (Chap 3), bench-top measurements (Chap. 4) and computational simulation tools (Chap. 5). As part of this we introduce new method for evaluating the quadrupolar and constant transverse coupling impedances of asymmetric structures using the coaxial wire bench technique, verified using simulated measurements of the technique on an asymmetric structure.

In Chap. 6 we introduce the various methods of impedance reduction, highlighting the situations in which each is appropriate, their limitations in use, and some rules of thumb for successful implementation. As part of this we carry out a study of the location of power loss in damped cavity structures with differing degreess of damping, relevant due to the relatively large losses that may occur in thermally sensitive material (i.e. ferrites) in high current machines.

In Chap. 7 begins the investigation of the beam coupling impedance reduction techniques as applied to a number of LHC collimation upgrades. The use of conductive coatings on the phase 2 secondary collimator jaws is discussed briefly, followed by a detailed examination of the RF screening placed in the phase 1 and phase 2-type transverse RF

system, using the example of the TCTP collimator. In this case the heating is evaluated, with attention paid to the temperature of the ferrite in the phase-2 damping system to ensure that it remains an effective damping material.

In Chap. 8 the case of the beam-induced heating of the LHC injection kicker magnets is studied. The history of the observed high temperatures and the impedance reduction techniques in place is discussed. A simulation model of this complex device is made, and the simulated impedance compared to bench-top measurements of the longitudinal and transverse impedances. Using the confidence given by the good agreement here, a number of alternative beam screen designs are evaluated for there longitudinal beam coupling impedance, with a constant concern for other requirements such as electrical breakdown and manufacturability.

Finally in Chap. 9 contains the concluding remarks and proposals for future work.

Chapter 2

Wakefields and Impedances

In this chapter the formalism of wakefields, and the frequency domain counterpart, impedances are introduced as they are key to understanding many phenomena in particle accelerators, particularly instabilities and beam-induced heating. Beam-induced heating will be introduced in depth, in relation to both impedance sources and to longitudinal beam parameters such as bunch length, bunch intensity, longitudinal profile and the number of circulating bunches.

2.1 Wakefields

Wakefields (in the context of accelerator physics) is the conventional name given to the phenomenon of induced electromagnetic fields due to charged particles traversing the beam pipe, RF cavities and many other pieces of equipment facing a particle beam in a particle accelerator. They have long been studied as a source of collective instabilities within particle accelerators [13], through the use of analytical models for different beam pipe geometries [14–16] and materials [17], using computational simulation tools, and both beam-based and bench-top measurement techniques. In this chapter we present a number of significant properties of wakefields and their frequency domain counterpart, beam coupling impedance, as well as selected examples of observable effects that wakefields produce.

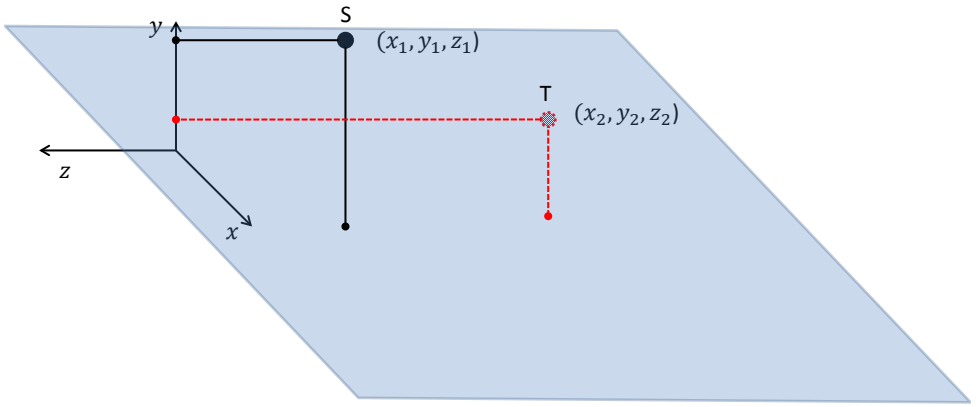

Figure 2.1: The relative displacements and velocities of the source (S) and test (T) particles.

To aid in the explanation there will first be a short definition of the relative positions and labels of particles used in the following section (this derivation follows the examples given by Stupakov [14] and Palumbo [18]). We define the source, or inducing particle as a charged particle with charge q_1 moving with velocity $\mathbf{v} = \beta c\hat{\mathbf{z}}$ at coordinate $(\mathbf{r_1})$, leading a test, or witness particle, with charge q_2, moving with velocity $\mathbf{v}$ at coordinate $(\mathbf{r_2})$ at a distance $z_1 - z_2$ behind the source particle. This relationship is visualised in Fig. 2.1.

2.1.1 The Electromagnetic Fields of a Moving Charged Particle in Free Space

If we consider the electromagnetic fields generated by the source particle moving in vacuum, it can be shown that the fields at a vector $\mathbf{R} = \mathbf{r_1} - \mathbf{r_2}$ are given by

$$\mathbf{E}(\mathbf{R}) = \frac{kq_1\mathbf{R}}{|\mathbf{R}|^3 \left(1 - \beta^2 sin^2\Psi\right)^{3/2}} \tag{2.1}$$

$$\mathbf{H}(\mathbf{R}) = \mathbf{v} \times \mathbf{E} \tag{2.2}$$

where $\gamma = (1 - v^2/c^2)^{-1/2}$ is the relativistic gamma factor, and

$$\Psi = cos^{-1}\left(\frac{\mathbf{R}}{|\mathbf{R}|}.\hat{\mathbf{z}}\right). \tag{2.3}$$

It can be shown that, if we take the ultrarelativistic limit (i.e. $\gamma \to \infty$) we can see that Eqn 2.2 becomes

$$\mathbf{E}(\mathbf{R}) = \frac{2kq_1\mathbf{r}}{r^3}\delta z - ct\mathbf{H}(\mathbf{R}) = \hat{\mathbf{z}} \times \mathbf{E} \tag{2.4}$$

where $\mathbf{r} = x\hat{\mathbf{x}} + y\hat{\mathbf{y}}$ is a purely transverse vector.

The following witness particle experiences the resulting Lorentz force

$$\mathbf{F}(\mathbf{r_1}, \mathbf{r_2}) = q_2[\mathbf{E} + \mathbf{v} \times \mathbf{B}]. \tag{2.5}$$

Looking at Eqn. 2.4, it can be seen that the force can be separated into longitudinal and transverse components

$$F_{\parallel}(\mathbf{r_1}, \mathbf{r_2}) = q_2 E_{\parallel} \tag{2.6}$$

$$\mathbf{F}_{\perp}(\mathbf{r_1}, \mathbf{r_2}) = q_2[\mathbf{E}_{\perp} + (\mathbf{v} \times \mathbf{B})] \tag{2.7}$$

where $\mathbf{E}_{\perp} = E_x\hat{\mathbf{x}} + E_y\hat{\mathbf{y}}$. $F_{\parallel}$ has only an electric component as the magnetic flux density $\mathbf{B}$ has magnitude = 0 in the $\hat{\mathbf{z}}$ direction. Considering just the longitudinal force, integrating over all space gives the total energy change of the source particle

$$U_1(\mathbf{r_1}) = -\int_{-\infty}^{\infty} d\mathbf{z}.\mathbf{F}(\mathbf{r_1}) \tag{2.8}$$

where $F(\mathbf{r_1}) = q_1 E(\mathbf{r_1})$. Similarly the energy change in the witness particle can be calculated by

$$U_2(\mathbf{r_1}, \mathbf{r_2}, \tau) = -\int_{-\infty}^{\infty} d\mathbf{z}\mathbf{F}(\mathbf{r_1}, \mathbf{r_2}) \tag{2.9}$$

where $\tau = (z_1 - z_2)/(\beta c)$ and $F(\mathbf{r_1}, \mathbf{r_2}) = q_2 E(\mathbf{r_1}, \mathbf{r_2})$. From these two energy losses two widely used terms can be extracted; the loss factor k_{loss}, given by

$$k_{loss}\left(\mathbf{r_1}\right) = \frac{U_1\left(\mathbf{r_1}\right)}{q_1^2} \tag{2.10}$$

and the longitudinal wake function, given by

$$w_{\parallel}\left(\mathbf{r_1}, \mathbf{r_2}, \tau\right) = \frac{U_2\left(\mathbf{r_1}, \mathbf{r_2}, \tau\right)}{q_1 q_2}, \tag{2.11}$$

denoting the normalised (with respect to source charge, and source and witness charge respectively) energy change of both the source particle (loss factor) and witness particle (wake function).

2.1.2 Longitudinal Wakefields of a Bunch

As colliders are often used to collide bunches of particles as opposed to single particles, it is useful to be able to define the wake function of a bunch distribution. It can be seen that the total source charge of a bunch q_1 is the integral of the longitudinal current distribution $i_b\left(\tau\right)$ integrated over all time

$$q_1 = \int_{-\infty}^{\infty} i_b\left(\tau\right) d\tau. \tag{2.12}$$

The wake function of a bunch distribution at a point at time τ can be calculated by the convolution of the single particle wake function with the bunch distribution. Thus, if the bunch is split into infinitesimally small slices, the change in energy of a witness particle of charge q at time τ due to a slice at time τ' is given by

$$dU\left(\mathbf{r_2}, \tau - \tau'\right) = q i_b\left(\tau'\right) w_{\parallel}\left(r_2, \tau - \tau'\right). \tag{2.13}$$

The longitudinal bunch wake function $W_{\parallel}\left(\mathbf{r_2}\right)$ can then be calculated using Eqn. 2.9

$$W_{\parallel}\left(\mathbf{r_2}, \tau\right) = \frac{U\left(r_2, \tau\right)}{q_1 q_2} = \frac{1}{q_1}\int_{-\infty}^{\infty} i_b\left(\tau'\right) w_{\parallel}\left(r_2, \tau - \tau'\right) d\tau'. \tag{2.14}$$

2.1.3 Transverse Wakefields

Similar to the longitudinal wakefield, we can see that the total tranverse momentum change of the witness particle is given by integrating the transverse force across all space

$$\mathbf{p}\left(\mathbf{r_1}, \mathbf{r_2}, \tau\right) = \int_{-\infty}^{\infty} \mathbf{F}_{\perp}\left(\mathbf{r_1}, \mathbf{r_2}\right) dz \tag{2.15}$$

where τ is the time delay between source and witness particles. And similarly to the longitudinal plane we can define a wake function normalised with regards to the source and witness particle charges

$$\mathbf{w}_{\perp}\left(\mathbf{r_1}, \mathbf{r_2}, \tau\right) = \frac{\mathbf{p}\left(\mathbf{r_1}, \mathbf{r_2}, \tau\right)}{q_1 q_2}. \tag{2.16}$$

And in a similar manner to the longitudinal bunch wake function a form for the transverse bunch wake function can be derived

$$W_{\perp}\left(\mathbf{r_2}, \tau\right) = \frac{U\left(r_2, \tau\right)}{q_1 q_2} = \frac{1}{q_1} \int_{-\infty}^{\infty} i_b\left(\tau'\right) w_{\perp}\left(r_2, \tau - \tau'\right) d\tau'. \tag{2.17}$$

2.1.4 Panofsky-Wenzel Theorem

Considering the force acting on the witness particle by the Lorentz force, it can be seen that the force is given by

$$\mathbf{F} = q_2 \left[\mathbf{E} + \mathbf{v} \times \mathbf{B}\right]. \tag{2.18}$$

Now, considering Faraday's law in integral form ($\mathbf{B} = -\int_{t_1}^{t_2} \left(\nabla \times \mathbf{E}\right) dt$, t_1 being sufficiently in the past that $\nabla \times \mathbf{E} \to 0$), Eqn. 2.18 can be rewritten as

$$\mathbf{F} = q_2 \left[\mathbf{E} - \mathbf{v} \times \left(\int_{t_1}^{t_2} \nabla \times \mathbf{E} dt\right)\right]. \tag{2.19}$$

Now, using the assumption that the velocity $\mathbf{v}$ is constant and Lagrange's formula (shown in Eqn. 2.21) this then becomes

$$\mathbf{F} = q_2 \left[\mathbf{E} - \int_{t_1}^{t_2} \left(\nabla \left(\mathbf{v}.\mathbf{E} \right) - \mathbf{v} \left(\nabla.\mathbf{E} \right) \right) dt \right]. \tag{2.20}$$

$$\mathbf{a} \times \left(\mathbf{b} \times \mathbf{c} \right) = \mathbf{b} \left(\mathbf{a}.\mathbf{c} \right) - \mathbf{c} \left(\mathbf{a}.\mathbf{b} \right) \tag{2.21}$$

If this force is seperated into the longitudinal and transverse components we see that they are the following

$$F_{\parallel} = q_2 E_z \tag{2.22}$$

$$\mathbf{F}_{\perp} = q_2 \left[\mathbf{E}_{\perp} - v \int_{t_1}^{t_2} \left(\nabla_{\perp} E_z - \frac{\partial \mathbf{E}_{\perp}}{\partial z} \right) dt \right] \tag{2.23}$$

where $\nabla_{\perp} = \frac{\partial}{\partial x} + \frac{\partial}{\partial y}$ in the differential operator only in the transverse coordinates. If these are now compared to the identities of the wake function for the longitudinal and transverse wake functions given in Eqns. 2.11 and 2.16 respectively, it can be seen that

$$w_{\parallel} \left(\mathbf{r_1}, \mathbf{r_2}, \tau \right) = -\frac{1}{q_1} \int_{-\infty}^{\infty} dz E_z \left(\mathbf{r_1}, \mathbf{r_2} \right) \tag{2.24}$$

$$\mathbf{w}_{\perp} \left(\mathbf{r_1}, \mathbf{r_2}, \tau \right) = \frac{1}{q_1} \int_{-\infty}^{\infty} dz \left[\mathbf{E}_{\perp} \left(\mathbf{r_1}, \mathbf{r_2} \right) - v \int_{t_1}^{t_2} \left(\nabla_{\perp} E_z \left(\mathbf{r_1}, \mathbf{r_2} \right) - \frac{\partial \mathbf{E}_{\perp} \left(\mathbf{r_1}, \mathbf{r_2} \right)}{\partial z} \right) dt \right]. \tag{2.25}$$

The next stage requires partially differentiating Eqn 2.25 by $s = v\tau = vt - z$. It can be seen from this relationship that $\partial/\partial s = -\partial/\partial z$ and $\partial/\partial s = 1/v\partial/\partial z$. Thus the first term can be replaced by $\partial/\partial s = -\partial/\partial z$, and the term in the interior integral becomes the value of the intergrand at τ.

$$\frac{\partial}{\partial s} \mathbf{w}_{\perp} \left(\mathbf{r_1}, \mathbf{r_2}, \tau \right) = \frac{1}{q_1} \int_{-\infty}^{\infty} dz \left[\frac{-\partial}{\partial z} \mathbf{E}_{\perp} + \left(\nabla_{\perp} E_z + \frac{\partial \mathbf{E}_{\perp}}{\partial z} \right) \right]. \tag{2.26}$$

It can be seen that the first and third integrand cancel. Also, the operator $\nabla_{\perp}$ may be moved to the front of the operation without changing the equation, thus

$$\frac{\partial}{\partial s}\mathbf{w}_{\perp}\left(\mathbf{r_1},\mathbf{r_2},\tau\right)=\frac{1}{q_1}\int_{-\infty}^{\infty}dz\nabla_{\perp}E_z=\nabla_{\perp}w_{\parallel}\left(\mathbf{r_1},\mathbf{r_2},\tau\right). \tag{2.27}$$

2.2 Impedances

In a particle accelerator there are a large number of components that have frequency dependent properties, either due to their geometry (for example resonant cavity structures) or material properties (frequency dependent permitivitty/permeability in devices, for example ferrite in normal conducting kicker magnets). In addition many instability mechanisms are strongly modal in nature, thus a frequency analysis of the possible sources of impedance is incredibly valuable.

2.2.1 Beam Coupling Impedance

The longitudinal beam coupling impedance $Z_{\parallel}$ and the transverse beam coupling impedance $Z_{\perp}$ are defined as the Fourier transforms of the single particle wake function, given by

$$Z_{\parallel}\left(\mathbf{r_1},\mathbf{r_2},\omega\right)=\int_{0}^{\infty}d\tau w_{\parallel}\left(\mathbf{r_1},\mathbf{r_2},\tau\right)e^{-j\omega\tau} \tag{2.28}$$

$$Z_{\perp}\left(\mathbf{r_1},\mathbf{r_2},\omega\right)=j\int_{0}^{\infty}d\tau w_{\perp}\left(\mathbf{r_1},\mathbf{r_2},\tau\right)e^{-j\omega\tau} \tag{2.29}$$

where $\omega=2\pi f$. In a similar way the bunch wake function (often called the wake potential) can be related to the longitudinal and transverse beam coupling impedance by considering the Fourier transform of the time dependent bunch current $\lambda\left(\omega\right)=\int_{-\infty}^{\infty}d\tau i_b\left(\tau\right)e^{-j\omega\tau}$, which allows it to be shown that

$$W_{\parallel}\left(\mathbf{r_2},\tau\right)=\int_{-\infty}^{\infty}d\omega Z_{\parallel}\left(\mathbf{r_1},\mathbf{r_2},\omega\right)\lambda\left(\omega\right)e^{j\omega\tau} \tag{2.30}$$

$$W_{\perp}\left(\mathbf{r_2},\tau\right)=\int_{-\infty}^{\infty}d\omega Z_{\perp}\left(\mathbf{r_1},\mathbf{r_2},\omega\right)\lambda\left(\omega\right)e^{j\omega\tau}. \tag{2.31}$$

2.2.2 Transverse Impedances

As can be seen in Eqn. 2.29, the transverse impedance is dependent on the displacement of both the source and witness particles. To evaluate the beam dynamics to only the first order (i.e. only small perturbations in x and y are considered allowing the use of perturbation theory. Coupling terms between x, y are then second order effects and maybe ignored), it is useful to distinguish the components dependent only on the transverse displacement of the source particle and that of the witness particle in the vertical and horizontal planes of the beam. This involves seperating the impedance firstly into horizontal and vertical components. Subsequently the impedance is seperated into components dependent only on the displacement of the source and of the witness particle: these are called the dipolar, or driving impedance, and the quadrupolar, or detuning impedance respectively. In addition it can be shown that constant transverse terms exist in asymmetric structures which should also be taken into account. These are given by

$$Z_{\perp,x}\left(x_1, x_2, \omega\right) = Z_{dip,x}\left(\omega\right) x_1 + Z_{quad,x}\left(\omega\right) x_2 + Z_{const,x}\left(\omega\right) \tag{2.32}$$

$$Z_{\perp,y}\left(y_1, y_2, \omega\right) = Z_{dip,y}\left(\omega\right) y_1 + Z_{quad,y}\left(\omega\right) y_2 + Z_{const,y}\left(\omega\right). \tag{2.33}$$

The relative displacements of the source and witness particles are shown in Fig. 2.2 for clarity.

2.2.3 Geometric Impedance

Geometric impedances are characterised by resonant fields at a resonant frequency, typically attributable to some characteristic dimension of the structure; for example a length of a structure (cavity size, antenna length), which may be part of a vacuum tank, or an internal structure to the device exhibiting the resonance.

As a simple example, consider a cylindrical pillbox cavity of radius r_{cav} and length L connected to a beam pipe of radius r_{pipe} located at the centre of the cavity, as shown in Fig. 2.3. For simplicity we shall assume that the cavity is made from a perfectly conducting material. It shall be assumed that the fields do not propogate along the attached beam

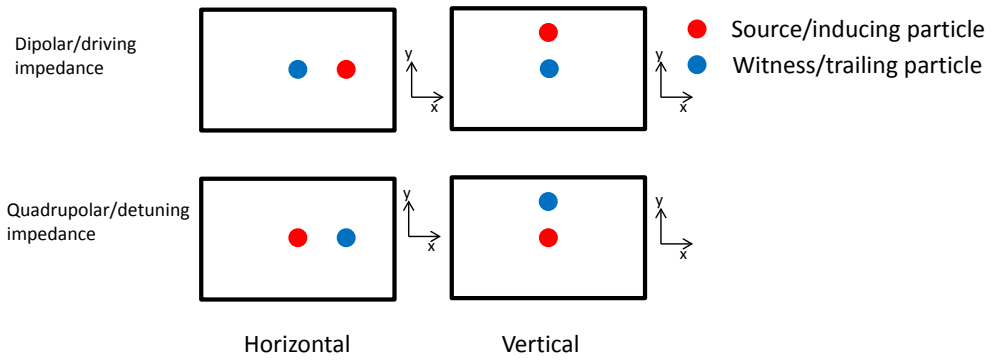

Figure 2.2: The relative displacements of the source particle and witness particle in the horizontal and vertical planes that identify the dipolar/driving and quadrupolar/detuning impedances.

pipe (i.e. for frequencies below beam pipe cutoff). In this example we shall consider a particle travelling on the axis of the beam pipe, and only the longitudinal wakefunction/impedance will be investigated to simplify matters. Further details can be found in [14, 19, 20]. It can be shown that there are two families of resonant modes in a pillbox cavity, TM-type modes and TE-type modes. The TE-type modes have no longitudinal electrical field by definition, and therefore do not contribute to the longitudinal wakefunction for an on axis particle. In a cylindrical coordinate system using coordinates (r, θ, z), the longitudinal electrical field of the n-th order TM-type modes can be shown to be

$$E_{z,n} = E_0 J_n\left(k_r r\right) cos\left(n\theta\right) cos\left(k_z z\right) e^{-j\omega t} \tag{2.34}$$

where E_0 is the magnitude of the electric field, J_n is n-th order Bessel function, $k_z = n\pi/L$, and n is an interger. A wakefunction for each mode can subsequently be defined as $w_{\parallel,n}\left((\mathbf{r}_1, \mathbf{r}_2, \tau\right)$, where the total wakefunction is thus defined as

$$w_{\parallel}\left(\mathbf{r}_1, \mathbf{r}_2, \tau\right) = \sum_{n=0}^{\infty} w_{\parallel,n}\left((\mathbf{r}_1, \mathbf{r}_2, \tau\right) = \frac{-1}{q_1} \sum_{n=0}^{\infty} \int_{-\infty}^{\infty} dz E_{z,n}\left(r, \theta, z\right) \tag{2.35}$$

To evaluate the problem in the frequency domain we shall introduce the RLC parallel circuit model to simplify the frequency domain representation.

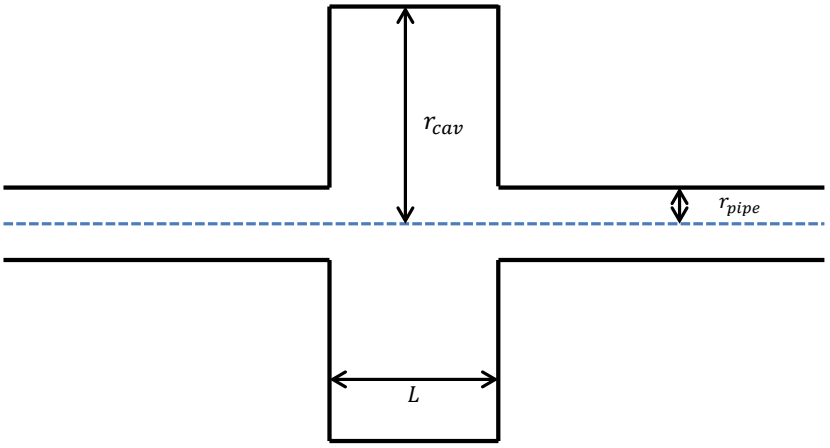

Figure 2.3: Cross section of a cylindrical pillbox cavity with an attached beam pipe.

RLC Circuit Model

We can define any given resonance by an equivalent RLC circuit, which is driven by a current i_b, shown in Fig. 2.4. The symbols represent the equivalent resistance (R_s), inductance (L) and capcitance (C). From this circuit a number of defining parameters are now deduced, and the physical equivalents in the actual cavity are described.

The first parameter to be derived is the resonant frequency of the cavity mode itself ω_{res}. This can be shown (by solving the time varying voltage build up of the circuit in Fig. 2.4) to be given by

$$\omega_{res} = \frac{1}{\sqrt{LC}}. \tag{2.36}$$

Next we define the quality factor of the n-th cavity mode, Q_n. This factor describes the damping of the wakefunction in the cavity for a given mode, larger values indicating a longer damping time. In terms of the cavity it is given by

$$Q_n = \frac{\omega_{res} W}{P_{surf}} = \omega_0 R_s C \tag{2.37}$$

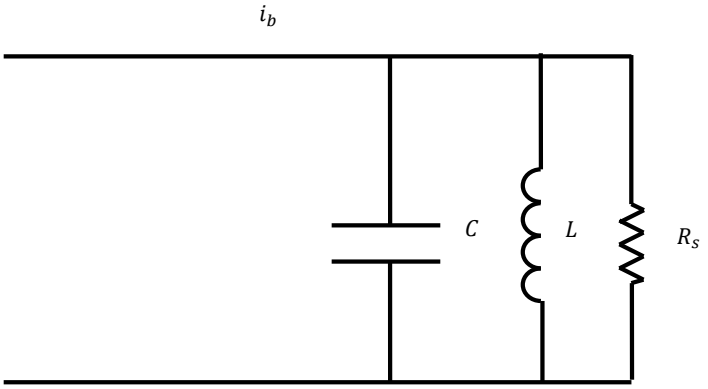

Figure 2.4: The equivalent RLC parallel circuit for a cavity resonance, driven by a current i_b, in this case the beam current.

where $W = \int_V \frac{\epsilon}{2} |\mathbf{E}|^2 \, dV$ is the time-averaged stored electromagnetic energy in the cavity due to the mode (sometimes given as U), $\epsilon = \epsilon_r \epsilon_0$ is the permitivitty, ϵ_r the relative permitivitty, ϵ_0 the permitivitty of free space and P_{surf} is the total losses in the cavity. Commonly the latter is dominated by conductive losses on the cavity walls, but as will be seen in later sections, also includes losses due to other mechanisms. The final figures of merit are the $R_{s,n}/Q_n$ of the cavity mode, and the shunt impedance $R_{s,n}$ of the mode. $R_{s,n}/Q_n$ is given by

$$\frac{R_{s,n}}{Q_n} = \frac{|V_{acc}|^2}{2\omega_{res} W} \tag{2.38}$$

where $V_{acc} = \int_{-\infty}^{\infty} E_{z,n} e^{-j\omega_{res} z/\beta c} dz$ is the effective voltage that a traversing particle sees due to the cavity mode. It can thus be seen that the $R_{s,n}/Q_n$ of a cavity mode gives some ratio of the acceleration of a traversing particle to the stored energy. The shunt impedance $R_{s,n}$ is then given by

$$R_{s,n} = \left(\frac{R_{s,n}}{Q_n} \right) Q_n = \frac{|V_{acc}|^2}{2P_{surf}} \tag{2.39}$$

or an equivalent ratio for power loss in the cavity to acceleration of the particle. From these quality factors is defined a broadband description of the beam coupling impedance at all frequencies due to all modes, given by [21]

$$Z_{\parallel}(\omega) = \sum_{n=0}^{\infty} Z_{\parallel,n}(\omega) = \sum_{n=0}^{\infty} \frac{R_{s,n}}{1 - jQ\left(\frac{\omega}{\omega_{res}} - \frac{\omega_{res}}{\omega}\right)}. \tag{2.40}$$

A number of examples of this type of impedance are shown in Sec. 2.3.1.

2.2.4 Resistive Wall Impedance

The resistive wall impedance is an impedance generated due to the finite conductivity of the material of the beam pipe wall. This can have a number of regimes dependent on whether the skin depth of the material δ, given in the general form by [22]

$$\delta = \frac{1}{\omega}\left[\frac{\mu\epsilon}{2}\left[\left(1 + \left(\frac{\sigma}{\omega\epsilon}\right)^2\right)^{\frac{1}{2}} - 1\right]\right]^{-\frac{1}{2}} \tag{2.41}$$

where $\epsilon = \epsilon^{'} + j\frac{\sigma}{\omega}$, σ is the conductivity of the material and μ is the permeability of the material. If σ is large or at low frequencies then this simplifies such that

$$\delta(\omega) = \sqrt{\frac{2}{\mu_0\mu_r(\omega)\sigma\omega}} \tag{2.42}$$

where μ_0 being the permeability of free space, μ_r the relative permeability of the material, σ the conductivity of the wall material. Conversely for the case of poor conductors and high frequencies, δ asymptotically approaches a value given by

$$\delta = \frac{2}{\sigma}\left(\frac{\epsilon}{\mu}\right)^{\frac{1}{2}} \tag{2.43}$$

.

The different regimes of resistive wall impedance are typically given by the following requirements; $delta$ is: much smaller than the thickness of the beam pipe wall [23], comparable to the thickness of the beam pipe wall [24, 25] or much larger than the thickness of the beam pipe wall [26, 27], in addition to the pipe radius and the thickness of the

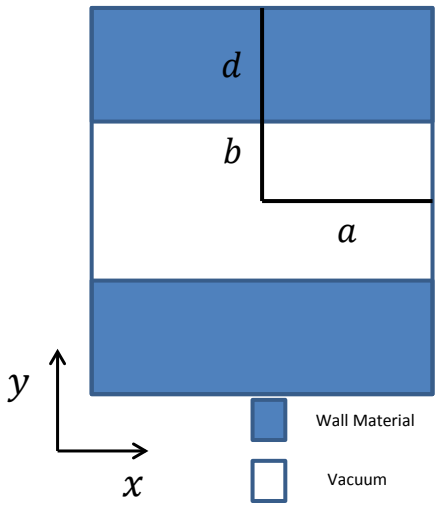

Figure 2.5: The geometry of the Tsutsui resistive wall formalism.

pipe wall (such as the case of a pipe wall of infinite thickness). In this instance, σ is the conductivity of wall material. It can also be shown that the shape of the beam pipe cross section also plays a significant role in defining the impedance [28, 29].

Here we shall not attempt a comprehensive summary of the various resistive wall impedance models, but simply give an example of a model in the form of the Tsutsui formalism to give a sense of how changing the wall conductivity affects the resistive wall impedance. A considerably more detailed overview of this derivation can be found in App. G [26, 30]. Consider two parallel plates of a resistive material, as shown in Fig. 2.5, between which moves a source particle of charge q_1 moving with velocity $\mathbf{v} = \beta c\hat{\mathbf{z}}$. In this case it shall be assumed that $\beta = 1$.

The longitudinal and dipolar impedances for this model can be seen in Fig. 2.6 for a comparison between two sample materials. It can be seen that for the given frequency range there are two regimes for both the longitudinal and transverse impedance (although the difference is more pronounced for the transverse impedance). For high frequencies, the classical thick wall formalism (as in [23]) applies, as the skin depth of the material is much smaller than the beam pipe aperture and the layer's thickness. Susequently this

formalism would predict a greater impedance at lower frequencies, as it gives $Z_\perp \propto \omega^{-1/2}$. At lower frequencies however this is not seen to be the case. This is due to the following reasons:

1. At high frequencies the beam induced current effectively flows on the surface of the material, thus the distance between the beam image current and the witness particle is constant at value b. Thus the transverse impedance seen is determined by the change in skin depth δ which is proportional to $\omega^{-1/2}$

2. At low frequencies the beam image current effectively flows some distance inside the wall material, greater than b. This increases the distance between the beam image current and the witness particle, thus decreases the force seen by the witness particle. This causes the real component of the transverse impedance to become linear with respect to ω. It is important to note this mechanism, as it indicates that this phenomena occurs at a "low" frequency for any thickness of wall material, even for a wall of infinite thickness.

3. The transition region occurs when these two phenomena become of similar magnitude. The frequency at which the real component of the transverse impedance reaches it's maximum can be shown to be proportional to $1/(\sigma b^2)$.

2.3 Example of the Effects of Wakefields

To give context to the effects that wakefields have on both the beam and equipment within a particle accelerator, two types of wakefield/impedance driven phenomena are discussed here. The first, beam-induced heating, is an example of beam induced wakefields having an effect on the machine itself and contributing to heat loads due to the energy lost by the beam and subsequently dissipated within the surrounding equipment. The second, beam instabilities, covers a number of examples of instability mechanisms that may be driven by wakefields, in particular due to the harmonic nature of particle and beam behaviour in a circular accelerator.

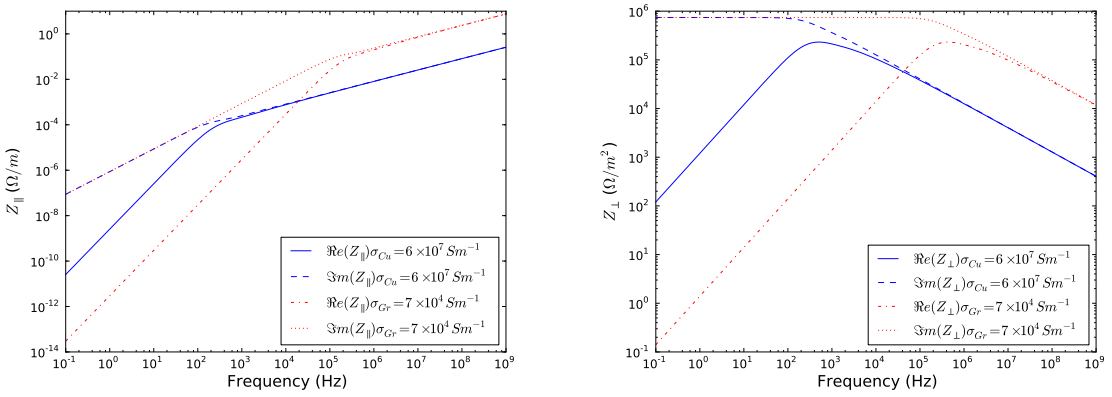

(a) (b)

Figure 2.6: Examples of the longitudinal (a) and transverse (b) resistive wall impedance per unit length of a beam pipe of aperture $a = 2\ cm$ made of of either copper ($\sigma = 6 \times 10^7\ Sm^{-1}$) or graphite ($\sigma = 7 \times 10^4\ Sm^{-1}$).

2.3.1 Beam Induced Heating

Defining and Deriving Power Loss in Circular Accelerators

When a charged particle interacts with a wakefield it's energy changes due to the field that it sees. Assuming a beam with a longitudinal distribution $\rho(\tau)$, normalised such that $\int d\tau\rho(\tau) = I_b$, where I_b is the beam current. Now a normalised longitudinal distribution ρ_n is introduced, such that $\rho = N_b f_{rev} e \int d\tau\rho_n$. Thus the energy change of the distribution ρ traversing a pipe for a distance L is given by [23, 31]

$$\Delta E = -\left(f_{rev} e N_b\right)^2 \int_{-\infty}^{\infty} d\tau^{'} \rho_n\left(\tau^{'}\right) \int_{-\infty}^{\infty} d\tau \rho_n\left(\tau\right) W_{\parallel}\left(\tau^{'} - \tau\right). \tag{2.44}$$

Written in terms of the Fourier transformed quantities this becomes

$$\Delta E = \frac{-1}{2\pi}\left(f_{rev} e N_b\right)^2 \int_{-\infty}^{\infty} d\omega \left|\lambda\left(\omega\right)\right|^2 \Re e\left[Z_{\parallel}\left(\omega\right)\right] \tag{2.45}$$

where

$$\lambda\left(\omega\right) = \frac{1}{\sqrt{2\pi}} \int_{-\infty}^{\infty} d\tau \rho_n\left(\tau\right) e^{j\omega\tau}. \tag{2.46}$$

For a mode expansion representation of the wakefunction as a sum of loss factors, the total energy change can be written as

$$\Delta E = \left(f_{rev} e N_b\right)^2 \sum_{n=0}^{\infty} k_n \left|\lambda\left(\omega_n\right)\right|^2 . \tag{2.47}$$

These terms are valid only for a single pass of the beam through the impedance (i.e. for a linear accelerator). In the case where the beam traverses the same impedance multiple times (i.e. a circular accelerator) it is necessary to take into account the wakefields induced by previous traversals. In this case the energy lost by the beam due to traversing the pipe is given by

$$\Delta E = -\left(f_{rev} e N_b\right)^2 \int_{-\infty}^{\infty} d\tau^{'} \rho_n\left(\tau^{'}\right) \int_{-\infty}^{\infty} d\tau \rho_n\left(\tau\right) \sum_{q=0}^{\infty} W_{\parallel,q}\left(q\frac{C}{c} + \tau^{'} - \tau\right) \tag{2.48}$$

where C is the circumference and q sums over revolutions. Here the term summed over gives the power loss due to the interaction with circulating bunches with the preceeding bunches wakefields. In general, impedance is a more useful property than wakefields for purposes of heating calculations. Using the Poisson sum formalism and the following identity

$$\sum_{n=-\infty}^{\infty} F\left(na\right) = \frac{1}{a} \sum_{p=-\infty}^{\infty} \tilde{F}\left(\frac{2\pi p}{a}\right) \tag{2.49}$$

where $F(\tau)$ and $\tilde{F}(\omega)$ are arbitary Fourier transformed pairs. This relationship shows that summing a function at regular intervals a is equal to summing over its Fourier transformed counterpart at regular intervals $\frac{2\pi}{a}$. In particular a useful special case is

$$\sum_{n=-\infty}^{\infty} e^{-j\omega\tau} = 2\pi \sum_{p=-\infty}^{\infty} \delta\left(x - 2\pi p\right) . \tag{2.50}$$

Thus for the total impedance over the accelerator $Z_{\parallel}$ the energy loss is

$$\Delta E = -\frac{\omega_0}{2\pi}\left(f_{rev} e N_b\right)^2 \sum_{n=-\infty}^{\infty} \left|\lambda\left(p\omega_{rev}\right)\right|^2 \Re e\left[Z_{\parallel}\left(p\omega_{rev}\right)\right] . \tag{2.51}$$

To find the power loss of the bunch distribution it is simply necessary to normalise by the revolution frequency. In addition we use the property of the longitudinal impedance that

$$\Re e\left[Z_{\parallel}\left(\omega\right)\right] = \Re e\left[Z_{\parallel}\left(-\omega\right)\right] \tag{2.52}$$

to give the power lost by a single bunch in a circular accelerator as

$$P_{loss,single} = -2\left(f_{rev}eN_b\right)^2 \sum_{n=-\infty}^{\infty} \left|\lambda\left(p\omega_{rev}\right)\right|^2 \Re e\left[Z_{\parallel}\left(p\omega_{rev}\right)\right]. \tag{2.53}$$

To consider the case of more than one bunch in a circular machine, it is possible to consider Eqn. 2.48, but in this case assume a time difference between the successive summed wakes as $\frac{C}{n_{bunch}c}$, in this case assuming that the bunches are equally space around the machine, giving the energy loss for one bunch in a machine with n_{bunch} is

$$\Delta E_{bunches} = -\left(f_{rev}eN_b\right)^2 \int_{-\infty}^{\infty} d\tau^{'} \rho_n\left(\tau^{'}\right) \int_{-\infty}^{\infty} d\tau \rho_n\left(\tau\right) \sum_{q=0}^{\infty} W_{\parallel,q}\left(q\frac{C}{n_{bunch}c} + \tau^{'} - \tau\right). \tag{2.54}$$

Following the previous derivation this leads to a power loss due to a single bunch in a train of

$$P_{loss,sbt} = -2n_{bunch}\left(f_{rev}eN_b\right)^2 \sum_{n=-\infty}^{\infty} \left|\lambda\left(pn_{bunch}\omega_{rev}\right)\right|^2 \Re e\left[Z_{\parallel}\left(pn_{bunch}\omega_{rev}\right)\right]. \tag{2.55}$$

Subsequently taking the sum over all n_{bunch} produces the total power loss

$$P_{loss} = -2\left(f_{rev}en_{bunch}N_b\right)^2 \sum_{n=-\infty}^{\infty} \left|\lambda\left(pn_{bunch}\omega_{rev}\right)\right|^2 \Re e\left[Z_{\parallel}\left(pn_{bunch}\omega_{rev}\right)\right]. \tag{2.56}$$

If the wakefield effectively decays to zero in less than the distance between two succeeding bunches, then this is simply equivalent to an integral. This indicates that for sharp resonant impedances that last over multiple bunch intervals/turns of the machine, only the sum formalism is valid.

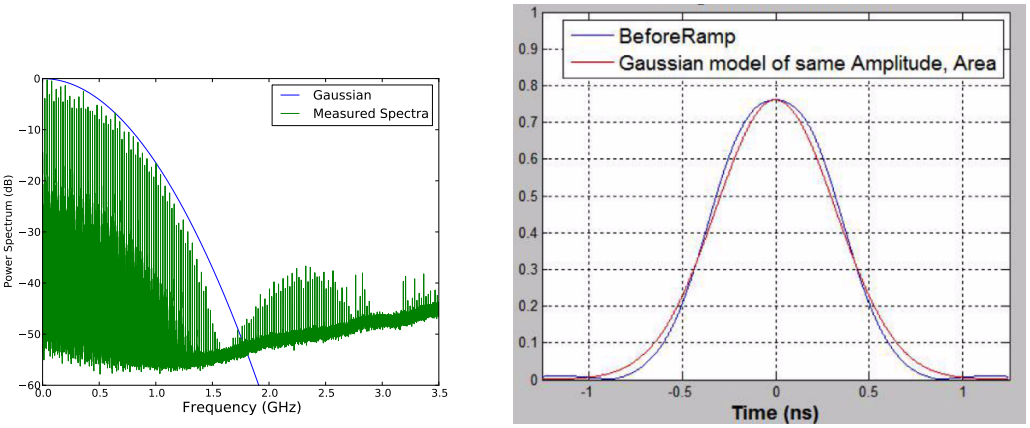

(a) (b)

Figure 2.7: A comparison of (a) a measured beam power spectrum and a Gaussian bunch of the same bunch length in the frequency domain and (b) the resulting time domain beam profile. The Gaussian has a bunch length ($4\sigma_z$ = 1.2 ns). Measured spectrum taken by P. Baundrenghien et al [32]. Time domain fit taken from E. Metral [33].

Longitudinal Beam Profiles

As shown by the derivations in Section 2.3.1, asides from the longitudinal impedance of the device under consideration, the longitudinal profile of the circulating bunches also contributes to the power loss in the machine. In past works it has generally been assumed that bunches in accelerators have a Gaussian profile [34], given by

$$\lambda\left(t\right) = e^{\frac{-t^2}{2\sigma^2}} \tag{2.57}$$

where $4\sigma_z = t_b$ is the RMS bunch length, when approaching the analytical treatment of beam induced heating, for both single-bunch and multiple bunches. Recent measurements of the power spectrum of particle beams, especially in the LHC [32], have shown characteristics that the Gaussian profile does not predict, for example the high frequency secondary peak as seen in Fig. 2.7(a). To make more realistic predictions of heat loss due to beam impedance in the machine it is thus necessary to find bunch profiles which reproduce this behaviour.

A number of different longitudinal bunch profiles have been investigated in the past. Here we shall look at 3 other bunch profiles; a parabolic line density (see Eqn. 2.58), $\cos^2$ (see Eqn. 2.59) and a water-bag (see Eqn. 2.60).

$$\rho(t) = \int_{-\infty}^{\infty} \lambda(\omega) e^{j\omega t} d\omega = \begin{cases} 1 - \left(\frac{2t}{t_b}\right)^2 & \text{if } |t| \leq t_b/2 \\ 0 & \text{if } |t| > t_b/2 \end{cases} \tag{2.58}$$

$$\rho(t) = \int_{-\infty}^{\infty} \lambda(\omega) e^{j\omega t} d\omega = \begin{cases} cos^2\left(\frac{\pi t}{t_b}\right) & \text{if } |t| \leq t_b/2 \\ 0 & \text{if } |t| > t_b/2 \end{cases} \tag{2.59}$$

$$\rho(t) = \int_{-\infty}^{\infty} \lambda(\omega) e^{j\omega t} d\omega = \begin{cases} \sqrt{1 - \left(\frac{2t}{t_b}\right)^2} & \text{if } |t| \leq t_b/2 \\ 0 & \text{if } |t| > t_b/2 \end{cases} \tag{2.60}$$

The corresponding frequency domain profiles are given by Eqn. 2.61 for the parabolic profile, and Eqn. 2.62 for the $\cos^2$ profile. The water-bag profile is not transformable analytically, thus the frequency domain profile is obtained by numerical Fourier transform.

$$\lambda(f) = 2sin(\pi f t_b)\left(\frac{-1}{2\pi f} - \frac{8}{(2\pi f)^3 t_b^2}\right) + \frac{8}{(2\pi f)^2 t_b} cos(\pi f t_b) \tag{2.61}$$

$$\lambda(f) = \frac{sin(\pi f t_b)}{\pi f t_b [1 - (f t_b)]}. \tag{2.62}$$

The comparison of these bunch profiles in the time domain are shown in Fig. 2.8. Note all bunch currents are normalised to their peak value. The corresponding current and power spectrums are shown in Fig. 2.9. There are several things to note about these spectra; firstly that the non-infinite time-domain distribution of the non-Gaussian bunch profiles gives rise to a number of high frequency lobes in the power spectrum, and secondly the interval of these nodes depends heavily on the bunch profile.

To illustrate more clearly the effect of changing the bunch length on the power spectrum, a number of bunch profiles and the corresponding power spectra with different bunch lengths are shown in Fig 2.10. Firstly, consider a Gaussian bunch profile. It can be seen in Fig. 2.10 that by increasing the bunch length that the magnitude at high frequencies is decreased quite substantially. If we consider a finite bunch profile (non-Gaussian), we note that we have high frequency lobes. The peak frequency of these lobes depends on the bunch length, as illustrated using a parabolic bunch profile for bunch lengths

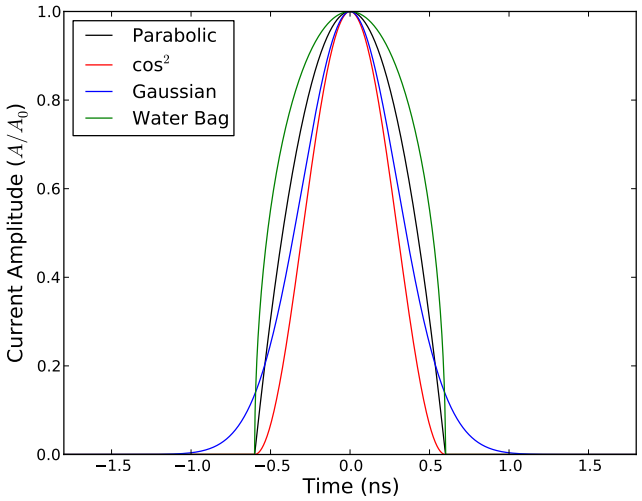

Figure 2.8: The longitudinal bunch profile of a number of bunch distributions. Note that all of these are normalised to have a peak bunch current of 1. For the Gaussian distribution the bunch length is the 4σ value. The bunch length $t_b = 1.2\ ns$.

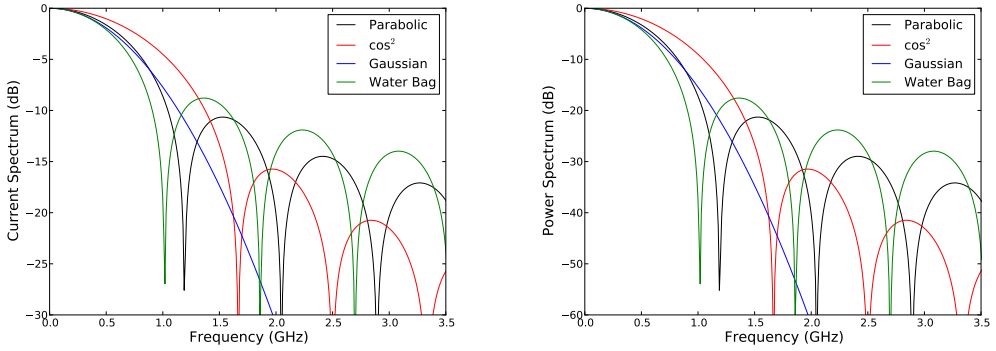

(a) (b)

Figure 2.9: The frequency domain (a) current spectrum and (b) power spectrum for a number of different bunch profiles with a bunch length $\tau_b = 1.2\ ns$.

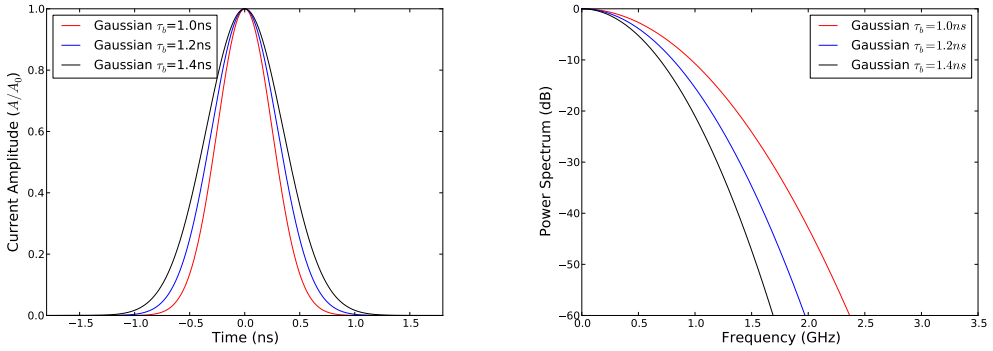

(a) (b)

Figure 2.10: (a) The longitudinal profile and the (b) associated bunch power spectrum for a number of bunch lengths assuming a Gaussian bunch profile.

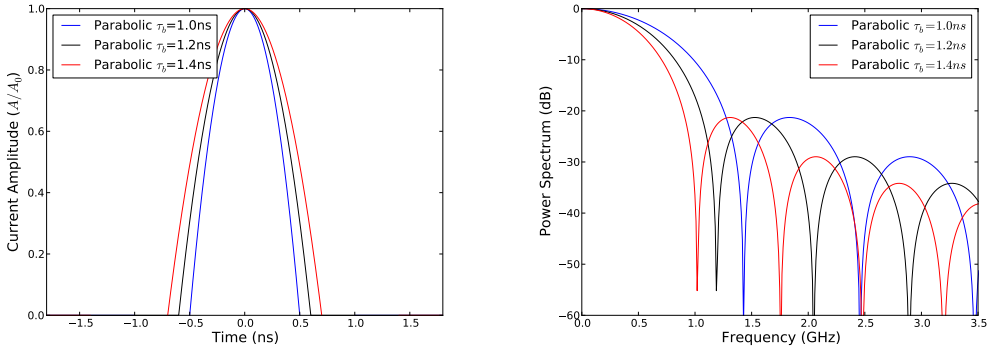

(a) (b)

Figure 2.11: (a) The longitudinal profile and the (b) associated bunch power spectrum for a number of bunch lengths assuming a parabolic bunch profile.

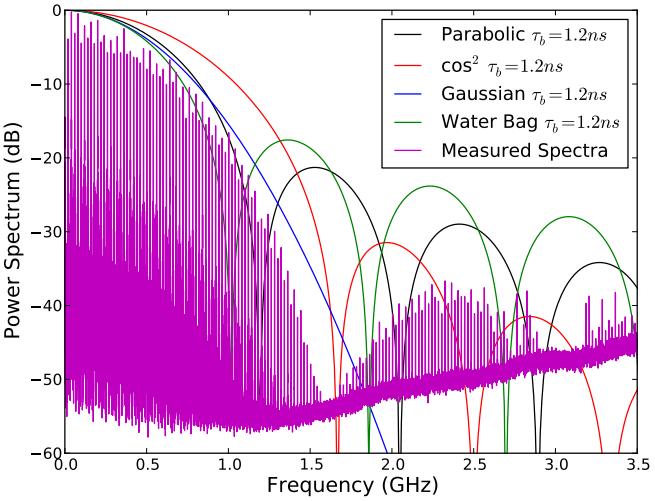

Figure 2.12: A comparison of a measured beam power spectrum and a number of analytical bunch profiles assuming a bunch length of 1.2 ns.

$\tau_b = 1\ ns, 1.2\ ns, 1.4\ ns$ in Fig. 2.11. As the bunch length is increased the lobes move to lower frequencies, and the width of the first shoulder decreases. Similar behaviour is observed with the cos^2 and water-bag bunch profiles.

Finally, a comparison of a measured bunch power spectra and the analytical power spectra is shown in Fig. 2.12. It can be seen that whilst it is possible to replicate some of the properties of the measured spectrum, an exact replication is non-trivial. Further investigation into the appropriate bunch profile is ongoing.

Beam induced heating due to a low Q impedance

For an impedance with a characteristic Q that is small (Q $<$ 10), it can be seen that the impedance peak will interact substantially with a number of beam harmonics (see Fig. 2.13) due to the broad frequency range it occupies.

Further investigation of the longitudinal beam spectrum reveals that there is significant structure between the major harmonics (which are due to the bunch spacing of the beam) which can be attributed to the other time structures of the beam, for example the bunch train spacing, or the interval between the pilot bunch train and the subsequent bunch

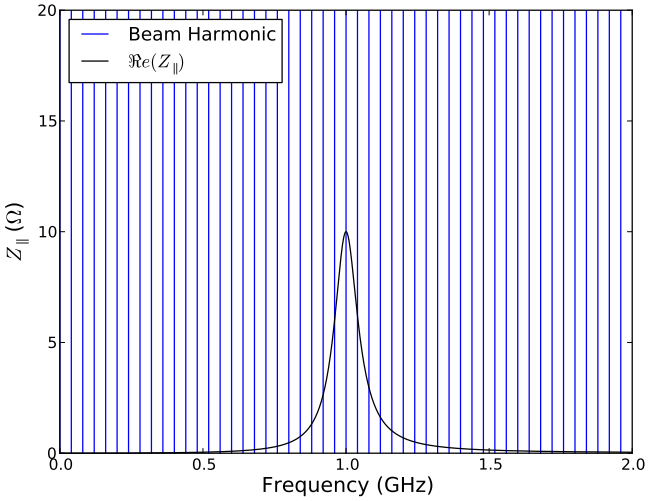

Figure 2.13: The beam harmonics of a beam with a bunch spacing of 25ns overlayed on the real component of the longitudinal impedance an example of a low Q impedance ($R_s = 10\ \omega$, Q = 10, $f_{res} = 1\ GHz$). The blue lines represent the frequency of a beam harmonic, not necessarily the magnitude of the power spectrum at that point. Note that a number of beam harmonics overlay non-zero impedance values.

train. As such the treatment of the estimation of beam losses requires a broad spectrum approach. If we consider Eqn. 2.56 we see that we can treat the power losses in an integral form. We can observe a number of properties using this assumption. The power loss is proportional to the beam properties in the following manner:

1. $P_{loss} \propto N_b^2$

2. $P_{loss} \propto n_{bunch}$

Beam induced heating due to a high Q impedance

In contrast to the overlap of the beam spectrum with a low Q impedance, for a high Q impedance only one beam harmonic lies upon the resulting impedance to any significant degree. This is illustrated in Fig 2.14. If we consider Eqn 2.56 and consider the situation where

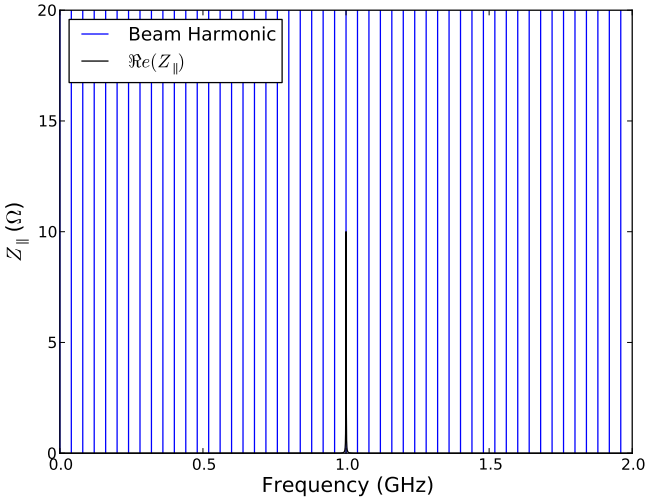

Figure 2.14: The beam harmonics of a beam with a bunch spacing of 25 ns overlayed on the real component of the longitudinal impedance of a sample of a high Q impedance ($R_s = 10\ \Omega$, Q = 1000, $f_{res} = 1\ GHz$). The blue lines represent the frequency of a beam harmonic, not necessarily the magnitude of the power spectrum at that point. Note that only a single beam harmonic overlays a non-zero impedance values.

$$\left(2\left|\lambda\left(p\omega_{rev}n_{bunch}\right)\right|^2 \Re e\left(Z_\parallel\left(p\omega_{rev}n_{bunch}\right)\right)\right) = \begin{cases} \left(2\left|\lambda\left(\omega_{res}\right)\right|^2 \Re e\left(Z_\parallel\left(\omega_{res}\right)\right)\right) & \text{if } p\omega_{rev}n_{bunch} = \omega_{res} \\ 0 & \text{if } p\omega_{rev}n_{bunch} \neq \omega_{res}. \end{cases} \tag{2.63}$$

It can then be seen that Eqn 2.56 simplifies to

$$P_{loss} = \left(\omega_{rev}eN_b n_{bunch}\right)^2 \left(2\left|\lambda\left(\omega_{res}\right)\right|^2 \Re e\left(Z_\parallel\left(\omega_{res}\right)\right)\right). \tag{2.64}$$

The following properties can subsequently be seen as a result:

1. $P_{loss} \propto N_b^2$
2. $P_{loss} \propto n_{bunch}^2$, provided that the resonant frequency of the resonance continues to coincide with a beam harmonic.

Some Examples of the Beam-Induced Heating

In this section we shall illustrate some important factors that have been covered in previous sections. In particular, the interaction of different bunch profiles, at different bunch lengths, with an example cavity resonance will be covered in some detail to illustrate how the estimated heating can change drastically depending on higher frequency lobes in the beam current spectrum. In addition, the heating due to two particle beams in the same vacuum chamber shall be briefly covered for interest.

The Effect of Bunch Length on Power Loss

As can be seen in Figs. 2.9 and Fig 2.11, the bunch profile and the bunch length can significantly alter the magnitude of the beam current at higher frequencies. To illustrate this, let us consider two resonant impedances, one broadband Z_{bb} and one narrow band Z_{nb} impedance, characterised by having a low-Q and a high-Q respectively. Both impedances shall have the same resonant shunt impedance $R_s = 100\ \Omega$. The broadband impedance shall have a $Q_{bb} = 1$, and the narrow band impedance $Q_{nb} = 1000$. The resonant frequency will be changed to illustrate effects in different regimes of the bunch length and of different bunch profiles.

We shall use the Gaussian bunch profile and the cos^2 bunch profile for these examples. The Gaussian is useful to illustrate the effect of just changing the bunch length, and the cos^2 due to the presence of a high frequency lobe in it's frequency domain current spectrum. The cos^2 frequency domain current profile is given by

$$I\left(\omega\right) = \frac{sin\left(\omega\tau_b/2\right)}{\omega\tau_b/2\left[1-\left(\omega\tau_b/2\right)^2\right]}. \tag{2.65}$$

First we shall consider a narrow band impedance which has a resonant frequency $\omega_0 = 2\ GHz$ which falls upon a beam harmonic such that $\omega_0 = n\omega_{rev}$, where n is an integer. It should be noted that for other cases the contribution of these sources of heating is negligible due to the small beam current at this frequency. There are two extreme cases; that of $\omega_0 \gg 1/\tau_b$, in which it can be seen that the current spectrum will be negligible

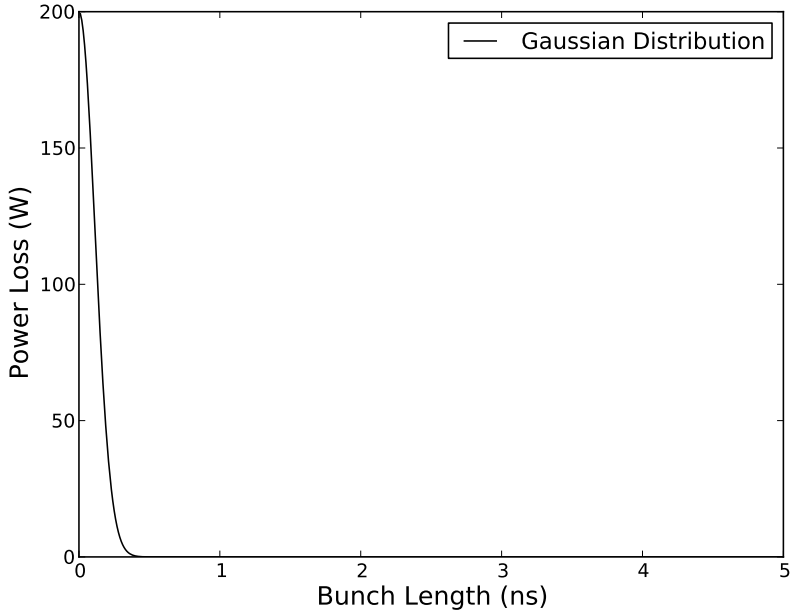

Figure 2.15: The change in power loss due to a narrow band resonance characterised by $\omega_0 = 2\ GHz$, $R_s = 100\ \Omega$, $Q = 1000$ with a Gaussian bunch distrbution of different lengths.

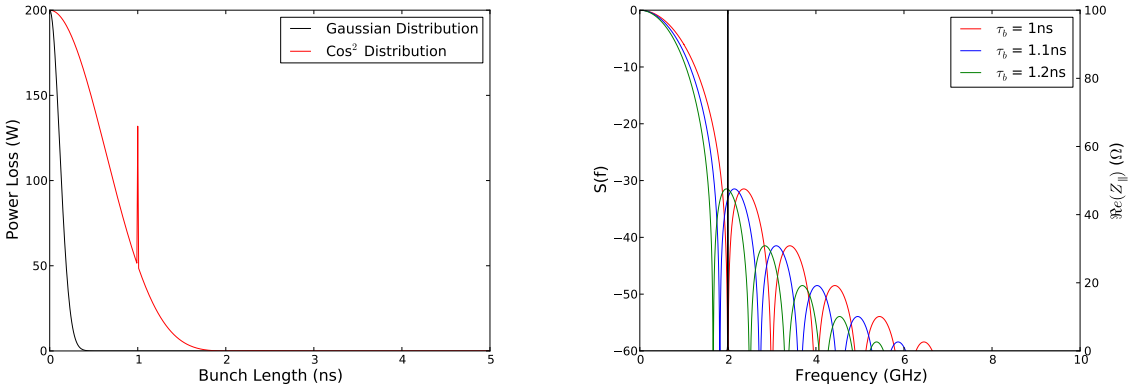

(a) (b)

Figure 2.16: (a) The change in power loss due to a narrow band resonance characterised by $\omega_0 = 2\ GHz$, $R_s = 100\ \Omega$, $Q = 1000$ interacting with a $\cos^2$ bunch distribution with different bunch lengths. The impedance and the beam power spectrum are shown in (b) to illustrate how this relates to the power loss.

at the frequency of the impedance, and $\omega_0 \ll 1/\tau_b$ where the beam current spectrum is essentially the same as the DC spectral component. The transition in this intervening regime is shown in Fig 2.15, assuming a bunch current of 1A. It can be seen that in this case the heating falls drastically as the bunch length increases.

If we consider a $\cos^2$ distribution we instead see the effect of the secondary lobes in the beam current spectrum. The power loss with bunch length is shown in Fig. 2.16(a) in comparison to that of the Gaussian profile. The beam power spectrum for a number of different bunch lengths are shown with the real component of the longitudinal impedance in Fig. 2.16(b). Here it can be clearly seen that the intersection of the secondary lobe with the resonant impedance causes a peak in the power lost by the beam, highlighting the neccessity to be aware of the frequencies of resonant impedances with relation to the beam harmonics.

For the broadband heating we shall consider a resonant impedance defined by the following parameters, $\omega_0 = 2\ GHz$, $Q = 1$, $R_s = 100\ \Omega$. To account for the multiple beam harmonics that will interact with the resonance, it is assumed that the beam harmonics in this case occur at 20 MHz intervals. The impedance and the beam power spectrum is shown in Fig. 2.17(b) and the resulting power loss in Fig. 2.17(a) where it can be seen

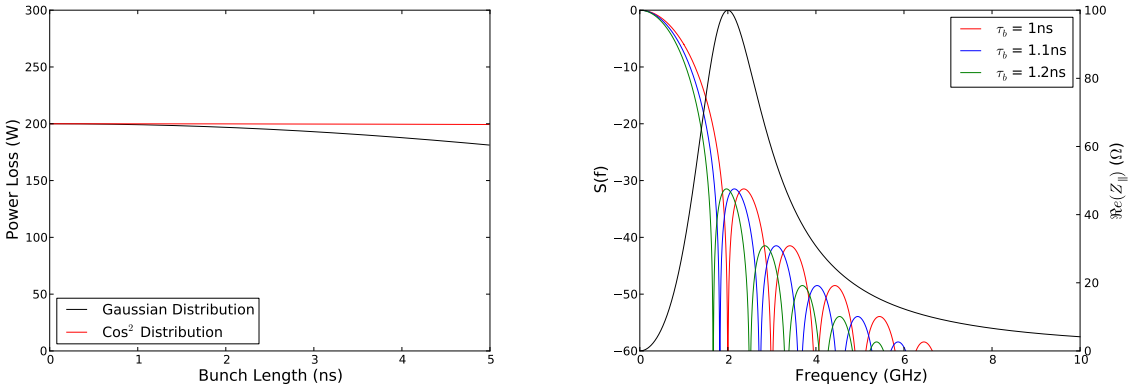

(a) (b)

Figure 2.17: (a) The change in power loss due to a narrow band resonance characterised by $\omega_0 = 2\ GHz$, $R_s = 100\ \Omega$, $Q = 1$ interacting with a $\cos^2$ bunch distribution with different bunch lengths. The impedance and the beam power spectrum are shown in (b) to illustrate how this relates to the power loss.

that the power loss decreases slowly with increasing bunch length. This is due to the significant contribution to the power loss at low frequencies, in which the component of the beam power spectrum decreases only marginally due to the increasing bunch length.

Beam-Induced Heating due to two traversing beams

Previous work [35] has investigated the effect of two beams in a vacuum on the beam-induced heating. This is restated here for the sake of completeness.

To begin, consider the two currents $I_{b1} = I_0 e^{i\phi_1}$ and $I_{b2} = -I_0 e^{i\phi_2}$ representing two counter rotating beams. I_0 represents the beam current, and $\phi_{1/2}$ the phase of beam 1 and beam 2 respectively. Each beam also sees a seperate potential when it traverses the impedance, given by $V_{b1} = \int_{b1} E_z e^{i\omega_0 z/c} dz$ and $V_{b2} = \int_{b2} E_z e^{i\omega_0 z/c} dz$ respectively. By Ohms law it can then be seen that

$$\begin{pmatrix} V_{b1} \\ V_{b2} \end{pmatrix} = \begin{bmatrix} Z_{11} & Z_{12} \\ Z_{21} & Z_{22} \end{bmatrix} \begin{pmatrix} I_{b1} \\ I_{b2} \end{pmatrix}. \tag{2.66}$$

The power loss due to both beams can then be seen to be

$$P_{loss} = \begin{pmatrix} V_{b1} & V_{b2} \end{pmatrix} \begin{pmatrix} I_{b1} \\ I_{b2} \end{pmatrix}^{*}. \tag{2.67}$$

In the worst case scenario, the values of the impedance matrix are real, and are equal in value to the peak values of the resonant impedance

$$Z_{11} = 2R_s^{b1};\ Z_{22} = 2R_s^{b2};\ Z_{12} = Z_{21} = 2\sqrt{R_s^{b1}R_s^{b2}}. \tag{2.68}$$

The power loss then becomes

$$P_{loss} = I_0^2 2\left(R_s^{b1} + R_s^{b2} - 2\sqrt{R_s^{b1}R_s^{b2}}cos\left(\delta\phi\right)\right) \tag{2.69}$$

where $\delta\phi = \phi_1 - \phi_2$ is the phase difference between beam 1 and beam 2. This can be found relatively easily by comparing the distance δs from a collision IP (location of experiments in the LHC) of the machine. Assuming the beams are ultrarelativistic $\delta\phi = \omega_{rev}2\delta s/c$. It can then be seen that the the last term may either reduce or increase the power loss depending on whether $cos\left(\delta\phi\right) = 1$ or $cos\left(\delta\phi\right) = -1$ respectively.

2.3.2 Beam Instabilities

Beam Instabilities is the collective term for a various group of mechanisms which contribute to the degradation of beam properties during the circulation of a beam within a synchrotron. These can typically be divided into a number of different subgroups, summarised below:

1. Coherent Effects - Occuring due to the bulk oscillation of the bunch(es)
2. Incoherent Effects - Occuring due to a mechanism that affects particles dependent on their position within the bunch
3. Single-Bunch - Occuring only on the scale of a single bunch
4. Multi-Bunch - Occuring due to coupling of the motion between multiple bunches.

The mechanisms driving these instabilities are multitudinous and of which beam coupling impedance is just one. Others include space charge effects (both direct and indirect) [36, 37], beam-beam interactions [38], electron cloud [39], intrabeam scattering [40, 41] amongst others. Here we shall give a brief overview of how these effects cause a degradation of the beam quality.

Tune Shift and Tune Spread

As seen in Sec. A.2, the transverse equation of motion can be viewed as an oscillatory system. If the particles experience an additional perturbative force F_x^{pert} due to an external mechanism, not due to the machine optics, it's equation of motion (in the horizontal plane, for example) can be written as

$$\frac{d^2x}{ds^2} + \left(\frac{Q_{0,x}}{R}\right)^2 x = \frac{F_x^{pert}}{\beta^2 E_{total}}, \tag{2.70}$$

where Q_{0x} is the unperturbed betatron tune and E_{total} is the particle energy. This subsequently leads to a perturbed oscillation frequency (assuming the force is linearised), characterised by the equation

$$\frac{d^2x}{ds^2} + \left(\frac{Q_{0,x} + \Delta Q_{pert,x}}{R}\right)^2 x = 0. \tag{2.71}$$

where $\Delta Q_{pert,x}$ is the part of the betatron frequency caused by the perturbing force. The perturbed tune may subsequently be further divided into coherent (the motion of the bunch centroid) and incoherent (motion of individual particles), such that $\Delta Q_{pert,x} = \Delta Q_{pert,x}^{coh} + \Delta Q_{pert,x}^{incoh}$. This seperation leads to the creation of a tune spread in a machine, in which the tune of the beam covers an area of the tune diagram as shown in Fig. 2.18. In this case particles may be lost when this tune shift causes them to lie upon a major resonance of the beam optics, thereby causing coherent oscillation growth and ultimately particle loss. This leads to negative effects such as emittance growth and lower beam lifetimes.

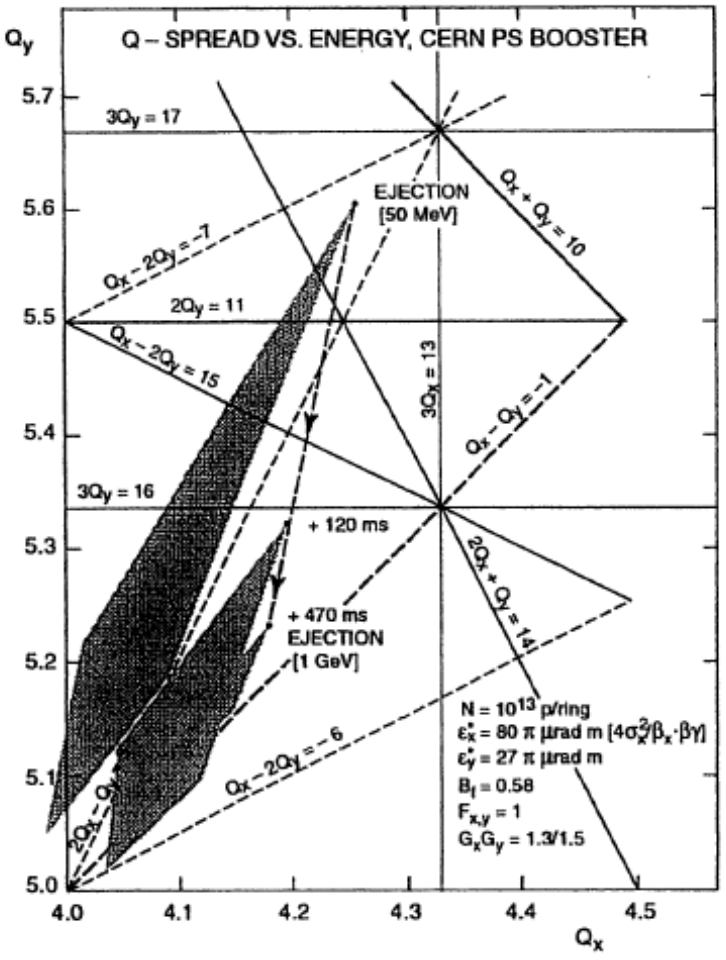

Figure 2.18: A tune diagram illustrating the unperturbed tune of a machine, and the resulting perturbed tune and the tune spread as a result of direct space charge interactions on a bunch. Note that the tune spread has caused some particles to lie upon a major resonance harmonic. Taken from K. Schindl [42].

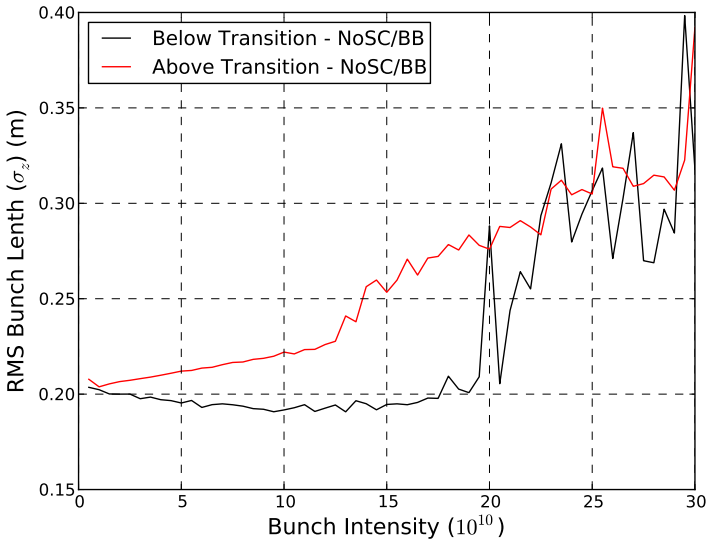

Figure 2.19: The change in the bunch length of a proton beam in the SPS due to the effects of a broadband resonator impedance ($f_{res} = 1\ GHz$, $R_s = 10\ \Omega$, $Q = 1$) without space charge. Note that the bunch length increases when the beam is above transition, and decreases below transition, as the bunch intensity is increased.

Longitudinal Single Bunch Instabilities

Similar to the change in the equations of transverse motion for particles, considering the induced fields in the longitudinal plane produces a perturbation in the longitudinal motion also. This can be thought of as an additional force alongside the electromagnetic force applied by the accelerating cavities, leading to two interesting phenomena. These are potential well distortion, occuring at bunch intensities below some stability criteria, and longitudinal mode coupling instability (LMCI) above some stability criteria.

The potential well distortion is a direct effect of the incoherent synchrotron tune shift (again, similar in nature to the tune shifts experienced in the transverse plane), which is responsible for a change in bunch length. This reveals itself from measurements by a change in the bunch length with increasing bunch intensity, as shown in Fig. 2.19. It should be noted that, depending on the source of impedance, the bunch length may increase or decrease depending on whether the bunch is above or below the transition energy of the accelerator.

LMCI occurs when a certain intensity threshold is crossed in the accelerator, leading to a regime known as *turbulent bunch lengthening*. In this mechanism the eigenfrequencies of the natural modes of oscillation of the particles within the RF bucket are shifted due to the changing potential resulting from the induced wakefield. In high intensity bunches two neighbouring modes may have their frequencies shifted to such an extent that the modes merge into one, thus leading to a case where the modes no longer have only a damped solution, but also a exponentially growing solution. This subsequently leads to the bunch oscillations becoming unstable. As can be seen in Fig. 2.19, the stable bunch intensity limit is higher below transition than above, in the case of LMCI with a broadband resonator impedance.

Transverse Single Bunch Instabilities

In the transverse plane a number of instability mechanisms apply, which can be separated into two forms, those that occur on a time scale much shorter than the synchrotron period, and those that occur on a longer time scale than the synchrotron period. In both cases the leading particles of the bunch, often called the head of the bunch, drives an oscillation in the end, or tails of the bunch. This gives these instabilities their names, the fast head-tail instability, or transverse mode coupling instability (TMCI), and the head-tail instability.

In the case of the fast head-tail instability, there are a number of transverse oscillation modes (see Fig. 2.20 for examples of the transverse oscillation modes of a bunch), which as with the LMCI experience some frequency shift due to the presence of a wakefield. If the shift is large enough, two of these modes may again couple together, causing an exponential growth of the transverse size of the bunch to occur.

In the case of the head-tail instability, the movement of a particle from the head of the bunch to the tail and vice versa becomes important in determining the rate of growth of any unstable modes, and whether any stabilisation mechanisms have sufficient time to damp the growth. This means that the chromaticity of the beam now takes on a great importance, as this relates the betatron tune to the longitudinal motion. This leaves the option of changing the chromaticity of the beam to act as an additional stability mechanism.

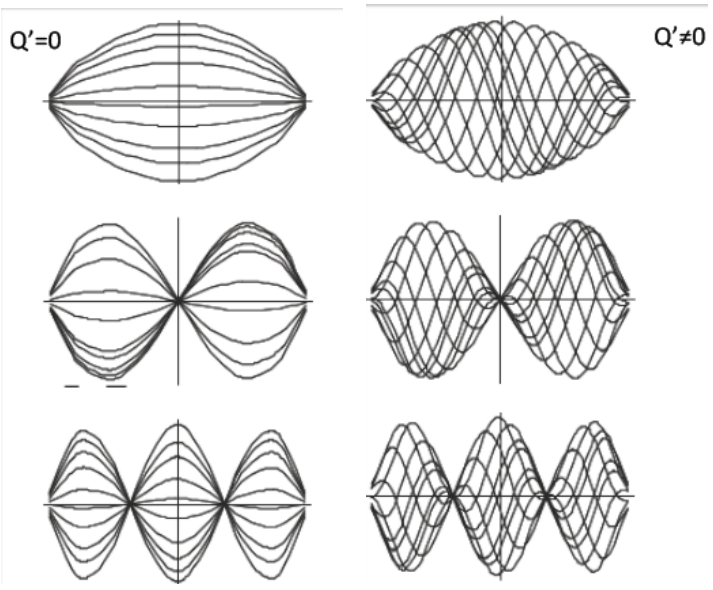

(a) (b)

Figure 2.20: Examples of a number of modes of headtail oscillations without 2.20(a) and with 2.20(b) chromaticity. Note that radial and azimuthal modes may occur, as may coupled modes, in which the motion of the horizontal and vertical planes is coupled. Images courtesy of G. Rumolo [43].

Coupled Bunch Instabilities

In addition to single bunch instabilities, it is possible in machines where multiple bunches circulate, and possessing wakefields that do not damp in the spacing between bunches (typically caused by high Q resonant impedances), that the motion of the bunch centroids themselves may become coupled together, thus driving what are called coupled bunch instabilities (TCBI for the transverse plane, LCBI for the longitudinal plane).

This can be understood by imagining the beam as possessing M equi-spaced, equi-populated bunches. This beam will then have M possible modes of oscillation (in each case with the phase shift of $\delta\phi = 2\pi n/M$ for $n = 0, 1, 2..., M-1$) with a characteristic frequency of ω_M, which may be driven by an impedance at some frequency ω_0. If $\omega_0 \approx n\omega_M$ where n is an integer, then the wakefield due to the impedance may drive the oscillation either in a damped fashion (wakefield is out of phase with the oscillation of the mode) or an anti-damped fashion (wakefield is in phase with the oscillation of the mode).

In the latter case, this driven oscillation may cause particle losses unless the oscillation is damped via an external mechanism, such as Landau damping (stability brought upon by a spread of the oscillation frequencies in a bunch [44]) or the use of a damper [45]. This motion can occur in both the longitudinal and transverse planes of motion.

2.4 Conclusion

In this section we have introduced the concept of wakefields and impedance, both in the lognitudinal and the transverse planes. We have shown that in the transverse plane the impedance may be represented as that dependent on the displacement of the source particle, that dependent on the displacement of the witness particle, and a constant term that is indepedent of the displacement of both. We have briefly covered instabilities that may be driven by beam coupling impedance in the longitudinal and transverse planes. Finally we have studied in depth the phenomenon of beam-induced heating, how it varies depending on the nature of the beam coupling impedance of the device where the heating occurs, on the lognitudinal profile of the bunches, and on the bunch train structure of the machine. This will be used extensively in later chapters when the model of longitudinal distribution of the bunch is shown to be highly important in determining the estimated heat loss, as is the bunch length used for collisions. Using this introduction to the wakefields and impedance, the methods of which they can be measured with both beam and using bench-top measurements shall be discussed, and the ways in which the impedance can be evaluated using simulation tools described.

Chapter 3

Beam Based Measurements of Beam Coupling Impedance

Beam based measurements are an incredibly useful measurement technique for beam coupling impedance studies. The direct measurements of impedance (either device specific or of the entire machine) provides a reliable comparison to bench top measurements, simulations and analytical calculations.

There are a number of measurement methods for both the longitudinal and transverse planes using the RF systems and beam instrumentation commonly placed in accelerators. A short introduction to some of the most commonly used of these methods is given here.

3.1 Longitudinal Beam Impedance Measurements

To understand the longitudinal impedance measurements a short introduction to longitudinal motion is given in App. A.1. Here is introduced some of the basics of longitudinal motion of a charged particle within an RF bucket.

3.1.1 Potential Well Distortion with Bunch Intensity

The equation for the longitudinal motion of a charged particle in an RF bucket can be linearised (assuming a small amplitude of the movement within the bucket) and solved to

find the so called incoherent synchrotron angular frequency [46, 47], that is its oscillation in phase space, given by,

$$\omega_s = \frac{\omega_{RF}}{\beta}\left(\frac{\eta V_T cos\bar{\phi}}{2\phi E/e}\right)^{\frac{1}{2}} \tag{3.1}$$

where $\omega_{RF} = h\omega_0$ is the RF frequency, ω_0 is the revolution frequency, h is the harmonic number of the RF, $\eta = \alpha_c - \gamma^{-2}$ is the slip factor, $\alpha_c = \gamma_t^{-2}$ is the momentum compaction factor, γ_t is the transition energy gamma factor, $E = \gamma E_0$ is the total particle energy, E_0 is the rest energy of the particle, $\bar{\phi}$ is the stable phase angle and V_T is the total voltage seen by the beam. For an empty bucket (i.e. no particles present) the voltage present is just that of the RF voltage V_{RF}, giving an associated synchrotron frequency ω_{s0}. We can subsequently see from Eqn. 3.1 that we have the ratio

$$V_T = V_{RF}\left(\frac{\omega_s}{\omega_{s0}}\right)^2. \tag{3.2}$$

Additionally the bunch length σ_z and the energy spread of the bunch $\Delta E/E$ can be shown to be related by

$$\sigma_z = \frac{|\eta|\, c}{\beta\omega_s}\frac{\Delta E}{E} \tag{3.3}$$

within the linear approximation. If we assume that the emittance of the bunch is preserved (usually the case in a proton machine), i.e. $L\Delta E = constant$, Eqn. 3.2 leads to

$$\sigma_z^2\omega_s = \sigma_{z0}^2\omega_{s0}. \tag{3.4}$$

where σ_{z0} is the effective bunch length for an empty bucket. The resulting induced voltage of the bunch depends heavily on the nature of the impedance on which the beam interacts with. In this case we shall illustrate the characteristics of the bunch lengthening with a simple inductive impedance ($Z = j\omega L$). The voltage induced by a bunch with a parabolic line density over a purely inductive impedance, results in a synchrotron frequency given by

$$\omega_s^2 = \omega_{s0}^2 \left[1 - \frac{C}{B^3} \frac{I_b}{hV_{RF} cos\bar{\phi}} \left(\left| \frac{Z}{n} \right| - \frac{gZ_0}{2\beta\gamma^2} \right) \right] \tag{3.5}$$

where $c = \frac{3}{\pi^2}$ is a constant dependent on the bunch profile, $B = f_0 2L$ is the bunching factor, given by the product of the revolution frequency and the bunch length in seconds (or alternatively the ratio of the bunch length to the revolution time), I_b is the bunch current, $g = 1 + 2ln\left(\frac{b}{a}\right)$ is the direct space charge factor, b is the beam pipe radius, a is the beam radius, and Z_0 (377Ω) is the impedance of free space.

If we consider an ultrarelativistic beam ($\gamma \to \infty$), the space charge factor $g = 0$. Then, considering the value of $\bar{\phi}$ (i.e. whether the bunch is above transition $cos\bar{\phi} > 0$, or below transition $cos\bar{\phi} < 0$), the bunch length increases with the larger bunch current above transition, and decreases below transition. All variables other than Z/n may be measured directly using various instrumentation.

Generalisation of this method to a general complex impedance shows that it is the imaginary component of the longitudinal impedance that contributes to the induced voltage, thus being the component of the impedance measured using this method.

3.1.2 Synchronous Phase Shift

As discussed in Sec. 2.3.1, a particle circulating in a circular accelerator losses energy due to the interaction with impedances in the machine. If the particle is not undergoing acceleration, it can be seen that to keep the same energy, the particle must have a phase relative to the RF that ensures that the energy losses due to wakefields are equal to the energy gained during the traversal of the RF cavities, given by the equivalence of the energy gain by transit and the energy loss by traversal,

$$U = qeV sin\phi \tag{3.6}$$

where U is the total energy lost by a particle per turn, q is the unit charge, e is the electron charge, V is the RF voltage amplitude and ϕ is the synchronous phase. The total energy lost is the sum of all energy losses in the machine, given by

$$U = -e^2 N_b k \tag{3.7}$$

$$= -e^2 N_b \sum_n k_n \tag{3.8}$$

$$= -e^2 N_b \sum_n \Re e \left(Z_{\parallel,n} (\omega) \right) |\lambda (\omega)|^2 \, d\omega \tag{3.9}$$

where k_n is the kick factor of device n in the accelerator and $Z_{\parallel,n}$ is the longitudinal impedance of device n. It can be seen that this allows the measurement of the impedance of the whole device. In addition where the movement of a device is permissible and can be carried out during operation (in collimation systems or insertion devices for example) it is possible to determine the impedance of specific devices by the change in their contribution to the total loss factor. Examples of this measurement method can be found in [48, 49].

3.2 Transverse Beam Impedance Measurements

For a bunch interacting with a transverse impedance there are two commonly used methods of measuring the transverse impedance - the variance of the coherent betatron tune shift with bunch intensity and the change of growth/decay rate of head-tail instabilities with the chromaticity of the beam [50].

When a bunch is exposed to a tranverse dipolar impedance $Z_\perp$, it undergoes a complex frequency shift in betatron frequency

$$\Delta\omega_\beta = \frac{N_p e c}{4\sqrt{\pi}\omega_\beta (E/e) T_0 \sigma_t} j \left(Z_\perp \right)_{eff} \tag{3.10}$$

where N_p is the number of particles in the bunch, E is the energy, T_0 is the revolution time, $\sigma_t = \sigma_z / c$ is the bunch length in the time domain, $\omega_\beta = 2\pi Q f_{rev}$ is the betatron frequency and $\left(Z_\perp \right)_{eff}$ is the effective transverse impedance. This is given by the impedance convolved with a weighting function h_m which is determined by the transverse bunch profile

$$\left(Z_\perp \right)_{eff} (\omega_\xi) = \int_{-\infty}^{\infty} Z_\perp (\omega) \, h_m (\omega - \omega_\xi) \, d\omega. \tag{3.11}$$

As an example, for the 0-mode coherent bunch oscillation and assuming a gaussian bunch profile the weighting function can be written as

$$h_0(\omega) = \frac{\sigma_t}{\sqrt{\pi}} e^{(\omega\sigma_t)^2}. \tag{3.12}$$

It can be seen from Eqn. 3.12 that the function is centred on ω_ξ (the chromatic frequency) which is dependent on the chromaticity ξ and the phase slip factor η as

$$\omega_\xi = \xi \frac{\omega_\beta}{\eta}. \tag{3.13}$$

Eqn 3.10 indicates that the imaginary component of the effective transverse impedance contributes to a real coherent tune shift, and the real component to an imaginary tune shift, visible as a growth/decay time in the oscillation. For a broadband impedance ($Q = 1$), at low frequencies it is possible to assume that $\Im m\left(Z_\perp\right) \approx const.$ It then follows that this is directly proportional to the real tune shift which can be obtained by measuring the coherent tune as a function of bunch intensity.

This can be thought of by considering the complex tune shift ($\Delta\omega_\beta = \omega_\beta + j\omega_i$) and considering the change to the solution of the transverse equation of motion

$$\begin{aligned} e^{j(\omega+\Delta\omega)t} &= e^{j\left(\omega+\omega_\beta+j\omega_i\right)t} \\ &= e^{j\left(\omega+\omega_\beta\right)t} e^{-\omega_i t} \\ &= e^{j\left(\omega+\omega_\beta\right)t} e^{t_g} \end{aligned} \tag{3.14}$$

where $t_g = f(\Im m(Z_\perp)_{eff})$ is the time constant.

3.2.1 Tune shift change with bunch intensity

The real component of the solution to Eqn 3.10 can be related to the integer betatron tune by

$$\Delta Q = \frac{\Omega - \omega_\beta}{\omega_0} \approx \frac{1}{\omega_0} \frac{N_p e c^2}{4\sqrt{\pi}\omega_\beta \left(E/e\right) T_0 \sigma_t} \Im m \left(Z_\perp\right)_{eff}, \tag{3.15}$$

where Ω is the measured betatron frequency. It can be seen that, by altering the bunch population, the tune shift ΔQ can be measured and subsequently the value for $\Im m\left(Z_{\perp}\right)_{eff} = Z_{\perp}^{dip} + Z_{\perp}^{quad}$ can be obtained.

3.2.2 Growth time change with chromaticity

Similarly to the tune shift measurements, we consider the imaginary component of the solution. Similarly to a harmonic oscillator, the imaginary part of the solution denotes a growing/damping time of the oscillation, τ, in this case given by

$$\frac{1}{\tau} = -T_0 \frac{N_p e c^2}{4\sqrt{\pi}\omega_\beta \left(E/e\right) T_0 \sigma_t} \Re e\left(Z_{\perp}\right)_{eff} . \tag{3.16}$$

$\Re e\left(Z_{\perp}\right)_{eff}$ is dependent only on the chromaticity ξ, being zero at $\xi = 0$ and different from zero for other values of chromaticity. Depending on whether the measurements are carried out above or below transition this produces either a damping for positive chromaticity above transition and growth below transition, and vice versa for negative chromaticity.

3.3 Conclusion

In this chapter we have introduced ways in which it is possible to measure the longitudinal and transverse impedance (real and imaginary components) of circular accelerators. This has been done to give an awareness of the ways in which it is possible to measure either the impedance of the machine as a whole, or in the case of devices that are moveable, their contribution to the machine impedance. Not all devices are suitable to bench-top meausrements, either due to structure (long, heavy, beam path not condusive to bench top measurements), safety concerns (maybe radioactive) or there not being sufficient time to carry out the measurements, thus beam based measurements are an exceptionally powerful tool in impedance evaluation.

Chapter 4

Bench Top Measurements of Beam Coupling Impedance

Due to the sensitivity of the beam coupling impedance to the boundary conditions of the equipment used, it is necessary to utilise different measurement techniques to fully analyse the impedance of accelerator structures.

4.1 Low Q-factor Impedances

For structures that are expected to contain mostly low Q-resonances (i.e. resistive wall impedance) it is appropriate to use the coaxial wire method [51–53], sometimes also called the stretched wire method. This method was first proposed by Sands and Rees in 1974 [51], before revisions in technique proposed by Gluckstern [52] and Vaccaro [53] more recently. This method relies on the similarity of the electromagetic field profile due to an ultrarelativistic charged particle and that of a short electrical pulse sent along a coaxial wire.

A moving charged particle produces an electromagnetic field in an arc transverse to its direction of motion, where the angle of the arc opening is inversely proportional to the relativistic factor of the particle γ. For an ultrarelativistic particle ($\gamma \rightarrow \infty$), the field becomes entirely perpendicular to the direction of motion. If we place a conductive wire

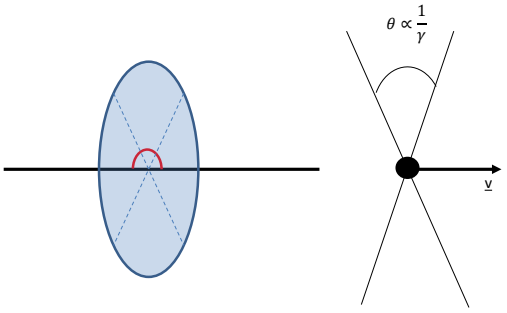

Figure 4.1: Comparison of the electromagnetic field profile of a moving charged particle and a short time pulse propagating along a coaxial wire.

along the same path we would expect the charged particle to take (in most cases this is well represented by a straight wire), a short electrical pulse sent along this wire would propogate in the TEM (Transverse Electrical and Magnetic field) mode, producing a field profile similar to that emitted by the ultrarelativistic charged particle (see. Fig. 4.1)

4.1.1 Classical Coaxial Wire Method

The classical coaxial wire method, first proposed in it's present form by V. Vaccarro in 1990 [53], is a transmission method that measures the complex transmission coefficient of a DUT (Device Under Test) made up of the equipment whose impedance is to be measured and a coaxial wire passing through it.

The experimental setup is as shown in Fig. 4.3. Firstly the external circuit (i.e. everything which is not the DUT such as VNA, cables, transition between connections etc.) is matched to the characteristic impedance of the coaxial line inside the DUT. This is done by measuring the reflection coefficient Γ for the setup with only one port connected to the DUT and the other end terminated by an open connection. Knowing the characteristic impedance of the VNA and associated cables (typically $Z_{c0} = 50\ \Omega$), we can easily calculate the characteristic impedance of the DUT, Z_c, from the relation,

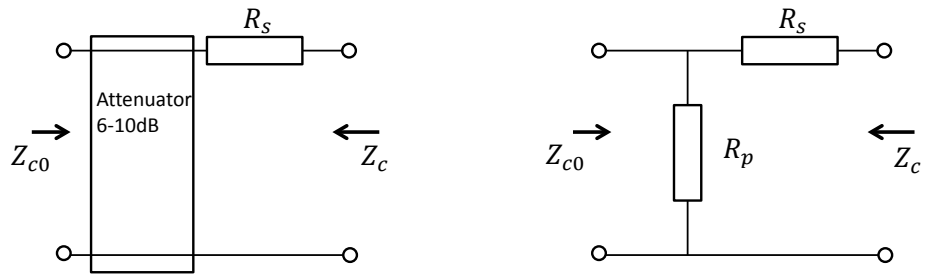

(a) (b)

Figure 4.2: The resistive networks for matching a DUT to the attached measuring network (VNA and connecting cables). (a) shows series resistive matching and (b) shows a two way matching network.

$$\Gamma = \frac{Z_c - Z_{c0}}{Z_c + Z_{c0}}. \tag{4.1}$$

It is then possible to electrically match the characteristic impedance by adding a resistive network between the DUT and the external circuit. This may be done in two ways:

1. Adding resistors in series just before the DUT to resistively match the characteristic impedance (as seen by the DUT) of the VNA and associated measurement setup to that of the DUT, such that the series resistance $R_s = Z_c - Z_{c0}$. Often an attenuator is used to reduce the effect of reflections from the mismatch between the VNA and the resistor, shown in Fig. 4.2(a).

2. The use of two way matching, using a parallel (R_p) and series (R_s) resistor, as shown in Fig. 4.2(b). The values for these resistances are given by

$$R_p = Z_{c0}\sqrt{\frac{Z_c}{Z_c - Z_{c0}}}$$
$$R_s = Z_c - \frac{Z_c R_p}{Z_c + R_p}$$

It is possible to use physical matching also using transition cones but these are costly, time consuming to construct, work only for a restricted frequency range and require new cones for each piece of equipment measured. And as can be seen in Fig. 4.4, matching with a resistor is highly effective at removing the presence of reflections in coaxial measurements.

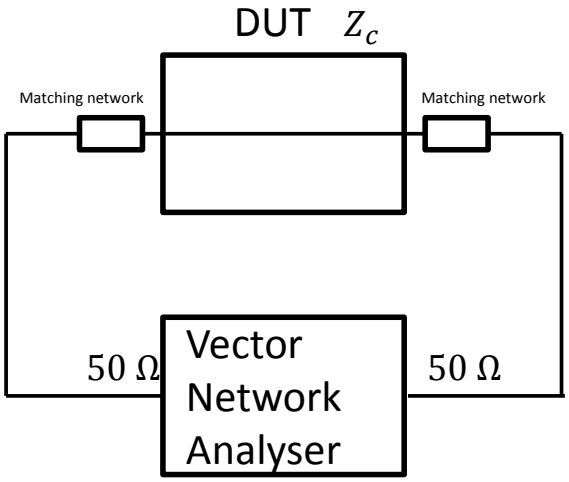

Figure 4.3: Experimental setup for a measurement of the beam coupling impedance using the classical coaxial wire method.

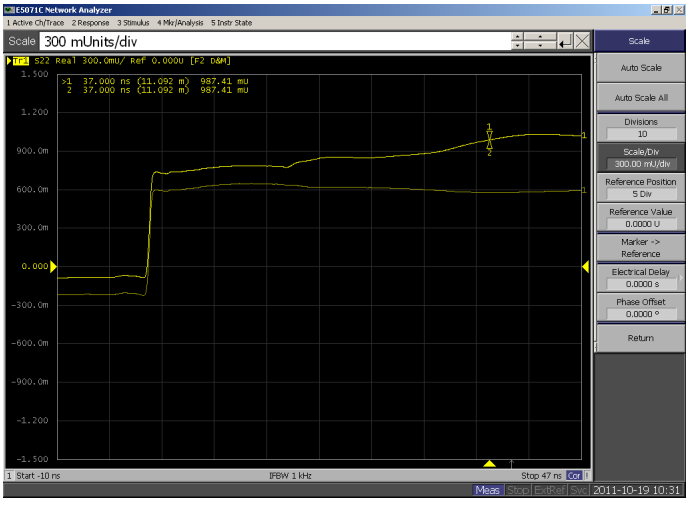

Figure 4.4: An example of a reflection measurement made with and without matching resistors. The faded line (lower trace) is the measurement with matching, the bold line (upper trace) that without. The reduction in the reflection can be seen due to the flatter line after the initial reflection.

The values that we wish to measure to evaluate the beam coupling impedance of a device are the scattering parameters of the resulting circuit, in particular S_{21}, the normalised transmission parameter through the DUT. S_{21} is calculated by taking the measured transmission parameter $S_{21,DUT}$ and dividing it by the transmission parameter through a reference line of the same physical length as the DUT,

$$S_{21} = \frac{S_{21,DUT}}{S_{21,REF}}. \tag{4.2}$$

The effect of this is to correct the measured phase change in the DUT to be that only caused by the imaginary component of the beam coupling impedance.

There are subsequently a number of ways to evaluate the beam coupling impedance of the DUT depending on it's expected properties. For devices that are expected to have either a small impedance, or those that are physically very short in length, it is possible to use the so called lumped impedance formula [54, 55];

$$Z = 2Z_c \frac{1 - S_{21}}{S_{21}}. \tag{4.3}$$

For distributed impedances, it is suitable to use the so called log formula (called so due to the exponential attenuation of the signal causing a log function to appear in the evaluation) [54–56],

$$Z = -2Z_c ln\left(S_{21}\right). \tag{4.4}$$

For long components or measurements at very high frequencies there exists the improved log formula. This takes into account more completely the electrical length of the device, given by

$$Z = -2Z_c ln\left(S_{21}\right)\left(1 + j\frac{ln\left(S_{21}\right)}{2\Theta}\right) \tag{4.5}$$

where $\Theta = 2\pi\frac{L}{\lambda}$ is the normalised electrical length of the device, L the length of the device. It is possible to see that the lumped impedance formula can be used when $\Theta \leq 1$, and the improved log formula becomes useful for $\Theta \geq 5$ [56].

4.1.2 Resonator Coaxial Wire Method

An alternative method for measuring the beam coupling impedance is by using the so called resonator method. The setup for this method is similar to that of the classical coaxial wire method, except that the matching resistor network between the VNA and DUT is replaced by a weak capacitive coupling ($S_{11} < 0.5dB$, remembering that $0dB$ means full reflection, i.e. no coupling) at both ends of the DUT. This then produces a structure which resonates at frequencies where the wavelength corresponds to the classical closed structure form,

$$\lambda = \frac{2L}{n} \tag{4.6}$$

where λ is the wavelength of the resonance, n the harmonic of the resonance and L the length of the device.

The resonant method enables accurate measurement of the transmission losses due to the real longitudinal impedance. Additional advantages are that no matching is required, and a large number of mechanical uncertainties (electrical connections, consistency of calibration) can be avoided. However it can be seen that the frequency resolution is limited due to the length of the DUT so the method is not recommended as the only measurement method for structures expected to contain high-Q, narrowband resonances. It can however be used to corroborate the results obtained using the classical method.

For each resonant peak, the loaded Q-factor and the frequency of the resonance are measured. For a weak coupling at both ends of the DUT, we can write the coupling coefficient k as

$$k = \frac{|S_{21}|}{1 - |S_{21}|}. \tag{4.7}$$

The difference between the unloaded Q-factor, Q_0 , and the loaded Q-factor, Q_L, is a function of k. The loaded Q is the Q of the DUT resonance coupled with the measurement circuitry, and the unloaded Q the Q of the DUT resonance in isolation. We can get an approximate correction by using the formula

$$Q_0 = Q_L \left(1 + k\right). \tag{4.8}$$

Subsequently the measured line attenuation (in Np/m) is then calculated

$$\alpha_m = \frac{\pi}{\lambda Q_0}. \tag{4.9}$$

Note that this attenuation includes both that from the beam coupling impedance as well as that due to the finite resistance of the wire material. We can estimate the attenuation due to the wire material as

$$\alpha_w = \sqrt{\pi \rho_w \epsilon f} \frac{1}{d ln\left(D/d\right)} \tag{4.10}$$

where ρ_w is the wire resistivity, ϵ the wire permitivitty, f the frequency, d the diameter of the inner conductor and D the diameter of the outer conductor (typically the vacuum beam pipe diameter). At very low frequencies the finite skin depth of the inner conductor would also have to be taken into account. Using the corrected attentuation $\alpha = \alpha_m - \alpha_w$, the real longitudinal impedance per unit length can be found to be

$$\Re e\left\{Z\right\} = 2 Z_c \alpha \tag{4.11}$$

It is more involved to calculate the imaginary impedance using the resonant method. In particular it is necessary to calculate the resonant frequencies of a pipe open at both ends of the same length of the DUT made of a good conducting material (i.e. the physical length is equal to the electrical length). This allows the comparison to the measured resonant frequencies of the DUT, the difference between which is dependent on the imaginary impedance.

Considering the complex impedance of the two measurements, Z_{DUT} for the DUT and Z_{REF} for a perfectly conducting reference pipe, they can be written as

$$Z_{DUT} = R + jX_1 = Z_1 e^{j\phi} \tag{4.12}$$

$$Z_{REF} = jX_2 = Z_2 e^{j.0} \tag{4.13}$$

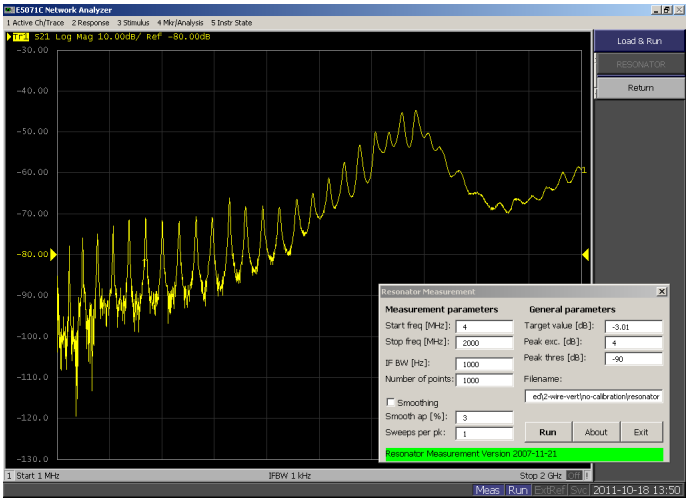

Figure 4.5: An example of the resonance pattern seen whilst performing measurements using the resonant method. Each peak corresponds to one data point in the final measurements. Taken from measurements of the LHC injection kicker magnets.

where R is the resistive component of the DUT impedance, $X_{1/2}$ the imaginary component of the impedance (DUT and reference pipe respectively), ϕ is the angle of DUT impedance projected onto a complex plane and $Z_2 = \sqrt{R^2 + X^2}$. If we consider a measured value depedent on the impedance, for example the transmission parameter S_{21} at a resonant peak, we have the following relations

$$S_{21}^{DUT} = S_0 e^{j(\omega_1 t + \phi)} \tag{4.14}$$

$$S_{21}^{REF} = S_0 e^{k(\omega_2 t)} \tag{4.15}$$

where S_0 is some normalised scalar, $\omega_{1/2}$ is the frequency of the resonance and $t = \frac{L}{c}$. Thus for a pair of corresponding peaks from resonance measurements for which we have measured ω_1 and ω_2 we can equate $S_{21}^{DUT} = S_{21}^{REF}$ and thus show

$$\phi = t\left(\omega_2 - \omega_1\right). \tag{4.16}$$

Subsequently we can see that

$$X = Z_{DUT} sin\phi = R\frac{sin\phi}{cos\phi} = Rtan\phi \tag{4.17}$$

where $R = \Re e(Z)$.

4.1.3 Transverse Impedance Measurements

The above methods give a general impression of how to carry out coaxial wire measurements of the impedance of accelerator components. Directly applied as described they allow the measurement of the longitudinal impedance of a DUT. However, from a beam stability point of view, it is also interesting to look at the transverse impedance of a device. In particular it would be useful to have a method of determining the vertical/horizontal dipolar (or driving) impedance and the vertical/horizontal quadrupolar (detuning) impedance of any device. In this section we describe how to do this for structures with top/bottom, left/right symmetry and then generalise to asymmetric structures, with illustration from simple examples evaluated using simulations.

To allow a complete explanation of how to verify the methods of measuring transverse impedances, let us first consider the general form of the m-th order ($m = 0, 1, 2, ...$) longitudinal beam coupling impedance, given by [23, 57]

$$\bar{Z}_m = \frac{-1}{I^2} \int dV \bar{\mathbf{E}}_\mathbf{m} . \bar{\mathbf{J}}^*_\mathbf{m} \tag{4.18}$$

where $\bar{J}_m$ is the current density of the source. For a beam propogating along the z-axis with an offset a and moment $cos\,(m\theta)$,

$$\bar{\mathbf{J}}_\mathbf{m} = \frac{I}{\pi a^{m+1}\,(1+\delta_{m0})} \delta\,(r-a)\,cos\,(m\theta)\,exp\,(j\,(\omega t - kz))\,\mathbf{e_z}. \tag{4.19}$$

The electromagnetic field associated with a given current source $\bar{\mathbf{J}}_\mathbf{m}$ is $\left(\bar{\mathbf{E}}_\mathbf{m}, \bar{\mathbf{H}}_\mathbf{m}\right)$.

It can be seen that any different azimuthal components of the m-th field of order n (i.e. $sin\,(n\theta)$ and $cos\,(n\theta)$ terms) are neglected in this treatment. To allow the treatment of coupling between different azimuthal orders we can define a longitudinal beam coupling impedance $Z_{m,n}$ (where $m, n = 0, \pm 1, \pm 2, ...$)

$$Z_{m,n} = \frac{-1}{I^2} \int dV \mathbf{E}_\mathbf{m} . \mathbf{J}^*_\mathbf{n} \tag{4.20}$$

where

$$\mathbf{J_m} = \frac{I}{2\pi a^{|m|+1}} \delta\left(r-a\right) exp\left(jm\theta\right) exp\left(j\left(\omega t - kz\right)\right) \mathbf{e_z}. \tag{4.21}$$

Importantly, this allows us to see that

$$\begin{aligned} \bar{\mathbf{J}}_\mathbf{0} &= \mathbf{J_0} \\ \bar{\mathbf{J}}_\mathbf{m} &= \mathbf{J_m} + \mathbf{J_{-m}}. \end{aligned} \tag{4.22}$$

From here we use the principle of superposition for electromagnetic fields (i.e. we neglect any non-linearities of the surrounding materials), and thus can derive

$$\bar{Z}_0 = Z_0 \tag{4.23}$$

$$\bar{Z}_x = \bar{Z}_1 = Z_{1,1} + Z_{1,-1} + Z_{-1,1} + Z_{-1,-1} = kZ_x^{dip} \tag{4.24}$$

$$\bar{Z}_x = \bar{Z}_1(\text{cos replaced with sin}) = Z_{1,1} - Z_{1,-1} - Z_{-1,1} + Z_{-1,-1} = kZ_y^{dip} \tag{4.25}$$

$$\bar{Z}_m = Z_{m,m} + Z_{m,-m} + Z_{-m,m} + Z_{-m,-m}, m = 1, 2, ... \tag{4.26}$$

From this start we will apply this to both two wire measurements and to displaced single wire measurements.

Two Wire Measurements

It is possible to directly measure the dipolar impedance of a device through the use of a two wire coaxial method. The measurement setup is identical to that of the single wire method, except that two wires, seperated by distance Δ, are placed in the device, and a 180° hybrid is place between the wires and the VNA at both ends of the device. This setup is illustrated in Fig. 4.6.

The measurements are done in the same way as described in the previous sections for either the classical transmission method or the resonator method. When using the classical coaxial wire method, both wires are individually matched to Z_{c0}. By using two wires each

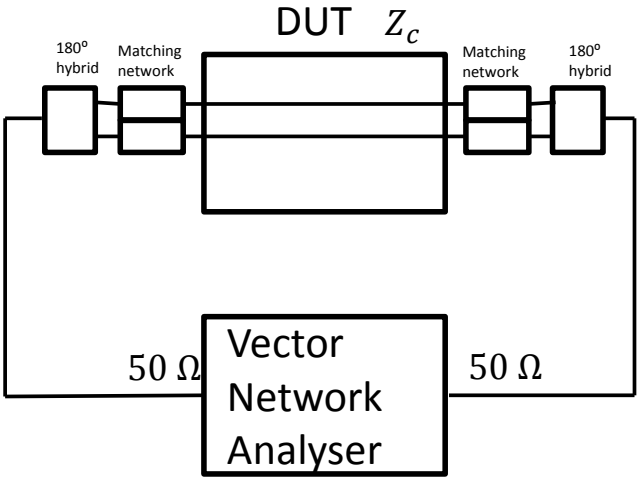

Figure 4.6: Measurement setup for measurements of the dipolar beam coupling impedance using the two wire setup for the classical coaxial wire method.

carrying a signal 180^o out of phase with one another we produce a field pattern similar to a dipole and thus measure the dipole impedance in either the horizontal or vertical plane depending on the orientation of the two wires.

What is directly measured is the longitudinal impedance of just the dipole impedance, as is to be expected from the Panofsky-Wenzel theorem (see Sec. 2.1.4 for further explanation).

For two wire placed at positions $x = \pm a$ relative to the centre of the aperture, the source current density is given by [57]

$$\begin{aligned} J &= I\left(\delta\left(x-a\right)-\delta\left(x+a\right)\right)\delta(y)exp\left(j\left(\omega t-kz\right)\right) \\ &= \frac{I}{\pi a}\sum_{m=-\infty}^{\infty} exp\left(j\left(2m+1\right)\theta\right)exp\left(j\left(\omega t-kz\right)\right) \\ &= 2\sum_{m=-\infty}^{\infty} a^{|2m+1|}J_{2m+1}. \end{aligned} \tag{4.27}$$

The impedance is then

$$
\begin{aligned}
Z &= -\frac{1}{I^2}\int dV \left(2\sum_{m=-\infty}^{\infty} a^{|2m+1|}E_{2m+1}\right)\left(2\sum_{n=-\infty}^{\infty} a^{|2n+1|}J^*_{2n+1}\right) \\
&= 4\sum_{m,n} a^{|2m+1|+|2n+1|}Z_{2m+1,2n+1} \\
&= (2a)^2\left(Z_{1,1}+Z_{-1,1}+Z_{1,-1}+Z_{-1,-1}\right)+O(a^4) \\
&= (2a)^2\bar{Z}_x + O(a^4). \qquad (4.28)
\end{aligned}
$$

Again using the Panofsky-Wenzel theorem we can deduce that the transverse dipolar impedance $Z^{dip}_{x/y}$ is given by

$$
Z^{dip}_{x/y} = \frac{\bar{Z}_{x/y}}{k} = \frac{c}{\omega}\frac{Z}{\Delta^2} \qquad (4.29)
$$

where $\Delta = 2a$ and Z is the measured complex impedance.

Structures with Top/Bottom, Left/Right Symmetry

If we consider a source particle at $x_1 = a_1 cos\theta_1, y_1 = a_1 sin\theta_1$ and a test particle at $x_2 = a_2 cos\theta_2, y_2 = a_2 sin\theta_2$, the source current density is

$$
\begin{aligned}
J_z &= I\delta\left(x-x_1\right)\delta\left(y-y_1\right)exp\left(k\left(\omega t - kz\right)\right) \\
&= \sum_{m=-\infty}^{\infty} a_1^{|m|}exp\left(-jm\theta_1\right)J_m \qquad (4.30)
\end{aligned}
$$

The impedance would therefore be

$$
\begin{aligned}
Z =& \frac{-1}{I^2} \int dV \left(\sum_{m=-\infty}^{\infty} a_1^{|m|} exp\left(jm\theta_1\right) E_m \right) \left(\sum_{n=-\infty}^{\infty} a_1^{|n|} exp\left(jn\theta_2\right) J_n^* \right) \\
=& \sum_{m,n=-\infty}^{\infty} a_1^{|m|} a_2^{|n|} exp\left(-jm\theta_1\right) exp\left(-jn\theta_2\right) Z_{m,n} \\
=& Z_{0,0} + \left(x_1 - jy_1\right) Z_{1,0} + \left(x_1 + jy_1\right) Z_{-1,0} + \left(x_2 + jy_2\right) Z_{0,1} + \left(x_2 - jy_2\right) Z_{0,-1} \\
&+ \left(x_1 - jy_1\right)^2 Z_{2,0} + \left(x_1 - jy_1\right)\left(x_2 - jy_2\right) Z_{1,-1} + \left(x_2 - jy_2\right) Z_{0,-2} \\
&+ \left(x_1 - jy_1\right)\left(x_2 + jy_2\right) Z_{1,1} + \left(x_1 + jy_1\right)\left(x_2 - jy_2\right) Z_{-1,-1} \\
&+ \left(x_1 + jy_1\right)^2 Z_{-2,0} + \left(x_1 + jy_1\right)\left(x_2 - jy_2\right) Z_{-1,1} + \left(x_2 - jy_2\right)^2 Z_{0,2} \\
&+ O\left(\left(x_1, y_1, x_2, y_2\right)^3\right).
\end{aligned} \tag{4.31}
$$

By applying Panofsky-Wenzel we see that

$$
\begin{aligned}
kZ_x = \frac{\partial Z}{\partial x_2} =& Z_{0,1} + Z_{0,-1} + \left(x_1 - jy_1\right) Z_{1,-1} + 2\left(x_2 - jy_2\right) Z_{0,-2} \\
&+ \left(x_1 - jy_1\right) Z_{1,1} + \left(x_1 + jy_1\right) Z_{-1,-1} + \left(x_1 + jy_1\right) Z_{-1,1} \\
&+ 2\left(x_2 + jy_2\right) Z_{0,2} + O\left(\left(x_1, y_1, x_2, y_2\right)^2\right) \\
=& Z_{0,1} + Z_{0,-1} + x_1 \bar{Z}_x + jy_1\left(-Z_{1,-1} - Z_{1,1} + Z_{-1,-1} + Z_{-1,1}\right) \\
&+ x_2\left(2Z_{0,-2} + 2Z_{0,2}\right) + jy_2\left(-2Z_{0,-2} + 2Z_{0,2}\right) + O\left(\left(x_1, y_1, x_2, y_2\right)^2\right)
\end{aligned} \tag{4.32}
$$

$$
\begin{aligned}
kZ_y = \frac{\partial Z}{\partial y_2} =& jZ_{0,1} - jZ_{0,-1} - j\left(x_1 - jy_1\right) Z_{1,-1} - 2j\left(x_2 - jy_2\right) Z_{0,-2} \\
&+ j\left(x_1 - jy_1\right) Z_{1,1} - j\left(x_1 + jy_1\right) Z_{-1,-1} + j\left(x_1 + jy_1\right) Z_{-1,1} \\
&+ 2j\left(x_2 + jy_2\right) Z_{0,2} + O\left(\left(x_1, y_1, x_2, y_2\right)^2\right) \\
=& j\left(Z_{0,1} - Z_{0,-1}\right) + y_1 \bar{Z}_y + jx_1\left(-Z_{1,-1} + Z_{1,1} + Z_{-1,-1} + Z_{-1,1}\right) \\
&+ y_2\left(-2Z_{0,-2} - 2Z_{0,2}\right) + jx_2\left(-2Z_{0,-2} + 2Z_{0,2}\right) + O\left(\left(x_1, y_1, x_2, y_2\right)^2\right).
\end{aligned} \tag{4.33}
$$

Two properties to note for later use are that

$$\mathbf{J}_{-m}(\omega) = \mathbf{J}_m^*(-\omega) \tag{4.34}$$

$$Z_{-m,-n}(\omega) = Z_{m,n}^*(-\omega). \tag{4.35}$$

If we now assume a single wire rather than a source and test particle, such that $x_1 = x_2 = x_0, y_1 = y_2 = y_0$. This gives a source current density

$$\begin{aligned} J &= I\delta(x-x_0)\,\delta(y-y_0)\,exp(j(\omega t - kz)) \\ &= \frac{I}{2\pi a}\delta(r-a)\sum_{m=-\infty}^{\infty} exp(jm(\theta-\theta_0))\,exp(jm(\theta-\theta_0))\,exp(j(\omega t-kz)) \\ &= \sum_{m=-\infty}^{\infty} a^{|m|} exp(-jm\theta_0)\,J_m. \end{aligned} \tag{4.36}$$

We can then define $x_0 = acos\theta_0, y_0 = asin\theta_0$. Entering this into Eqn. 4.31 gives

$$\begin{aligned} Z = \quad & Z_{0,0} + (x_0 - jy_0)\,Z_{1,0} + (x_0 + jy_0)\,Z_{-1,0} + (x_0 + jy_0)\,Z_{0,1} \\ & + (x_0 - jy_0)\,Z_{0,-1} + (x_0 - jy_0)^2\,Z_{2,0} + (x_0 - jy_0)^2\,Z_{1,-1} + (x_0 - jy_0)^2\,Z_{0,-2} \\ & + (x_0 - jy_0)(x_0 + jy_0)\,Z_{1,1} + (x_0 + jy_0)(x_0 - jy_0)\,Z_{-1,-1} + (x_0 + jy_0)^2\,Z_{-2,0} \\ & + (x_0 + jy_0)^2\,Z_{-1,1} + (x_0 + jy_0)^2\,Z_{0,2} + O\left((x_0, y_0)^2\right) \\ = \quad & Z_{0,0} + x_0(Z_{1,0} + Z_{-1,0} + Z_{0,1} + Z_{0,-1}) + jy_0(-Z_{-1,0} + Z_{-1,0} + Z_{0,1} - Z_{0,-1}) \\ & + x_0^2(Z_{1,-1} + Z_{1,1} + Z_{-1,-1} + Z_{-1,1} + Z_{2,0} + Z_{0,-2} + Z_{0,2} + Z_{-2,0}) \\ & + y_0^2(-Z_{1,-1} + Z_{1,1} + Z_{-1,-1} - Z_{-1,1} - Z_{2,0} - Z_{0,-2} - Z_{0,2} - Z_{-2,0}) \\ & + 2jx_0y_0(-Z_{2,0} - Z_{0,-2} + Z_{-2,0} + Z_{0,2} + Z_{-1,1} - Z_{1,-1}) \\ = \quad & Z_{0,0} + x_0(Z_{1,0} + Z_{-1,0} + Z_{0,1} + Z_{0,-1}) + jy_0(-Z_{-1,0} + Z_{-1,0} + Z_{0,1} - Z_{0,-1}) \\ & + x_0^2\left(\bar{Z}_x + Z_{2,0} + Z_{0,-2} + Z_{0,2} + Z_{-2,0}\right) \\ & + y_0^2\left(\bar{Z}_y - Z_{2,0} - Z_{0,-2} - Z_{0,2} - Z_{-2,0}\right) \\ & + 2jx_0y_0(-Z_{2,0} - Z_{0,-2} + Z_{-2,0} + Z_{0,2} + Z_{-1,1} - Z_{1,-1}). \end{aligned} \tag{4.37}$$

It can then be seen that if measurements are made with $x_0 = 0$ and taking different values of y_0 that one obtains data with a parabolic fit in the y_0 axis. By fitting a curve to this we obtain constant (equal to the longitudinal impedance), linear and quadratic terms. Doing the same for $y_0 = 0$ allows us to derive two quadratic terms

$$Z_x^{\perp} = \left(\bar{Z}_x + kZ_{quad}\right)\frac{1}{k} = Z_x^{dip} + Z_{quad} \tag{4.38}$$

$$Z_y^{\perp} = \left(\bar{Z}_y - kZ_{quad}\right)\frac{1}{k} = Z_y^{dip} - Z_{quad} \tag{4.39}$$

$$\tag{4.40}$$

where $Z_{quad} = \frac{1}{k}\left(Z_{0,2} + Z_{2,0} + Z_{0,-2} + Z_{-2,0}\right) = \frac{2}{k}\left(Z_{0,2} + Z_{0,-2}\right)$ (shown in the case of 2D structures externally bounded by a perfectly conducting boundary in [57]), representing the impedance due to the displacement of the test particle in an accelerator. As we can measure $\bar{Z}_{x/y}$ independently using the two wire method we can thus indepedently measure Z_{quad} using a displaced single wire scan in both the x- and y-planes.

It can also be seen that

$$Z_x^{\perp} + Z_y^{\perp} = \frac{1}{k}\left(\bar{Z}_x + \bar{Z}_y\right) = Z_x^{dip} + Z_y^{dip} \tag{4.41}$$

where $\bar{Z}_{x/y}$ can be measured independently which gives a method of obtaining confidence in the wire measurements.

Asymmetric Structures

If Eqn. 4.37 is transformed from (x, y) coordinates to (a, θ), the result is

$$
\begin{aligned}
Z = & Z_{0,0} \\
& + a\left[cos\theta\left(Z_{-1,0}+Z_{0,1}\right)+jsin\theta\left(Z_{-1,0}+Z_{0,1}\right)cos\theta\left(Z_{1,0}+Z_{0,-1}\right)-jsin\theta\left(Z_{1,0}+Z_{0,-1}\right)\right] \\
& + a^2\left[cos^2\left(Z_{1,1}+Z_{-1,-1}\right)+sin^2\left(Z_{1,1}+Z_{-1,-1}\right)\right] \\
& + a^2\left[cos^2\left(Z_{2,0}+Z_{0,-2}+Z_{1,-1}\right)+2jsin\theta cos\theta\left(Z_{2,0}+Z_{0,-2}+Z_{1,-1}\right)\right] \\
& - a^2\left[sin^2\left(Z_{2,0}+Z_{0,-2}+Z_{1,-1}\right)\right] \\
& + a^2\left[cos^2\left(Z_{-2,0}+Z_{0,2}+Z_{-1,1}\right)+2jsin\theta cos\theta\left(Z_{-2,0}+Z_{0,2}+Z_{-1,1}\right)\right] \\
& + a^2\left[sin^2\left(Z_{-2,0}+Z_{0,2}+Z_{-1,1}\right)\right]. \qquad (4.42)
\end{aligned}
$$

Grouping terms by order of depedence on a and θ this becomes

$$
\begin{aligned}
Z = & Z_{0,0}+a\left[e^{-j\theta}\left(Z_{-1,0}+Z_{0,1}\right)+e^{j\theta}\left(Z_{1,0}+Z_{-0,1}\right)\right] \\
& + a^2\left[\left(Z_{1,1}+Z_{-1,-1}\right)+e^{-2j\theta}\left(Z_{2,0}+Z_{0,-2}+Z_{1,-1}\right)+e^{2j\theta}\left(Z_{-2,0}+Z_{0,2}+Z_{-1,1}\right)\right] \\
& = A_1+ae^{-j\theta}A_2+ae^{-j\theta}A_3+a^2e^{-2j\theta}A_4+a^2e^{2j\theta}A_5+a^2A_6 \qquad (4.43)
\end{aligned}
$$

where $A_1 = Z_{0,0}$, $A_2 = Z_{0,1}+Z_{-1,0}$, $A_3 = Z_{0,-1}+Z_{1,0}$, $A_4 = Z_{0,2}+Z_{-1,1}+Z_{-2,0}$, $A_5 = Z_{2,0}+Z_{1,-1}+Z_{0,-2}$ and $A_6 = Z_{1,1}+Z_{-1,-1}$. Taking the earlier definition of Z_{quad} it can be deduced that

$$
\begin{aligned}
Z_{quad} &= \left(A_4+A_5+A_6-\bar{Z}_x\right)\frac{1}{k} = \frac{A_4+A_5+A_6}{k}-Z_x^{dip} \qquad (4.44)\\
&= \left(A_4+A_5-\frac{\bar{Z}_x-\bar{Z}_y}{2}\right)\frac{1}{k} = \frac{A_4+A_5}{k}-\frac{Z_x^{dip}-Z_y^{dip}}{2}. \qquad (4.45)
\end{aligned}
$$

Consideration of Eqn. 4.43 lets it be seen that

$$
\begin{aligned}
A_4+A_5+A_6 &= \frac{Z\left(a,0\right)+Z\left(a,\pi\right)-2Z\left(0,0\right)}{2a^2} \qquad (4.46)\\
A_4+A_5 &= \frac{Z\left(a,0\right)+Z\left(a,\pi\right)-Z\left(a,\frac{\pi}{2}\right)-Z\left(a,\frac{3\pi}{2}\right)}{2a^2}. \qquad (4.47)
\end{aligned}
$$

The constant impedance can also be seen to be found by taking a linear fit of the longitudinal impedance of a wire displaced in either the $\theta = 0$ or $\theta = \pi/2$ plane, and taking the linear term of the fit.

4.1.4 Measurements on Example Geometries

In this section shall be presented a number of example analyses of coaxial wire measurements done on geometries exhibiting top/bottom, left/right symmetry and an asymmetric structure. This permits a step-by-step guide to analysis of the wire measurements, which may not be immediately clear from the mathematical introduction. These simulations are carried out using both Ansoft HFSS [58] and Maxwell [59] using a driven modal solution.

The simulations with HFSS are carried out in the following manner: for representing the single wire measurement the measurement system is simulated by placing waveguide ports at either end of the geometry with a conducting cylinder placed as the inner conductor of the coaxial system. The transmission parameters are then acquired as a result of the simulations. The wire may then be displaced as neccessary for the displaced single wire measurements. For two wire measurements a quarter geometry may be simulated, using a quarter geometry with a perfect H boundary in the plane of the wires, and a perfect E boundary between the wires to enforce the dipolar field pattern.

Maxwell is a frequency domain code optimised for low frequencies (less thans 10s of MHz). It does not permit the use of waveguide ports, however it does allow the definition of current segments with phase changes between them. By considering the current (either a single current segment to simulate a single wire, or two current carrying segments 180° out of phase for two wires) to be the equivalent of a beam current, and assuming the inclusion of the current carrying component is a negligible perturbation to the geometry, the real impedance can be found by summing the power loss in the system. This can be seen to be equivalent to the beam induced heating experienced by a beam interacting with an impedance.

This can be thought of by comparing the system to a homogenous transmission line. The power P of a wave travelling along the line is given by [60]

$$P = P_0 e^{-2\alpha z} \tag{4.48}$$

where P_0 is the power at the beginning of the transmission line, α is the attenuation

coefficient and z the distance along the line. By differentiation it can be seen that

$$\alpha = -\frac{1}{2P}\frac{dP}{dz} \approx \frac{1}{2P}\frac{\delta P}{\delta z} \tag{4.49}$$

where δP is the power lost over the short distance δz. The transmission parameter of a line S_{21} is given by

$$S_{21} = e^{-\alpha \delta z}. \tag{4.50}$$

If the impedance is evaluated using the log formula ($Z = Z_c ln S_{21}$), it can be seen that the real impedance is subsequently given by

$$\Re e\,(Z) = Z_c \frac{2\delta P}{P}. \tag{4.51}$$

Assuming a peak current I_0 on the wire, $P = I_0^2 Z_c/2$, which gives

$$\Re e\,(Z) = \frac{2\delta P}{I_0^2}. \tag{4.52}$$

To acquire the transverse impedance for two wire simulations it is simply neccesary to normalise by the wavenumber $k = \omega/c$ and the seperation of the wire Δ

$$Z_{dip} = \frac{c}{\omega \Delta^2}\frac{2\delta P}{I_0^2}. \tag{4.53}$$

Structure with Top/Bottom, Left/Rght Symmetry

For the structure exhibiting top/bottom, left/right symmetry we use the Tsutsui model of two parallel plates as shown in Fig. 4.7(a). We use this due to the model allowing the prediction of the longitudinal, dipolar and quadrupolar impedances for a wide variety of materials and frequency ranges [26, 30, 61]. For these simulations a short segment of a Tsutsui geometry is simulated using two different materials, in this case graphite, to represent a structure with a poor conductivity ($\sigma_{graphite} = 7 \times 10^4\ Sm^{-1}$), and 4A4 ferrite, to represent a magnetically lossy material (in this case, $\epsilon_r = 10$, $\sigma_{4A4} = 10^{-6}\ Sm^{-1}$ (a mild conductivity is applied to prevent static build up in ferrite components in accelerators),

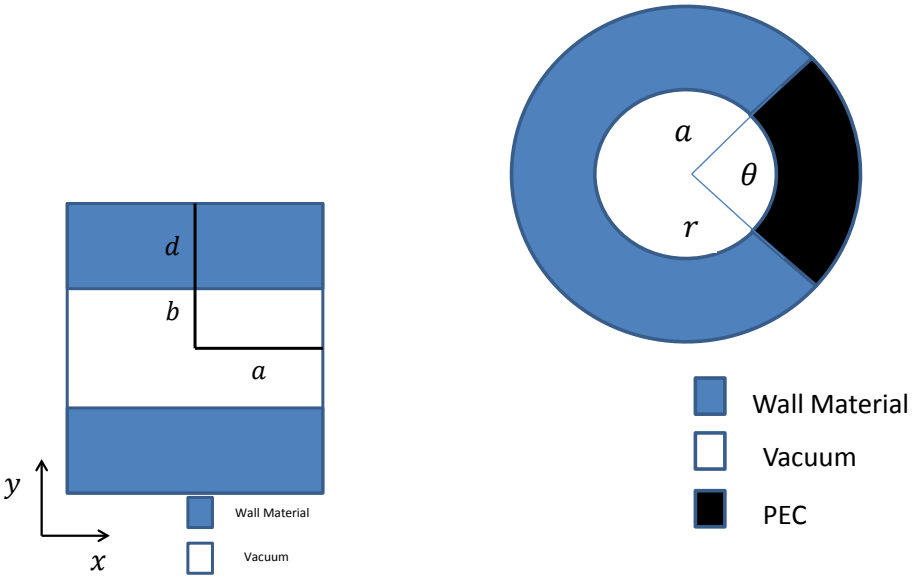

(a) (b)

Figure 4.7: The geometries used for coaxial wire measurement simulations. For the geometry with top/bottom, left/right symmetry we use the Tsutsui model ((a)) using two parallel plates. For the asymmetric structure we use the Zannini-model for a C-core ferrite kicker magnet ((b)), which generates a constant term and a noticeable asymmetric term.

and $\mu_r = \mu^{'} + j\mu^{''}$, shown in Fig. 4.8.). In both cases the following dimensions are used: $a = 25\ mm$, $b = 5\ mm$, $d = 5\ mm$. A structure of 150 mm in length is used to reduce numerical noise due to the small losses given by the short length of the simulated DUT.

Two Parallel Ferrite Plates

For the simulations of two parallel ferrite plates the following parameters were used in HFSS; for the displaced single wire measurements a wire of 0.3 mm in radius, and the following displacement used to acquire the total transverse terms:

1. In the horizontal axis - displaced between -6 mm to +6 mm at intervals of 2 mm
2. In the vertical axis - displaced between -4 mm to +4 mm at intervals of 2 mm.

For the two wire simulations, two wires of radius 0.3 mm are used, with a seperation of 4 mm in the x-dimension, and 3 mm in the y-dimension. 4 simulation configurations

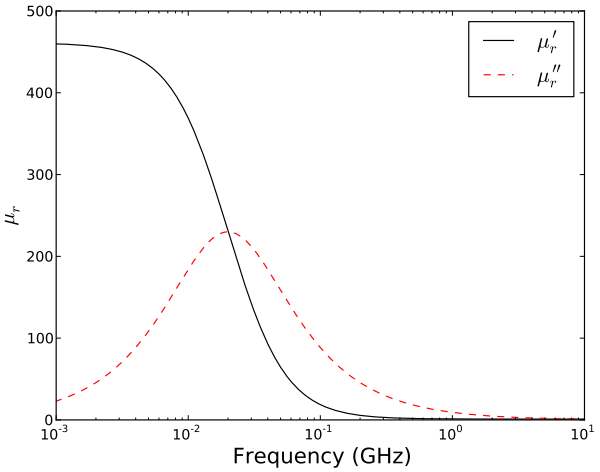

Figure 4.8: The complex permeability of 4A4 ferrite.

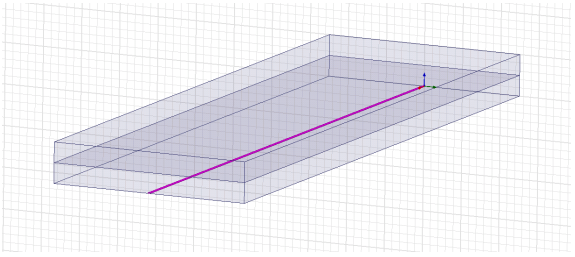

Figure 4.9: An example of the simulation model used for coaxial wire simulations. In this case a displaced single wire between two parallel plates. The wire is highlighted in purple.

are used described below:

1. an adaptive mesh generation set to a convergence criterion of S_{21} diverging by less than 0.005 between two subsequent solutions, at an adaptive frequency of 20 MHz solving to a second order basis. A discrete frequency sweep is then carried out in the range 1-10 MHz at 1 MHz intervals.

2. an adaptive mesh generation set to a convergence criterion of S_{21} diverging by less than 0.005 between two subsequent solutions, at an adaptive frequency of 200 MHz solving to a second order basis. A discrete frequency sweep is then carried out in the range 10-100 MHz at 10 MHz intervals.

3. an adaptive mesh generation set to a convergence criterion of S_{21} diverging by less than 0.005 between two subsequent solutions, at an adaptive frequency of 2 GHz solving to a second order basis. A discrete frequency sweep is then carried out in the range 100 MHz-1 GHz at 100 MHz intervals.

4. an adaptive mesh generation set to a convergence criterion of S_{21} diverging by less than 0.005 between two subsequent solutions, at an adaptive frequency of 10 GHz solving to a second order basis. A discrete frequency sweep is then carried out in the range 1-10 GHz at 1 GHz intervals.

These parameters are used to benefit from an appropriate mesh count for the given frequency range, thus increasing simulation speed by not using a high density mesh at frequencies where no benefits would be gained.

The longitudinal impedance is determined by taking the constant term for a series of simulated displaced wire measurements in both the vertical and horizontal planes is shown in Fig. 4.10. It can be seen that in the frequency range below 100 MHz the agreement between the coaxial wire results and the analytical results is very good in both the vertical and horizontal plane. Above 100 MHz the agreement for the real components is very good for both results, however the imaginary component in the vertical plane displays some substantial disagreement. This is likely due to the high mesh density required to

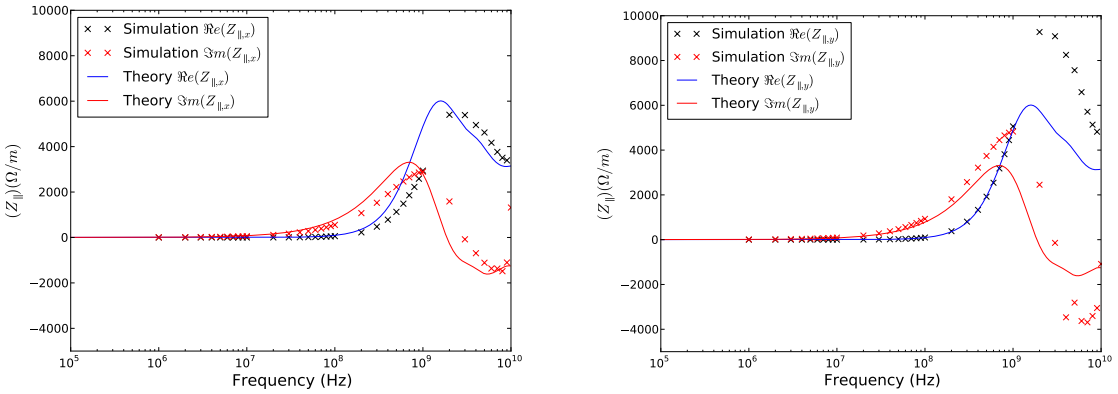

(a) (b)

Figure 4.10: The longitudinal impedance of two parallel ferrite plates simulated using a longitudinal coaxial wire. Presented is the impedance as measured in the horizontal plane ((a)) and in the vertical plane (b).

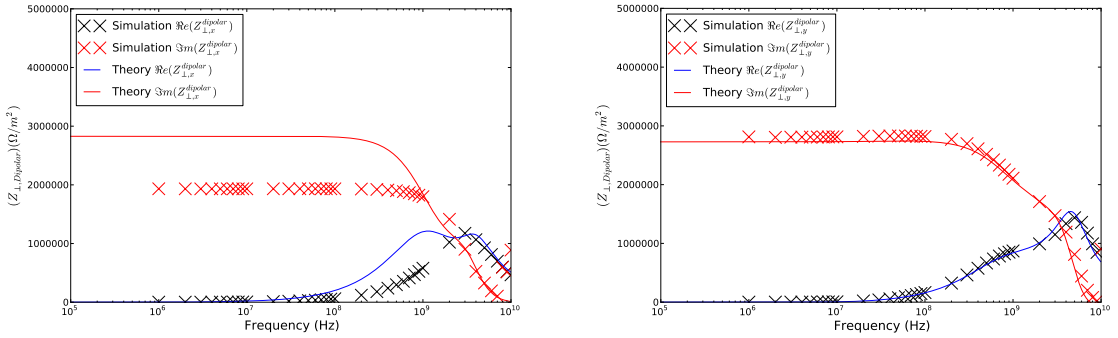

(a) (b)

Figure 4.11: The dipolar impedance of two parallel ferrite plates simulated using two longitudinal coaxial wires. Presented are the impedances as measured in the horizontal plane ((a)) and in the vertical plane (b).

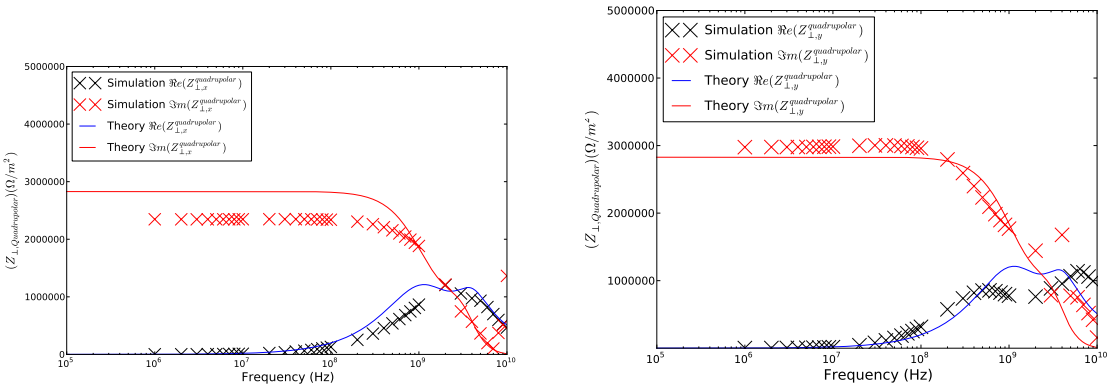

(a) (b)

Figure 4.12: The quadrupolar impedance of two parallel ferrite plates simulated using a combination of displaced single wire simulated measurements and two wire simulated measurements. Presented is the impedance as measured in the horizontal plane ((a)) and in the vertical plane (b).

correctly evaluate the phase change along the length of the simulated structure. A higher mesh density may correct this, however limits of computational resource presently make this unfeasible.

The agreement between the simulations of the vertical dipolar impedance and the theoretical model is excellent across all frequencies for both the real and imaginary components. The agreement below 100 MHz and above 1 GHz is very good for the horizontal dipolar, with some divergence in the constant term of the imaginary impedance. The key difference is the failure of the coaxial method to resolve one of the peaks in the real impedance. The results for the dipolar impedance are shown in Fig. 4.11.

The results for the quadrupolar impedance are shown in Fig. 4.12. The vertical simulations agree well with the theory, correctly identifying the two peaks in the quadrupolar impedance. The agreement for the horizontal simulations with theory is less good. This can be explained by the derivation of the horizontal quadrupolar being highly dependent on the quality of the horizontal dipolar impedance results due to them cancelling each other to form the total transverse impedance. As the horizontal dipolar impedance does not resolve the subpeaks neither does the horizontal quadrupolar impedance calculations.

Two Parallel Graphite Plates

For the simulations of measurements of two parallel graphite plates, two different methods were used. Due to the non-ferritic properties of the graphite, it is possible to use Maxwell3D to simulate the power loss at lower frequencies, thus acquiring the real component of the impedance for low frequencies, in addition to using the classical coaxial wire method at higher frequencies in HFSS.

For the simulations of the power loss in Maxwell3D the following parameters were used; for the displaced single wire measurements a wire of 0.5 mm radius is modelled, and the following displacement used to acquire the total transverse terms:

1. In the horizontal axis - displaced between -6 mm to +6 mm at intervals of 2 mm
2. In the vertical axis - displaced between -4 mm to +4 mm at intervals of 2 mm.

For the two wire simulations, two wires of radius 0.3 mm are modelled, with a seperation of 8 mm in the x-dimension, and 4mm in the y-dimension. Five simulation configurations are used as described below:

1. an adaptive mesh generation set to a convergence criterion of S_{21} diverging by less than 0.005 between two subsequent solutions, at an adaptive frequency of 20 kHz solving to a second order basis. A discrete frequency sweep is then carried out in the range 1-10 kHz at 1 kHz intervals.
2. an adaptive mesh generation set to a convergence criterion of S_{21} diverging by less than 0.005 between two subsequent solutions, at an adaptive frequency of 200 kHz solving to a second order basis. A discrete frequency sweep is then carried out in the range 10-100 kHz at 10 kHz intervals.
3. an adaptive mesh generation set to a convergence criterion of S_{21} diverging by less than 0.005 between two subsequent solutions, at an adaptive frequency of 2 MHz solving to a second order basis. A discrete frequency sweep is then carried out in the range 100 kHz-1 MHz at 100kHz intervals.

4. an adaptive mesh generation set to a convergence criterion of S_{21} diverging by less than 0.005 between two subsequent solutions, at an adaptive frequency of 10 MHz solving to a second order basis. A discrete frequency sweep is then carried out in the range 1-10 MHz at 1 MHz intervals.

5. an adaptive mesh generation set to a convergence criterion of S_{21} diverging by less than 0.005 between two subsequent solutions, at an adaptive frequency of 100 MHz solving to a second order basis. A discrete frequency sweep is then carried out in the range 10-100 MHz at 10 MHz intervals.

These parameters are used to benefit from an appropriate mesh count for the given frequency range, thus increasing simulation speed by not using a high density mesh at frequencies where no benefits would be gained.

For the simulations of the single displaced wire in HFSS the following parameters were used; for the displaced single wire measurements a wire of 0.3 mm in radius is modelled, and the following displacements to acquire the total transverse terms:

1. In the horizontal axis - displaced between -6 mm to +6 mm at intervals of 2 mm

2. In the vertical axis - displaced between -4 mm to +4 mm at intervals of 2 mm.

For the two wire simulations, two wires of radius 0.3 mm are modelled, with a seperation of 4 mm in the x-dimension, and 3 mm in the y-dimension. Three simulations configuration are used as described below:

1. an adaptive mesh generation set to a convergence criterion of S_{21} diverging by less than 0.005 between two subsequent solutions, at an adaptive frequency of 20 MHz solving to a second order basis. A discrete frequency sweep is then carried out in the range 1-10 MHz at 1 MHz intervals.

2. an adaptive mesh generation set to a convergence criterion of S_{21} diverging by less than 0.005 between two subsequent solutions, at an adaptive frequency of 200 MHz solving to a second order basis. A discrete frequency sweep is then carried out in the range 10-100 MHz at 10 MHz intervals.

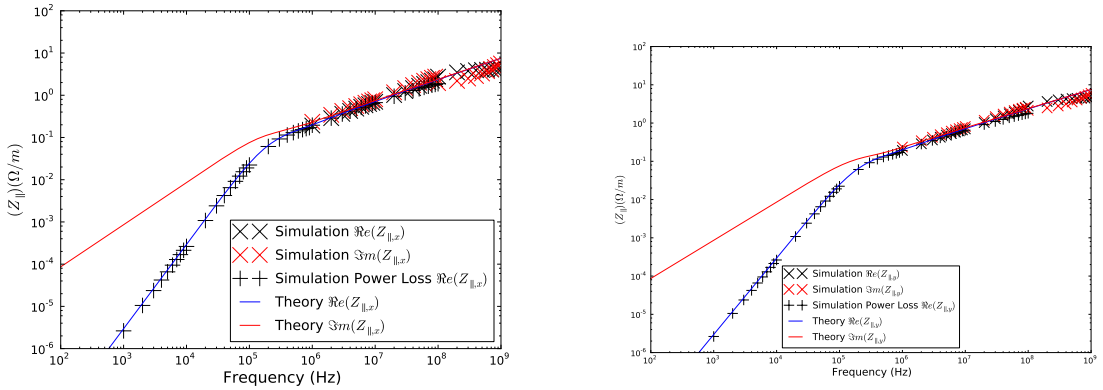

(a) (b)

Figure 4.13: The longitudinal impedance of two parallel graphite plates as measured by taking the constant term of a quadratic equation fitted to a series of displaced single wire simulated measurements. Shown are simulated measurements acquired from fitting displacements in (a) horizontal axis and in (b) the vertical axis.

3. an adaptive mesh generation set to a convergence criterion of S_{21} diverging by less than 0.005 between two subsequent solutions, at an adaptive frequency of 2 GHz solving to a second order basis. A discrete frequency sweep is then carried out in the range 100 MHz-1 GHz at 100 MHz intervals.

As before these parameters are used to benefit from an appropriate mesh count for the given frequency range, thus increasing simulation speed by not using a high density mesh at frequencies where no benefits would be gained.

The longitudinal impedance is shown in Fig. 4.13. It can be seen that the agreement for both the real component is excellent across the entire frequency range, for simulations using both the classical coaxial wire method and the power loss method of Maxwell3D. The agreement is also good for the imaginary component over much of the frequency range, becoming worse above 100 MHz. This is likely due to insufficient mesh density to catch the relatively small phase shift at this frequency range.

The agreement between simulations and theory for the vertical dipolar impedance can be seen to be very good over the entire frequency range also (see Fig. 4.14(b)). The results at low frequencies (below 100 kHz) for the power loss method and at all frequencies for the classical coaxial wire method for the horizontal dipolar impedance agree very well

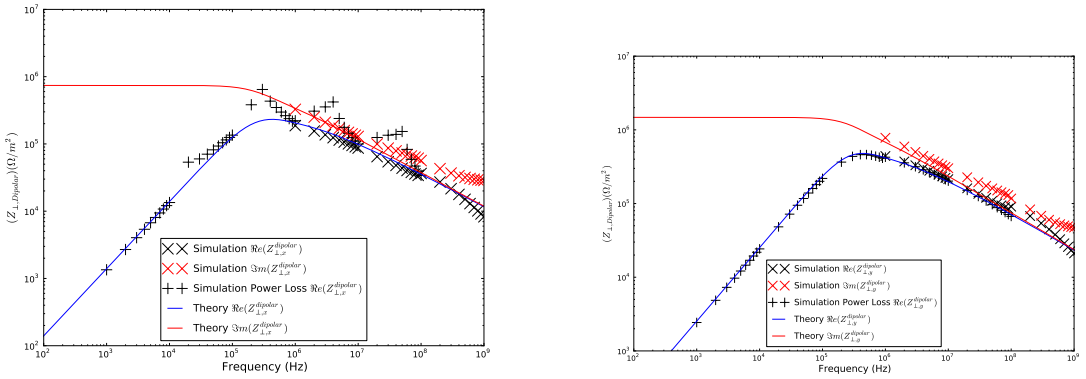

(a) (b)

Figure 4.14: The dipolar impedance of two parallel graphite plates measured using two longitudinal coaxial wires. Presented is the impedance as measured in the horizontal plane ((a)) and in the vertical plane (b).

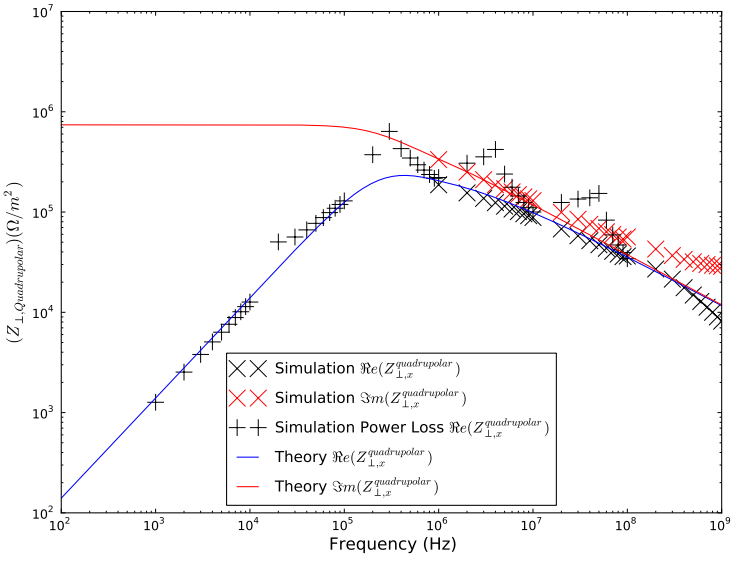

Figure 4.15: The quadrupolar impedance of two parallel graphite plates measured using a combination of displaced single wire measurements and two wire mesurements.

with theory (see Fig. 4.14(a)). The quadrupolar impedance is shown in Fig. 4.15, and again the agreement between the simulated measurements and theory can be seen to be good over the entire frequency range, using both the power loss method and the classical coaxial wire method. However, the power loss method does predict peaks at the lower part of each frequency sweep that are not predicted in either the theoretical model or the measurements with the coaxial wire method in HFSS.

C-Core Ferrite Kicker

To test the measurement method for an asymmetric structure a model of the C-core ferrite kicker magnet was used, as shown in Fig.4.7(b), the analytical details of which are given in [62]. Key in this type of structure is that it predicts a non-zero constant transverse impedance term as well as the quadrupolar terms, thus we may completely evaluate the asymmetric measurement method. For these simulations a structure of $a = 15$ mm, $r = 20$ mm, $\theta = \pi/2$, and 100 mm in length was used. Simulations were carried out using the classical coaxial wire method as simulated in HFSS.

The following parameters were used for the simulations; wire of 0.2 mm in radius, and the following displacement used to acquire the total transverse terms:

1. In the horizontal axis - displaced between -5 mm to +5 mm at intervals of 1 mm.

2. In the vertical axis - displaced between -5 mm to +5 mm at intervals of 1 mm.

For the two wire simulations, two wires of radius 0.2 mm are modelled, with a separation of 2 mm in the x-dimension, and 2 mm in the y-dimension. Four simulation configurations were used which are described below:

1. an adaptive mesh generation set to a convergence criterion of S_{21} diverging by less than 0.005 between two subsequent solutions, at an adaptive frequency of 20 MHz solving to a second order basis. A discrete frequency sweep is then carried out in the range 1-10 MHz at 1 MHz intervals.

2. an adaptive mesh generation set to a convergence criterion of S_{21} diverging by less than 0.005 between two subsequent solutions, at an adaptive frequency of 200 MHz solving to a second order basis. A discrete frequency sweep is then carried out in the range 10-100 MHz at 10 MHz intervals.

3. an adaptive mesh generation set to a convergence criterion of S_{21} diverging by less than 0.005 between two subsequent solutions, at an adaptive frequency of 2 GHz solving to a second order basis. A discrete frequency sweep is then carried out in the range 100 MHz-1 GHz at 100 MHz intervals.

4. an adaptive mesh generation set to a convergence criterion of S_{21} diverging by less than 0.005 between two subsequent solutions, at an adaptive frequency of 10 GHz solving to a second order basis. A discrete frequency sweep is then carried out in the range 1-10 GHz at 1GHz intervals.

These parameters are used to benefit from an appropriate mesh count for the given frequency range, thus increasing simulation speed by not using a high density mesh at frequencies where no benefits would be gained.

It can be seen that the longitudinal impedance agrees well over the entire frequency range below 1 GHz (Fig. 4.16(a)). The analytical calculations breakdown above 1 GHz due to the family of Bessel functions used for the calculations being optimised for low frequency calculations. Similarly the agreement for the dipolar impedance can be seen to be exceptionally good over the majority of the frequency range, with an increasing descrepency at high frequencies (Fig. 4.16(b)).

To test the asymmetric method we should look at the constant and quadrupolar terms. In this case it can be seen that the agreement with the constant transverse term is exceptionally good across the entire frequency range (Fig. 4.16(d)). The agreement for the quadrupolar impedance is good in the range of frequencies below 1 GHz. Above this the unsuitability of the family of Bessel functions used for this frequency range becomes more apparents and the simulated and analytical results diverge.

It can be seen that the proposed asymmetric method can replicate the beam coupling

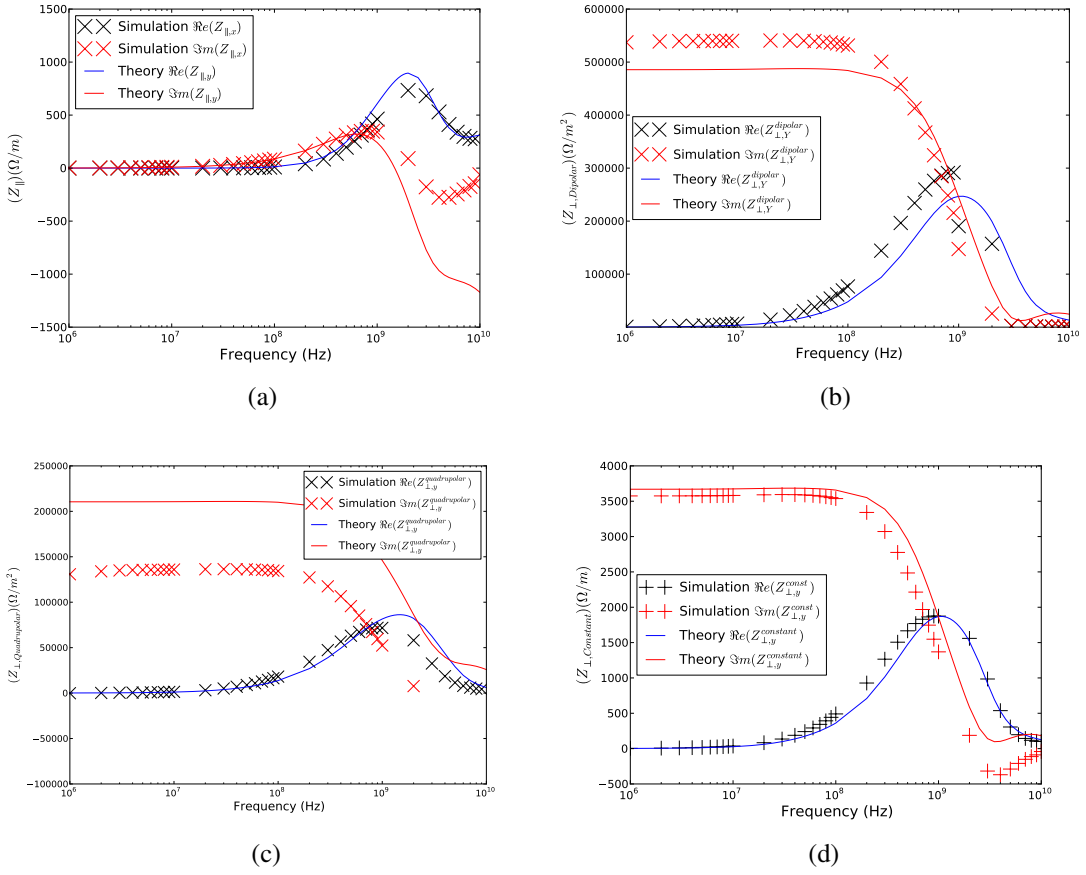

Figure 4.16: The impedance of the C-core ferrite kicker as acquired by simulating the classical coaxial wire method in HFSS. Shown is the (a) longitudinal impedance, (b) the dipolar impedance, (c) the quadrupolar impedance and (d) the constant transverse impedance.

impedance of an asymmetric structure, correctly predicting both longitudinal and transverse (dipolar, quadrupolar and constant) terms below 1GHz.

4.2 High Q-factor Impedances

For high Q-factor impedances (high such that the addition of propogation losses by the coaxial line drastically lower the measured Q, Q ≈ 100), such as cavity impedances, it is not appropriate to use a coaxial wire method to measure the impedance due to the large perturbation of the boundary conditions that it causes [63], in particular below the cut-off frequency of the connecting beam pipes. This is due to the presence of the coaxial wire reducing the cut-off frequency to 0Hz due to addition of TEM modes to the system that do not exist without the coaxial wire, thus allowing propogation losses at all frequencies rather than just above cut-off. To illustrate this, we can consider the total Q of a cavity to be related to the "trapped" cavity mode Q and the propogation losses as;

$$\frac{1}{Q_{total}} = \frac{1}{Q_{cavity}} + \frac{1}{Q_{prop}} \tag{4.54}$$

During excitation by a charged particle beam, propogation losses do not exist below the cutoff frequency and thus $Q_{prop} = 0$. However, the addition of the coaxial wire causes these propogation losses to occur at all frequencies. Importantly, the Q-factor of these propogation losses is of a similar magnitude or smaller than that of the cavity resonance, leading to a great distortion of the measured Q. Similarly, the perturbation of the conductive wire in the centre of the structure leads to a shift in the resonance frequency of the cavity modes. This has been well studied in [63], an example setup of which is given in Fig. 4.17 and the simulated measurements of which is given in Fig. 4.18.

4.3 Conclusion

In this section we have covered in depth the bench-top measurement techniques for low-Q impedances using the coaxial wire technique. We have described the practical details of

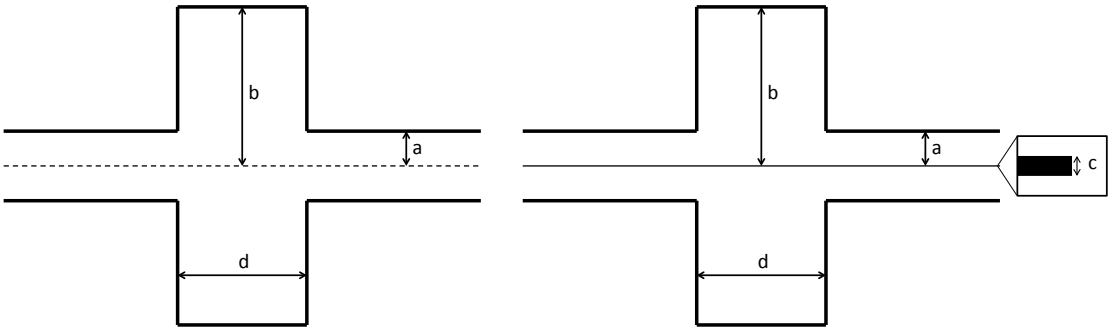

(a) (b)

Figure 4.17: Comparison of the geometries of a cavity and attached beampipes (a) without and (b) with the coaxial wire in place. Note the dimensions and that the dashed line in (a) and the solid line in (b) represent the rotational plane of symmetry

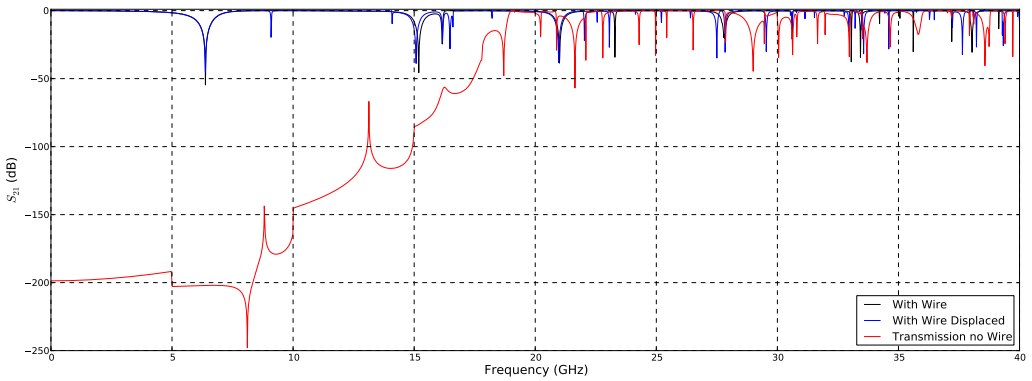

Figure 4.18: A comparison of the transmission parameters through a pillbox cavity with and without a coaxial wire. A displaced coaxial wire is also shown to illustrate the possibility of exciting dipolar modes also. It can be seen that the transmission signals are drastically changed depending on the presence or not of the wire.

setting up the measurement bench, as well as the ways of measuring the longitudinal and transverse impedances for symmetric and asymmetric structures using one and two coaxial wires. Two methods of measurement have been described, the classical coaxial wire measurement method, a transmission measurement through the DUT using a matched VNA circuit, and the resonant coaxial wire measurement method, a transmission method that involves turning the DUT into a coxial resonator, providing a highly sensitive measurement method but at the expense of reduced frequency resolution of the impedance measurements.

We have described a method of measuring the quadrupolar and constant transverse impedances of asymmetric structures using the coaxial measuring techniques, and subsequently evaluated this technique using simulated measurements of a C-core ferrite kicker in HFSS, showing excellent agreement between the analytical calculations and simulated measurements for the longitudinal (real and imaginary), dipolar (real and imaginary), quadrupolar (real only) and constant (real and imaginary) impedances over a large frequency range (1 MHz-10 GHz). The discrepency for imaginary component of the quadrupolar impedance is considered and attributed to insufficient simulation accuracy.

Futher comments are made on the suitability of coaxial wire measurements of high-Q impedances (for example cavity modes), showing that they can provide inaccurate measurements of the resonant frequency and Q factors of these impedances below cutoff due to additional propogation losses not present when a traversing charged particle sees the structure.

These methods will be used extensively in the evaluation of the beam coupling impedance of the LHC injection kickers in Chap. 8 in order to verify the complex simulation model against measurements of the physical magnet.

Chapter 5

Computational Simulations of Beam Coupling Impedance

Whilst beam-based measurements and bench-top measurements techniques have been used for some time to measure the impedance of devices and machines, the use of numerical codes to solve 2D and 3D structures is relatively young as a method of identifying the impedance of devices. Recent progress in computational power has now made these a powerful tool in the regime of impedance evaluation. Codes exist that solve simple 2D structures (ECHO2D [64], ABCI [65]), 3D structures (CST Particle Studio [66], HFSS [58], Maxwell 3D [58], MAFIA [67]) and 3D structures using highly parallelised codes (GdFidl [68], ACE3P [69]) which allow the simulation of large, complex structures. The codes may be seperated into two seperate families; time-domain, which calculate the EM fields in a structure by solving Maxwell's equations in the time domain due to a signal impulse, and frequency-domain which can be used in a number of ways to simulate the beam coupling impedance.

Each of these families of codes has its own relative advantages and disadvantages and peculiarities to use. In this chapter there will a general introduction to a number of the techniques that may be used to calculate the beam coupling impedance from both time-domain and frequency-domain simulations, along with the limitations of each method.

5.1 Time Domain Simulations

Time domain simulations typically rely on direct simulations of the propogation of an EM signal through a structure and evaluating the response in some manner. In this section we shall primarily discuss the use of direct particle beam simulation, that is the simulation of the beams EM profile via a source signal and then subsequently evaluating the trailing field to acquire the wakefield of the source signal and thus the electromagnetic fields in the structure simulated.

5.1.1 Direct Simulation of a Particle Beam

A large majority of time domain simulation codes (ECHO, MAFIA, CST Particle Studio, GdfidL) use a method that in effect simulates the passage of a particle beam through the structure and evaluates the subsequent electromagnetic fields in the structure by this signal. This is done in the following way:

1. A signal representing the source bunch is defined using a given profile, and then passed through the structure from a defined starting displacement and at a given velocity. Additionally a line of integration is defined along which the witness signal will be taken. This in effect defines a source bunch and a witness particle.

2. The simulation is run for a given period of time to acquire a significant quantity of the wakefield to correctly analyse the frequency components. It can be seen that for both high-Q resonances and low frequencies this requires a longer wakelength, to encompass the long damping time and correctly resolve the signal frequency, respectively.

3. The observed signal is subsequently deconvolved from the source signal to obtain a single particle wakefunction.

4. This may then be Fourier transformed (using an FFT algorithm or other numerical methods) to acquire the beam coupling impedance.

These steps are illustrated for clarity in Fig. 5.1 using a simple pillbox cavity as an example, using the time domain code CST Particle Studio.

By comparison to the definition of the transverse impedances in Chap. 2, it can readily be seen that by defining either the source signal or witness at different displacements it is possible to acquire both the dipolar and quadrupolar impedances. Additionally, by taking the gradient of the transverse impedances any constant transverse impedance terms can also be calculated.

5.2 Frequency Domain Simulations

There are a number of methods of analysing the beam coupling impedance of a structure using frequency domain simulations. These involve evaluating the structure with no beam present via the use of eigenmode solvers, simulating measurement setups, particularly the coaxial wire technique for systems in which the impedance structure is largely unknown. Finally it is possible to simulate the particle beam also, however this requires a high resolution frequency scan for structures that are expected to be resonant in nature.

5.2.1 Eigenmode Simulations

Eigenmode solvers are a subset of frequency domain solvers that are used to identify strongly resonant modes in a structure. These can be cavity modes, antenna like oscillations or a number of other resonances within the structure. The resulting output of the simulation is typically the resonant frequency of the eigenmode(s), the quality factor Q of the mode (if lossy boundary materials are defined) and the field pattern of the eigenmode solution.

From the field pattern it is possible to readily calculate the longitudinal and transverse R/Q of each cavity mode as defined in Sec. 2.2.3. The field patterns may also be used to calculate a number of other properties for each eigenmode, such as surface losses and stored energy in the cavity, which will be explained in further details in Sec. 6.6. Further details on this method are available in [34].

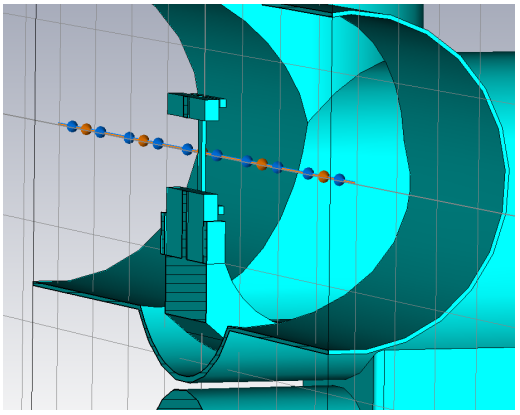

(a)

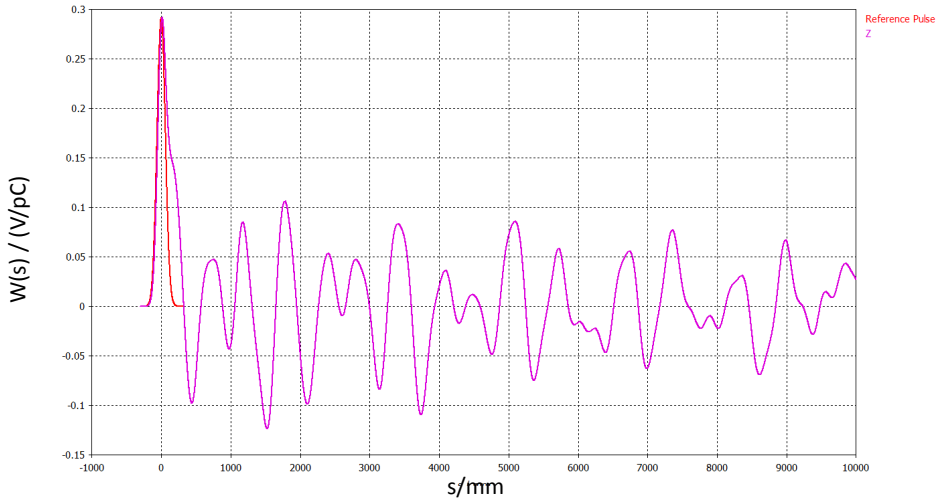

(b)

Figure 5.1: An illusration of the (a) source signal and witness integration in a time domain code. Here a sample from the UA9 goniometer is shown. The source signal and the resulting wakefield are shown in (b).

5.2.2 The Coaxial Wire Method by Simulation

The coaxial wire method as described in Sec. 4.1 can be directly simulated using waveguide ports to represent matched connections at the ends of the device under test. The resulting simulations provide a transmission coefficient S_{21} which may subsequently be evaluated in the same manner as measurements made with a physical wire. As with the measurements used in practice, a displaced wire and two wires may be simulated and again treated as measurements.

5.2.3 Simulation of the particle beam

It is also possible to simulate a particle beam directly in the frequency domain. This is done by defining a wave source that produces a field similar to that of the particle beam. For ultrarelativistic beams this neccessitates a source field that is tangential to the direction of motion, and this may technically be possible for cases in which $\beta < 1$. The field components due to the source may be acquired and are the equivalent of the wakefield contribution at a given frequency. The beam impedance Z can subsequently be evaluated from the resulting fields. Further details of this method may be seen in [70].

5.3 Conclusion

In this chapter we have given a basic introduction to some of the simulation tools that are available for impedance evaluation in both the time domain and frequency domain. We have discussed the advantages and disadvantage of both, and their parallels to either beam-equipment interactions or to bench-top measurement methods. These codes are subsequently used extensively in later chapters for the evaluation of beam coupling impedances of differents devices.

Chapter 6

Beam Coupling Impedance Reduction Techniques

Due the effects of wakefields on both beam stability and machine equipment it is often necessary to consider reducing the beam impedance of different components in particle accelerators. There are a number of ways in which it is possible to reduce the impedance depending on whether the impedance is primarily geometric or material dependent in nature and the most commonly used will be reviewed. Different solutions from mechanical changes in the structures to damping materials placed to damp resonances are discussed. Further references are given to provide more in depth knowledge as required. In particular the use of ferrite to damp cavity modes that may not be removed by redesign, due to either time or mechanical constraints, has recently become a product of intensive study due to the high temperatures seen in many devices that have ferrite placed in them, with concern that the ferrites may heat beyond their Curie temperature (the temperature at which a magnetic material starts to experience significant changes in magnetic properties, drastically affecting their use as either damping material or as electromagnet yokes) during regular operation leading to a deteriorating case for the machine impedance.

6.1 Tapering of Step Transitions

Although the ideal beam pipe of an accelerator would be of unchanging diameter, it is often necessary to vary the width of the beam pipe for the use of beam instrumentation, insertion devices and machine protection, amongst others. As was shown in Sec. 2.2.3, the presence of changes in the pipe diameters gives rise to beam impedance originating at the point of transition. It has been previously demonstrated that this impedance is heavily influenced by the angle of the transition [71], in addition to the frequency of the resonance of the resulting cavity structure. In particular, this has an influence on the "low"-frequency broadband impedance, with gentler slopes causing a reduction in the "low"-frequency impedance.

There are of course space constraints which restrict the length which tapers may have, both in terms of machine length and the neccessities of size due to the correct operation of the device (for example, collimators or beam instrumentation such as synchrotron radiation monitors). An example of this approach is shown in Fig. 6.1. This reduction technique has a strong effect on the broadband impedance contribution of a strong resonant impedance caused by step transitions. In particular, it is effective at reducing the imaginary component of the longitudinal beam coupling impedance, as can be seen in the design of the LHC Yellow Book design report for instance [72]. In this case it was determined that all transitions must observe a maximum gradient of 15° unless a design requirement neccessitated otherwise.

6.2 Transition Pieces

Often it is necessary to have transitions in the beam pipe which can not be tapered, either due to space constraints or the operational requirements of the device containing the transition. This a common requirement in devices that require some mechanical freedom of movement (i.e. longitudinal or transverse movement is expected), such as bellows, or electrical isolation from the beam pipe, such as kicker magnets. For these devices it is

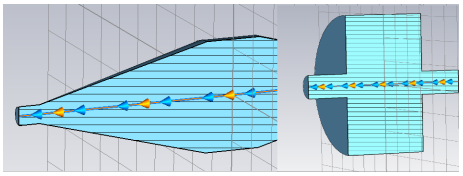

(a)

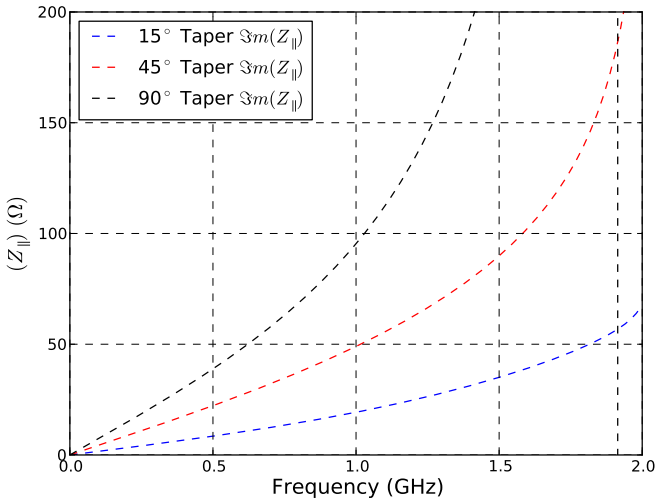

(b)

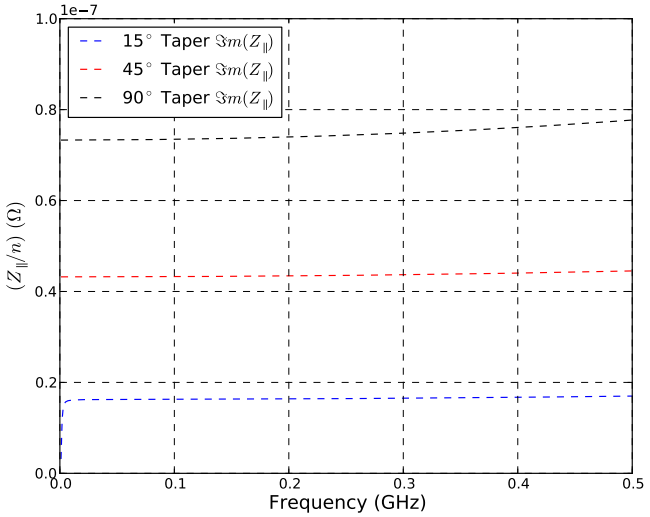

(c)

Figure 6.1: An example pillbox structure with and without a tapered transition region (a), in this case with the taper of 15°. The resulting imaginary component of the longitudinal impedances are shown in (b), with Z/n shown in (c), as these are the most significant for beam stability.

Figure 6.2: Example of RF fingers (in this case for the PIMS (Plug In ModuleS) module, placed between cryo-modules in the LHC).

often possible to use a transition piece, that is one or several pieces of conducting material to screen any transition. These may be rigid or moveable as shown in Fig. 6.2, often referred to as RF fingers.

This method of impedance reduction is effective for a number of reasons. Firstly it provides a short, good conducting path for the image currents to flow that does not make the cavity created by the transition visible to the beam, and, in the case of bellows, the image current does not have to follow to long contoured path of the bellows, such as shown in Fig. 6.2. This serves to reduce the broadband impedance increase and, by shielding the contours of the bellows, prevents an increase in the imaginary longitudinal impedance due to the increased electrical length of the device. Secondly, by correctly designing the spacing in the transitions, it is possible to minimise field leakage to the surrounding cavities therefore decreasing the visibility of cavity resonances. As an example of a cavity with and without RF fingers and a number of intermediatary steps, see Fig. 6.3, which illustrates the case of the VMTSA, a vacuum interconnect in the injection region of the LHC [73] containing a double bellow module. It is characterised by a large vacuum chamber (due to the need to contain two circulating beams) with a long set of bellows. The bellows were screened by a long set of RF fingers, which functioned well when good surface contact was maintained between the fingers and the beam pipe. However, when this connection was disrupted (easily created via mechanical stress due to the weak pressure exerted by the afixing spring) the real component of the longitudinal beam coupling impedance increased drastically at around 200 MHz, shown by the large decrease in the

transmission parameter S_{21} in the case of spring failure, causing further mechanical failure. This highlights the need to correctly consider the mechanical and electromagnetic properties of an impedance reduction system, especially it's possible failure points.

6.3 Conductive Coatings

As was seen in Sec. 2.2.4, a higher conductivity in the material seen by the beam in a particle accelerator results a lower beam coupling impedance. Typically this rule of thumb is followed in the design of particle accelerators, however the operational requirements of devices in the machine often require that they not be made from a good conducting material. Examples of this include collimators (requiring high strength, mechanical stability and certain radiation properties), beam instrumentation and numerous other devices.

It has been shown [74] that a thin layer of high conductivity material placed on the surface of a poorly conducting material can effectively screen the beam from interacting with the poorly conducting material for a large frequency range. This can be explained by considering the skin depth δ of a material. As shown in Sec. 2.2.4,

$$\delta(\omega) = \sqrt{\frac{2}{\mu_r(\omega)\mu_0\sigma\omega}}. \tag{6.1}$$

The skin depth can be thought of as the distance of penetration of the magnetic field into the material. It can thus be seen that for a good conducting material like copper ($\sigma_{cu} \approx 6 \times 10^7\ Sm^{-1}$), for frequencies of the order of a hundred megahertz or above, a thickness of $10\ \mu m$ is larger than the skin depth at 100MHz ($\delta\,(100\text{ MHz}) = 6\ \mu m$), thus effectively screening the layer below. The frequency range of concern is dependent on the machine: for beam-induced heating the concern is at high frequencies (high depending on the machine, to a couple of gigahertz for proton machines, to tens of gigahertz for electron machines) where thin coating are effective, whereas for coupled bunch instabilities low frequencies are a concern, necessitating thicker conductive coatings to be effective. It is possible to use thicker coatings (on the order of millimetres) for machines that require a very broad frequency range screened. This is investigated in detail in Sec. 7.2.

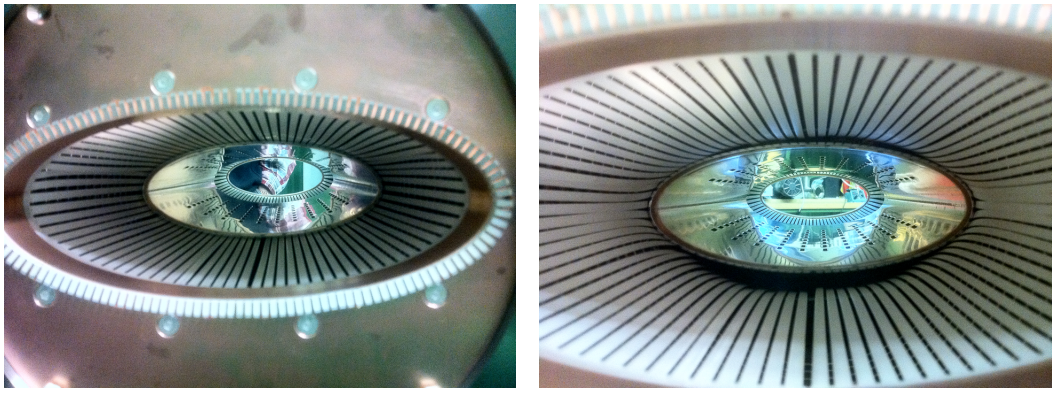

(a) (b)

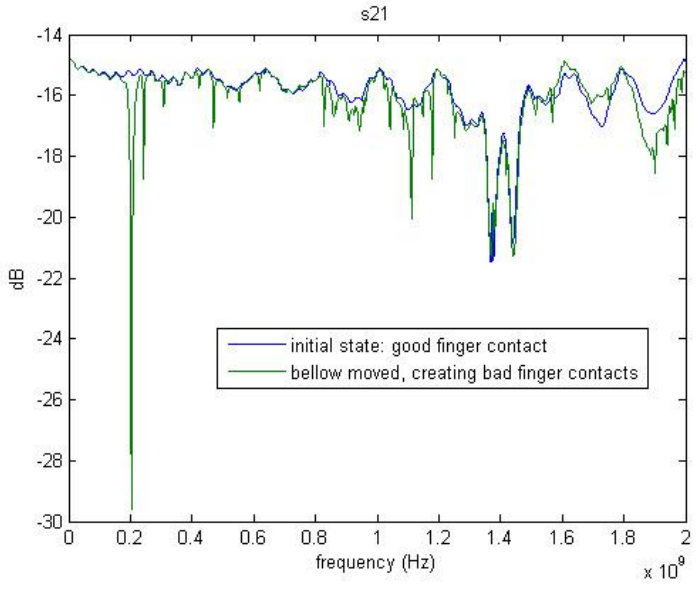

(c)

Figure 6.3: The layout of the RF fingers in the VMTSA both in (a) the fully operational configuration and (b) when some RF fingers lose contact. (c) shows the transmission parameter S_{21} for the VMTSA module with and without good electrical contact between the fingers and the beam pipe as acquired by coaxial wire measurements. Photos and measurements courtesy of J.L. Nougaret.

6.4 Beam screens in Kicker Magnets

Substantial contributors to the beam coupling impedance in many machines, in both the longitudinal and transverse planes, are kicker magnets. These are magnets that generate a fast pulsed magnetic field for a limited period of time (i.e. not always on during beam operation as the dipoles and quadrupoles used for beam optics are) for extraction (either to other machines or beam dumps) or injection. They have been known to be a problematic component of particle accelerators for a number of decades, mostly in lepton machines due to the traditionally higher beam currents in these machines.

In lepton machines kicker magnets can suffer from problems of heating due to eddy currents induced by traversing bunches, and the neccessity that a remedy to this solution maintain the rapid rise time of the magnetic field required for normal kicker magnet operation, which typically requires a field rise time on the order of the bunch or bunch train seperation in a machine [74].

In the LHC, gaps are deliberately left between batches of beams in order to allow for the rise/fall of the magnetic field of kicker magnets. Thus in order to maximise the integrated beam intensity, the rise and fall time must be kept to a minimum, bearing in mind technical and economic constraints: for the LHC injection kickers the field rise (from 0.5%-99.5% field strength) and fall (from 99.5%-0.5% field strength) times are 900ns and 3μs respectively.

As mentioned above, kicker magnets contribute a substantial fraction of the beam coupling impedance of an accelerator. In order to reduce the beam coupling impedance of a kicker magnet, a thin conductive coating or longitudinal conductors can be incorporated between the beam and the yoke of the kicker magnet to shield the yoke against the beam image current. However any such beam impedance reduction measures must not significantly increase the field rise and fall time of the kicker magnet which presents a challenge to prevent the electromagnetic fields of the beam from penetrating the beam screen, but allowing the kicker field to do so.

For the LHC injection system a ceramic chamber is incorporated in the aperature of

each kicker magnet: the purpose of the ceramic chamber is to mechanically support the conductors which shield the yoke against the beam image current. In addition the ceramic chamber electrically isolates the shield from the high voltage and return busbar of the kicker magnets.

However the ceramic chamber contributes a large imaginary component to the longitudinal impedance, due to its high permitivitty and poor conductivity. In addition it is liable to build up static charges due to being an insulator in a region subject to high electric and magnetic fields.

Shielding will be studied in further depth in Chap. 8, with particular attention to the limitations in a high current hadron machine.

6.5 Serigraphy on Kicker Magnets

As described in Sec. 6.4, kicker magnets are often a substantial contributor towards beam coupling impedance. For many machines they were not foreseen to be a limiting factor to beam operation during construction due to either low beam current, long bunch lengths, large bunch separations or both. However, with increasing improvements in machine performance, it is possible that they may become a limiting factor, as was the case for the SPS extraction kicker magnets [75].

For existing devices, limitations of both time and budget may require the use of retroactive solutions to reduce large beam impedances. Often these must be added to the original equipment, as the continued correct operation of the device requires minimal disruption to the geometry and surfaces of the device. In the case of the SPS extraction kicker magnet (SPS-MKE), the aperture size had to be preserved, as well as the field rise time of the kicker. In this case an innovative solution was found - the use of serigraphy. This entailed the printing of a set of interleaved fingers (see Fig. 6.4) made from a good conductor (silver), which form a good conductive path for the beam image currents: the ferrite dielectric provides a reasonable capacitive coupling between the interleaved fingers. This serves to replace the broadband impedance typically associated with a ferrite

dominated resistive wall impedance with a low broadband impedance, with strong resonant impedances due to the capacitive coupling and physical length of the fingers. The results in the case of the SPS-MKE can be seen in Fig. 6.4(c).

6.6 Use of damping materials to de-Q resonant cavities

For a number of devices it is unavoidable to have a cavity present in the structure. In addition it is often not possible to design the cavity with either tapering or transition pieces due to the need for moveable components; this is the case for a wire scanner or a collimator whose aperture changes with beam parameters. In this case it is necessary to find a way of reducing the beam impedance by altering the properties of resonances. Often it is only the peak value of the impedance attributable to a resonance that is of concern from a beam stability/beam induced heating point of view.

If we consider the defining properties of a resonant impedance, f_{res}, R/Q and Q, there are a number of properties that should be noted in changing them. Both f_{res} and R/Q are strongly determined by the geometry of the structure, and thus cannot be significantly modified without possibly neccessitating a modification of the device, which may hinder the intended operation. Thus one approach to use is to alter the Q of the resonance. A well known method of altering the Q of a resonant cavity is to add a dispersive or ferritic material to the cavity volume [76], that is a material that has complex permitivitty or permeability , given by $\epsilon_r = \epsilon^{'} - j\epsilon^{''} = \epsilon^{'}(1 - jtan\delta_{\epsilon})$ and $\mu_r = \mu^{'} - j\mu^{''} = \mu^{'}(1 - jtan\delta_{\mu})$ respectively, where $tan\delta_{\epsilon} = \epsilon^{''}/\epsilon^{'}$ and $tan\delta_{\mu} = \mu^{''}/\mu^{'}$. An example of the complex relative permeability of some sample ferrite damping materials is shown in Fig. 6.5. More examples are shown in App. E.

The addition of this family of materials to the cavity has the following effect on the cavity resonances:

1. The resonant frequency of any resonance ω_{res} is reduced by the inclusion of the dispersive material. This can be understood either by considering:

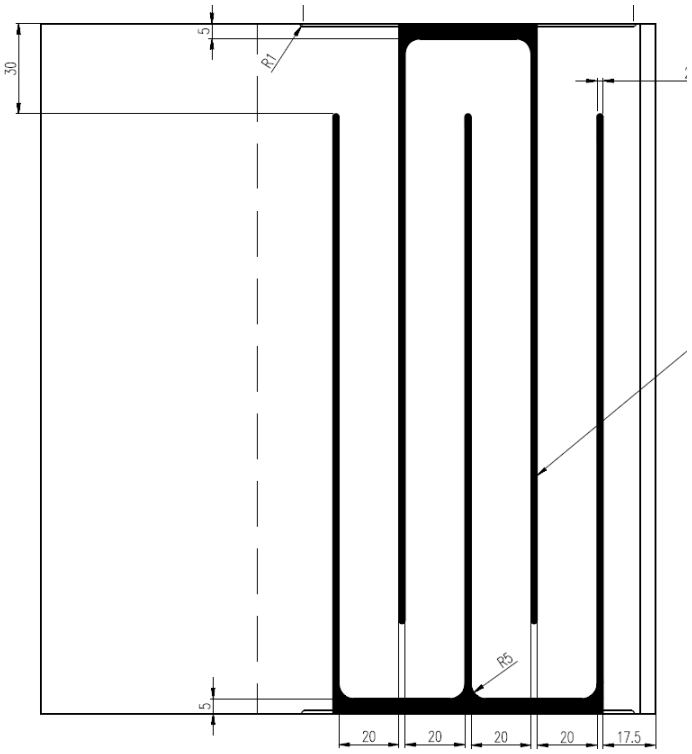

(a)

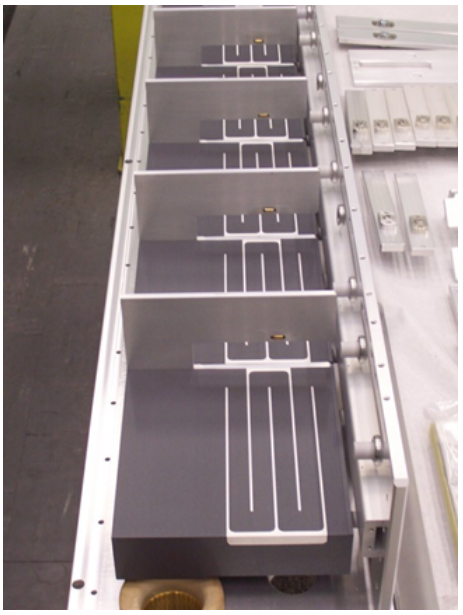

(b)

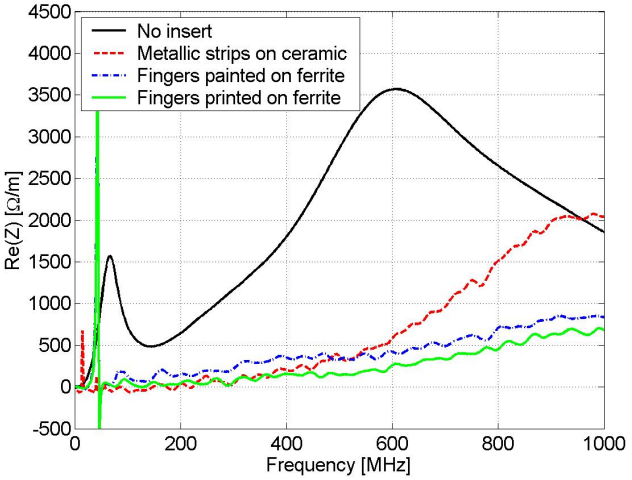

(c)

Figure 6.4: An example of serigraphy in the SPS Extraction Kicker Magnets (SPS-MKE). The layout of the interleaved fingers is shown in (a) and the actual serigraphed ferrites in (b). A comparison of the measured real component of the longitudinal beam coupling impedance with and without the serigraphy is shown in (c).

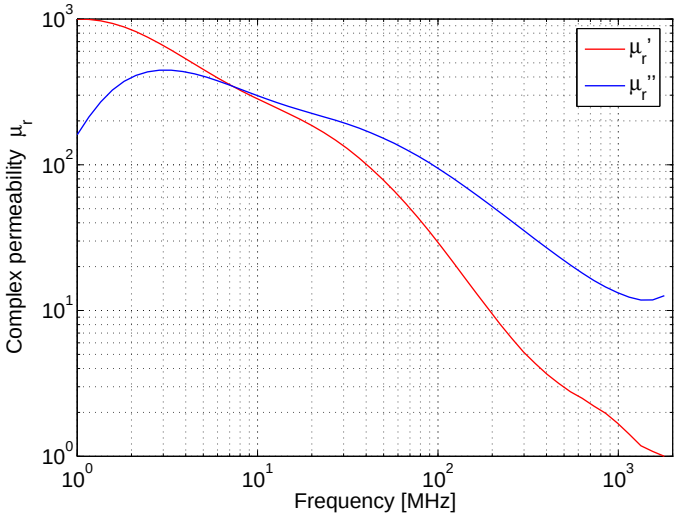

Figure 6.5: The complex permeability of a sample ferrite of the sort used for damping. In this case 8C11. In usage a high Curie temperature (T_c) ferrite is recommended, such as TT2-111R.

- the μ_r/ϵ_r increasing the effective electrical volume of the cavity by it's inclusion, thereby increasing the effective dimensions of the resonant cavity.
- the RLC equivalent circuit of a cavity resonance, the inclusion of the dispersive material increases either or both of (depending on the properties of the material) the inductance and capacitance of the cavity, causing the resonant frequency to decrease as $\omega_{res} = 1/\sqrt{LC}$.

2. The R/Q of the cavity experiences little change. There is a slight modification; either an increase that can be attributed to the increased stored energy in the cavity mode due to $\epsilon^{'} \neq 1$ or a decrease due to the rearranging of the field patterns (caused by the incluson of the dispersive material) decreasing the stored energy.

3. The Q of the resonance is drastically reduced. This is due to the strong change in the damping time of the resonance due to the addition of the damping material. In terms of cavity properties, this can be thought of as the losses in the cavity increasing more rapidly than the stored energy in the cavity. In terms of the RLC circuit

representation $Q = R_s\sqrt{C/L}$, thus is it can be seen that the inductance must increase more rapidly than the capacitance, or the capacitance decrease more rapidly than the inductance for the drastic reduction in the quality factor to occur.

As can be seen, the resulting effect is to drastically reduce the Q of a cavity resonance, and then by the relation $R_s = (R_s/Q)Q$ it can be seen that the shunt impedance will decrease proportionally to Q. This reduces the peak value of the resonance R_s, but broadens the width of the resonance peak. This indicates two effects of using damping materials as an impedance reduction technique; effects dependent on the shunt impedance R_s are suppressed, however effects dependent on the broadband behaviour may suffer negatively as a result. Due to the strong frequency dependent nature of many impedance-driven instability mechanisms and beam-induced heating, these negative side effects rarely outweigh the benefits of using damping material in a cavity if necessary.

The placement of the damping material within the cavity is key to determining how effective the damping will be. This requires knowledge of the field patterns in the cavity modes of the structure. To effectively damp the cavity modes, the damping material must be placed in a position where it strongly interacts with the field associated with it's damping, normally the region of strongest fields. For dielectric materials this would be a region of strong electric fields and for ferritic materials a region of strong magnetic fields. In addition, if possible, the materials should not directly be seen by the beam due to the high resistive wall type impedance associated with these types of materials. Requirements for mechanical support often subsequently necessitate that these materials be placed by the wall of the vacuum tank of the cavity also. This location maybe where it is convenient to mount the damping materials, even away from the location of the cavity mode if it can be shown that the induced fields will be absorbed by the damping material.

6.6.1 Heat Loads on the Damping Material

During the estimating the heat loads on ferrite damped cavities in high intensity hadron machines (see Sec. 7.3 for more details), a number of surprising observations were made.

In particular the placement of ferrite in a cavity does not always produce a significant reduction in the Q of a resonance and that in such cases the percentage of the power loss in the ferrite was comparatively small compared to conventional wisdom: that in a ferrite damped cavity the majority of power loss would be in the ferrite. It was thus decided to investigate how the addition of a damping material, in this case a ferrous material, to a cavity would alter both the characteristic resonance properties of the cavity and the location of the power load due to interaction with the beam in the cavity.

Two different geometries were used, one of which could be treated analytically to provide a benchmark for the simulation code, and one in which the ferrite is shielded from being directly seen by the traversing beam, as is normally done to reduce the effects of a resistive wall type impedance due to the ferrite. These geometries are shown in Fig. 6.6. A single eigenmode of each cavity is investigated, both with and without a damping material.

For this analysis, a cavity of dimensions $a = 60\ mm$, $b = 5\ mm$, $c = 20\ mm$, made from a material with a conductivity $\sigma = 1.1 \times 10^6\ Sm^{-1}$ is used for the simulations of an unshielded cavity. A layer of "ferrite" 0.5mm thick is placed as shown in Fig 6.6(a). This material is given the following properties: $\epsilon^{'} = 10$, $\epsilon^{''}/\epsilon^{'} = 0$ and $\mu^{'} = 10$. $\mu^{''}/\mu^{'}$ is changed between 0 and 0.2 in steps of 0.02 in order to alter the Q of the resonant mode in incremental steps with the intent of observing how the properties of the cavity change with different scales of damping of the resonance. The "ferrite" is also given a mild conductivity ($\sigma_{ferr} = 10^{-6}\ Sm^{-1}$). This is commonly done to ferrites used in particle accelerators to reduce electrostatic charge build up.

For the shielded geometry, we use a cavity of the same dimensions as for the unshielded case, with a layer of conductive material 1 mm thick placed on the interior of the cavity. A gap of 5 mm is left between the beam pipe and the cavity for the beam to couple to the cavity. A ring of ferrite 0.5 mm in thickness is then placed on this surface as is shown in Fig. 6.6(b).

Before carrying out the analysis of the location of the heat loss, it is prudent to verify that the losses calculated using the field calculator in HFSS are self-consistent and well

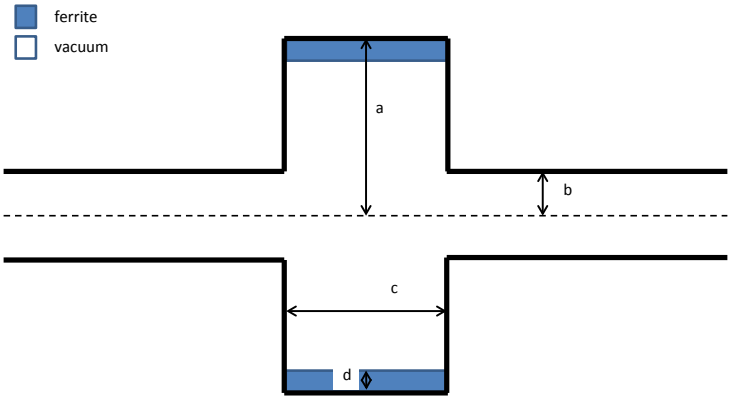

(a)

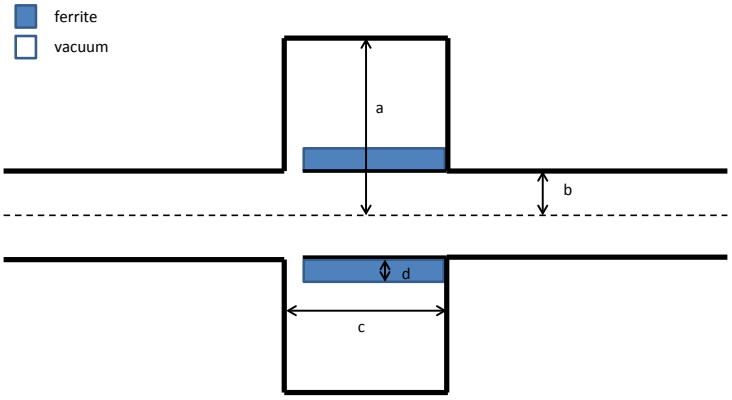

(b)

Figure 6.6: Two sample geometries used to examine the effects of ferrite damping material on cavity resonances. (a) shows a cavity with the ferrite unshielded, and (b) shows a more realistic case in which the ferrite is shielded from directly seeing the traversing beam.

understood. HFSS calculates two losses internally; the surface loss density and volume loss density. The surface loss density p_s is defined in HFSS as

$$p_s = \Re e\left(\mathbf{S}.\mathbf{n}\right) \tag{6.2}$$

where $\mathbf{S}$ is the Poynting vector and n is the out normal vector to the surface boundary [58]. By integrating this over all surfaces the total surface losses in the cavity are obtained. The total wall losses are also given by

$$P_{loss,wall} = \frac{R_{wall}}{2}\int_S \left|\mathbf{H_{surf}}\right|^2 dS \tag{6.3}$$

where R_{wall} is the surface resistance of the wall and $\mathbf{H_{surf}}$ is the surface magnetic field.

HFSS defines the volume loss density p_v as

$$p_v = \frac{1}{2}\Re e\left(\mathbf{E}.\mathbf{J} + \left(-\nabla \times \mathbf{E}\right).\mathbf{H}\right) \tag{6.4}$$

where again this may be integrated over all space to obtain the total volume losses. In addition to these methods of calculations of the losses due to the fields in the cavity, it is possible to calculate an equivalent loss of a particle traversing on axis by considering of ohmic losses, with the voltage V that is experienced by the particle traversing the cavity, $R = R_s$ the shunt impedance of the cavity resonance and I the beam current. As the eigenmode simulation does not directly simulate a beam, the effective power loss is given by

$$P_{loss} = \frac{V^2}{R_s}. \tag{6.5}$$

The surface losses and volume losses are subsequently seperately compared. For the surface losses, the internal surface loss density integrated over all surfaces calculated by HFSS, wall losses as given by Eqn. 6.3 and the equivalent losses of a particle on axis are compared. For this we use the unscreened cavity with no ferrite present to have only surface losses present. The calculated results are shown in Tab. 6.1, given in Watts normalised

Table 6.1: Comparison of the power loss on the surface of a pillbox cavity by both direct calculation and internal calculation by HFSS (in units normalised to 1 V/m maximum electric field).

Calculation Type	Normalised Power Loss (W)
Direct calculation	6.2e-10
HFSS internal loss calculations	6.22e-10
Loss of an on-axis particle	5.1e-10

Table 6.2: Comparison of the power loss in the volume of a pillbox cavity by both direct calculation and internal calculation by HFSS (in units normalised to 1 V/m maximum electric field).

Calculation Type	Normalised Power Loss (W)
Direct calculation	1.28e-8
HFSS internal loss calculations	1.29e-8
Loss of an on-axis particle	1.33e-8

to a peak electric field of $1\ Vm^{-1}$ in the cavity. It can be seen that the two calculations due to the surface fields themselves agree exceptionally well, and the calculation for the equivalent loss of an on-axis particle agrees within 20%.

For the volume losses the cavity geometry for the unshielded case is used, with a layer of ferrite 0.5 mm thick on inside surface of the cavity. This ferrite has the following material properties; $\epsilon^{'} = 10$, $\epsilon^{''} = 0$, $\mu^{'} = 10$ and $\mu^{''}/\mu^{"} = 0.1$. For this comparison the internal volume loss density integrated over the whole volume as calculated by HFSS, the volume losses calculated using Eqn. 6.4 and the equivalent loss of an on axis particle are calculated, again with loss normalised to a peak electric field of $1\ Vm^{-1}$ in the cavity. The results are shown in Tab. 6.2. It can be seen that the agreement between all three methods of calculating the losses in the cavity is exceptionally good, differing by less than 4%.

The resulting real component of the longitudinal beam coupling impedance for the case of unshielded ferrite is shown in Fig. 6.7. The reduction in the resonant frequency and the increase in the peak impedance from the cavity without any damping material to that with is due to the presence of a region of $\epsilon^{'} > 1$. Clearly seen can be the effect of the presence of increasing loss tangent of the ferrite, greatly broadening the impedance peak,

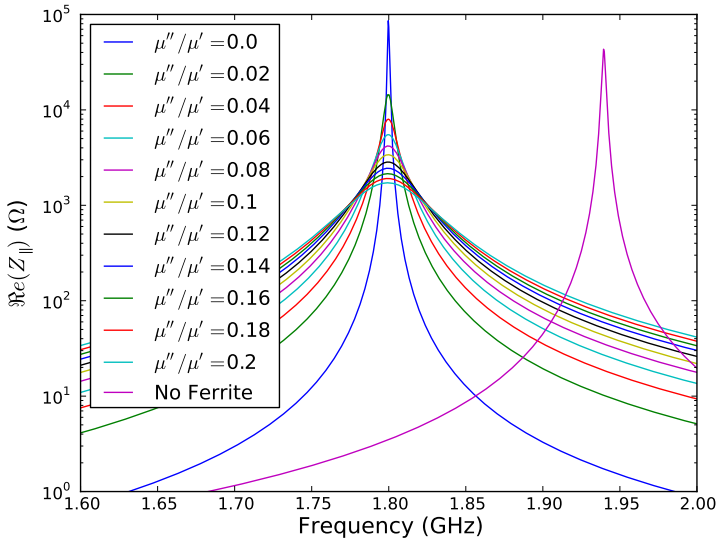

Figure 6.7: The real component of the longitudinal beam coupling impedance of a cavity without and with a damping material with $\epsilon^{'} = 10$, $\mu^{'} = 10$ and $\mu^{''}/\mu^{'}$ is varied. The non-damped cavity is shown for comparison. The change in resonanct frequency and shunt impedance is due to the increased $\epsilon^{'}$ of the damping material.

with the effect of reducing R_s of the resonance. The cause of this reduction of R_s can be attributed to the reduction in Q for each resonance, as shown in Fig. 6.8(a). It can be clearly seen that the presence of a small piece of ferrite very strongly decreases the Q of a resonance. The corresponding change in the percentage of the power loss in the ferrite itself as the Q is decreased is shown in Fig. 6.8(b). It can be seen that the power loss is rapidly localised to the ferrite as the Q decreases. To quantify this power loss: the power loss due to this cavity resonance is calculated assuming a beam with 1.15×10^{11} particles per bunch, 288 bunches, a ring circumference 6911 m and a bunch length $4\sigma = 0.04\ m$ assuming a Gaussian bunch distribution and that the resonance falls on a beam harmonic is shown in Fig. 6.9. Here it can be clearly seen that the power loss in the ferrite rapidly converges to the total losses in the cavity, confirming the assumption that most of the power loss for a cavity resonance damped by a damping material is lost in the damping material.

For the case of the shielded ferrite, the real component of the beam coupling impedance

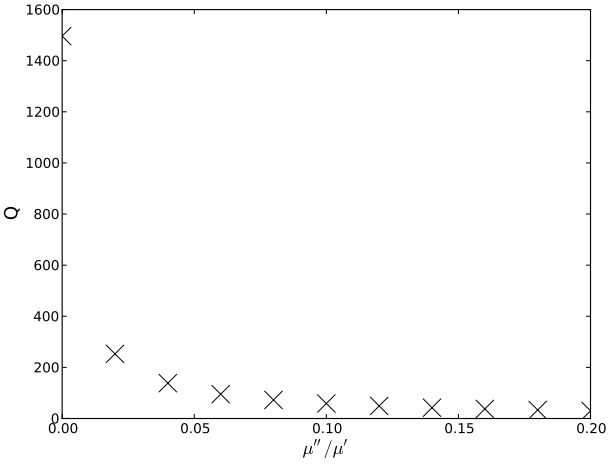

(a)

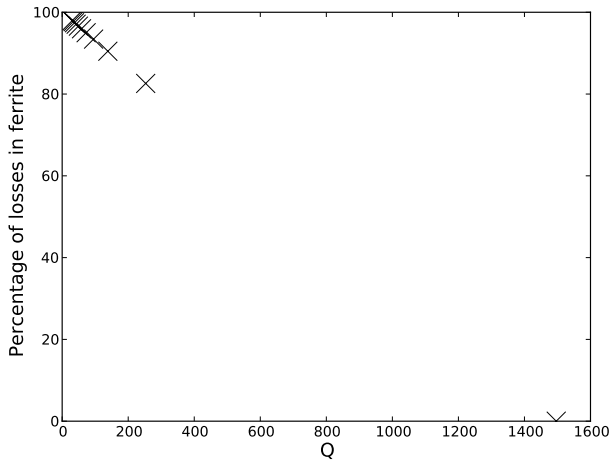

(b)

Figure 6.8: (a) The reduction in the Q of the cavity resonance with the increasing loss tangent of the ferrite damping, showing a strong decrease of the resonant Q with a small increase in loss tangent. (b) The percentage of the power loss in the ferrite as the resonant Q decreases. This can be seen to tend towards 100% as the Q approaches 0.

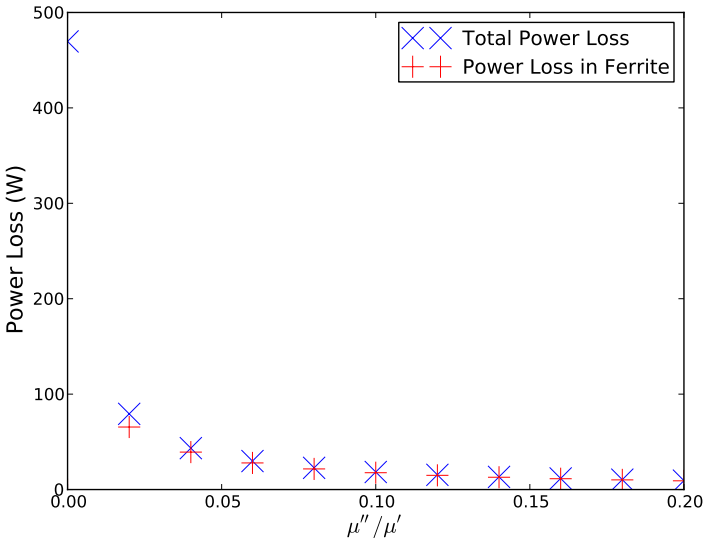

Figure 6.9: The power loss due to a beam with 1.15×10^{11} particles per bunch, 288 bunches, a ring circumference 6911 m and a bunch length $4\sigma = 0.04$ m assuming a Gaussian bunch distribution in the unscreened cavity.

is shown in Fig. 6.10. As with the case of the unshielded ferrite, the addition of the damping material causes a decrease in the resonant frequency of the cavity mode, again due to the addition of a material with $\epsilon^{'} > 1$. In addition, the shielding causes a further decrease in the resonant frequency, in this case due to the rearrangement of the field lines due to the changed boundary conditions.

As can be seen from Fig. 6.11(a) the decrease in the Q of the resonance by the increasingly more lossy ferrite follows a similar pattern to that shown by the unshielded structure, as does the increase in the percentage of power loss in the ferrite for the increasing damping of the resonance, shown in Fig. 6.11(b). The corresponding change in the power loss in both the cavity as a whole and the ferrite is shown in Fig. 6.12. As with the unscreened case, the power lost in the ferrite rapidly converges with the power loss in the entire cavity, indicating that magnetic losses are dominating the losses.

From these results it can thus be seen that the inclusion of the shielding does not substantially effect the losses due to strong cavity resonances, whilst aiding in reducing the effects of image current flowing through the ferrite (a broadband effect, and thus not

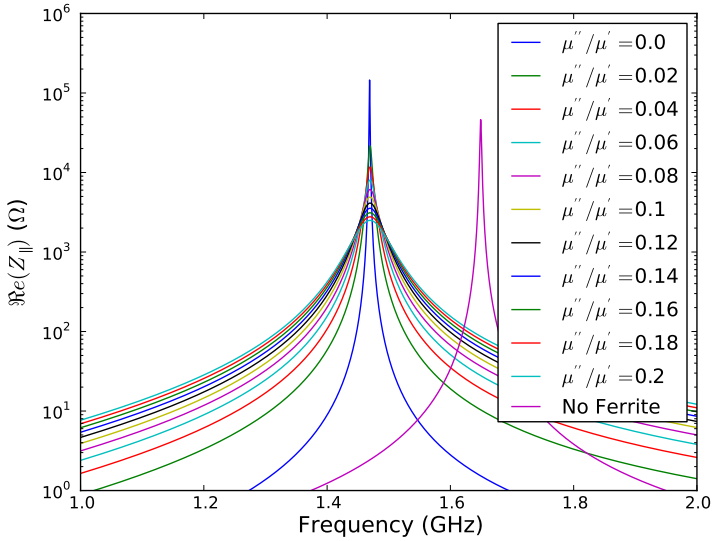

Figure 6.10: The real component of the longitudinal beam coupling impedance of a cavity without and with shielded damping material with $\epsilon^{'} = 10$, $\mu^{'} = 10$ and $\mu^{''}/\mu^{'}$ is varied. The non-damped cavity is shown for comparison. The change in resonance frequency and shunt impedance impedance is due to the increased $\epsilon^{'}$ of the damping material.

considered in the eigenmode simulations). In addition, we see that if the cavity mode is strongly damped by the presence of ferrite (i.e. the Q is reduced by a factor 20 or so) it should be expected that the vast majority of the remaining power lost by particles interacting with the cavity resonance should ultimately be lost in the damping material.

6.7 Conclusion

In this section we have given a thorough review of the beam coupling impedance reduction measures that are presently in use in many particle accelerators. We have described in detail the use of each reduction method, giving notes as to the side-effects each may have, how they may be tuned to give the desired impedance response and some of the limits on their implementation. Some examples of the successful implementation of these impedance reduction measures on real devices is given for clarity.

In addition an indepth study of the location of power loss due to EM fields in the

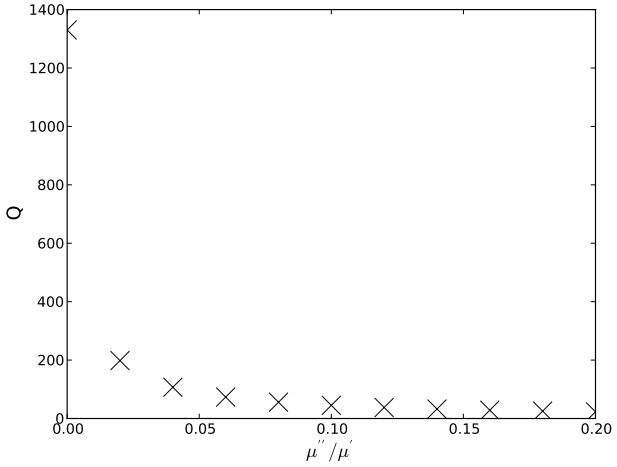

(a)

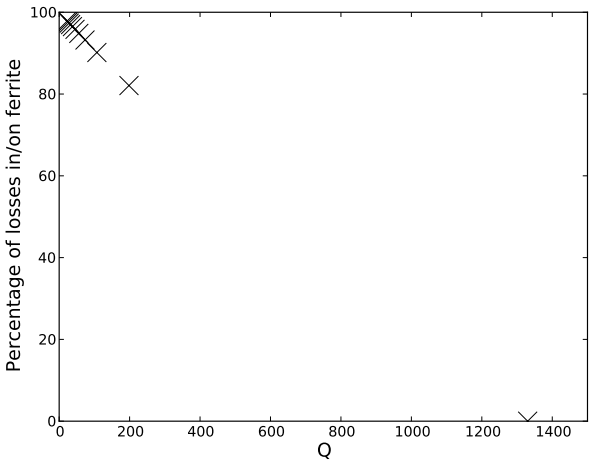

(b)

Figure 6.11: (a) The reduction in the Q of the cavity resonance with the increasing loss tangent of the ferrite damping, showing a strong decrease of the resonant Q with a small increase in loss tangent. (b) The percentage of the power loss in the ferrite as the resonant Q decreases. This can be seen to tend towards 100% as the Q approaches 0.

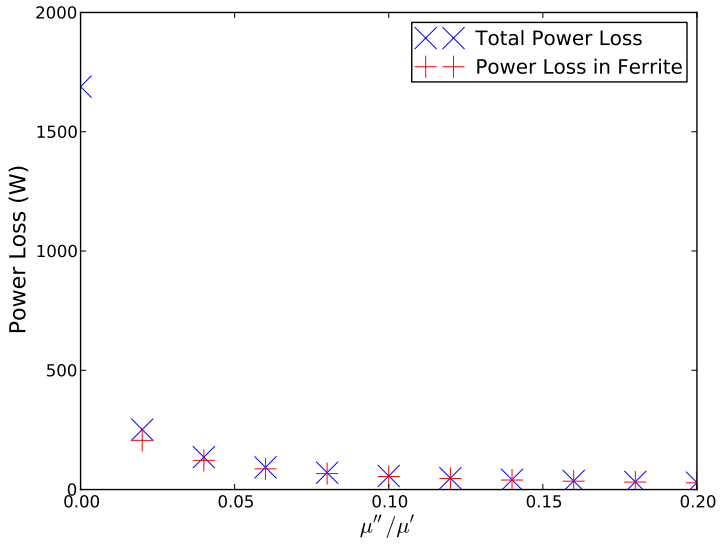

Figure 6.12: The power loss due to a beam with 1.15×10^{11} particles per bunch, 288 bunches, a ring circumference 6911 m and a bunch length $4\sigma = 0.04$ m assuming a Gaussian bunch distribution in the screened cavity.

case of ferrite damped cavity structures is presented. It has been found that for the case of mildly damped structures (either due to a weakly damping material or placement of the ferrite in a location where it does not interact strongly with the cavity fields) that the percentage of the power loss that occurs within the ferrite is linear with the reduction of the Q-factor of the cavity mode (i.e. percentage of power lost in the ferrite is negatively correlated with the Q-factor). The absolute value of power loss reaches a peak value for a very low degree of damping, upon increasing the damping strongly decreases the power loss in the damping material. This has given a better understanding of how the power loss in a structure changes as it's damping is modified, essential for the correct treatment of the thermal evolution of the structure under heat load.

These impedance reduction techniques are now implemented in the context of the LHC collimators and the injection kicker magnets, where their usefulness will discussed, and the other design restrictions that might limit their performance become more prominant in decision making.

Chapter 7

LHC Collimation Upgrades

7.1 Introduction

The LHC collimation system is a key part of the machine protection system in the LHC. Due to extremely high stored beam and magnetic energy in the LHC [77], amounting to some 360 MJ of beam energy and 10GJ of stored magnetic energy, it is neccessary to keep close control on the losses experienced by the system. In the LHC this is done by a combination of monitoring the losses within the machine, carefully controlled losses by the collimation system, and a rigorous interlock system designed to dump the beam safely in the event of the development of dangerous behaviour by the circulating beam or a malfunction by safety critical equipment [77].

The collimation system in the LHC is a four-stage system, composed mainly of primary (TCP), secondary (TCS), and tertiary (TCT) collimators. These serve to scatter the particle halo, then further scatter and absorb the scattered particles: the schematic of the process shown in Fig. 7.1. Further protection is provided by absorbers (TCLA), collimators at the injection regions (TCLI and TDI) and at the extraction region (TCDQA). In particular the TCTs are placed near the experimental IPs (Interaction Points) to protect the inner triplet magnets (used for final focusing of the beam before collision). In total the collimation system is broken down into two IPs; IR3 for momentum cleaning, in which there are:

1. 1 primary collimator
2. 4 secondary collimators
3. 4 absorbers

per beam and IR7 for betatron cleaning, which is composed of:

1. 3 primary collimators
2. 11 secondary collimators
3. 5 absorbers

per beam, with an additional 8 tertiary collimators (2 per experimental IP) per beam. In summary, with the addition of the collimators at the injection and extraction regions each beam is exposed to 44 different moveable collimators per circulation of the machine. The primary and secondary collimators presently all have a jaw material of carbon reinforced graphite (conductivity $\sigma_{graphite} = 7 \times 10^4\ Sm^{-1}$). This material was chosen due to the requirement for a robust jaw material (mechanically stable under large thermal shock) from a machine protection point of view, however not optimised from a beam impedance point of view.

The current collimation system has demonstrated to be exceptionally effective at it's job of providing machine protection to the LHC [79], however it has some drawbacks. The very large imaginary component of the transverse impedance gave some worry of being a contributor to instabilities in the LHC, but recent work has shown that there is still some substantial overhead in the stability limit driven by beam coupling impedance. However, interactions with other mechanisms such as beam-beam and electron cloud may produce instabilities at lower intensities [17].

The phase 1 collimator (those presently (as of 2012) in place in the LHC) design has a number of features that are designed to reduce the beam coupling impedance of each device. Although the resistive wall contribution to the beam coupling impedance, due to the poorly conducting jaw material, is significant, the use of longitudinal RF fingers in

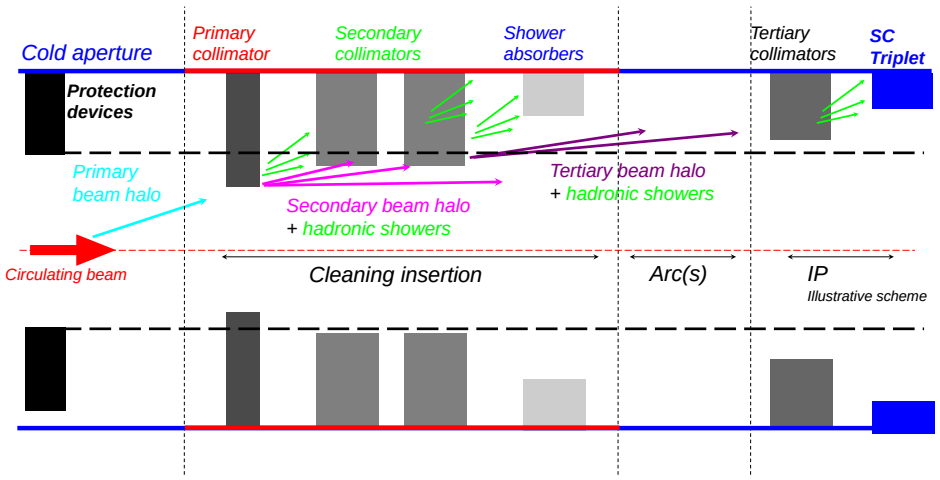

Figure 7.1: The processes by which the collimation system in the LHC acts to clean the beam and manage losses in a controllable way. Taken from [78].

the transition between the beam pipe to the collimator jaws and of a system of sliding contact fingers isolates the beam from seeing the collimator vacuum tank (see Fig 7.2 for more details). These function well as impedance reduction techniques, however have some limitations from a mechanical point of view. In particular, the sliding contacts have been suspected to be a significant producer of dust in the LHC due to the moving physical contact during collimator alignment and some collimators were suspected (and a number observed) with RF fingers with broken contact.

Due to these factors (high transverse impedance due to the resistive wall impedance, problems of dust due to sliding contacts and possible RF fingers not touching) a phase 2 upgrade of the LHC collimation system has been proposed. This entails two components;

1. The supplementation of the current secondary collimators (the prime contributor to the large transverse impedance) by a phase 2 design using a good conducting material as the jaw material. There will be some loss of mechnical robustness but it is thought that this will not be detrimental to the requirements of machine protection with a suitable choice of material.

2. Replacing the existing sliding RF contacts with a contactless RF system (shown in Fig. 7.3). This is designed to suppress the problem of dust caused by the sliding

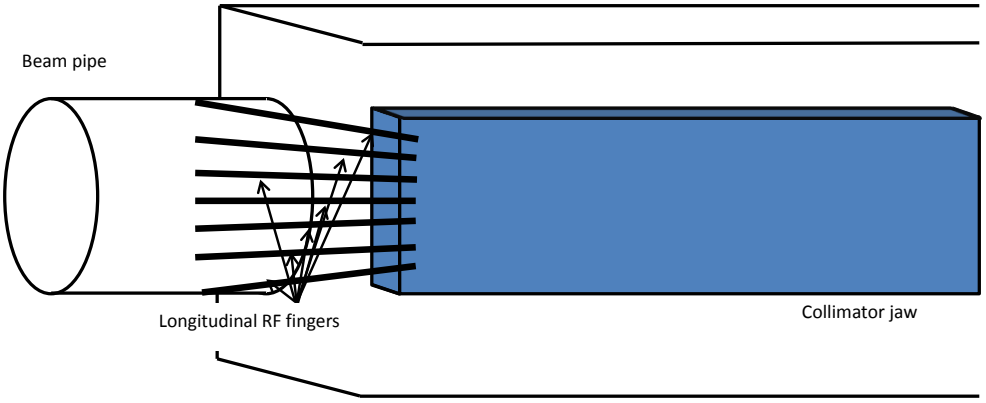

(a)

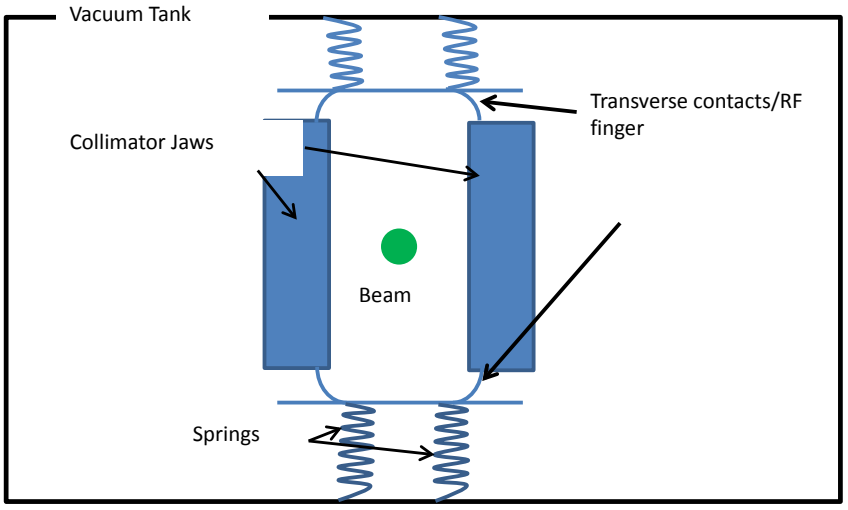

(b)

Figure 7.2: Different components of impedance reduction measures in the phase 1 collimator design. (a) shows the longitudinal RF fingers, ensuring a good conducting path for the beam image currents, and (b) shows the sliding RF contacts on the collimators jaw. These are intended to minimise the volume seen by the beam, thus confining any cavity modes that may be excited by the beam to very high frequencies where the beam power spectrum is very small.

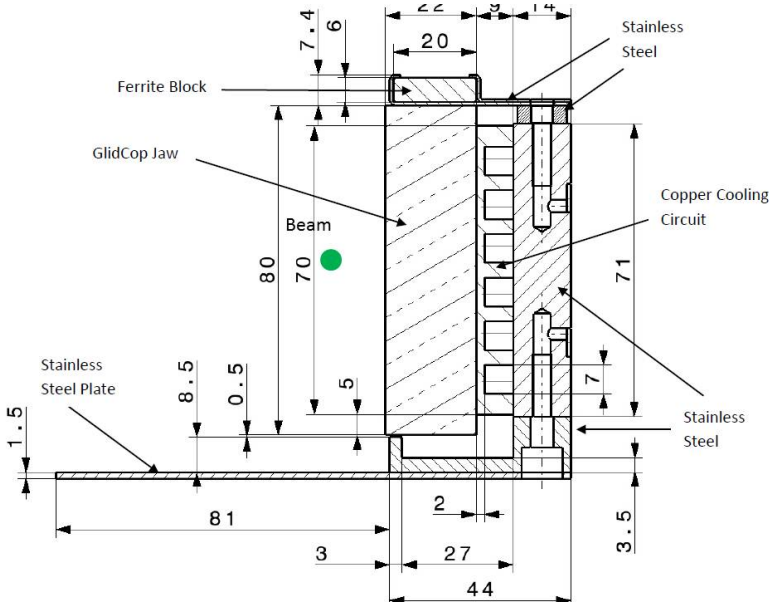

Figure 7.3: The RF system for use in the phase 2 collimation system. The sliding RF contacts of the phase 1 design are replaced with a ferrite damping system. The RF contacts are removed, allowing the beam to see the entire RF cavity, causing resonances at lower frequencies. The Q of these resonances are decreased by the use of ferrite damping tiles (see Sec. 6.6). The location of the beam is shown in green.

RF contacts in the phase 1 system by removing the moving physical contacts in addition to being more mechanically robust. This increases the volume of the cavity visible to the particle beam, decreasing the frequency of the lowest cavity modes. To counteract these new resonances, ferrite is placed in the cavity to decrease the resulting Q of the resonances.

In this chapter shall be presented a comparison of the different jaw materials proposed for use in the phase 2 secondary collimators. In particular a combination of jaw materials aimed at combining extremely robust materials with highly conductive metals, and the results of full 3D simulations of a TCTP collimator - a tertiary collimator for use in the LHC - which incorporates the ferrite damping system, is compared to the sliding contacts of the phase 1 RF system.

7.2 LHC Phase 2 Secondary Collimator Jaw Material

The phase 2 secondary collimators are proposed as an addition to the current phase 1 secondary collimators. They have stringent mechanical requirements, particularly due to the neccessity to withstand impacts by a limited number of bunches in the LHC during mis-injection. In addition they must meet a stringent limit on beam impedance - new devices in the LHC must not increase the total impedance of the machine due to the stability limits imposed due to the existing large transverse and longitudinal impedance. If possible, the effective impedance in the machine should be reduced during operation. The requirements for the material requirements are detailed and summarised in [80].

To meet the strict requirements of the different physical requirements on the jaw material, both from a mechanical point of view and an impedance point of view, a number of different jaw design solutions have been proposed. These include both single material jaw designs, mixtures of composites and pure metals, and variations on a design including ceramic. The proposed jaw material combinations are listed below:

1. GlidCop, a copper compositie including aluminium oxide particles. The conductivity is marginally worse than pure copper (see Tab. 7.1), but the addition of the aluminium oxide greatly increases the resistance to thermal softening and increases the strength at high temperatures.

2. Molybdenum - A metal with good mechanical properties and a conductivity comparable to copper.

3. Copper Diamond Composite - A copper composite formed by hot pressing copper with the addition of boron powder and small synthetic diamonds. This is a very mechanically robust material.

4. Molybdenum Diamond Composite - As with the above, a molybdenum composite formed by the use of sintering molybdenum with artificial diamonds.

5. Carbon reinforced carbon (CFC) - The current material of the phase 1 secondary collimators. Included for comparison.

Table 7.1: The electrical conductivity of the different jaw materials proposed for use in the phase 2 design. All results are given for measurements at room temperature (20^{o}C)

Material	Conductivity (Sm^{-1})
Glidcop	5.4×10^7
Molybdenum	1.87×10^7
Copper Diamond Compositie (CuCD)	1.25×10^7
Molybdenum Diamond Composite (MoCD)	5.5×10^6
Graphite (used for CFC)	7×10^4

More information on the material choices can be found in [80, 81]. The conductivities of the different materials can be found in Tab. 7.1. The layouts of the various possible jaw designs can be found in Fig. 7.4.

7.2.1 Impedance Studies and Analysis

To analyse the jaw material impedance the Mounet model [29] for 2D infinite parallel plates is used. This model assumes infinite parallel plates with n-layers of material. It supports non-symmetric structures in addition. The representation of this structure is shown in Fig. 7.5. For this model we assume a jaw separation of 4 mm (half-width of 2 mm), the closest nominal seperation of the secondary collimators and hence a worst-case for beam coupling impedance.

The frequency range of concern is determined by the instability mechanism driving the stability limit in the LHC. It has been demonstrated that this range of concern is from 8 kHz up to a few GHz [82] in the transverse plane, covering regions where TCBI and TMCI may develop. This neccessitates investigating the transverse beam coupling impedance over a very large frequency range, hence the choice of using an analytical method of investigation.

The beam coupling impedances for the various jaw materials are shown in Figs. 7.6 and 7.7 calculated using the Mounet model assuming either one or two layers (depending on the jaw material) surrounded by a perfectly conducting layer of infinite thickness. From the consideration of the longitudinal impedance, the collimator jaw material is not a

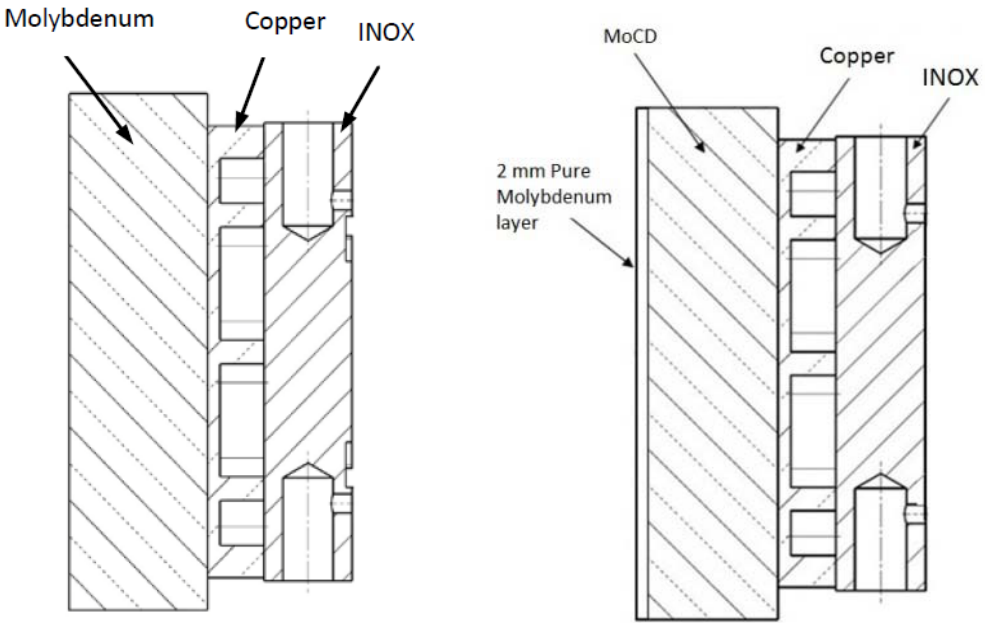

(a) (b)

Figure 7.4: A number of the proposed jaw designs for the phase 2 secondary collimators. (a) shows the jaw made entirely from molybdenum. Glidcop maybe substituted for molybdenum in this design. (b) shows the jaw made from a mixture of molybdenum diamond composite with a 2 mm coating of pure molybdenum on the surface. The composite ensures a mechanically strong jaw, whilst the coating screens the higher resistivity composite and provides a smooth surface on the beam-facing part of the jaw. In this case the composite maybe substituted with copper diamond composite, and likewise the coating may be replaced with GlidCop.

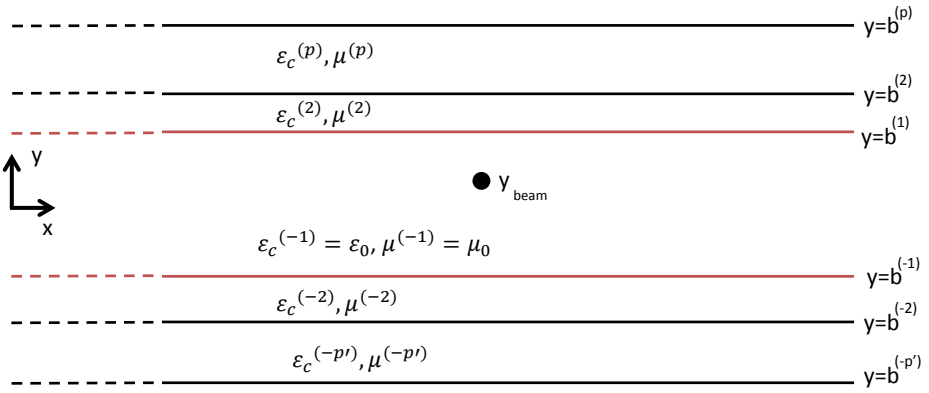

Figure 7.5: The physical model of the Mounet model of parallel plate impedance. Note that the two sides of the structure do not have to be symmetric. The materials maybe any material provided it's frequency dependent properties are well defined.

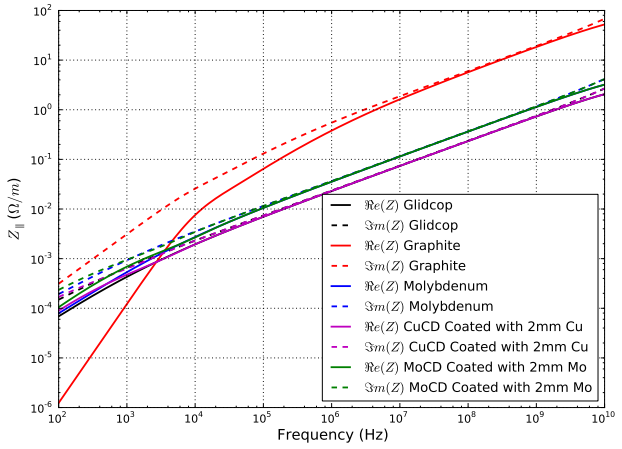

(a)

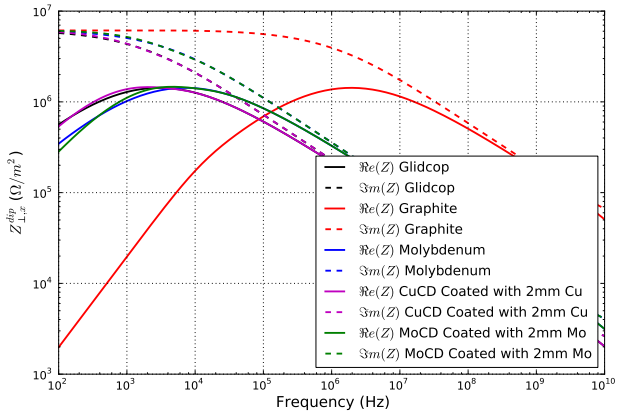

(b)

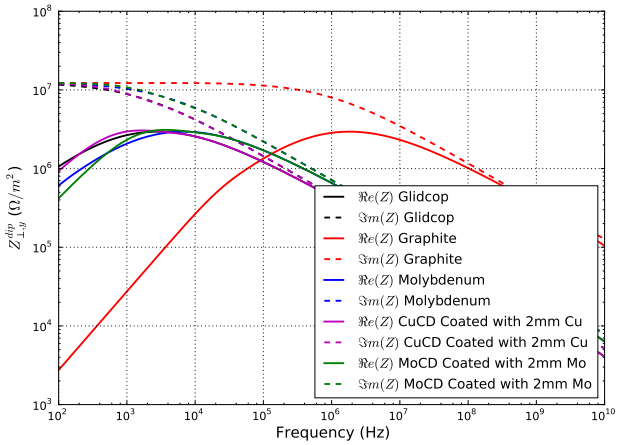

(c)

Figure 7.6: The impedances of different jaw materials for the phase 2 secondary collimators. (a) The longitudinal impedance, (b) the horizontal dipolar impedance, (c), the vertical dipolar impedance per unit length.

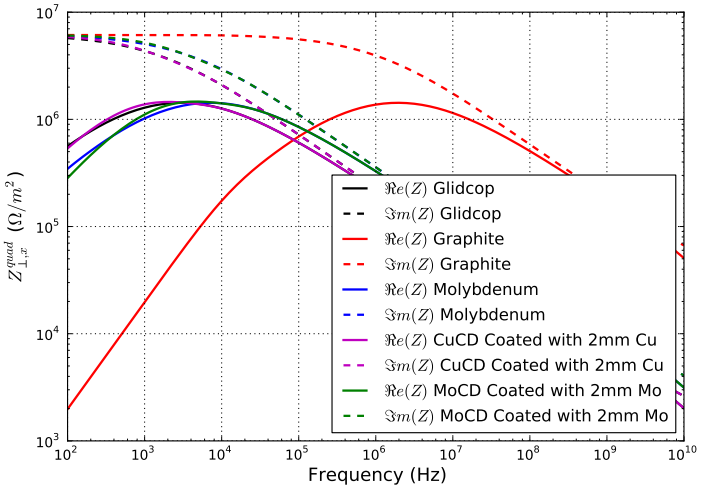

(a)

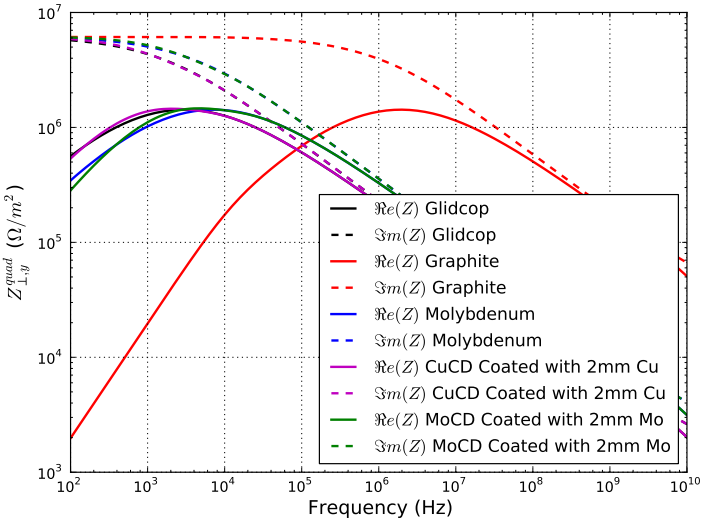

(b)

Figure 7.7: The impedances of different jaw materials for the phase 2 secondary collimators. (a) the horizontal quadrupolar impedance and (b) the vertical quadrupolar impedance per unit length.

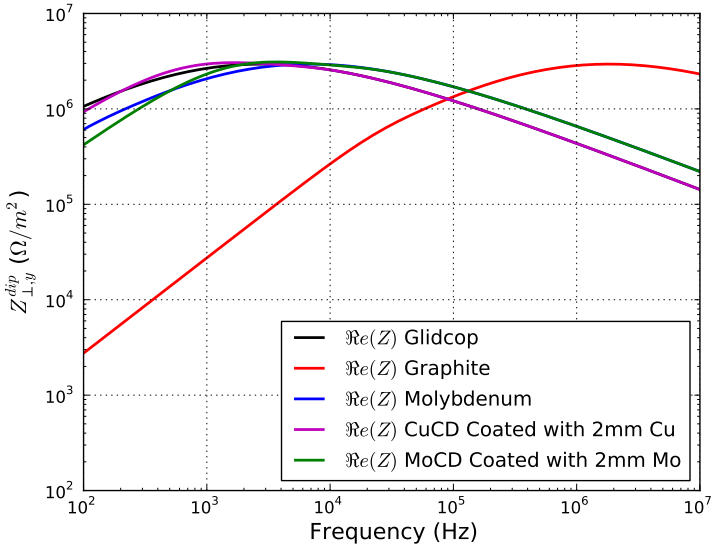

Figure 7.8: The real component of the vertical dipolar impedance of the various collimator jaw materials assuming a 2mm half gap.

significant contributor to the machine impedance. The significant concern is the transverse impedance. It can be seen from Figs. 7.6(b), 7.6(c), 7.7(a), 7.7(b) that all the potential jaw materials reduce the imaginary component of the transverse impedance (dipolar and quadrupolar) above 10^3 Hz. By comparison with the change in tune shift discussed in Sec. 3.2.1 it can be seen that this reduces the magnitude of the imaginary component of the impedance - i.e. the change in real part of the betatron tune is reduced.

Conversely, the peak of the real component of the transverse impedance is moved to lower frequencies as the conductivity of the innermost jaw material increases (shown in greater magnitude for the vertical dipolar impedance in Fig. 7.8). Significantly, this causes the high conductivity jaw materials to present a larger real component of the impedance in the important frequency range below 10^5 Hz, in particular at the 1st unstable betatron line at $\approx$ 8kHz. Reviewing Sec. 3.2.2 it can be seen that this produces an decrease in the growth time of any associated instability.

7.3 TCTP Impedance Studies

As part of the ongoing collimation upgrade in the LHC, several advances in the LHC design have been proposed. These are as follows:

1. For the reasons given in Sec. 7.2, the jaw material of the collimators, specifically the secondary collimators, is under review in an effort to reduce the beam impedance, improve cleaning efficiency and continue the present robustness and excellent performance of the LHC collimation system.

2. The inclusion of on-collimator BPMs. This is due to the present method of alignment of the collimators, relying on investigating the beam loss patterns in the LHC as a function of collimator aperture, being a very time intensive procedure due to the inherently slow nature of beam loss. The use of on collimator BPMs allows a near instantaneous feedback on the position of the beam relative to the collimator jaw thus greatly reducing collimator setup time [83, 84].

3. A new RF system (shown in Fig. 7.3) to reduce the side effects of the sliding RF contacts used in the phase 1 collimators.

As part of the upgrade, a series of TCTP collimators shall be installed in the LHC to replace a number of tertiary collimators (TCTs). In total, 8 TCTP and 1 TCSG will be added to the LHC. These collimators are in part intended to act as a test for two of these upgrades, the use of on-collimator BPMs and the new RF system [85]. As part of the ongoing effort to limit increases to the LHC machine impedance (shown in Tab. 7.2) and due to continuing concerns about beam-induced heating [33, 86], all new devices to be placed in the LHC must be examined for both their effect on the beam and as a possible luminosity limiter. Due to the large number of phase 2 secondary collimators that are planned to be put in the LHC (30 additional secondary collimators to be installed during long shutdown 2) it is vital that the new collimator design, especially the new RF system, is verified for it's efficacy as an impedance reduction technique.

Table 7.2: The impedance budgets (both transverse and longitudinal) for LHC at injection and collisions. Taken from the LHC Design Report [72].

Beam Operation	$\Im m(Z_{\parallel}/n)\ (\Omega)$	$\Im m(Z_{\perp})\ (M\Omega/m)$
Total Broadband (450GeV)	0.07	1.34
Total Broadband (7TeV)	0.076	2.67

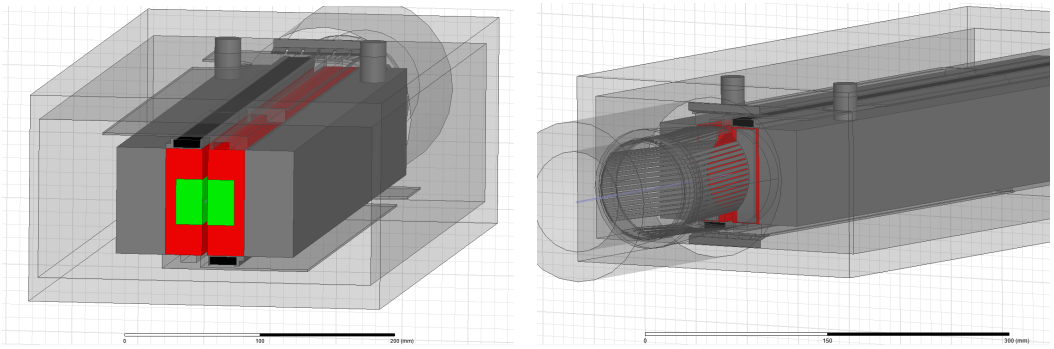

(a) (b)

Figure 7.9: The TCTP collimator has a number of important impedance reduction techniques present in its design. Ferrite tiles replace the sliding transverse RF contacts of the phase 1 design, shown in (a) (ferrite tiles shown in black) to reduce the resonant Q of the structure. The longitudinal RF fingers, shown in (b), provide a good conducting path for the beam image current in the transition from the beam pipe to the collimator jaw.

7.3.1 TCTP Collimator - Design and Geometry

The TCTP is a tertiary type collimator with a jaw made of tungsten. The principle components of interest from a beam impedance reduction point of view are the longitudinal RF fingers that cover the transition from the beam pipe to the collimator structure, and the RF system utilising ferrite blocks and a screen structure, shown in Fig. 7.9(a).

The RF system is designed to work in the following way, where comparison is given to the phase 1 RF system to clarify the differences and the design choices made. The phase 1 sliding contacts adequately masked the surrounding vacuum cavity from the beam, causing the resonant modes of the structure to be dominated by the geometry of the internal structure of the collimator jaw. Due to the small dimensions of this volume the resonant frequencies are thus very high (in the realm of gigahertz) where the beam power spectrum is very small and thus the beam-structure interaction is relatively small thus avoiding both impedance driven instabilities due to cavity modes and beam-induced heating. However

the sliding contacts are believed to produce a large quantity of dust which is problematic for beam losses.

Conversely, the TCTP RF system removes the sliding contacts to solve the dust problem. This allows the beam to 'see' the entire vacuum tank of the collimator. This increases the characteristic dimensions driving the resonant frequency modes, thus lowering the minimum frequency of the cavity modes. Hence the frequency of the cavity modes is moved into an area over the beam power spectrum where the spectrum is comparable to the DC beam current in the machine. To counteract this the Q of the cavity modes is reduced by the placement of ferrite tiles in the device to act as a damping material. This strongly reduces the peak of the impedances thus reducing their effect on both instability and beam-induced heating.

7.3.2 Impedance Simulations and Results

The impedance of the TCTP collimator is examined through the use of simulation codes. In order to verify the simulation results it was decided to use both a time domain and a frequency domain code, in this case CST Particle Studio for the time domain and Ansoft HFSS for the frequency domain. Due to the reduced simulation time for time domain simulations compared to frequency domain simulations (which must be evaluated mode by mode to correctly evaluate the eigenmodes), the preliminary comparisons are done using the time domain code and the most promising solutions are subsequently investigated in depth using the frequency domain model.

For this comparison we investigate a number of different designs of the RF system for comparison to the ferrite damping solution chosen for construction;

1. The phase 1 sliding RF contacts. Shown in Fig. 7.2.

2. The proposed RF system including the ferrite damping tiles and the RF screen as shown in Fig. 7.3.

3. The proposed RF system without the ferrite damping tiles. This is too investigate the benefit of including the ferrite tiles.

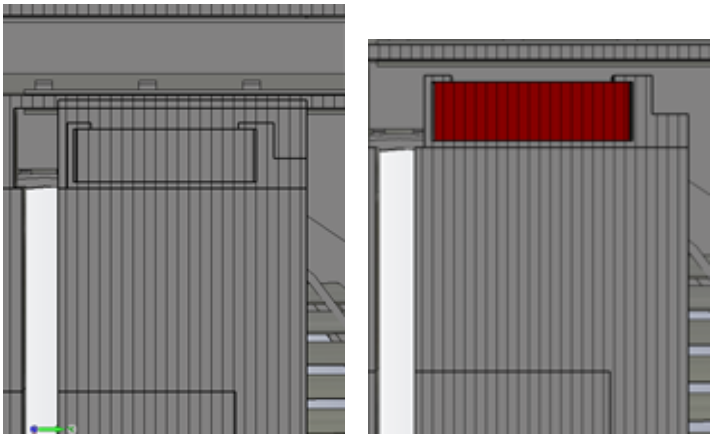

(a) (b)

Figure 7.10: The different RF systems considered for the TCTP collimator. (a) shows an RF system similar to the phase 1 RF system. In these simulations the sliding RF contacts are replaced by a perfect connection - for frequencies lower than 2-3 GHz this is a good approximation and greatly simplifies the simulation model. (b) shows the RF circuit complete with ferrite. Two further variants may be considered, where the ferrite is replaced by either vacuum (to indentify how the ferrite damps the otherwise present modes) and replacing the ferrite with PEC (to see whether it is the ferrite or the small aperture that reduces the coupling of the beam to the surrounding vacuum tank).

The three different systems are shown in Fig. 7.10. The impedance results for these three options are shown in Fig. 7.11 simulated in CST Particle Studio. It can clearly be seen the differences between the two RF systems. The phase 1 RF system screens the surrounding vacuum tank from the beam, meaning any cavity modes occur at a relatively high frequency, above 1 GHz. The phase 2 system allows the beam to see the vacuum cavity, decreasing the lowest frequency cavity mode. The presence of the ferrite in this system subsequently strongly reduces the Q of these resonances, reducing the impedance. Both the real and imaginary longitudinal impedance is strongly reduced as a result. Similar results have been observed in the transverse plane [87].

7.3.3 Beam-Induced Heating

As seen in Sec. 7.3.2, the longitudinal impedance of the phase 2 RF design indicates a significant number of beam impedance resonances below 1GHz. Although their contribution

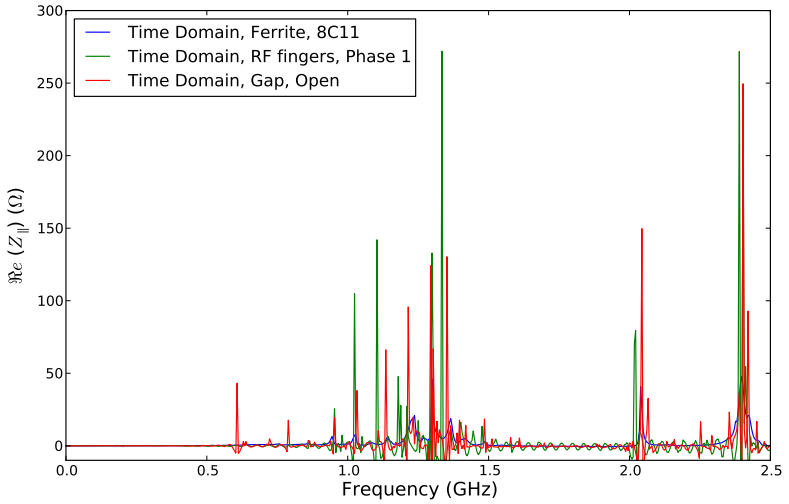

(a)

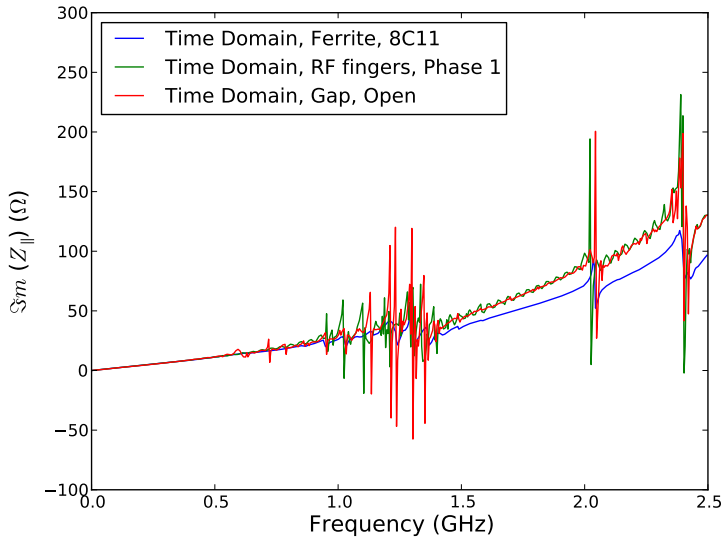

(b)

Figure 7.11: The longitudinal impedance of the TCTP collimator for a number of different configurations. Shown is the system using the ferrite damping system (ferrite being 8C11 in this case), RF fingers as in phase 1, and the RF system with the ferrite replaced by PEC. The real (a) and imaginary (b) components are shown.

in the imaginary component of the beam coupling impedance is not significant enough to be of concern from a stability point of view, the resonances may present a problem from the point of view of beam-induced heating. To fully investigate both the effectiveness of the ferrite in damping the cavity resonances and to identify the locations of the power loss, the phase 2 structure is investigated using the frequency domain code HFSS.

For these simulations we model half of the structure (due to the reflective symmetry in the longitudinal plane), using alternatively perfect E-field (enforcing perpendicular electric fields at the boundary) and H-field (enforcing perpendicular magnetic fields at the boundary) boundary conditions at the symmetry plane to indentify and characterise the eigenmodes up to 2 GHz (to cover the majority of the beam spectrum). The structure with and without ferrite is simulated to characterise the effect of the ferrite in damping the cavity modes. Simulations are carried out using the following parameters:

- Using a 2^{nd} order basis function solver to ensure good resolution of the fields for R/Q and localised loss calculations.
- The ferrite is assumed to be 8C11, the materials data for which is imported from an external data file and interpolated fit is used between data points.
- We simulate using a single jaw seperation, in this case a half-seperation of 2 mm. This is an extremely close jaw seperation, closer in fact than the TCTP collimator would be placed at, but similar to that which the phase 2 collimators would be placed at. This allows some prediction of a worst case scenario for the TCTP and also an analysis of the efficacy of the RF system for the type of operational parameters the phase 2 secondary collimators would be placed at.
- The mesh was auto-generated by the HFSS mesh generator, and run for a convergence criteria of a 0.5% convergence of the eigenmode frequency between two successive meshes with a 30% refinement of the mesh between successive solutions.

Here we shall evaluate the resonances as a whole, or a few key resonances from a heating point of view. For a complete listing of the eigenmodes please see App. B for

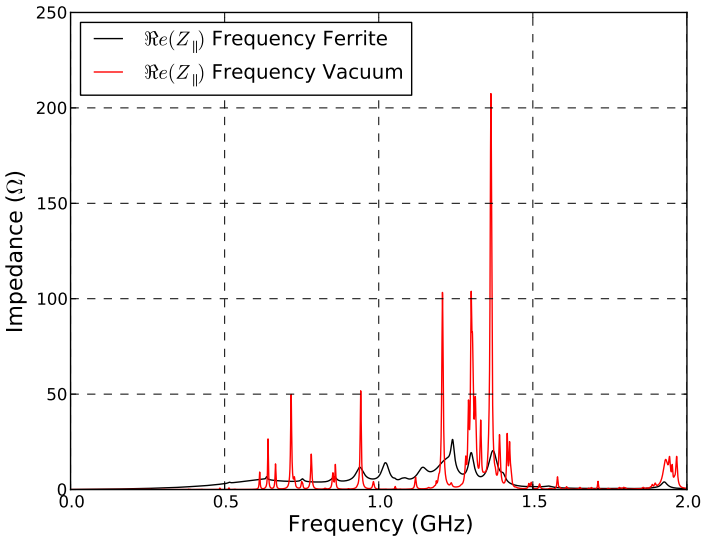

Figure 7.12: The real component of the longitudinal impedance for the TCTP collimator as simulated in the frequency domain for the case with and without ferrite damping tiles. The strong resonances present in the case without ferrite can be seen to be strongly damped when the ferrite tiles are added. However a substantial broadband component occurs in addition due to the broadened resonance peaks.

a complete breakdown of the TCTP eigenmode simulations. To have a comprehensive review of the heating we consider the following heating possibilities

- A beam harmonic occuring exactly on the resonant frequency with a certain bunch profile. Here we consider Gaussian (for which all bunch lengths quoted are for the $4\sigma_z$ length) and $\cos^2$ bunch profiles. Parameters for a number of different beam operating modes (summarised in Tab. 7.3) are considered.

- Taking theoretical spectra for both 50 ns and 25 ns bunch spacings. In this case we consider the heating for both nominal operational parameters (1 ns bunch length), running conditions from 2012 (bunch length between 1.0-1.5 ns) and for HL-LHC parameters. These parameters are summarised in Tab. 7.3. Different bunch profiles are considered - Gaussian and $\cos^2$ to account for high frequency lobes observed in measured beam spectra.

The heating estimates assuming on resonance beam harmonics can be seen in Tab. 7.4

Table 7.3: The LHC operational parameters considered for heating estimates for the TCTP. Operational parameters include the nominal LHC parameters for 25 ns bunch spacing, the peak operational intensity for 50 ns bunch spacing used in 2012, and the two possible HL-LHC operational schemes, using both 25 ns and 50 ns bunch spacing. Here the bunch length is assumed to encompass the 4σ Gaussian width.

Operational Mode	t_b (ns)	t_{bunch} (ns)	N_b	$n_{bunches}$
50 ns, 2012 LHC Operation	1.2	50 ns	1.7×10^{11}	1380
25 ns, Nominal LHC Operation	1.0	25 ns	1.15×10^{11}	2808
HL-LHC 25 ns	1.0	25 ns	2.0×10^{11}	2808
HL-LHC 50 ns	1.0	50 ns	3.3×10^{11}	1380

Table 7.4: The power loss of a the TCTP collimator with ferrite for a number of operational modes in the LHC and HL-LHC assuming each cavity mode falls upon a beam harmonic. All losses are in Watts using the parameters found in Tab. 7.3

t_b (ns)	50 ns, 2012		25 ns nominal		50 ns, HL-LHC		25 ns, HL-LHC	
	$P_{loss,g}$	$P_{loss,c}$	$P_{loss,g}$	$P_{loss,c}$	$P_{loss,g}$	$P_{loss,c}$	$P_{loss,g}$	$P_{loss,c}$
1.0	2.8	7.1	5.3	15	10	27	16	41
1.1	1.9	5.1	3.6	9.8	7	19	11	30
1.2	1.4	3.7	2.5	7.0	5	13	7.7	21
1.3	0.9	2.7	1.8	5.0	4	10	5.5	15
1.4	0.7	1.9	1.3	3.7	3	7	3.9	11
1.5	0.5	1.4	1.0	2.7	2	5	2.9	8.2

for a variety of bunch lengths between 1-1.5 ns assuming either Gaussian or $\cos^2$ bunch distributions. The same data for the TCTP without the ferrite damping tiles can be seen in Tab. 7.5. A number of things are immediately evident; the addition of the ferrite drastically reduces the power loss in the TCTP collimator, by a factor of ≈ 10. In addition, the consideration of the higher frequency lobes in the heating estimates for the TCTP is significant as can be seen by the large differences (factor ≈ 3 between Gaussian and $\cos^2$ profiles). In this case the usefulness for the ferrites is clear.

Considering the heating taking beam harmonics seperated by the inverse of the bunch seperation (40 MHz for $t_{bunch} = 25\ ns$ and 20 MHz for $t_{bunch} = 50\ ns$) we acquire the results presented in Tab. 7.6 and Tab. 7.7 respectively, again for a variety of LHC operational parameters and assuming either a Gaussian or a $\cos^2$ longitudinal bunch profile

Table 7.5: The power loss of a TCTP collimator without the ferrite damping tiles for a number of operational modes in the LHC and HL-LHC assuming each cavity mode falls upon a beam harmonic. All losses are in Watts using the parameters found in Tab. 7.3

t_b (ns)	50 ns, 2012		25 ns nominal		50 ns, HL-LHC		25 ns, HL-LHC	
	$P_{loss,g}$	$P_{loss,c}$	$P_{loss,g}$	$P_{loss,c}$	$P_{loss,g}$	$P_{loss,c}$	$P_{loss,g}$	$P_{loss,c}$
1.0	21	52	41	100	81	197	123	301
1.1	15	38	29	72	56	143	86	218
1.2	10	28	20	53	40	105	61	160
1.3	7.7	21	15	39	29	78	43	119
1.4	5.4	15	10	30	20	60	31	91
1.5	4.0	12	7.3	23	15	46	22	70

Table 7.6: The power loss of a TCTP collimator with ferrite for a number of operational modes in the LHC and HL-LHC assuming beam harmonics spaced at the reciprocal of the bunch spacing. All losses are in Watts using the parameters found in Tab. 7.3

t_b (ns)	50 ns, 2012		25 ns nominal		50 ns, HL-LHC		25 ns, HL-LHC	
	$P_{loss,g}$	$P_{loss,c}$	$P_{loss,g}$	$P_{loss,c}$	$P_{loss,g}$	$P_{loss,c}$	$P_{loss,g}$	$P_{loss,c}$
1.0	9.5	18	9.1	17	36	68	27	53
1.1	7.4	14	7.1	14	28	55	21	42
1.2	5.9	11	5.6	11	22	45	17	34
1.3	4.8	9.6	4.5	9.2	18	36	14	28
1.4	3.9	8.0	3.7	7.5	14	29	11	22
1.5	3.2	6.6	3.0	6.3	12	25	9.1	19

($P_{loss,g}$ and $P_{loss,c}$ respectively). In this case it can be seen that the power loss for the ferrite case is larger than that experienced by the case without ferrite. This can be understood due to the fixed frequencies of the beam harmonics - if a high-Q resonance does not occur at or near a beam harmonic then the beam does not couple to the resonance. Due to the broad resonance peaks of the ferrite damped TCTP design the beam may couple to the resonance even if the resonant frequency of the cavity mode does not match the beam harmonic precisely due to the low-Q of the resonance.

A judgement must be made with regards as to which simulations provide a more realistic safety margin for operation in the LHC. For this we must consider both the worst case scenarios in each case and their likelihood. Considering the worst cases in both the cases with and without ferrite we can see that for any given operational mode the worst case

Table 7.7: The power loss of a TCTP collimator without ferrite for a number of operational modes in the LHC and HL-LHC assuming beam harmonics spaced at the reciprocal of the bunch spacing. All losses are in Watts using the parameters found in Tab. 7.3

t_b (ns)	50 ns, 2012		25 ns nominal		50 ns, HL-LHC		25 ns, HL-LHC	
	$P_{loss,g}$	$P_{loss,c}$	$P_{loss,g}$	$P_{loss,c}$	$P_{loss,g}$	$P_{loss,c}$	$P_{loss,g}$	$P_{loss,c}$
1.0	2.2	6.0	2.4	6.6	8	22	7.2	20
1.1	1.5	4.2	1.6	4.5	6	15	4.7	14
1.2	1.1	2.9	1.0	3.1	4	11	3.1	9.5
1.3	0.8	2.1	0.7	2.2	3	8	2.1	6.7
1.4	0.5	1.5	0.5	1.6	2	6	1.5	4.7
1.5	0.4	1.2	0.3	1.1	1	5	1.0	3.5

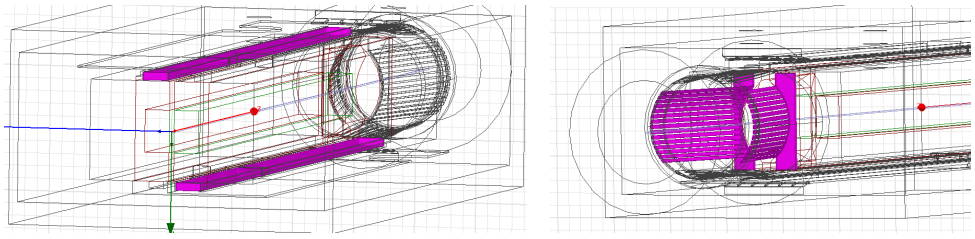

(a) (b)

Figure 7.13: The different thermally sensitive components of the TCTP collimator highlighted in purple. (a) shows the ferrite tiles, and (b) the longitudinal RF fingers.

for the collimator without ferrite is substantially worse than that with ferrite. Considering the possibility of inaccuracy of the frequencies of the eigenmodes or their Q factors it is typically considered prudent to take the worst case scenario to avoid the need for costly repairs. In the case of adding ferrite it is possible to simply remove the ferrite if it proves detrimental to operation, therefore present installation plans for the TCTP collimator include the ferrite damping system.

Location of Power Deposition

Due to the poor cooling available in vacuum (cooled by thermal radiation only. Although surrounded by a housing/in contact with adjacent components, the thermal contact between different components within the collimator is poor) it is important to know the proportion of beam-induced power loss that is lost in thermally sensitive areas. These are areas where large increases in temperature can either lead to direct physical damage (as is

Table 7.8: The percentage of power loss lost in thermally sensitive components in the TCTP.

Component	Percentage of Power Loss
Whole Device	100
Ferrite Tiles	5
Longitudinal RF Fingers	4

Table 7.9: The power loss in the ferrite of the TCTP collimator. The most pessimistic of the losses estimated in Tab. 7.4 and Tab. 7.6 for the 1.0 ns case. All losses are in Watts using the parameters found in Tab. 7.3

t_b (ns)	50 ns, 2012	25 ns nominal	50 ns, HL-LHC	25 ns, HL-LHC
	$P_{loss,c}$	$P_{loss,c}$	$P_{loss,c}$	$P_{loss,c}$
1.0	0.9	0.9	3.4	2.7

the case with RF fingers) or may lead to a worsening physical condition of the collimator (if the ferrite tiles go above their Curie temperature). The components are highlighted in Fig. 7.13

The losses on or in different surfaces and volumes are calculated using the loss calculations within HFSS, and then normalised to the total losses in the TCTP structure for each mode. This produces a variety of losses depending on the field pattern of the mode. These are collated in App. B. To provide a conservative estimate of the power load we take the highest proportions of power loss of all the modes and assume this is the case for all modes. The percentages for the total device, the ferrite tiles and the longitudinal RF fingers are shown in Tab. 7.8.

The thermal behaviour as a result of this power load can be analysed using design software such as ANSYS [88]. The results of these thermal simulations can be seen in [89], a summary of which is given in Fig. 7.14. The important figure of merit is whether the temperature of the ferrite increases beyond its Curie temperature. For the ferrite TT2-111R, T_c=375 °C [90]. The power loss for the worst cases of the nominal, HL-LHC and HL-LHC parameters without crab cavities (bunch length 0.5 ns rather than 1.0 ns) is considered, in this case with a factor of two margin of error included to be conservative (i.e.

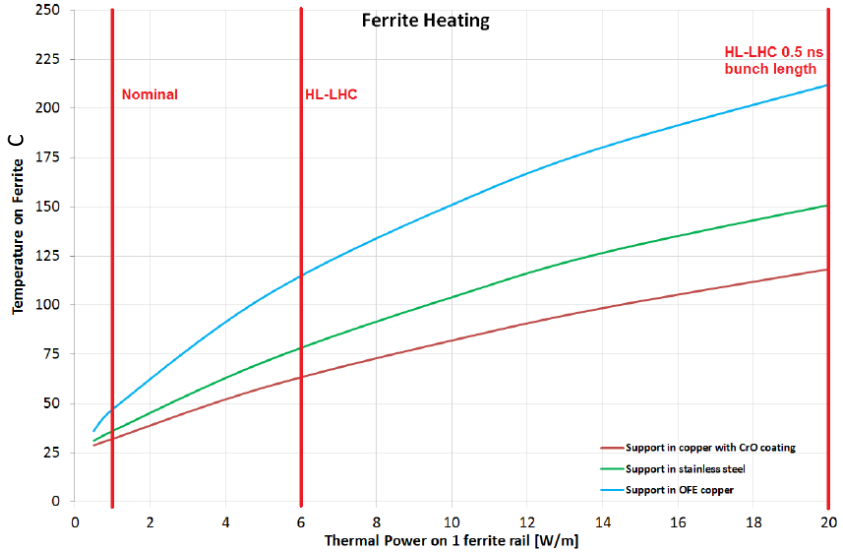

Figure 7.14: The temperature increase of the ferrite damping tiles in the TCTP collimator under a number of beam operating conditions and for a number of different jaw support materials. Plot taken from [89].

we assume double the power on the ferrite tiles), and it can be seen that the temperature increase for even the worst case results in the temperature being significantly below the Curie temperature for this material.

7.4 Conclusion

In this chapter we have evaluated in depth the longitudinal impedance due to resistive wall and cavity modes in the TCTP collimator, a tertiary collimator to be placed in the LHC. The beam induced heating expected in this collimator has been evaluated, significant as it is the first collimator to be installed in the LHC with a new RF system, designed to damp cavity modes by the use of RF tiles rather than screen the surrounding volume by the use of transverse RF fingers, done as the RF fingers were suspected to be a cause of dust in the LHC. It has been found that the placement of the ferrite tiles was not ideal from the point of view of damping the cavity modes, and as such the Q of the cavity

modes is not as reduced as could be the case. However studies of the thermal evaluation of the ferrite and the collimator indicate that the layout is compatible with the thermo-mechanical requirements of the structure, and the present design is well understood and thus likely to be kept. The proposed ferrite has some vacuum issues, and alternative damping materials are being investigated.

In addition a small study of the possible materials for the phase 2 secondary collimator jaw material is carried out, with a recommendation for a good conducting material given, either copper or molybdenum of the possibilities given.

Chapter 8

LHC Injection Kicker Magnets

The injection kicker magnets in the LHC are part of the injection system for the LHC machine. This system is used to match the trajectory of the injected beam to that of the stable beam path in the accelerator. An example schema for the LHC can be seen in Fig. 8.1. Injection systems typically use two components: a septum, which may provide a slowly rising and falling (or possibly constant), but strong, field, and kickers, which may provide a rapidly rising and falling, but comparatively weak, field to match the injected beam to the correct trajectory. Similar components are used for the fast extraction of beam (for systems such as the abort system) also.

By design kickers are generally always visible to the beam due to the need to quickly

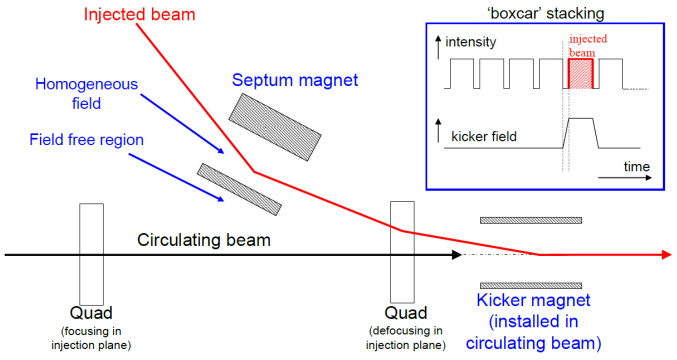

Figure 8.1: An example layout of a injection system for an accelerator with the timing of the kicker field with an injected bunch train. Taken from [91].

apply their kick. In order to achieve a fast field rise/fall time and field qualities desired, the yoke of the kicker magnet is usually a NiZn ferrite. In addition the need for a highly homogeneous field whilst the kick is applied, as well as the strength of the field and the costs of large aperture magnets, neccesitates that the aperture for kickers often be relatively small, meaning they are in close proximity to the beam. This leads to two concerns - that the close proximity of the beam to such a device, that may be made of either a highly lossy material [92–94] or a source of strong geometrical impedance [95], may be source of impedance that drives instabilities in the beam [96], and secondly that the large real component of the ferrite impedance may be subject to intense heating in high beam current machines [94].

8.1 LHC Injection Kicker Magnets

Each LHC injection kicker magnet (LHC-MKI, or MKI) is a 3m long travelling wave transmission line kicker magnet (ferrite length 2.45 m). A transmission line magnet is a magnet that is composed of multiple cells each capacitively coupled to ground. This means that the effective inductance that the pulse is exposed to is reduced, allowing for shorter rise times to be achieved. For LHC there are two injection regions, near IPs 2 (ALICE) and 8 (LHCb), each consisting of a septa system and four MKIs injecting vertically into the machine (the positions of the LHC injection systems are shown in Fig. 8.2). As a transmission line magnet the magnet is constructed of a c-core ferrite yoke, segmented by alternating HV (High Voltage) and ground plates capacitively coupled together by ceramic capacitors to form a magnet of 5 Ω characteristic impedance, the cross sections of which are shown in Fig. 8.3. The magnet out of its tank and the magnets in place in the tunnel are shown in Fig. 8.4 for clarity. The pulse is generated in a Pulse Forming Network (PFN) and is subsequently carried by 10 parallel coaxial cables with a total characteristic impedance of 5Ω, matching the characteristic impedance of the MKI and the PFN. The performance parameters of the magnets rise time, fied strength and homogeneity are given in Tab. 8.1 [97].

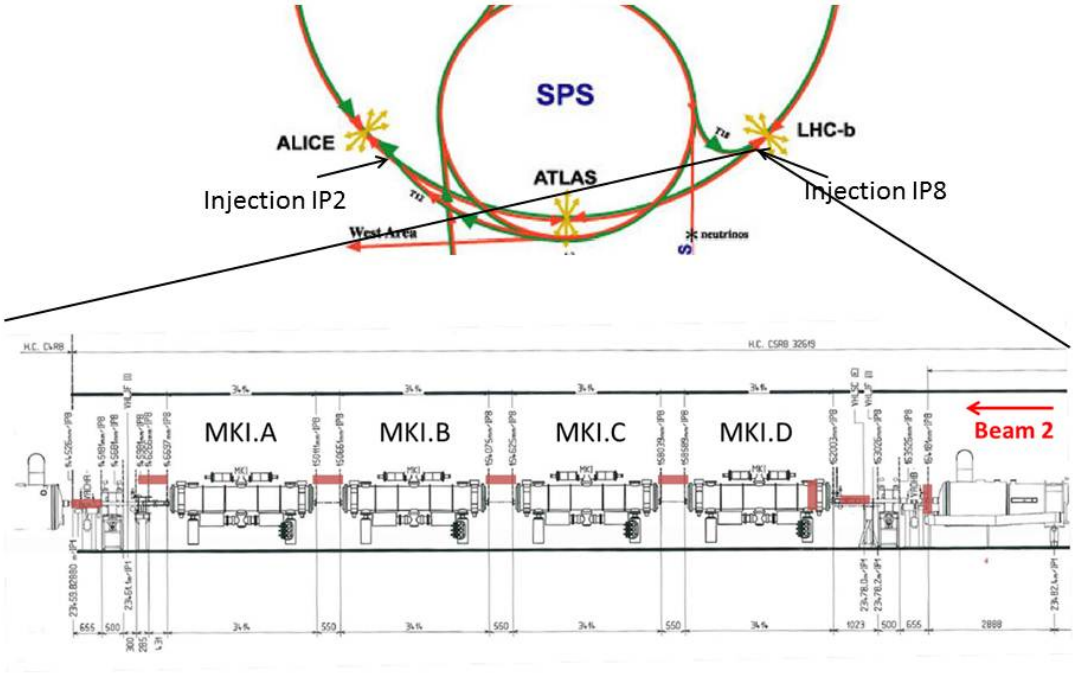

Figure 8.2: The location of the LHC injection systems in the LHC ring, with the layout of an injection line.

Table 8.1: MKI operational parameters

Number of Kickers per System	4	
Kick strength per magnet	0.3	T.m
Beam aperture (diameter)	38	mm
Characteristic Impedance	5	Ω
Operating charging voltage (PFN)	54	kV
Field flat top ripple	$< \pm 0.5$	%
Field flat top duration	up to 7.86	μs
Field rise time 0.5%-99.5%	0.9	μs
Field fall time 99.5%-0.5%	3.0	μs
Magnet length	2.7	m

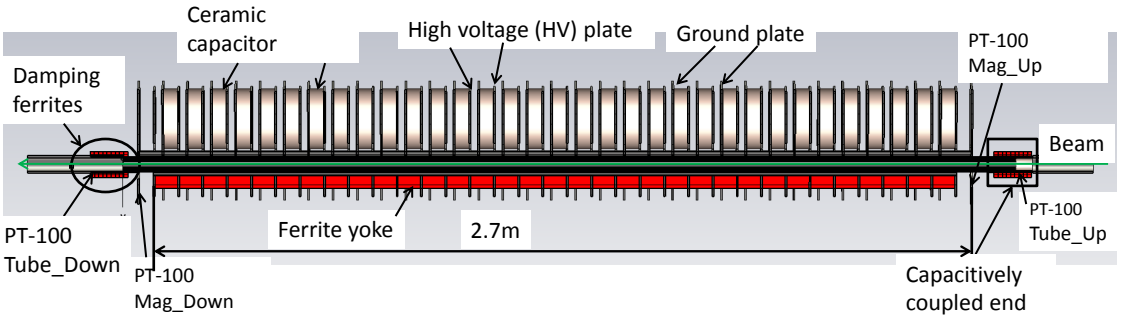

(a)

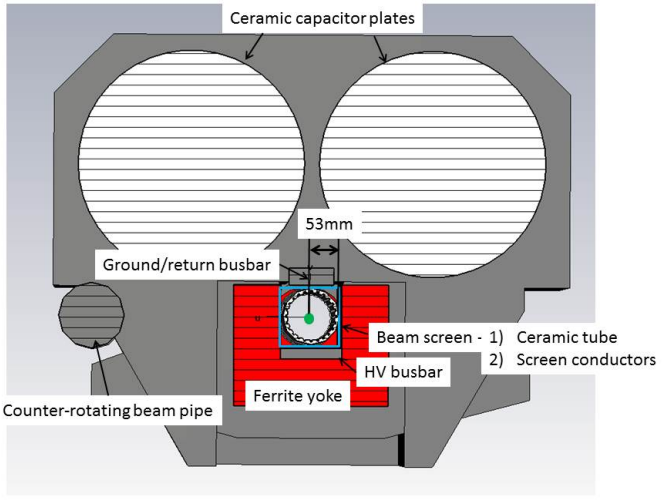

(b)

Figure 8.3: Cross sections of the MKI parallel to (a) and perpendicular to (b) the direction of travel of the beam. Ferrite is indicated in red and the beam path in green.

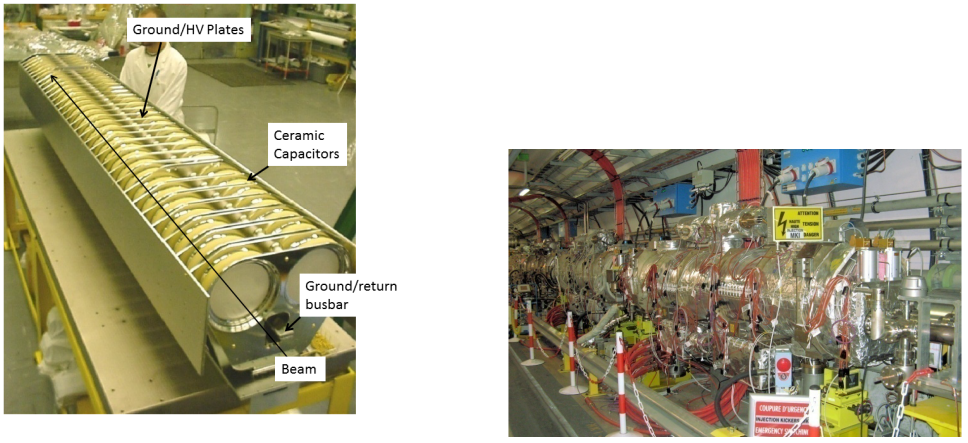

(a) (b)

Figure 8.4: (a) An MKI out of its tank, showing the internal components. (b) MKIs in the LHC tunnel connected together in the complete injection line.

8.1.1 Development of the LHC-MKI Beam Screen

Concerns about the beam coupling impedance of the SPS extraction kicker magnets (MKEs), and thus beam induced heating with LHC type beam with high current, led to detailed investigation of the SPS kicker magnets [98]. During an extensive measurement campaign, it was deduced that extensive beam-induced heating was due to the large real component of the longitudinal impedance of the MKEs. Subsequently a number of retroactive impedance reduction methods were proposed and evaluated for their effectiveness in decreasing the longitudinal impedance [75].

There had previously been debate on the need for a beam screen for the LHC-MKIs [99]: however the beam screen was considered early in the design [100], which ultimately was implemented in the final design [101]. The beam screen is composed of a ceramic tube housing up to 24 screen conductors - conductive wires which extend beyond the length of the ferrite yoke, connected directly to the LHC beam pipe at one end, and capacitively coupled to it at the other. A scheme involving printed conductive strips on the inside surface of the ceramic was tested but was not implemented due to extensive surface electrical breakdown between the strips during pulsing of the kickers. The capacitive

coupling is required due to the short rise time requirement of the kicker field - direct connections at both ends would create a short-circuit secondary, causing the characteristic rise time of the system to dramatically increase. In this case electrical simulations indicate that the optimum is with the capacitive coupling at the pulse input end, i.e. the upstream end of the kicker [101]. This will become relevant during the evaluation of heating patterns of the MKI during operation.

The use of the capactive coupling gives rise to a discontinuity of the conducting path of the beam image current. This results in the possibility of exciting resonances in the surrounding structure of the image current path. In this case, resonant modes of a characteristic frequency due to the screen conductors acting as $n\lambda/4$ resonators. To damp these low frequency modes (the screen conductors are some 3m in length), nine ferrite (NiZn) toroids are placed at each end of the beam screen [102–104]. Cross sections of the beam screen are shown in Fig. 8.5 for clarity.

During testing and conditioning of the MKIs it was discovered that, even with 24 radiused screen conductors there was still significant surface electrical breakdown/sparking occuring on the inside surface of the ceramic tube during pulsing. Measurements showed that above a PFN voltage of 30 kV large quantities of discharge were observed originating from the screen conductors. In particular, the highest induced voltage was known to occur on the screen conductors closest to the HV busbar [101]. Due to the operational voltage requirements, and as it is not feasible to operate the kicker magnets with a PFN voltage below approximately 51k V, a solution had to be found. Following detailed electromagnetic simulations it was decided to remove the screen conductors with the highest induced voltages (those closest to the HV busbar) in an effort to reduce the number of discharges. Removing the 9 screen conductors closest to the HV busbar increased the PFN voltage reached, before discharges began, to 57 kV, above the required 54kV to meet the design parameters for the MKI. Measurements demonstrated that this would worsen the longitudinal beam coupling impedance but this was determined to not be large enough to pose a problem from the point of view of beam induced heating [101].

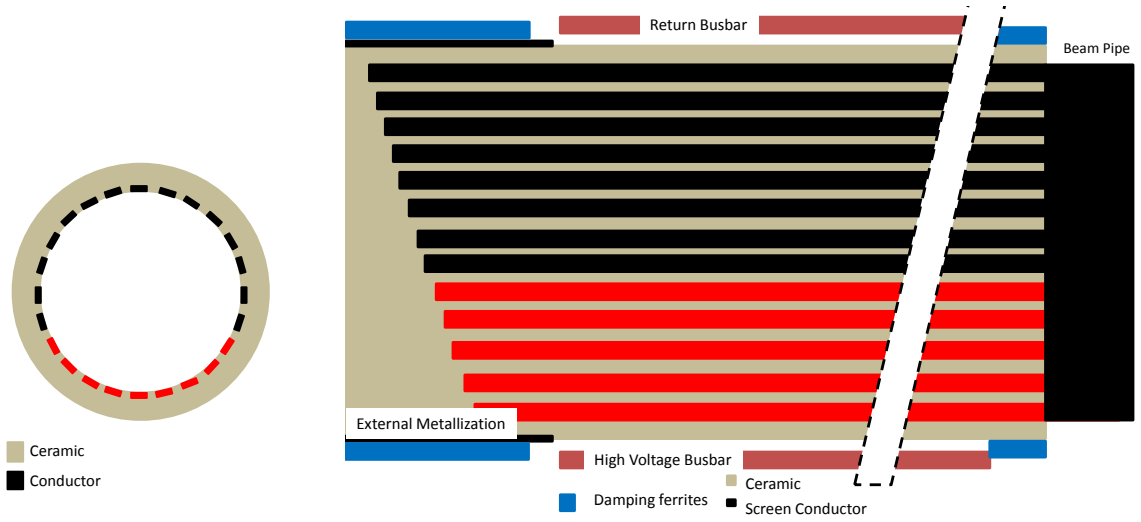

(a) (b)

Figure 8.5: Cross sections of the beam screen perpendicular to (a) and parallel to (b) the direction of beam travel. The screen conductors removed from the majority of the MKIs during the original construction phase are highlighted in red.

8.1.2 Observations of heating during 2011 and 2012 until Technical Stop 3 (23.09.2012 - 27.09.2012)

Beginning with the increasing intensity in the LHC during operation in 2011 a number of devices within the LHC were observed to be heating [33, 86]. Observations and calculations demonstrated a strong relationship between the observed heating and the increasing intensity (first the number of bunches, then the increase in bunch population) indicating that the source of the heating was due to the stored beam interacting strongly with the impedance of many structures - evidenced also by the deteriorating vacuum in some components also. A number of key devices were observed to be exposed to significant heating, in particular devices around the injection region (injection protection collimators, injection kickers, VMTSA (a two beam vacuum interconnect in the injection region in which two beams circulate) and some small insertion devices (ALFA roman pot), as explained at the workshops in Evian in 2011 [86] and Chamonix 2012 [33].

Four PT-100 thermocouples are used for measuring temperatures in each MKI tank, the locations of which are shown in Fig. 8.3(a). The purpose of these PT-100s is to give an indication of the temperature of the ferrite yoke and also of the temperature of the

ferrite toroids. Ideally the 2 PT-100s used to indicate the temperature of the ferrite yoke woud be directly in thermal contact with the ferrite; however this is not possible as the ferrite is also pulsed to high voltages. Thus, instead, these two PT-100s are connected to the outermost ground plates, up and down stream. Thus the temperatures measured using these two PT-100s read lower than the actual ferrite yoke temperature. In addition since the magnet is in high vacuum, heat transfer between the different parts of the magnet is not well defined due to the lack of heat transfer via convection, and the complex transfer of heat by conduction and radiation within the magnet structure.

The measured heating of the LHC-MKI is shown in Fig. 8.6. Some important notes about the heating can be made, firstly that MKIs 8b and 8d both show high measured temperatures, MKI8d in particular demonstrating much higher measured temperatures, showing temperatures at least 20 °C higher than that measured for by the other MKIs. Secondly, that the cooling time to return below the interlock temperature is very long (on the order of 4 hours [105]), indicating a large portion of the ferrite yoke is heating. Additionally the temperature reached was detrimental to magnet operation (i.e. the ferrite yoke was close to its Curie temperature, thus the magnetic field quality may not be suitable for injection), hence the necessary cool-down time was substantial enough to affect machine operational schedules. It can also be seen that the peak temperature only gets worse as the beam intensity is increased.

The temperature of concern in the MKI is that of the ferrite yoke - to ensure that it is below the Curie point - but as mentioned above there are no direct temperature measurement on this component, hence one difficulty in analysing the heating of the MKI is to identify the actual temperature of the ferrite yoke corresponding to the measured temperature. This is a problem which has been analysed in depth in [106], in particular inferring the inductance of the magnet under a softstart condition (the pulsing of the magnet with no beam to inject). The softstart is carried out very soon after a beam dump when the ferrite yoke is at its highest temperature. Hence this analysis gives a certain margin of safety to the interlock level, but due to the possible damage that may be done due to a misinjection of the beam a conservative approach is necessary. Thus a few hours of cool

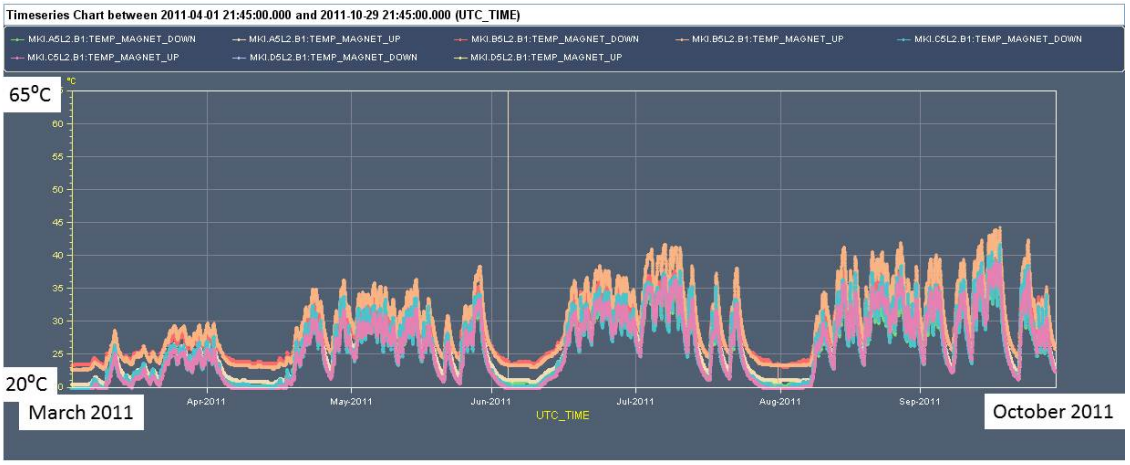

(a)

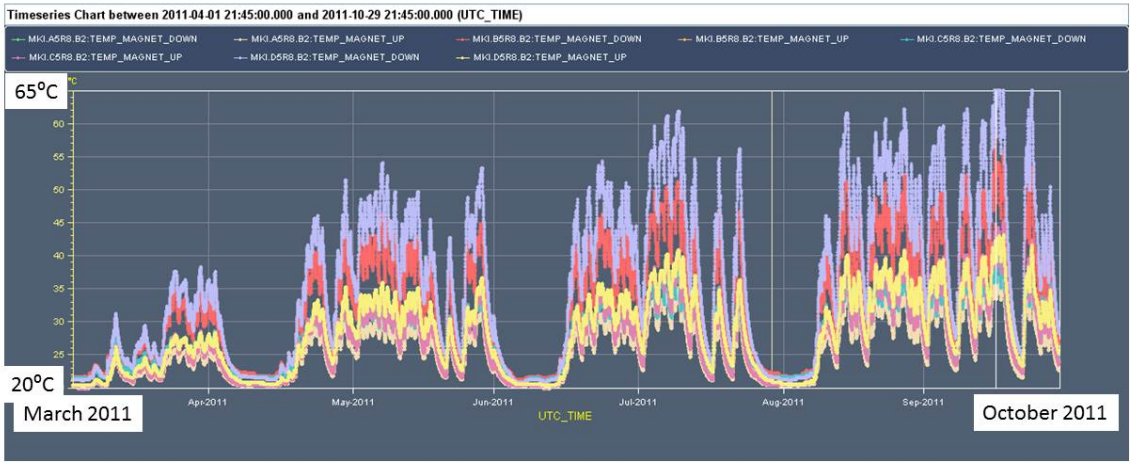

(b)

Figure 8.6: The measured temperature of the MKIs at (a) IP2 and (b) IP8 during 2011 in the LHC. Note MKI8b and MKI8d show significantly higher measured temperatures than the other MKIs.

down time between injections may still be required.

Prior to technical stop 3 in 2012 there were 2 configurations of the beam screen in the LHC-MKIs - 7 MKIs were in place with 15 (some staggered, some tapered) screen conductors, the 9 screen conductors closest to the HV busbar having been removed due to the electrical breakdown concerns mentioned in Sec. 8.1.1 [101]. A single MKI, MKI8c, was fitted with 24 screen conductors, 15 tapered and 9 shortened screen conductors (trimmed such they do not overlap with the external metallization at the capacitively coupled end). This was to reduce the electric field at the end of the screen conductors closest to the HV busbar, but did not significantly improve the beam coupling impedance of the MKI [101].

8.2 Simulations and Measurements of the MKI with 15 Screen Conductors

To begin an analysis of the heating of the MKIs, and to verify the use of simulations as a tool for evaluating different designs of the MKI impedance reduction methods, it was important to measure an existing MKI configuration as a benchmark. Due to the expected low beam coupling impedance of the MKI even with 15 screen conductors (on the order of 100 Ω longitudinal beam coupling impedance) it was decided to do the measurements using the resonant coaxial wire method, described in Sec. 4.1.2. This method limits the frequency resolution of the measurements ($\Delta f = c/(\Delta\lambda) = c/(2L_{device}) \approx 40\ MHz$ where c is the speed of light and $L_{device} \approx\ 3.5m$ is the length of the MKI in it's vacuum tank), but the accuracy in this measurement is considered appropriate in this case.

The measurements were carried out on a fully assembled MKI inside it's vacuum tank, with a ceramic tube housing 15 tapered screen conductors. For the single wire measurements a silver coated copper wire of radius 0.5 mm with 2.1 μm thickness of silver was placed in the central beam pipe, suspendedat each end on a vacuum flange modified to take a Sucobox connection allowing a small capacitance, in a seperate sucobox, to be attached to the connecting box. The soft copper wire has a tensile strength of 250 N/mm^2: soft wire is used as it can be readily straightened by gentle pulling. The wire is not

enamelled so as to avoid contamination of the kicker magnet during soldering of the wire. To displace the wire for displaced single wire measurements, a pair of nylon screws (one at each flange) were used to physically displace the wire. Displacements were taken at 3 mm intervals in both the vertical and horizontal planes, between -9 mm and +9 mm displacement.

For the two wire measurements, two wires were suspended in the device, separated by 7mm. The wires were connected to a single VNA, each connection run through a 180° hybrid to generate the appropriate phase difference between the two wires. The experimental setup for the two wire measurements is shown in Fig. 8.7.

The VNA is calibrated using an 8532E calibration kit, using an IF bandwidth of 1 kHz (chosen to ensure that the frequency of each data point is well defined, but not so restricted that the sweep time is excessively long). 2000 equally spaced data points are used over a frequency range of 1 MHz-2 GHz. The Q factors and resonant frequencies of the resonant modes are calculated using a peak finding algorithm on the VNA, and the conductive losses due to the wire calculated analytically and compensated for.

The simulations of the MKI are carried out using CST Particle Studio, a time domain simulation code. The particle beam was simulated traversing the kicker magnet and the trailing signal Fourier transformed to acquire the beam coupling impedance in the longitudinal and transverse planes. A simplified model of the magnet is created, shown in Fig. 8.8. An integrated wakelength of 15 m is used in the simulations, and a simulated bunch of a Gaussian profile with σ_z =45 mm used. A half model is used for displacements of the source/integration path in the vertical axis due to the symmetry plane in the y-z plane, giving a mesh count of $\approx$ 16 million for vertically displaced simulations and $\approx$ 32 million for horizontally displaced simulations. In this case the mesh size is defined as 10 mesh cells per σ_z, with higher densities placed in areas which contribute strongly to the impedance (region of overlap between the screen conductors and the external metallization). To acquire the dipolar and constant transverse impedance terms, the source signal is displaced whilst the path of integration is kept on axis. The linear variation in the resulting impedance can be seen to be the dipolar term and the constant impedance

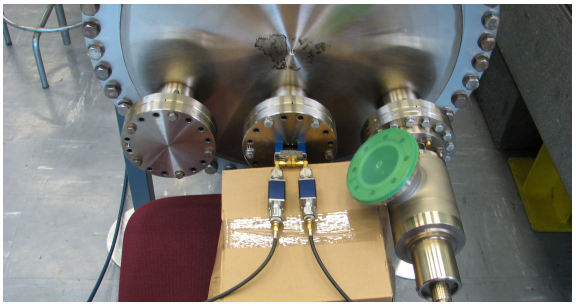

Figure 8.7: The measurement setup for the two wire measurement setup.

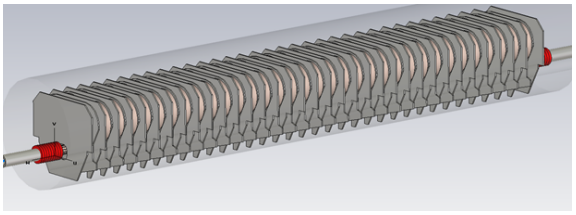

Figure 8.8: The simulation model of the LHC injection kickers implemented in CST Particle Studio.

the constant term. Similarly for the quadrupolar term the source signal is kept on axis and the integration path displaced.

The results for the measurements can be seen in the following figures:

1. Fig. 8.9 the longitudinal impedance
2. Fig. 8.10(a) the horizontal dipolar impedance
3. Fig. 8.10(b) the vertical dipolar impedance
4. Fig. 8.11 the quadrupolar impedance
5. Fig. 8.12 the constant transverse impedance

It can be seen that there is generally fairly good agreement between the measurements and simulations in all planes. In particular the agreement for the real component of the longitudinal impedance between measurements and simulations is very good below 1.5 GHz (Fig. 8.9). This is considered an important verification of the simulation model

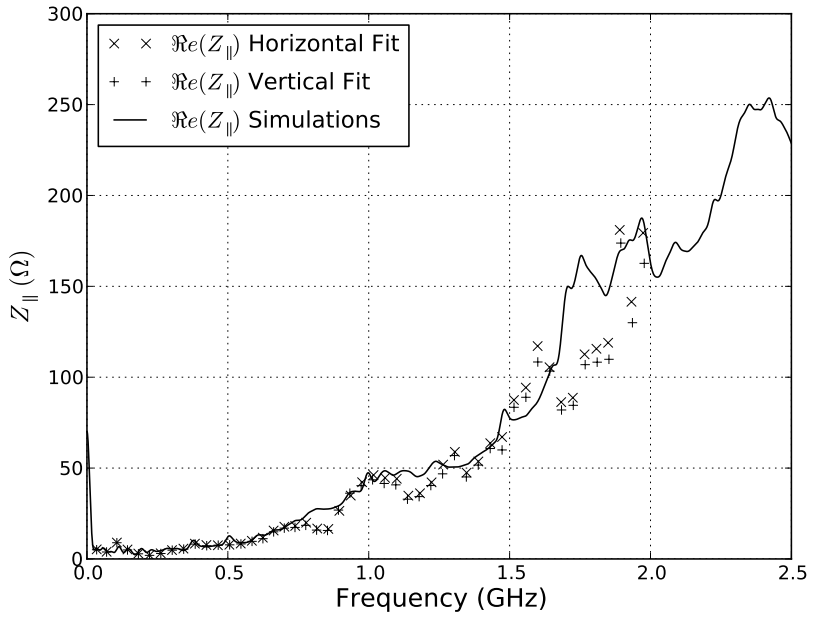

Figure 8.9: The real component of the longitudinal impedance of the LHC MKI acquired by measurements using the resonant coaxial wire method and time domain simulations using CST Particle Studio. (15 tapered screen conductors).

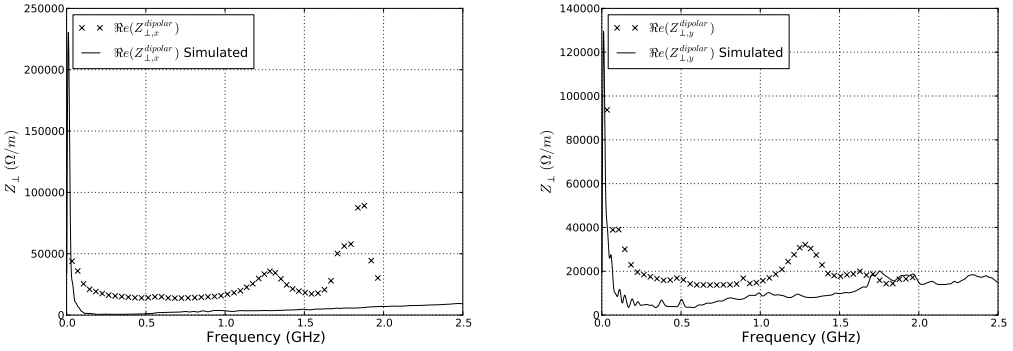

(a) (b)

Figure 8.10: The real component of the dipolar impedances of the LHC MKI acquired by measurements using the resonant coaxial wire method and time domain simulations using CST Particle Studio. (a) shows the real component of the horizontal dipolar impedance, and (b) the real component of the vertical dipolar impedance. (15 tapered screen conductors).

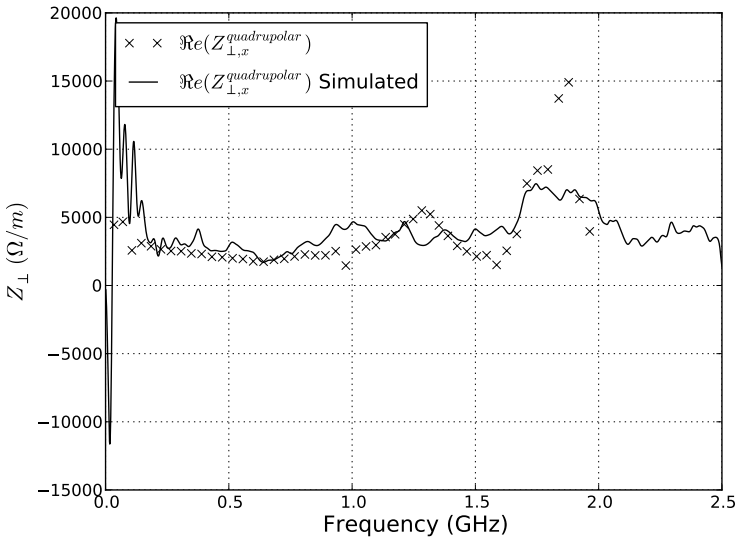

Figure 8.11: The real component of the quadrupolar impedances of the LHC MKI acquired by measurements using the resonant coaxial wire method and time domain simulations using CST Particle Studio. (15 tapered screen conductors).

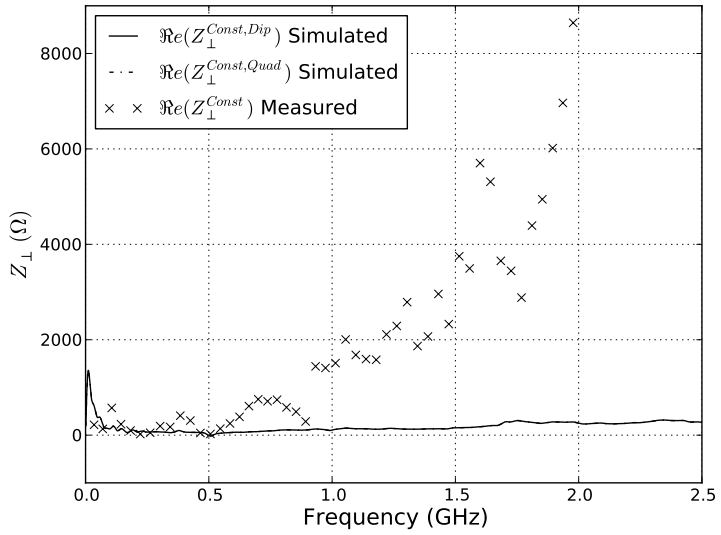

Figure 8.12: The real component of the constant transverse impedances of the LHC MKI acquired by measurements using the resonant coaxial wire method and time domain simulations using CST Particle Studio. The simulated results from taking the displaced source signal and the displaced witness signal lie on top of one another. (15 tapered screen conductors).

as this is presently the impedance of concern with respect to beam-induced heating. Discrepencies can be seen in the longitudinal measurements above 1.5 GHz - this is likely due to differences between the internal structure of the magnet and that represented by the simulation model as well as the presence of the sucoboxes in the measurements which become more visible to the signal at higher frequencies (or lower wavelengths).

In the transverse plane the real component of the dipolar impedance in both the vertical and horizontal plane show reasonable agreement between the simulations and the measurements (Fig. 8.10) in as much that the simulated impedance predicts a small transverse impedance and the measured impedance is likewise small. Similarly the agreement for the real components of the quadrupolar impedance is good over much of the frequency range, although the simulation and measurement results begin to diverge above 1.7 GHz (Fig. 8.11). The real component of the constant transverse term shows a good agreement up until $\approx$ 1 GHz whereupon the results diverge (Fig. 8.12). This is due to the sentivity of these results to the systematic and random errors in the measurement of the longitudinal impedance. The comparatively small longitudinal impedance measured in this instance leads to large errors in these results.

For reference the noise floor for the measurements is approximately 0.06 dB. In terms of the longitudinal impedance this is approximately 5Ω, and in the transverse plane approximately 240 Ω and 0.2 Ω for values of 1 MHz and 1 GHz respectively, to illustrate that this decreases in significance at higher frequencies. For the transverse plane this is determined by taking the longitudinal noise floor, and normalising by the wavenumber k at the frequency of measurement. With uncertainties in the displacement of the wire and the additional losses generated by the addition of the sucoboxes and other electrical connections this goes someway to explaining the discrepencies between measurements and simulations.

8.2.1 Beam Induced Heating Estimates for 15 Screen Conductors

It can clearly be seen from the measurements of the real longitudinal impedance (Fig. 8.9) that there is a significant broadband impedance to the structure which would cause beam

Table 8.2: The upper 2012 LHC operational parameters used for estimating the power loss in the MKI with 15 screen conductors.

Bunch Spacing	50	ns
Number of bunches	1380	
Particles per bunch	1.7×10^{11}	

Table 8.3: Power loss estimates for the LHC-MKI with 15 screen conductors in the beam screen (in Watts) for a number of different bunch lengths and profiles ($4\sigma_z$ for the Gaussian profile).

Bunch Length (ns)	$P_{loss,gaussian}$	$P_{loss,parabolic}$	P_{loss,cos^2}
1.0	134	137	210
1.1	113	115	171
1.2	98	99	143
1.3	86	88	123
1.4	79	80	108

induced heating. This strongly indicates that the removal of the 9 screen conductors closest to the HV busbar has drastically decreased the screening of the ferrite yoke from the beam image current.

To provide a first estimate of the expected heating of the MKI it is neccesary to estimate the power loss in the MKI. Taking the simulation impedance (due to allowing a finer resolution of frequency) the power is estimated using the broadband method of heat calculation given in Sec. 2.3.1. For these calculations we consider the operational parameters for the 2012 proton run in the LHC, summarised in Tab. 8.2. Estimates for power loss for longitudinal profiles of Gaussian, parabolic and $\cos^2$ profiles assuming bunch lengths between 1.0 and 1.4 ns are shown in Tab. 8.3. The thermal evolution of the MKI with this power load (assuming all the power is lost in the ferrite yoke for a worst case scenario) has been evaluated extensively by Garlasche et al [107], and has been found to be compatible with the measured temperature of the MKI thermal probes [106]. In response to this the MKI interlock temperatures were increased a number of times during 2011 and 2012 as analysis of the softstart data demonstrated that the ferrite was below its Curie temperature.

It has thus been shown that the power loss due to the beam induced wakefields into

the MKI can describe the temperature behaviour seen during 2011 and 2012 operation, giving us confidence in our understanding of the sources of, and heating processes occuring within, the MKI. To propose workable improvements to the beam screen, it is first neccesary to understand both the sources of the impedance due to the beam screen layout and the limitations that both manufacturability and the transient electrical potential on the screen conductors produces. In addition other methods of decreasing both the power load and of improving the cooling of the ferrite yoke are complementary avenues of study to reduce the problem of beam-induced heating in the MKIs, the problem ultimately being the high temperature of the ferrite yoke.

8.3 Other Concerns for the MKI Operation and Temperature Reduction

Given the breadth of concerns that must also be considered alongside beam impedance when discussing the heating of the MKIs, and alterations to the beam screen design, it is suitable to include a brief discussion on these matters here.

First of the concerns is the transient induced electrical potential on the screen conductors during the pulsing of the kicker magnet. It is due to this high induced voltage (up to 30 kV on the conductor closest to the HV busbar during the field rise and -15 kV during the field fall) and the resulting surface flashover between screen conductors and to the end of the beam screen, at the capacitively coupled end, that was the initial motivation to remove the 9 screen conductors from the beam screen. A flashover along the surface of the ceramic, from a screen conductor to ground, can result in the MKI field pulse prematurely falling to a low-level, thus mis-kicking some of the bunches being injected. These mis-kicked bunches can cause significant damage to the downstream equipment.

In addition to improving the screening of the ferrite yoke from the beam any proposed beam screen design must also thus allow the magnet to be pusled without electrical breakdown of the screen. Work by Barnes et al [108] has found there are a number of factors that can reduce the electric field on the screen conductors. These include the use

of spheres on the ends of the screen conductors to reduce the high electric fields at the ends of the screen conductors (Fig. 8.13), tapering the length of the screen conductors (Fig. 8.26) and replacing the outer metallization (at the capacitively coupled end) with a cylindrical metal tube with a 1-3 mm vacuum gap between the cylinder and the outer surface of the ceramic tube near the ends of the screen conductors (Fig. 8.31). The aim of this last measure is to remove the external ground from the outside of the ceramic tube, as the metallization has been observed to effectively force the ground plane closer to the screen conductors due to the high permitivitty of the ceramic tube. The effects of these changes on the beam coupling impedance are discussed in later sections.

The second major concern is the transfer of thermal energy out of the kicker magnets, especially from the ferrite yoke. Due to the HV pulsed nature of the kicker magnet operation there is no active cooling within the device, thus cooling is reliant primarily on thermal radiation of the heat from the ferrite yoke to the vacuum tank. Conduction contributes moderately to the heat transfer from the ferrite yoke, but it is not well defined or expected to contribute significantly. Experiments have shown that the internal surface of the vacuum tank has a very low emissivity (< 0.1) in the infrared (IR) frequency range ($\lambda \approx 7-10\ \mu m$) [109](indicating that radiative heat transfer to it is very poor), and subsequent thermal simulations have shown that the steady state temperature of the MKI yoke is very sensitive to the emissivity of the vacuum tank internal surface [110]. Subsequently a significant quantity of work has been carried out on methods to improve the emissivity of the internal surface of the vacuum tank so as to more effectively passively cool the device, without degrading the ultra-high vacuum within the tank.

8.4 Simulations and Measurements of the MKI with 19 Screen Conductors

As can be seen from Fig. 8.6(b), MKI8d had experienced significantly higher measured temperatures than the other kicker magnets during operation. Analysis of the softstart data for MKI8d shows that ≈70 °C measured corresponds to the Curie point (≈120 °C)

of the ferrite yoke [111]. Although estimated to experience the same degree of power loss within the structure as the other kicker magnets (due to the similarity of the beam screen layout) a particularly low emissivity of the internal surface of the MKI8d vacuum tank has probably contributed to the higher temperatures observed. As a result of this, and the necessity to find a solution to the high temperatures of the MKIs, in particular MKI8d which was acting as a severe limiter on the integrated luminousity delivered by the LHC, it was decided to implement an improved beam screen in a replacement magnet in an effort to reduce the power loss in this magnet, and at the same time test new features of future beam screen designs.

The following design features were implemented in the replacement MKI8d (explanations are given with the description, see Fig. 8.13):

1. 19 screen conductors are placed within the beam screen in order to improve the shielding of the ferrite yoke from the beam. These are clustered together, with the 5 empty screen conductor slots closest to the HV busbar to limit the maximum induced voltage on the screen conductors. Impedance and electrical simulations have indicated that this will drastically reduce the beam coupling impedance of the MKI, relative to 15 screen conductors. Electrical simulations show that the maximum induced voltage is $\approx$12% less than with 24 screen conductors [112].

2. Elongated metal spheres are placed on the capacitively coupled end of the screen conductors. These are intended to reduce the electric field amplification due to any sharp edges at the ends of the screen conductors, thus reducing the possibility of electrical breakdown. This method has some drawbacks due to the need to drill out the slots, using a diamond coated drill, housing the screen conductors to accept the larger elongated spheres.

3. The screen conductors are arranged to alternate in length (i.e. there are two lengths of screen conductor in the beam screen) to increase the distance between the ends of adjacent screen conductors, thus reducing the probability of breakdown between them. However tapering of the length is considerably more effective: the effect here

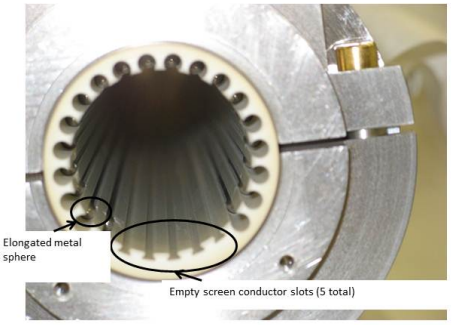

Figure 8.13: The additional screen conductors and the elongated spheres place in MKI8d to reduce both beam coupling impedance and the electric field.

is for the longer length screen conductors to effectively shield the shorter screen conductors, thus reducing the electric field associated with the screen conductors [101]. Although alternating length is less effective than tapering the length of the screen conductors, with the shortest length close to the HV busbar, for the first prototype it was necessary due to time constraints.

4. A preliminary attempt was made to ensure that the emissivity of the inside of the new MKI8d tank was greater than 0.1, by using an ion bombardment technique [112].

Due to the primary motivation for altering the beam screen being the high beam-induced heating seen in the kicker magnets' ferrite yoke, the impedance studies were primarily motivated by reducing the real component of the longitudinal beam coupling impedance. Simulations carried out prior to the final assembly of the new MKI predicted that the beam-coupling impedance would be strongly reduced by the inclusion of 4 additional screen conductors. A full complement of 24 screen conductors would be even better but with a higher risk of surface flashover. Measurements taken of the magnet confirmed these simulations to very good accuracy: Fig. 8.14 shows measurements and simulations for an MKI with both 15 and 19 screen conductors. It can be seen that the real component of the beam coupling impedance is reduced drastically across the entire frequency range of concern, by using 4 additional screen conductors, and the predicted power loss, as a

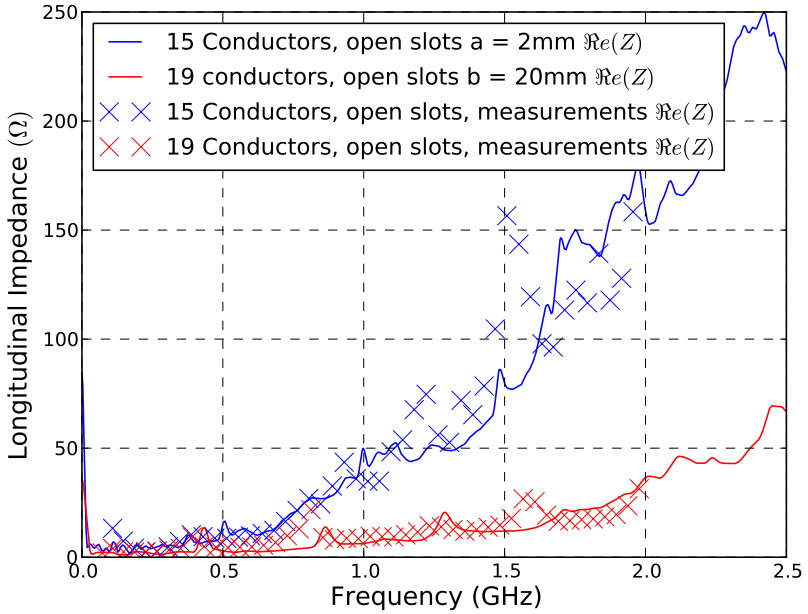

Figure 8.14: The real component of the longitudinal beam coupling impedance of the replacement MKI8d with 19 screen conductors from both simulations and measurements. The corresponding impedance for an MKI with 15 screen conductors is shown for comparison.

result of the simulated impedance (see Tab. 8.4), shows that the expected power loss is reduced by a factor of 2-3. Calculations of the thermal evolution of the proposed MKI8d replacement also indicated that the maximum ferrite temperature reached would decrease significantly (≈30 °C) due to this reduced power load [110].

8.4.1 Temperature of MKI8d after Technical Stop 3

Due to the promising results of the impedance, electrical and thermal simulations of the proposed MKI8d replacement with 19 screen conductors, it was decided to replace the 15 screen conductor version during technical stop 3 (TS3) [113]. It is said the proof is in the pudding, and in this case mine is exceptionally tasty; Fig. 8.15 shows the temperatures for the kicker magnets at IP8 both before and after TS3. It can clearly be seen that MKI8d (solid red trace) changes from being the magnet with the highest measured temperature in IP8 to the lowest - an excellent confirmation of the understanding of the sources of power

Table 8.4: The power loss due to the impedance calculated for the MKI with 15 (most common configuration) and 19 (as for the new MKI8d) screen conductors. Estimates are given assuming a beam with 1380 bunches, seperated by 50 ns, with each bunch containing 1.7×10^{11} particles. Estimates of the power loss assuming a Gaussian, a parabolic and a $\cos^2$ longitudinal bunch profile are calculated (in Watts), and a range given for the lowest (typically the Gaussian distribution) and highest (typically the $\cos^2$ distribution due to the large high frequency lobes) values calculated ($4\sigma_z$ for Gaussian profile).

Bunch Length (ns)	P_{loss} 15 Screen Conductors	P_{loss} 19 Screen Conductors
1.0	134-210	50-66
1.1	113-171	44-58
1.2	98-143	41-52
1.3	86-123	40-47
1.4	79-108	36-43

loss within the kicker magnet and the thermal evolution due to the power loss. From these very promising results a great deal of confidence in the simulation tools, for predicting the beam coupling impedance, and the understanding of the causes of the beam coupling impedance were acquired. As such more significant changes to the MKI design maybe investigated using simulation tools with confidence given the good predictions acquired so far.

8.5 The Dependence of the Beam Coupling Impedance on the Kicker Components

As part of the study to improve the beam screen it was decided to investigate systematically the effect of the various components of the kicker magnet on the resulting beam coupling impedance. This is divided into two sections, the study of the effect of the beam screen on the beam coupling impedance of the ferrite yoke, and subsequently a study of the effects of the dimensions of the beam screen and screen conductors on the beam coupling impedance.

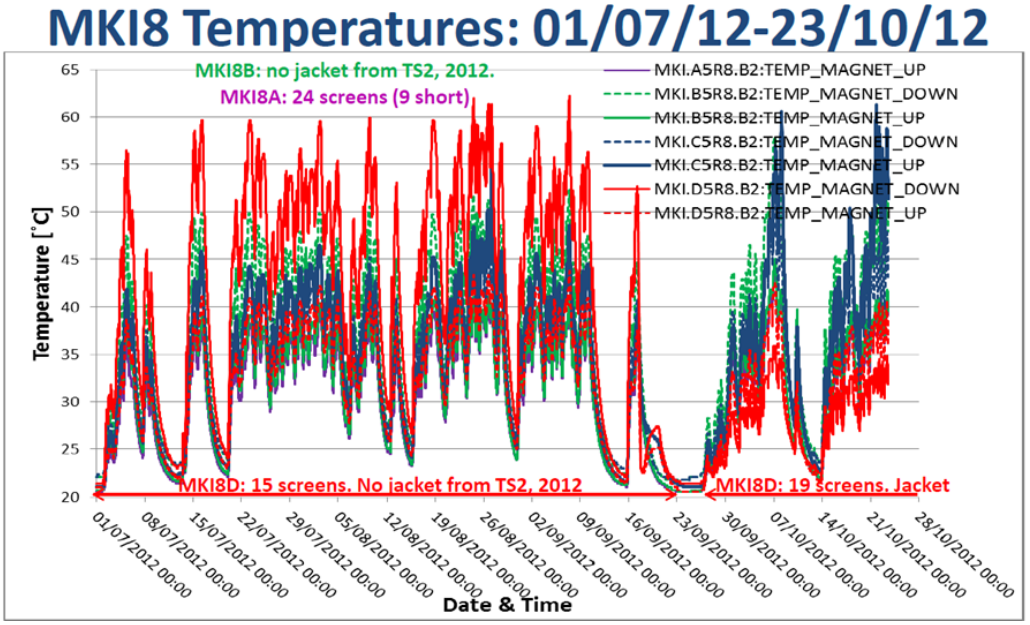

Figure 8.15: The temperature profile of the IP8 injection kicker magnets during the time period before and after technical stop 3 (TS3), when the MKI8d was changed from a kicker magnet with 15 screen conductors to one with 19 screen conductors. It can be seen this magnet (solid red trace) goes from being the magnet with the highest measured temperature to the magnet with the lowest measured temperature after TS3 (17/09/2012 - 27/09/2012).

8.5.1 The Impedance of the MKI - Effects of the Inclusion of the Beam Screen

To first judge the effectiveness of the concept of the beam screen as an impedance reduction technique we simulate the MKI by systematically adding components to the magnet to determine their effect on the beam coupling impedance. We consider the following configurations of the MKI:

1. The C-core ferrite yoke
2. The C-core ferrite yoke with a ceramic tube in the aperture
3. As "2" above but with 24 screen conductors inserted into the ceramic tube, capactively coupled at one end
4. The internal magnet structure including the vacuum tank, HV and ground plates and the surrounding connections

These geometries are shown in Fig. 8.16, and the resulting impedance simulations for the real component are shown in Fig. 8.17. Several points can be seen; firstly that the inclusion of the beam screen with screen conductors very effectively screens the beam from the other components of the kicker magnet - including the ceramic tube, the surrounding structures and the ferrite yoke itself. This indicates that for a beam screen in which the ceramic tube holds a large number of screen conductors, the beam is effectively screened from the surrounding structure up to a frequency characterised by the seperation of the screen conductors. This has benefits for the impedance simulations as it is valid to use a reduced simulation model considering just the capacitively coupled end provided we can assume the ferrite is well screened (i.e. we have 24 screen conductors in place). And lastly that the use of the ceramic tube contributes significantly to the imaginary component of the longitudinal impedance of the complete magnet (evidenced by the linear increase of the imaginary impedance, in cases 3 and 4 in the simulation results, with frequency due to the inductive component of the impedance) even with the presence of screen conductors.

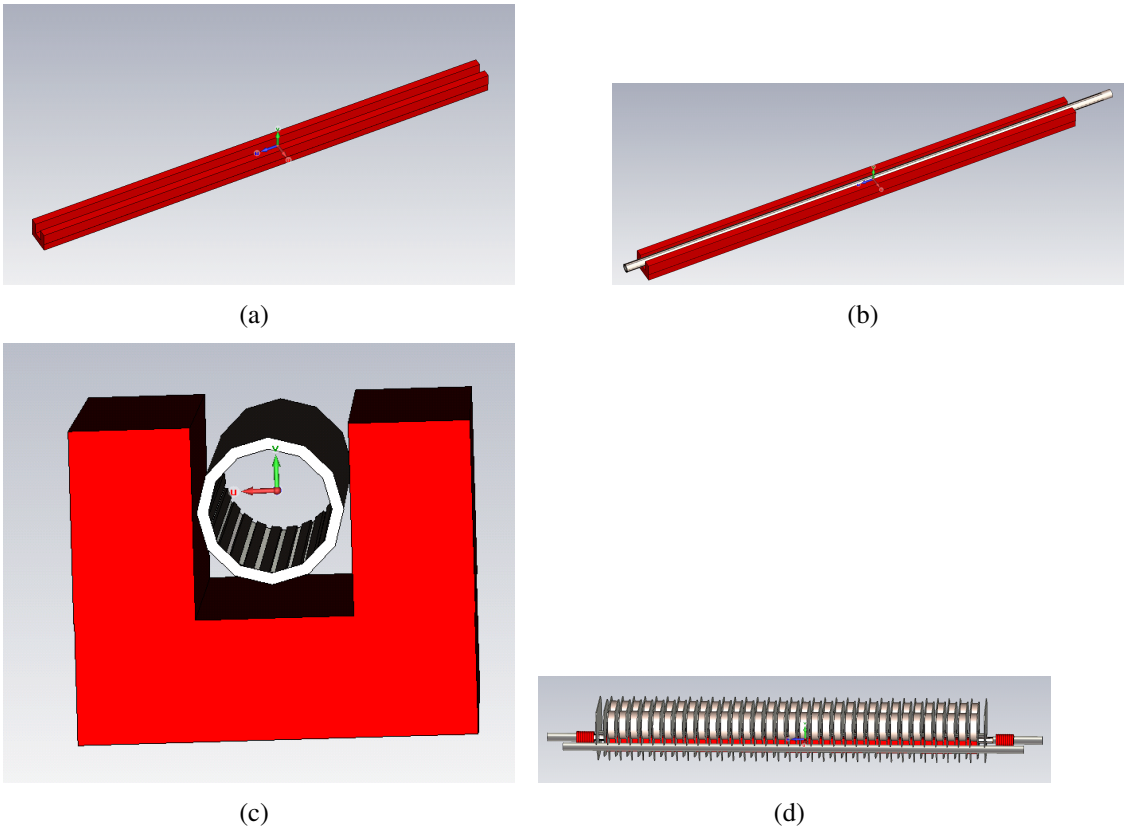

(a) (b)

(c) (d)

Figure 8.16: The geometries simulated for the various components in the LHC-MKI. These are c-core ferrite only (a), c-core ferrite and the ceramic tube (b), c-core ferrite with the ceramic tube containing 24 screen conductors (c) and finally the complete MKI magnet (without vacuum tank for clarity) (d).

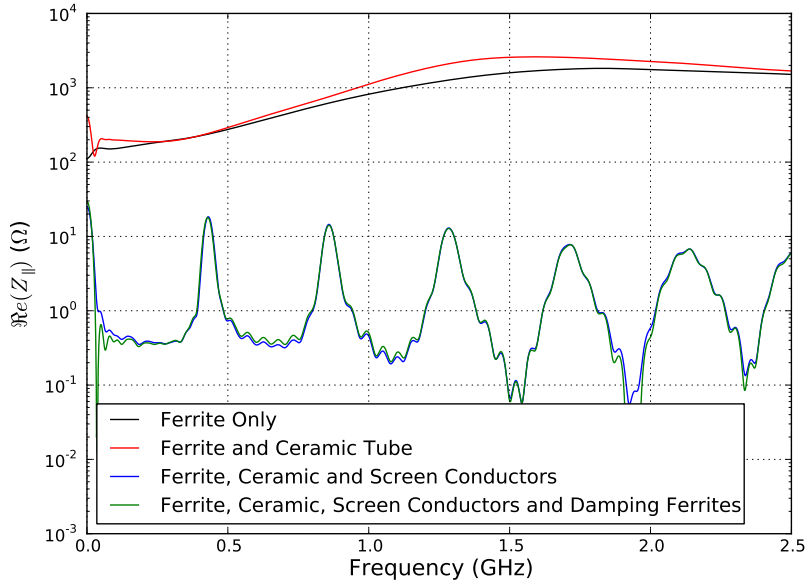

(a)

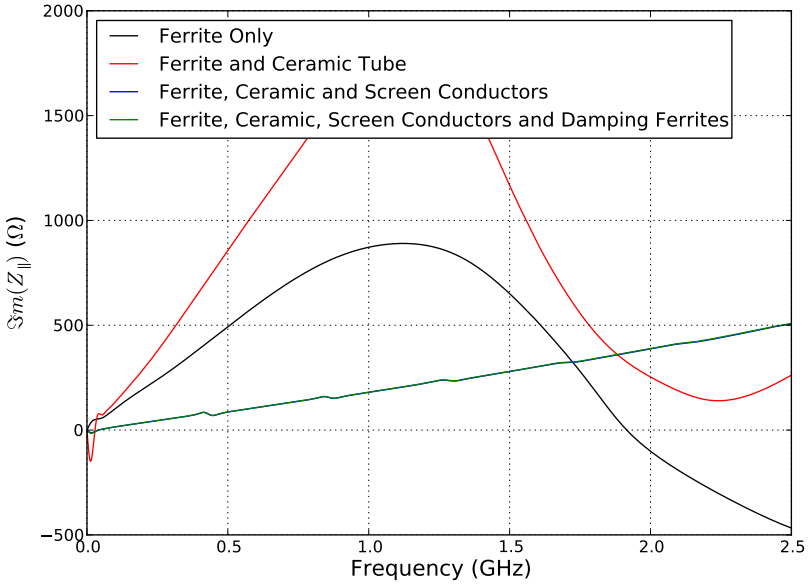

(b)

Figure 8.17: The (a) real component and the (b) imaginary components of the LHC MKI kicker magnet impedances for different components in the magnet.

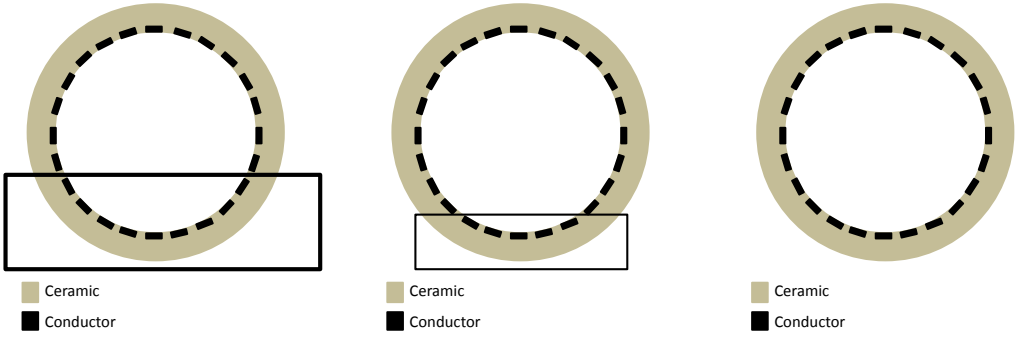

(a) (b) (c)

Figure 8.18: Beam screens with different numbers of screen conductors removed from the design quantity of 24. Models of 15 (a), 19 (b) and 24 (c) screen conductors are considered for the impedance simulations. Conductors surrounded by the boxes are removed in this case.

Concerning the role of the beam screen layout there are two areas to examine - the effect of different quantities of screening of the beam by having more or less screen conductors (in this case removing those closest to the HV busbar due to concerns of electrical breakdown) and of the effect of different lengths of the screen conductors at the capacitively coupled end of the beam screen.

8.5.2 How Screening Changes with the Number of Screen Conductors

For the changes in the number of screen conductors two variations are carried out: the first is to examine the case of removing several screen conductors in the beam screen towards the HV busbar (shown in Fig. 8.18). This direction is chosen as these screen conductors experience the highest induced voltage during the pulsing of the kicker magnet, and additionally it was initially thought that on this side the HV busbar would provide some screening of the beam from the ferrite yoke. The second variation is to remove a selection of screen conductors towards the HV busbar (shown in Fig. 8.19), in this case to examine whether it is possible to acquire some shielding through using some screen conductors and benefitting from removing some screen conductors to further reduce the rate of electrical breakdown.

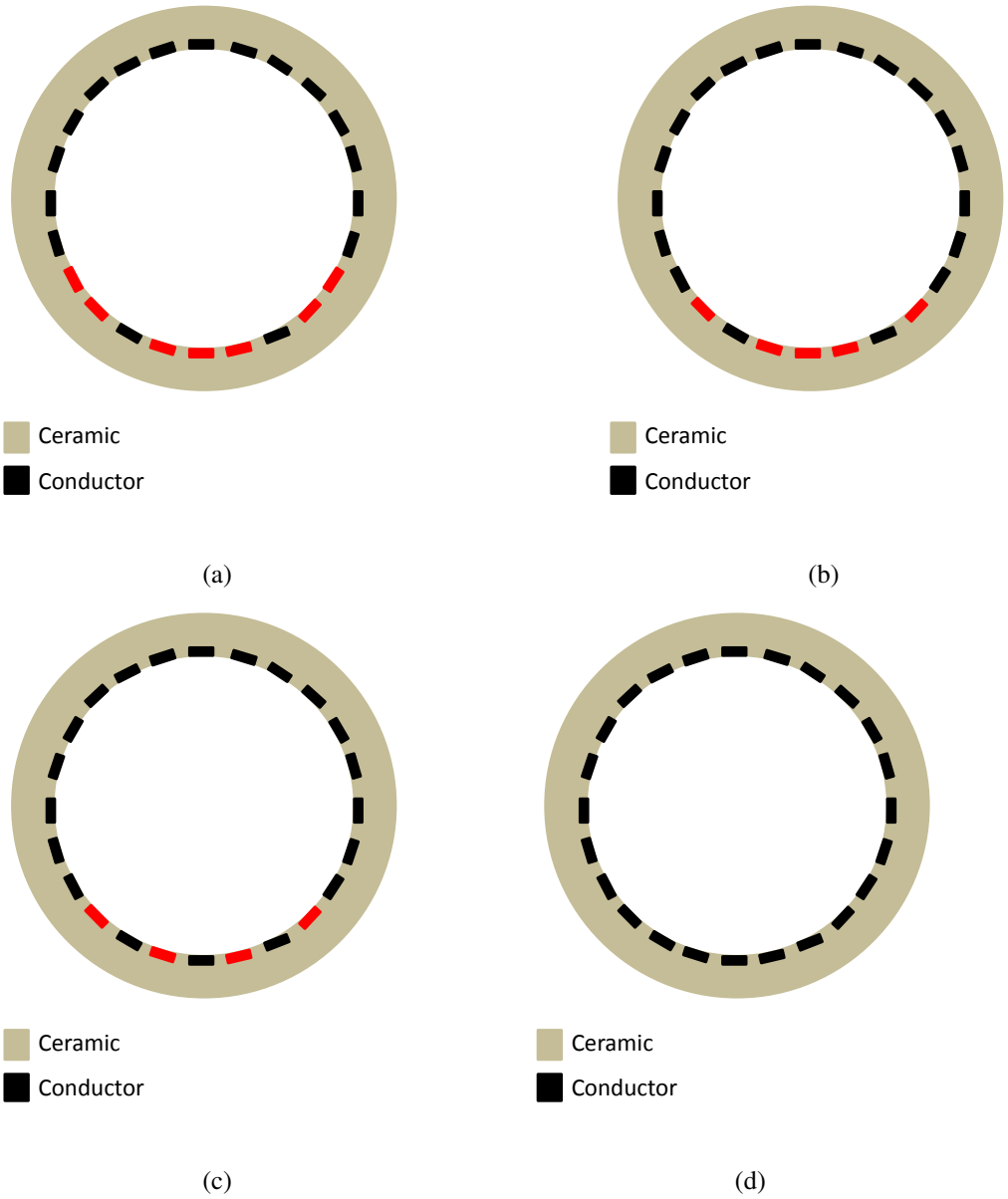

Figure 8.19: Beam screens with different numbers of screen conductors removed from the design quantity of 24. Models of 17 (a), 19 (b), 20 (c) and 24 (d) screen conductors are considered for the impedance simulations. Conductors that are coloured red are the removed in each case.

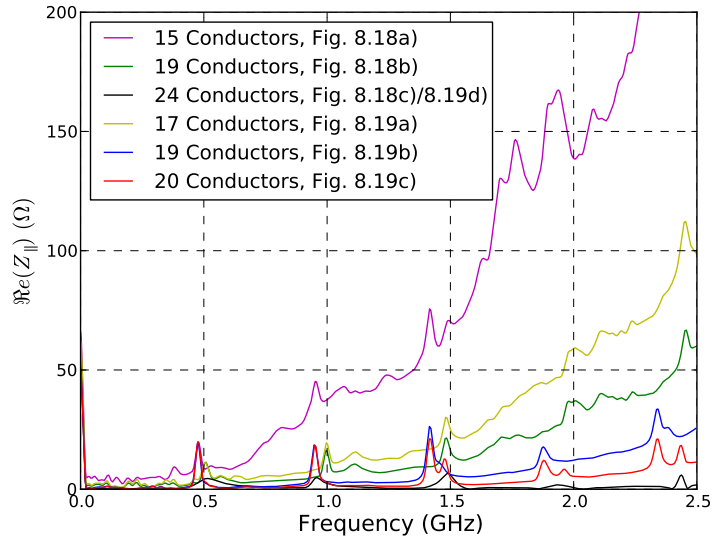

(a)

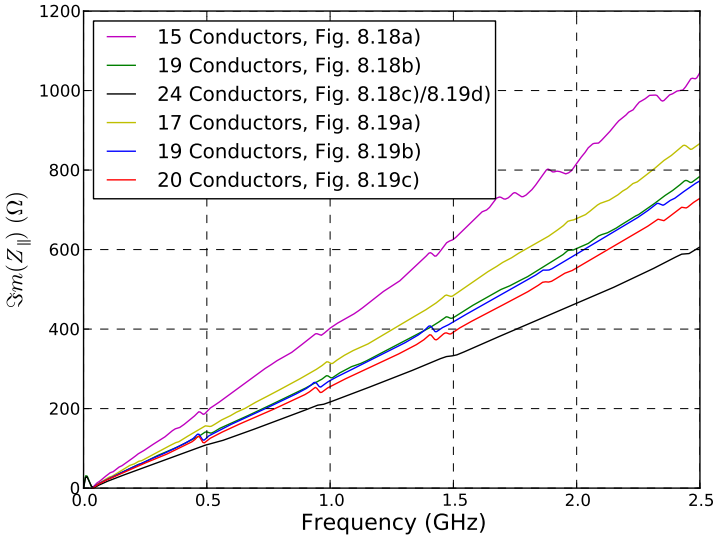

(b)

Figure 8.20: The longitudinal impedance of the MKIs with different numbers of screen conductors included in the beam screen. Shown is the real component (a) and the imaginary component (b) of the longitudinal impedance.

The longitudinal impedance for these configurations is shown in Fig. 8.20. It can be seen that for both components of the impedance that more screen conductors reduces the magnitude of the impedance at all frequencies - this can simply be understood as improving the screening of the ferrite yoke from the beam with additional screen conductors. This can particularly be seen in the increase of the number of screen conductors from 15 to 19 to 24 conductors in total; the screening is improved dramatically in each subsequent case.

In addition it can be seen that it is preferable to distribute the screen conductors such that the maximum arc of the beam screen without screen conductors is minimised. This can clearly be seen by comparing the case of 19 screen conductors where all conductors are clustered together (as was done for the replacement MKI8d (Fig. 8.18(b)) and for 19 screen conductors, where only 3 are missing close to the HV busbar (Fig. 8.19(b)). Again this advantage is bourne out in the power lost in the structure. This is however not beneficial without consideration of the induced electric field during kicker pulsing, as the induced voltage on a given screen conductor is still the same, and thus surface flashover along the ceramic tube to the external metallization is not made worse by this layout. It can thus be seen that the beam screen design itself must be optimised with regards to the induced screen conductor voltage before more conductors can be added to the ceramic tube to improve screening.

8.5.3 Dependence of the Impedance on the Beam Screen Dimensions

It will now be shown that with 24 screen conductors placed in the ceramic tube that the resulting impedance is dominated by the dimensions of the ceramic tube, the screen conductors and the external metallisation at the capacitively coupled end of the beam screen. To investigate how changes to certain parameters (specifically the length of the overlap between the screen conductors and the external metallization and the thickness of the ceramic tube) a cut down model of the kicker magnet is used, considering just the capactively coupled end of the kicker magnet (shown in Fig. 8.21). This is done to allow a larger mesh density in this important (from the electrical and impedance point of view)

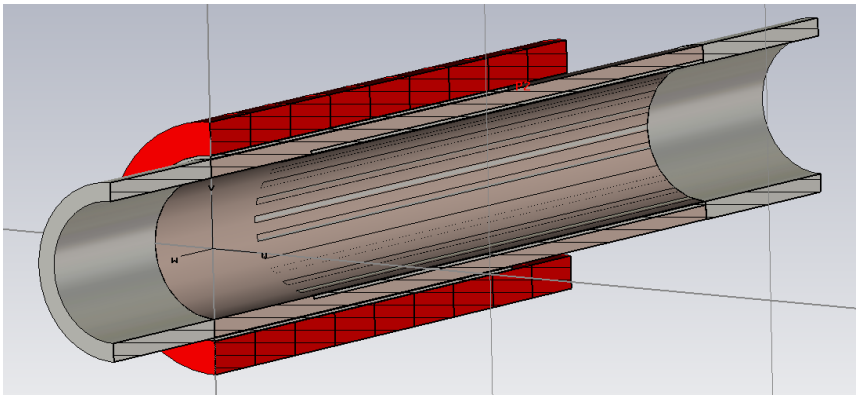

Figure 8.21: The cut down simulation model used for simulations of the MKI beam screen with 24 screen conductors.

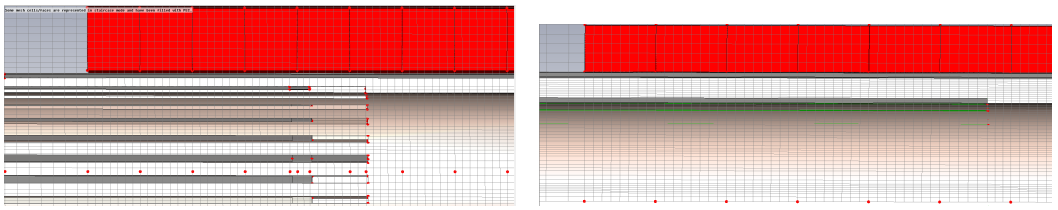

(a) (b)

Figure 8.22: A comparison of the mesh that may be generated in CST Particle Studio using both the full model (a) and the cutdown model (b). Note the greatly increased mesh density in the important overlap region between the screen conductors and external metallization. The simulation time for the first is on the order a of day, for the second 30 minutes.

region of the kicker magnet. In models of the full kicker magnet the mesh density is severely limited due to the large mesh generated in the entire magnet volume which subsequently may make the mesh very limited in near beam areas (for example in the ceramic tube between the screen conductors and the external metallization. A comparison of the meshes is shown in Fig. 8.22).

First we shall consider the effect of the impedance for different lengths of overlap of the capacitively coupled sections. To do this we consider just the end section, and change the length of the external metallization to change the length of the overlap (the length of the screen conductors used is kept fixed to avoid changing any potential resonances due to the modelled length of the screen conductors acting as $\lambda/4$ resonators). Overlaps of

between 0.08 m and 0.12 m at 0.01 m intervals are simulated, and the results are shown in Fig. 8.23(a). It can be seen that each overlap has a distinct set of resonance frequencies. The source of these resonances can be seen to be the result of the overlap between the external metallization and the screen conductor acting as a $n\lambda/2$ resonator. End effects cause the effective length of the overlap to be extended to some degree, which fitting to the resonance frequencies has shown to be ≈ 9mm for all lengths for a ceramic tube thickness of 7 mm. This gives a resonant frequency f_{res} of

$$f_{res} = \frac{nc}{\sqrt{\epsilon_r} 2 \left(L_{overlap} + \delta_{fringe} \right)} \tag{8.1}$$

where n is an integer, c is the speed of light ϵ_r is the relative permitivitty of the volume material ($\epsilon_r = 10$ for the alumina beam screen), $L_{overlap}$ is the length of overlap and δ_{fringe} is the effective increase in length due to fringe fields. This gives an empirical fit for the resonant frequencies of the resonances due to the overlap between the screen conductors and an external conductor (metallization or external metal pipe) in a beam screen with capacitive coupling. The resonant frequency calculated using Eqn. 8.1 is shown for the first resonances for all the effective lengths of overlap in Fig. 8.23(b), and up to 2.5 GHz for the case of the overlap being 100 mm in Fig. 8.24. It can be seen that the calculated resonant frequencies match the simulated very well. Work is still under way as to how to determine the peak impedance of each resonance. In addition predictions for the power loss due to the impedances for different effective overlaps calculated assuming either a broadband heating scenario or assuming a beam harmonic at the resonant frequency are shown in Tab. 8.5. It can be seen that changing the length of the overlap does not strongly effect to the change in power loss assuming a broadband heating scenario. It can be seen that increasing the length of the effective overlap causes an increase in the power loss assuming a resonant heating scenario, but this correlation is not clear as there is much variance in the values.

Secondly the influence of the thickness of the ceramic tube is considered. This is a concern as increasing this thickness has two effects - to change the value of the capacitance at the capacitively coupled end, which affects the low frequency impedance, and the

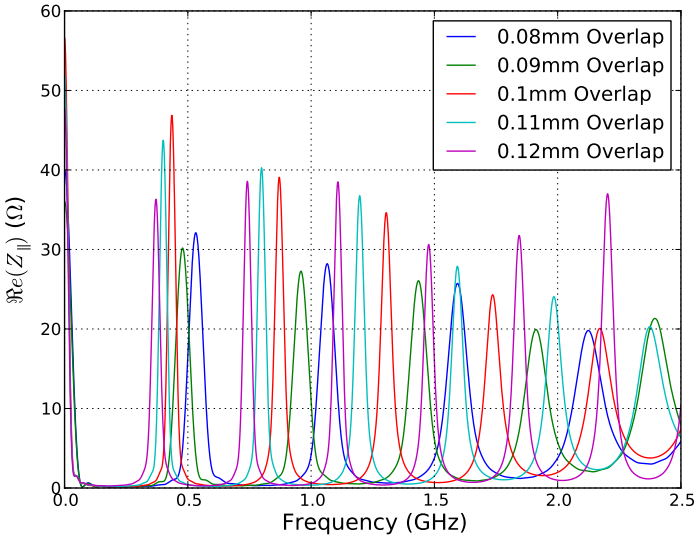

(a)

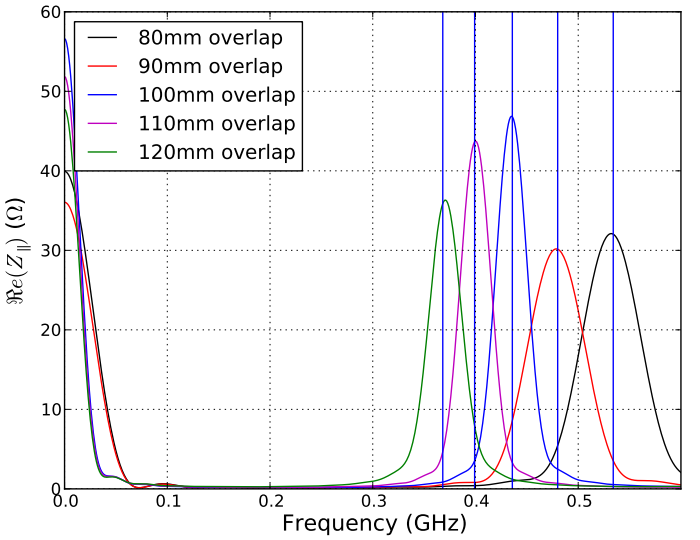

(b)

Figure 8.23: (a) The simulated real component of the longitudinal beam coupling impedance for different lengths of the overlap, and (b) a zoomed in plot of the first resonances of all the overlaps with the calculated resonance frequency (shown as vertical lines) for each based on the effective length. For each the thickness of the ceramic tube is 7 mm.

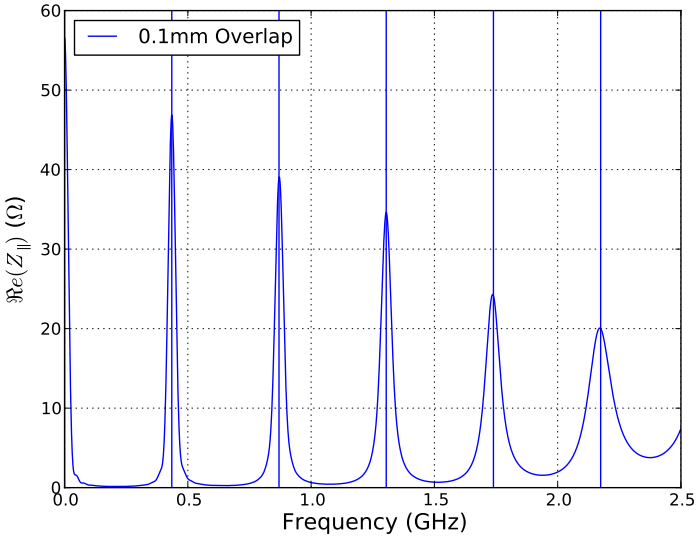

Figure 8.24: The simulated impedance of the beam screen with 24 screen conductors with an overlap $L_{overlap} = 100\ mm$ and the predicted resonance frequencies from Eqn. 8.1 shown as vertical lines.

Table 8.5: The beam induced heating calculated for a number of beam screen designs with 24 screen conductors with equal thickness of ceramic tube (thickness of 7mm) with different effective overlaps assuming 50 ns bunch spacing LHC conditions (1380 bunches, 1.7×10^{11}ppb with a bunch length of 1 ns assuming a Gaussian bunch profile (length is $4\sigma_z$ value)). It can be seen that the broadband heating component is relatively constant for the change in overlap, whilst the resonant component only significantly changes with a large increase in the effective overlap.

Overlap (mm)	LHC, 50ns, 1.7e11ppb		LHC, 25ns, 1.15e11ppb	
	BB (W)	Res(W)	BB (W)	Res (W)
80	38.5	6.9	30.0	13.0
90	39.1	6.9	31.0	13.1
100	35.3	12.1	28.8	23.0
110	36.1	13.1	31.6	24.9
120	36.7	12.7	28.9	24.1

Table 8.6: The beam induced heating calculated for a number of beam screen designs with 24 screen conductors of equal length (overlap of 100mm) with different tube thicknesses assuming 50 ns bunch spacing LHC conditions (1380 bunches, 1.7×10^{11}ppb with a bunch length of 1 ns). It can be seen that the change in broadband heating component does not strongly correlate with the change in tube thickness, whilst the resonant component can increase drastically due to the increasing peak impedance as a result of increasing the tube thickness.

Outer Tube Diameter/Tube Thickness (mm)	$P_{loss,BB}$	$P_{loss,Res}$
50/4	30	4
53/5.5	26	10
56/7	35	12

increase in the volume of the overlap region due to the increased thickness. The internal diameter of the ceramic tube is kept at 42 mm, whilst external diameters of 50, 53 and 56 mm are considered, giving tube thicknesses between 4 and 7 mm. The resulting real components of the longitudinal impedances are shown in Fig. 8.25, where it can be seen that increasing the ceramic tube thickness has two effects - a slight lowering of the resonant frequency, but also a significant increase of the peak impedance of the resonance, by almost a factor 2 from a tube 4 mm thick to a 7 mm thick tube. The difference that the peak impedances make to the expected heating of the MKI can be seen in Tab. 8.6, where it can be seen that the change in the power loss due to the increased thickness could be expected to be small assuming a broadband heating scenario, but increases (significantly in terms of percentage, but little in absolute terms) if we assume a beam harmonic falls upon the resonant frequency.

The small reduction in the resonant frequency as the thickness of the ceramic tube is increased is expected as the fringe fields will increase with greater thickness. The examination of the prediction shows that the increase in effective length, due to a non-zero thickness of the ceramic tube, is given (for ϵ_r=10 for all frequencies) by an increase in effective length (in mm) of $\approx 1.25\times$thickness (in mm).

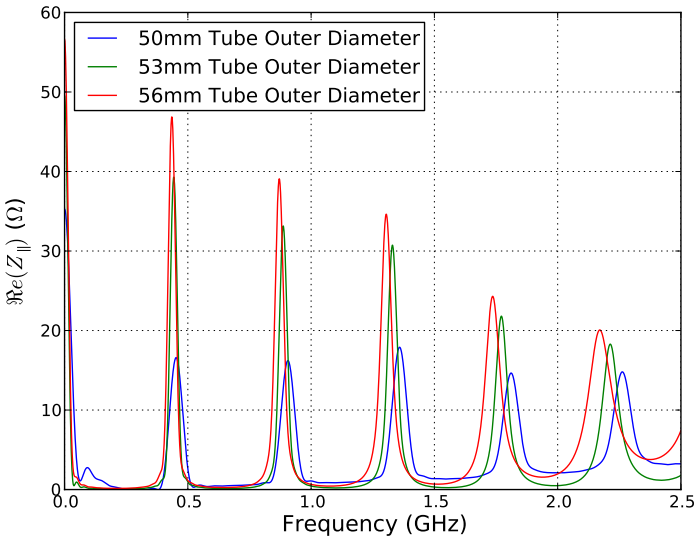

Figure 8.25: The variance of the real beam coupling impedance with the tube thickness. External diameters of 50, 53 and 56mm correspond to tube thicknesses of 4, 5.5 and 7mm respectively. The physical overlap is 100mm in all cases.

8.6 New Beam Screen Designs

Using the knowledge acquired from examining the beam coupling impedance dependence on the layout of the beam screen from the previous section, and additionally the electrical field simulations of the induced voltages on the screen conductors during magnet pulsing, a number of alternative beam screen designs have been proposed. The motivation in these designs has been to reduce the power loss into the MKI (in this case to reduce the temperatures reached by the ferrite yoke) and to reduce the surface electric field of the ceramic tube, near the end of the screen conductors during magnet pulsing, to further reduce surface flashover between the screen conductors and along the ceramic tube to a ground plane.

The proposed designs are described below:

- 24 screen conductors of alternating length, as shown in Fig. 8.26. The alternating length screen conductors layout has been demonstrated to reduce the surface electric field associated with the shorter length screen conductors, thus being beneficial to

the electrical breakdown rate of the shorter conductors. However the electric field associated with the longer screen conductors is increased.

- 24 screen conductors tapered in length, as shown in Fig. 8.27. The tapering of the screen conductors has previously been shown to help reduce the surface electric field of the shorter conductors [101]: thus the shorter conductors are those with the highest induced voltage, i.e. towards the HV busbar.

- 24 screen conductors some with an alternating length and then tapered towards the HV busbar, as shown in Fig. 8.28. This mixture of the above two designs is intended to use the reduction of surface electric field of the shorter conductors due to the tapering, whilst keeping a relatively high capacitance at the capacitively coupled end so as to not increase the beam coupling impedance of frequencies below 50 MHz. Note that the alternating length screen conductors are closest to the return busbar and hence have the lowest induced voltage: hence an increase in the electric field of the longer conductors is not so important an effect.

- 24 screen conductors in enclosed slots in the ceramic tube, as shown in Fig. 8.29. The intention of this design is to increase the necessary induced voltage on the screen conductors before breakdown occurs, because surface flashover is no longer a possile breakdown path. This possible solution is discounted because of extreme difficulties associated with the manufacture of the ceramic tube [114].

- An alternative screen conductor layout, in which two conductors are conductively connected to ground at one end and all others are capacitively coupled to ground at both ends [115], as shown in Fig. 8.30. This design is intended to reduce the maximum induced voltage on the screen conductors by having all the screen conductors be connected to one another at the capacitively coupled end and being referenced to a voltage level approximately mid-way between the minimum and maximum induced voltage. To counter possible longitudinal eddy currents during pulsing increasing the field rise time, the majority of the screen conductors are capacitively

coupled at both ends of the magnet, with only two conductors connected to ground at the downstream end of the magnet.

- 24 alternating length screen conductors with part of the metallization replaced by a external metal cylinder, as shown in Fig. 8.31. This design is intended to reduce the electric field at the capacitively coupled end by replacing the metallization on the external surface of the ceramic tube close to the ends of the screen conductors, with a metal cylinder some millimetres off the ceramic tube outer surface. Electric field simulations have shown that the high permittivity of the ceramic was in effect pushing the ground plane into the ceramic tube, reducing the effective spacing between the screen conductors and the metallization, whereas this physical vacuum gap should reduce this effect [115].

- 24 screen conductors of a mixture of alternating and tapered lengths with part of the metallization replaced with an external metal cylinder [116], as shown in Fig. 8.32: the cylinder is 1 mm from the outside surface of the ceramic tube at the return busbar side, and 3 mm from the outside surface of the ceramic tube at the HV busbar side. This is intended to improve on the above design by using the combined alternating and tapered design to further reduce the electric field on the surface of the ceramic tube associated with the screen conductors. Due to difficulty of manufacturing the step out of the metal cylinder is continued to the end of the ceramic tube. **This is the proposed final design for implementation in the replacement MKIs for installation during long shutdown 1 (2013-2014)**.

In this analysis of these designs we shall focus mainly on the resulting power loss from interaction of the beam with the real component of the longitudinal beam impedance as this is the present primary limitation from the MKIs. The real component of the longitudinal beam coupling impedance is shown in Fig. 8.33(a), and the imaginary in Fig. 8.33(b).

The estimated heating for both 25 ns and 50 ns bunch spacing operation in the LHC are shown in Tab. 8.7 for 1ns bunch length, and the variation in power loss with the bunch length for 25 ns and 50 ns bunch spacing shown in Fig. 8.34. Comparing the designs, it can

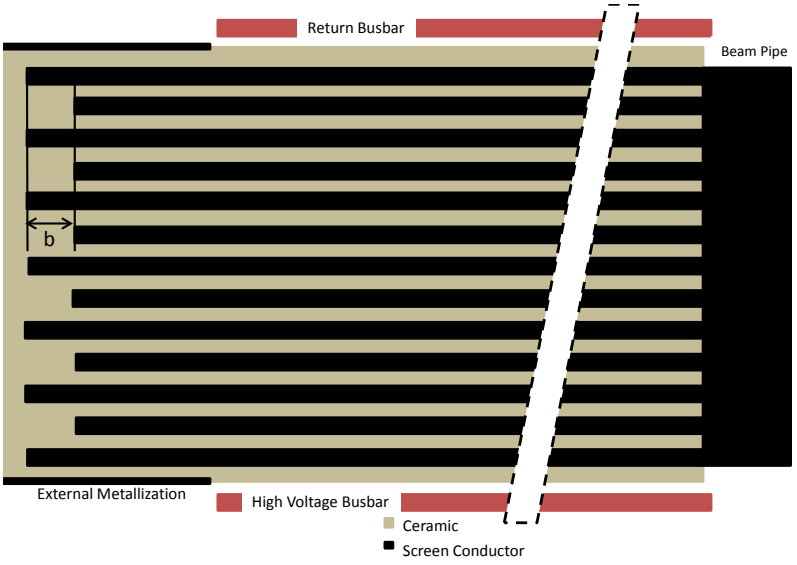

Figure 8.26: A MKI beam screen design with alternating lengths of screen conductors - with a difference in length b.

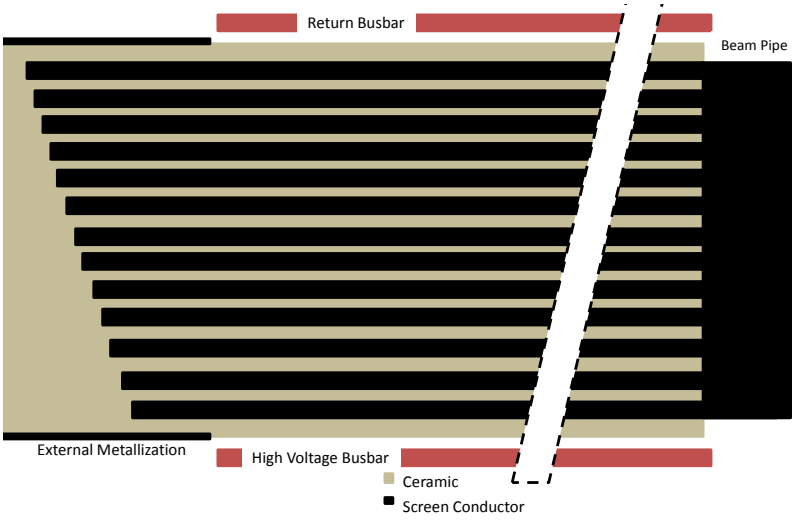

Figure 8.27: A MKI beam screen design with tapered lengths of screen conductors. The taper may be altered to acquire the desired combination of impedance and surface electric field on the ceramic tube.

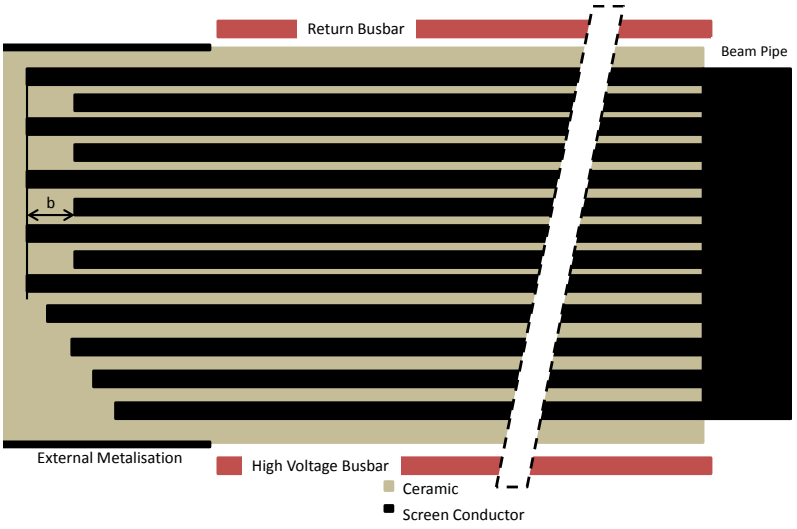

Figure 8.28: A MKI beam screen design with a combination of tapered and alternating screen conductors. The degree of alternating and tapering may change dependent of the desired impedance and surface electric field associated with the screen conductors. The alternating length conductors are closest to the return busbar (those with the lowest induced voltage).

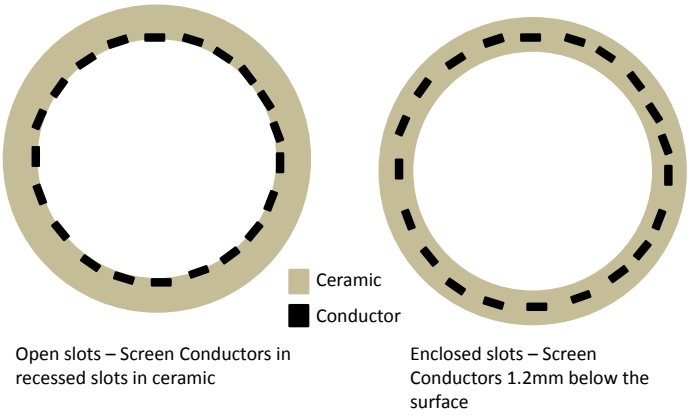

Figure 8.29: A MKI beam screen design with enclosed slots (shown in comparison to the usual beam screen design with open slots) for the screen conductors.

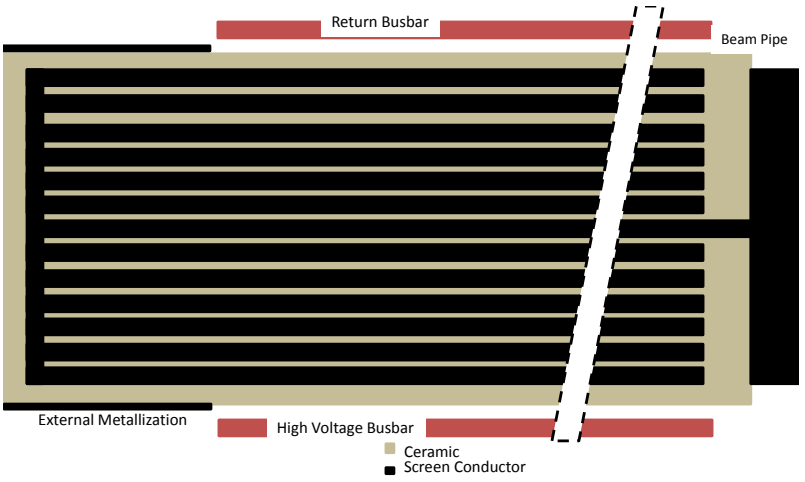

Figure 8.30: A MKI beam screen design using an alternative screen conductor layout in which 2 (cross section shown here) conductors are connected to ground at one end of the screen, and all conductors are connected together at the other end. Both ends have capacitive coupling.

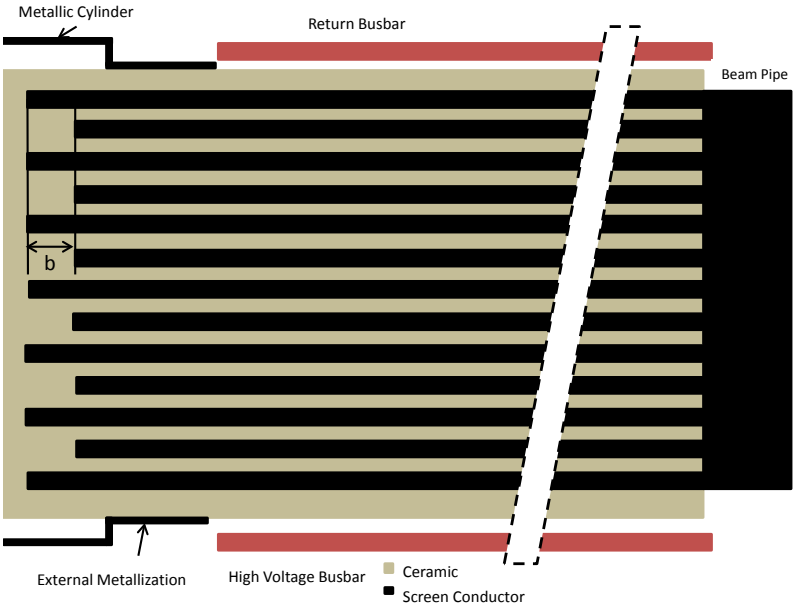

Figure 8.31: A MKI beam screen design implementing a replacement of some of the external metallization with a metallic cylinder so as to remove the ground plane closest to the ends of the screen conductors from the outer surface of the ceramic tube.

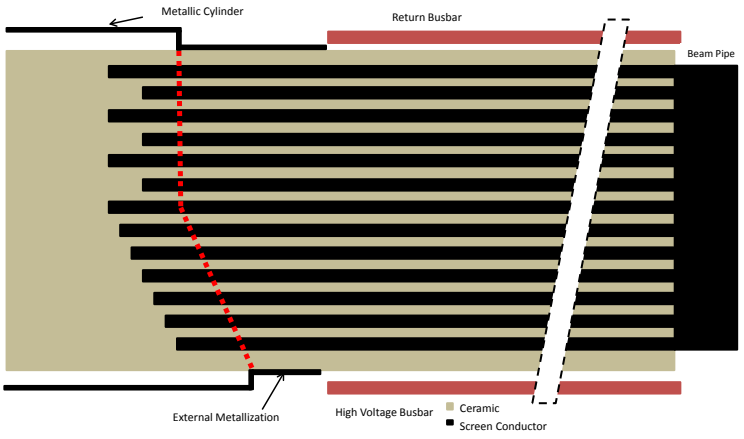

Figure 8.32: The proposed final MKI design. A combination of alternating and tapered screen conductors is used, along with a step out of the external metallization to a metal cylinder. The outline of the step out is shown by the red-dashed line.

be seen that in terms of power loss, the enclosed screen conductor design is best, giving the lowest power loss by almost 50%. However this design has a great many difficulties in manufacturing (extruding a beam screen with sealed slots is difficult) and thus was not further pursued. The alternative conductor layout produces a significantly higher power loss than all the other designs, due to the decreased capacitance of the structure. All the other designs are very similar in their resulting power loss. It can be seen that the power loss can be very strongly reduced for very short bunch lengths (as has been proposed for HL-LHC operation without crab cavities [117]) by increasing the bunch length, but for nominal bunch lengths (τ_b =1 ns) it can be seen that there is not much benefit in further increasing the bunch length.

8.7 Upgrade Plans for Long Shutdown 1 and Beyond

During long shutdown 1 (LS1) measurements of the beam impedance of the proposed new beam screen design, to verify the design before upgrading 8 kicker magnets, implementing the new screen design and the additional proposed changes to the inside of the vacuum tank to reduce the temperatures reached in the ferrite yoke. Thermal simulations

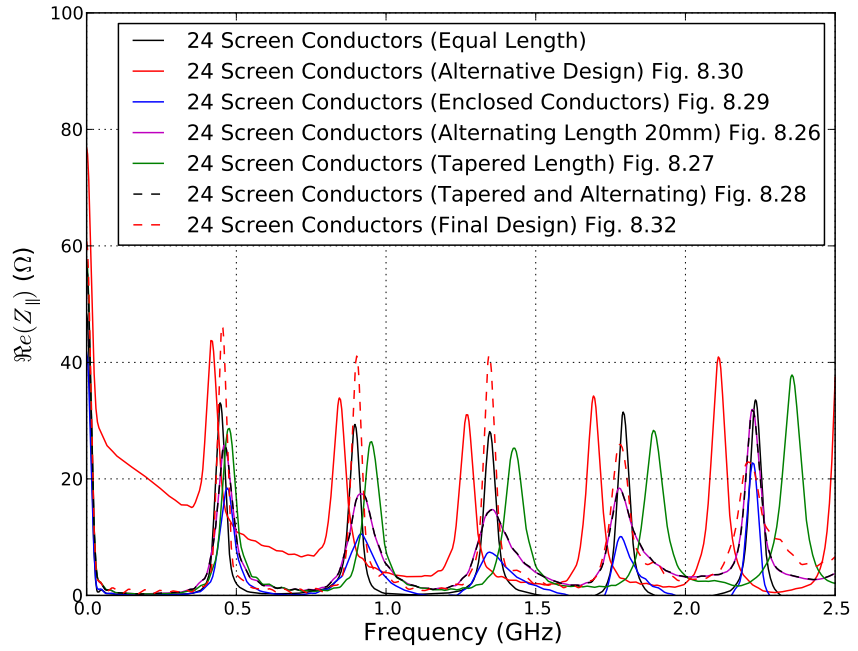

(a)

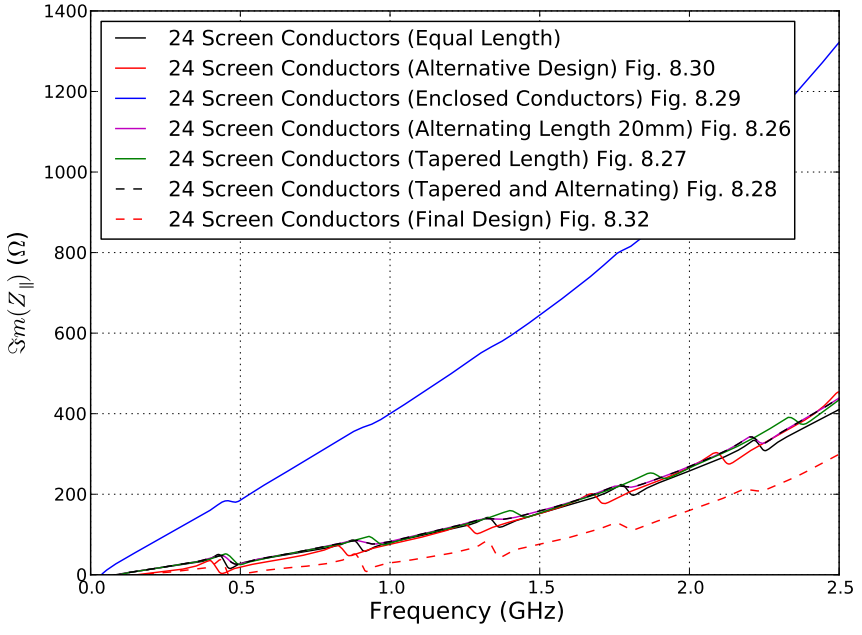

(b)

Figure 8.33: The real component of the beam coupling impedance for a number of the proposed beam screen designs (a). In addition the imaginary component of the longitudinal impedance is shown for completeness (b). In all cases the outside diameter of the ceramic tube is 56mm.

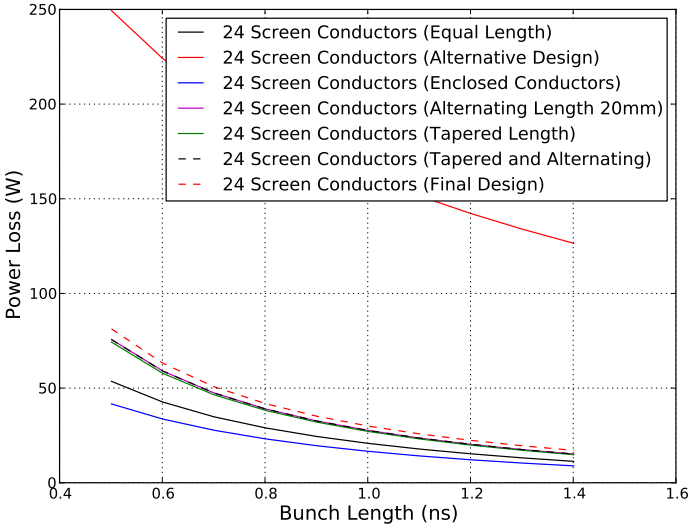

(a)

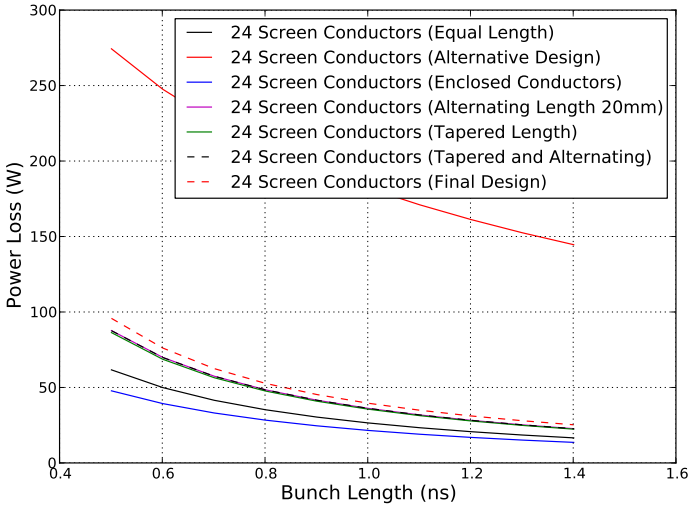

(b)

Figure 8.34: The variation of the predicted beam induced power loss with bunch length for a number of screen designs. The variation for 25 ns (a) and 50 ns (b) machine settings.

Table 8.7: The power loss expected due to beam-wakefield interactions in the MKIs for a number of proposed beam screen designs. Estimates are given for 50 ns and 25 ns bunch spacing in the LHC (1380 bunches, 1.7×10^{11} particles per bunch for 50 ns, 2808 bunches, 1.15×10^{11} particles per bunch for 25 ns) assuming a $\cos^2$ bunch distribution with a bunch length $t_b = 1\ ns$.

Screen Design	$P_{loss,50\ ns}$ (W)	$P_{loss,25\ ns}$ (W)
24 Conductors, Alternating Length	36	28
24 Conductors, Tapered Length	36	27
24 Conductors, Alternating and Tapered	36	28
24 Screen Conductors, Enclosed Conductors	21	17
24 Conductors, Alternate Design	182	161
24 Conductors, Step out	37	30
24 Conductors, Final Design	37	30

have indicated that the proposed screen design will be capable of reducing the maximum temperature reached in the ferrite yoke below the Curie temperature for the nominal operating conditions for the LHC, and for a number of proposed HL-LHC operating conditions also (see Fig. 8.35). In addition electric field simulations have strongly indicated that the transient electric field on the inner surface of the ceramic tube, associated with the screen conductors, will not be sufficient to induce surface flashover. Electrical breakdown tests with a metal cylinder, instead of metallization over the end of the screen conductors, have commenced. Preliminary results indicate that the voltage at which the surface flashover occurs is increased by at least 30%.

To estimate whether the proposed design would be viable in the HL-LHC case, this case is considered as well from a future-proofing point of view. A set of proposed HL-LHC parameters and the resulting power losses are shown in Tab. 8.8. By comparing to the estimated ferrite yoke temperature from Fig. 8.35, the power loss from both the 25 ns operating parameters and the 50 ns operating parameters both result in a steady-state temperature of the ferrite yoke that is below the ferrite Curie temperature. This indicates that the present design should be viable through the HL-LHC upgrade, assuming simulation results are accurate.

Further monitoring of the MKIs will be necessary, as the stored current in the LHC

Table 8.8: Possible HL-LHC bunch parameters and the estimated heating for the LHC beam screen to be installed during LS1. Here the bunch length is assumed to encompass the 4σ Gaussian width.

Operational Mode	t_b (ns)	t_{bunch} (ns)	N_b	$n_{bunches}$	P_{loss} (W)
25 ns	1.0	25 ns	2.5×10^{11}	2808	142
50 ns	1.0	50 ns	3.8×10^{11}	1380	200

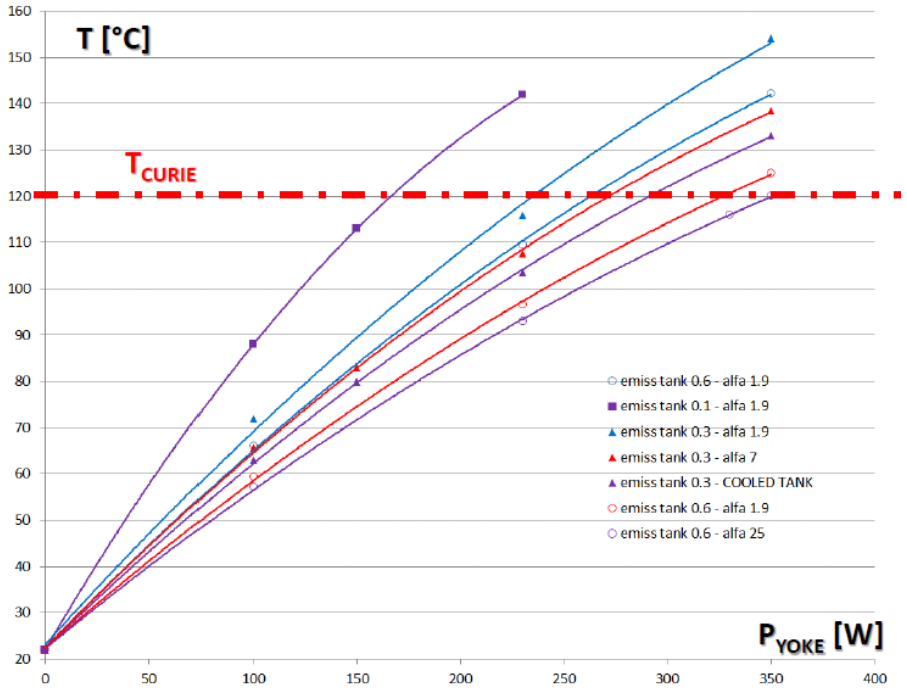

Figure 8.35: The maximum steady-state temperature reached by the ferrite yoke in the MKI depending on the power load in the ferrite yoke as calculated using a 2D cross section of the MKI assuming different tank emissivities and rates of convection outside of the tank (alfa). P_{yoke} is the power lost in the ferrite yoke and T the maximum steady state temperature of the ferrite yoke. Provided by M. Garlasche et al [118]. The worst case scenario is for alfa=1.9 W/(m^2 K).

is increased, due to possible further sources of heating within the magnets. However the work done on the understanding of the beam impedance, the heat transfer within the magnet and the electric field during kicker pulsing has greatly improved the knowledge of possible limitations in the future and the variety of solutions/counter measures that may be implemented.

8.8 Conclusion

In this chapter we have introduced the background of the LHC MKIs, of the reasons behind changing the screen conductor layout due to electrical breakdown and of the observed temperature increase during the increase in bunch intensity in the LHC during operation in 2011 and 2012. The impedance of the beam screen with 15 screen conductors has been thoroughly evaluated using both computational simulations and bench-top measurements, which show a good agreement between the two. Based on this confidence in the simulation model, a new design with 19 screen conductors was evaluated, and placed in the LHC (MKI8d) during technical stop 3 in September 2012. Temperatures measured before and after the change show a drastic reduction in the observed maximum temperature reached, demonstrating that the proposed solution was effective in reducing the real component of the longitudinal beam coupling impedance of the MKI. Using this confidence in the simulation tools, a new design that would further reduce the heat load on the magnet, whilst reducing the likelihood of electrical breakdown on the ceramic tube of the beam screen was proposed, the impedance evaluated, and the heat load calculated. This design was shown to further reduce the maximum temperature reached during operation, whilst satisfying electrical breakdown requirements. As a result this design is being pushed for deployment in all 8 MKI magnets.

Soon electrical breakdown measurements of the new design are to be carried out, along with bench-top impedance measurements using the coaxial wire method. The resulting magnets are intended to placed in the LHC during long shutdown 1.

Chapter 9

Summary and Conclusions

9.1 Summary

In this thesis has been presented a number of studies into the impedance reduction techniques employed in two key systems of LHC, the collimation systems and the injection kicker magnets. Problems with these systems have been examined, focusing on their shortcomings from an operational standpoint especially the high temperatures experienced due to beam-induced heating, using both computational and bench-top measurements to identify and characterise the beam-coupling impedance responsible for this. As part of this a new method for measuring the transverse beam impedances of asymmetric structures has been derived and verified using simulated measurements in comparison to an analytical model of an asymmetric structure (in this case C-core ferrite kicker). Applications of this method to bench top measurements of an injection kicker magnet in the LHC show promise for the method when compared to simulated impedances of the same structure. In addition a study of the power loss in ferrite damped cavities with different extents of damping and screening of the ferrite has been studied in order to better understand the heat loads in structures with a complex structure which may limit the effective damping of cavity modes by ferrite.

Subsequently improvements to the existing systems have been proposed, with a focus on the expected power load due to beam-induced heating, resulting in a new RF damping

system for use in the TCTP collimators, and possibly for further use in the phase 2 secondary collimators. An intermediate improvement to the beam screen in the LHC injection kickers was proposed and implemented in MKI8d during technical stop 3 (23/09/12-27/09/12) which contributed to greatly reducing the measured temperature in this magnet. Following from this a further improved beam screen design for use in the LHC injection kicker magnets has been implemented: this will be constructed, detailed measurements carried out to verify the predicted beam coupling impedance, tested for electric field surface flashover and installed during Long Shutdown 1 in 2013/14. This is expected to reduce the power deposition in the magnets by a factor of 4-5 after LS1 when compared to operation 2012, from 150 W per magnet for 50 ns bunch spacing, to 30 W per magnet for 25 ns bunch spacing. This improved beam screen has achieved better screening by modifying the layout at the capacitively coupled end to to allow complete coverage of the ferrite yoke, as opposed to only partial coverage as was the case with the old screen design. This necessitated the alteration of the capacitvely coupled end to introduce a step away from the surface of the ceramic tube near the ends of the screen conductors which served to greatly reduce the electric field strength in this region.

9.2 Future Directions

It has become clear during this work that with the increasing high beam currents demanded at high energy hadron colliders, in addition to the very long fill times, that beam-induced heating must seriously be considered as a potential limitation on the integrated luminosity delivered to the experiments due to both high temperatures that may damage equipment, or due to long cool down times necessary between the fills. Beam-induced heating has been observed previously in lepton machines (for example PEP-II at SLAC [119]) where the beam power spectrum is Gaussian in profile (due to synchrotron radiation) and extends to many tens of gigahertz. Hadron colliders conversely have a power spectrum that extends to a couple of gigahertz, and typically non-Gaussian profiles. This causes higher order lobes to form in the power spectrum which cause complicated

interactions with beam impedance at high frequencies which is heavily dependent on the bunch length in the machine. During operation of the LHC in 2011 and 2012 numerous examples of equipment damaged by beam induced heating have been observed, and in this thesis has been presented a study of the LHC injection kicker magnets, in which a new beam screen design was chosen to be implemented in the after LS1 to combat this heating. Many of these devices have subsequently been examined and solutions proposed to reduce the heating. With the increased beam current proposed for both post-LS1 and HL-LHC in the future, careful study of the beam coupling impedance and the resulting instabilities and heating will remain an important issue for the coming future.

The possible impedance reduction techniques must be understood and applied as appropriate to a given problematic impedance. It has been shown that a good understanding of the beam coupling impedance of a device is exceptionally important in understanding both the sources and possible paths of mitigation for high impedances. In particular modern simulation and measurement tools allow very detailed analysis to do be done efficiently and rigerously on highly complex structures.

Bibliography

[1] R. Bailey, J. L. Baldy, A. E. Ball, P. Bonnal, M. Buhler-Broglin, C. Détraz, K. Elsener, A. Ereditato, P. E. Faugeras, A. Ferrari, G. Fortuna, A. L. Grant, A. M. Guglielmi, A. Hilaire, K. Hubner, M. Jonker, K. H. Kissler, L. A. López-Hernandez, J. M. Maugain, P. Migliozzi, V. Palladino, F. Pietropaolo, J. P. C. Revol, P. R. Sala, C. Sanelli, G. R. Stevenson, N. Vassilopoulos, H. H. Vincke, E. Weisse, and M. Wilhemsson, "The CERN Neutrino beam to Gran Sasso (NGS)." CERN, Geneva, Tech. Rep. CERN-SL-99-034-DI. INFN-AE-99-05, Jun 1999, addendum to report CERN 98-02, INFN-AE-98-05.

[2] "n-TOF Technical Design Report on Experimental Area," CERN, Geneva, Tech. Rep. CERN-INTC-2000-018, Nov 2000.

[3] G. Gabrielse, R. Kalra, W. S. Kolthammer, R. McConnell, P. Richerme, D. Grzonka, W. Oelert, T. Sefzick, M. Zielinski, D. W. Fitzakerley, M. C. George, E. A. Hessels, C. H. Storry, M. Weel, A. Mullers, and J. Walz, "Trapped Antihydrogen in Its Ground State," *Phys. Rev. Lett.*, vol. 108, no. arXiv:1201.2717, p. 113002, Jan 2012.

[4] M. Hori, "The ASACUSA experiment at CERN's Anti-proton Decelerator," *Nucl.Phys.*, vol. A692, pp. 119–128, 2001.

[5] J. S. Hangst and P. Bowe, "ALPHA Proposal," CERN, Geneva, Tech. Rep. CERN-SPSC-2005-006. SPSC-P-325, Jan 2005.

[6] Y. Kadi, A. P. Bernardes, Y. Blumenfeld, S. Calatroni, R. Catherall, M. A. Fraser,

B. Goddard, D. Parchet, E. Siesling, W. Venturini Delsolaro, D. Voulot, and L. R. Williams, "Status and Future Perspectives of the HIE-Isolde Project at CERN," *Conf. Proc.*, vol. C1205201, no. CERN-ATS-2012-251, p. PAGE. 4 p, May 2012.

[7] C. J. Maggiore, N. Agazaryan, N. Bassler, E. Blackmore, G. Beyer, J. J. De Marco, M. Doser, C. R. Gruhn, M. H. Holzscheiter, T. Ichioka, K. S. Iwamoto, H. V. Knudsen, R. Landua, W. H. McBride, S. P. Møller, J. Petersen, J. B. Smathers, L. D. Skarsgard, T. Solberg, U. Uggerhøj, H. R. Withers, and B. G. Wouters, "Biological effectiveness of antiproton annihilation," *Nucl. Instrum. Methods Phys. Res., B*, vol. 214, pp. 181–5, 2004.

[8] *ATLAS detector and physics performance: Technical Design Report, 1*, ser. Technical Design Report ATLAS. Geneva: CERN, 1999, electronic version not available.

[9] "CMS : the Compact Muon Solenoid; 1993 ed." CERN, Geneva, Tech. Rep. CERN-LHCC-93-48, 1993.

[10] *LHCb : Technical Proposal*, ser. Tech. Proposal. Geneva: CERN, 1998.

[11] C. Lourenco, "Heavy Ion Collisions at the LHC: the ALICE Experiment. oai:cds.cern.ch:315992," no. hep-ph/9612221. LIP-96-02, 1996.

[12] E. McCrory and V. Shiltsev, "Characterizing Luminosity Evolution in the Tevatron," 2005.

[13] L. Laslett, V. Neil, and A. Sessler, "Transverse Resistive Instabilities of Intense Coasting Beams in Particle Accelerators," *Rev.Sci.Instrum.*, vol. 36, pp. 436–448, 1965.

[14] G. V. Stupakov, "Wake and Impedance," SLAC, Stanford, CA, Tech. Rep. physics/0011011. SLAC-PUB-8683, Nov 2000.

[15] G. V. Stupakov, "Surface roughness impedance," pp. 141–152, 2000.

[16] G. V. Stupakov, "Advances in Impedance Theory," 2009.

[17] N. Mounet, "The LHC Transverse Coupled-Bunch Instability," Ph.D. dissertation, Lausanne, EPFL, Mar 2012, presented 2012.

[18] L. Palumbo, V. Vaccaro, and M. Zobov, "Wake fields and impedance," 1994.

[19] A. Wolski, "Theory of Electromagnetic Fields," RF for Accelerators, CERN Accelerator School, 2010.

[20] E. Jensen, "Cavity Basics," RF for Accelerators, CERN Accelerator School, 2010.

[21] B. W. Zotter and S. A. Kheifets, *Impedances and Wakes in high energy accelerators*. Singapore: World Scientific, 1998.

[22] E. Jordan, *Electromagnetic Waves and Radiating Systems*. Prentice Hall, 1968.

[23] A. W. Chao, *Physics of collective beam instabilities in high energy accelerators*. New York, NY: Wiley, 1993.

[24] F. Roncarolo, F. Caspers, T. Kroyer, E. Metral, N. Mounet, B. Salvant, and B. Zotter, "Comparison between laboratory measurements, simulations, and analytical predictions of the transverse wall impedance at low frequencies," *Phys. Rev. Lett.*, vol. 12, no. CERN-BE-2010-005. 8, p. 084401. 1 p, Aug 2009.

[25] E. Métral, "Transverse resistive-wall impedance from very low to very high frequencies," CERN, Geneva, Tech. Rep. CERN-AB-2005-084, Aug 2005.

[26] H. Tsutsui, "Some Simplified Models of Ferrite Kicker Magnet for Calculation of Longitudinal Coupling Impedance," CERN, Geneva, Tech. Rep. CERN-SL-2000-004-AP, Jan 2000.

[27] N. Biancacci, V. Vaccaro, E. Métral, B. Salvant, M. Migliorati, and L. Palumbo, "The mode matching method applied to beam coupling impedance calculations of finite length devices," CERN, Geneva, Tech. Rep. CERN-ATS-2012-187, May 2012.

[28] N. Mounet and E. Métral, "Electromagnetic fields created by a macroparticle in an infinitely long and axisymmetric multilayer beam pipe," CERN, Geneva, Tech. Rep. CERN-BE-2009-039, Nov 2009.

[29] N. Mounet and E. Métral, "Electromagnetic fields and beam coupling impedances in a multilayer flat chamber," CERN, Geneva, Tech. Rep. CERN-ATS-2010-056, Dec 2010.

[30] H. Tsutsui and L. Vos, "Transverse Coupling Impedance of a Simplified Ferrite Kicker Magnet Model," CERN, Geneva, Tech. Rep. LHC-PROJECT-NOTE-234, Sep 2000.

[31] K. Y. Ng, *Physics of Intensity Dependent Beam Instabilities*. New Jersey, NJ: World Scientific, 2006.

[32] P. Baudrenghien, M. E. Angoletta, T. Argyropoulos, L. Arnaudon, T. Bohl, O. Brunner, A. Butterworth, E. Ciapala, F. Dubouchet, J. Esteban-Muller, J. Ferreira-Bento, D. Glenat, G. Hagmann, W. Hofle, D. Jacquet, M. Jaussi, S. Kouzue, D. Landre, J. Lollierou, P. Maesen, P. Martinez Yanez, T. Mastoridis, J. Molendijk, C. Nicou, J. Noirjean, G. Papotti, A. Pashnin, G. Pechaud, J. Pradier, J. Sanchez-Quesada, E. Shaposhnikova, M. Schokker, D. Stellfeld, J. Tuckmantel, D. Valuch, U. Wehrle, and F. Weierud, "The LHC RF System - Experience with beam operation," Tech. Rep. CERN-ATS-2011-048, Aug 2011.

[33] E. Métral and et al, "Beam-induced heating/bunch length/RF and lessons for 2012." Geneva: Presented at Chamonix 2012 LHC Performance Workshop, February 2012.

[34] A. Grudiev, "Simulation of Longitudinal and Transverse Impedances of Trapped Modes in LHC Secondary Collimator," CERN, Geneva, Tech. Rep. AB-Note-2005-042. CERN-AB-Note-2005-042, Dec 2005.

[35] A. Grudiev, "Simulation and reduction of longitudinal and transverse impedances

of a collimation device with two beams in one vacuum chamber," Tech. Rep. LHC-Project-note-413, Mar 2008.

[36] A. Burov and V. Lebedev, "Transverse Instabilities of Coasting Beams with Space Charge," Tech. Rep. arXiv:0812.3887. FERMILAB-PUB-08-479-AD, Dec 2008.

[37] O. Boine-Frankenheim, I. Hofmann, and V. Kornilov, "Instabilities and Space Charge Effects in High Intensity Ring Accelerators," p. 5 p, 2006.

[38] T. Pieloni, "A study of beam-beam effects in hadron colliders with a large number of bunches," Ph.D. dissertation, Ecole Polytechnique, Lausanne, Milan U., 2008, presented on 4 Dec 2008.

[39] K. S. B. Li and G. Rumolo, "Review of beam instabilities in the presence of electron clouds in the LHC," no. CERN-ATS-2011-095, p. 3 p, Sep 2011.

[40] M. Schaumann, J. Jowett, and R. Bruce, "Intra-beam Scattering and Luminosity Evolution for HL-LHC Proton Beams," CERN, Geneva, Tech. Rep. CERN-ATS-2012-290, Dec 2012.

[41] T. Mertens, "Intrabeam scattering in the LHC," Ph.D. dissertation, Porto U., Porto, 2011, presented 17 Jun 2011.

[42] S. Karlheinz, "Space Charge," Introductory CERN Accelerator School, 2006.

[43] G. Rumolo, "Beam Instabilities," Intermediate CERN Accelerator School, 2011.

[44] L. Palumbo and M. Migliorati, "Landau Damping," Advanced CERN Accelerator School, Chios, Greece, 2011.

[45] H. Schmickler and M. Lonza, "Multibunch Feedback Systems," Advanced CERN Accelerator School, Chios, Greece, 2011.

[46] E. Métral, "Longitudinal Bunched-Beam Coherent Modes: from Stability to Instability and Inversely," CERN, Geneva, Tech. Rep. CERN-AB-2004-002-ABP, Jan 2004.

[47] E. Métral, "Stability Criterion for the Longitudinal Mode-Coupling Instability in the Presence of Both Space-Charge and Resonator Impedances," CERN, Geneva, Tech. Rep. CERN-PS-2001-063-AE, Oct 2001.

[48] T. Bohl, A. Hofmann, T. P. R. Linnecar, E. Shaposhnikova, and J. Tückmantel, "Energy loss of a single bunch in the SPS," CERN, Geneva, Tech. Rep. AB-Note-2004-017, Mar 2004.

[49] T. Argyropoulos, T. Bohl, A. Burov, R. Calaga, L. Ficcadenti, E. Metral, N. Mounet, T. Mastoridis, J. Esteban Muller, V. Kain, G. Papotti, F. Roncarolo, and E. Shaposhnikova, "Studies of the LHC impedance at injection energy," Tech. Rep. CERN-ATS-2012-060 MD, Jul 2012.

[50] F. J. Sacherer, "Single-beam collective phenomena: transverse II Bunched beams," 1st International School on Particle Accelerators, 1977.

[51] M. Sands and J. Rees, "A Bench Measurement of the Energy Loss of a Stored Beam to a Cavity," Lawrence Berkeley Nat. Lab., Berkeley, CA, Tech. Rep. LBL-PEP-NOTE-95. PEP-95. SLAC-TN-2005-051, Aug 1974.

[52] R. L. Gluckstern and R. Li, "Analysis Of Coaxial Wire Measurement Of Longitudinal Coupling impedance," *Part. Accel.*, vol. 29, no. DOE-ER-10666-1. CONF-890803-7, pp. 159–166. 8 p, 1989.

[53] V. G. Vaccaro, "Coupling impedance measurements: an improved wire method," INFN, Rome, Tech. Rep. INFN-TC-94-023, Nov 1994.

[54] H. Hahn, "Interpretation of Coupling Impedance Bench Measurements," *Phys. Rev. ST Accel. Beams*, vol. 7, p. 012001, Jan 2004. [Online]. Available: http://link.aps.org/doi/10.1103/PhysRevSTAB.7.012001

[55] H. Hahn, "Validity of coupling impedance bench measurements," *Phys. Rev. ST Accel. Beams*, vol. 3, p. 122001, Dec 2000. [Online]. Available: http://link.aps.org/doi/10.1103/PhysRevSTAB.3.122001

[56] E. Jensen, "An improved log-formula for homogeneously distributed impedance," CERN, Geneva, Tech. Rep. CERN-PS-RF-NOTE-2000-001, Jan 2000.

[57] H. Tsutsui, "On single wire technique for transverse coupling impedance measurement," CERN, Geneva, Tech. Rep. SL-Note-2002-034-AP, Oct 2002.

[58] "Ansoft HFSS `http://www.ansys.com`."

[59] "Ansys Maxwell `http://www.ansys.com`."

[60] T. Kroyer, "Simulation of the low-frequency collimator impedance," CERN, Geneva, Tech. Rep. CERN-AB-Note-2008-017, Apr 2008.

[61] B. Salvant, N. Mounet, C. Zannini, E. Métral, and G. Rumolo, "Quadrupolar Transverse Impedance of Simple Models of Kickers," Tech. Rep. CERN-ATS-2010-076, Jun 2010.

[62] C. Zannini, G. Rumolo, and V. Vaccaro, "Effect of the Tem Mode on the kicker Impedance," CERN, Geneva, Tech. Rep. CERN-ATS-2012-134, May 2012.

[63] M. Masullo, V. Vaccaro, and M. Panniello, "The Stretched Wire Method: A Comparative Analysis Performed by Means of the Mode Matching Technique," in *LINAC'10*, no. THP081, Napoli, Italy, May 2010.

[64] I. Zagorodnov and T. Weiland, "TE/TM field solver for particle beam simulations without numerical Cherenkov radiation," *Phys. Rev. ST Accel. Beams*, vol. 8, p. 042001, Apr 2005.

[65] Y.-H. Chin, "User's guide for ABCI version 9.4 (Azimuthal beam cavity interaction) and introducing the ABCI Windows application package," Tech. Rep., 2005.

[66] "CST Microwave Studio `http://www.cst.com`."

[67] T. Weiland, M. Bartsch, U. Becker, M. Bihn, U. Blell *et al.*, "MAFIA Version 4," *AIP Conf.Proc.*, vol. 391, pp. 65–70, 1997.

[68] "https//:www.gdfidl.de."

[69] C. Ng, V. Akcelik, A. Candel, S. Chen, N. Folwell, L. Ge, A. Guetz, H. Jiang, A. Kabel, K. Ko, L. Q. Lee, Z. Li, E. Prudencio, G. Schussman, R. Uplenchwar, and L. Xiao, "State of the Art in EM Field Computation," Tech. Rep. SLAC-PUB-12020, Sep 2006.

[70] O. Kononenko and A. Grudiev, "Transient beam-loading model and compensation in Compact Linear Collider main linac," *Phys. Rev. ST Accel. Beams*, vol. 14, p. 111001, Nov 2011.

[71] B. Podobedov and S. Krinsky, "Transverse impedance of axially symmetric tapered structures," *Phys. Rev. ST Accel. Beams*, vol. 9, p. 054401, May 2006.

[72] F. Ruggiero, "Single-beam collective effects in the LHC," *Part. Accel.*, vol. 50, no. CERN-SL-95-09-AP. LHC-NOTE-313. CERN-LHC-Note-313, pp. 83–104. 21 p, Feb 1995.

[73] B. Salvant, H. Day, A. Grudiev, O. Kononenim, and E. Métral, "CST Simulations of VMTSA." Geneva: Presented at 03/04/2012 LRRF Task Force Meeting. Available at http://emetral.web.cern.ch/emetral/LRFF/LRFF20meetings.htm, April 2012.

[74] F. Caspers, G. Dôme, C. González, E. Jensen, E. Keil, M. Morvillo, F. Ruggiero, G. Schröder, B. W. Zotter, and M. Dyachkov, "RF screening by thin resistive layers," Tech. Rep. LHC-Project-Report-300. CERN-LHC-Project-Report-300, Apr 1999.

[75] T. Kroyer, F. Caspers, and E. Gaxiola, "Longitudinal and Transverse Wire Measurements for the Evaluation of Impedance Reduction Measures on the MKE Extraction Kickers," CERN, Geneva, Tech. Rep. AB-Note-2007-028. CERN-AB-Note-2007-028, Jul 2007.

[76] H. Klingbeil, "Ferrite Cavities," RF for Accelerators, CERN Accelerator School, 2010.

[77] R. Schmidt, R. W. Assmann, E. Carlier, B. Dehning, R. Denz, B. Goddard, E. B. Holzer, V. Kain, B. Puccio, B. Todd, J. Uythoven, J. Wenninger, and M. Zerlauth, "LHC Machine Protection," no. LHC-PROJECT-Report-1053. CERN-LHC-PROJECT-Report-1053, p. 5 p, 2007.

[78] S. Radaelli, "Introduction from LHC Collimation." Geneva: Presented at the LHC Collimation Review 2011, 14th-15th June 2011., June 2011.

[79] M. Zerlauth, "Machine Protection." Geneva: Presented at Chamonix 2012 LHC Performance Workshop, February 2012.

[80] A. Bertarelli, G. Arnau Izquierdo, F. Carra, A. Dallocchio, M. Gil Costa, and N. Mariani, "Research and development of novel advanced materials for next-generation collimators," Tech. Rep. CERN-ATS-2011-224, Nov 2011.

[81] A. Bertarelli, "Preliminary Results of advanced material tests using sample holder." Geneva: Presented at 15th October 2012 Meeting of the Collimator Working Group, CERN, October 2012.

[82] E. Métral, F. Caspers, A. Grudiev, T. Kroyer, B. Zotter, F. Roncarolo, and B. Salvant, "Impedance Studies for the Phase 2 LHC Collimators," Tech. Rep. CERN-ATS-2009-040, Sep 2009.

[83] G. Valentino, R. Aßmann, R. Bruce, S. Redaelli, A. Rossi, N. Sammut, and D. Wollmann, "Semiautomatic beam-based LHC collimator alignment," *Phys. Rev. ST Accel. Beams*, vol. 15, p. 051002, May 2012.

[84] G. Valentino, "Preliminary Results from SPS BPM-equipped Collimator MDs." Geneva: Presented at 26th November 2012 Meeting of the Collimator Working Group, CERN, November 2012.

[85] A. Dallocchio, A. Bertarelli, C. Boccard, F. Carra, M. Gasior, L. Gentini, and M. A. Timmins, "LHC Collimators with Embedded Beam Position Monitors: A New Advanced Mechanical Design," no. CERN-ATS-2011-228, p. 4 p, Nov 2011.

[86] B. Salvant, "Beam induced heating." Geneva: Presented at Evian LHC Beam Operation Workshop, December 2011.

[87] B. Salvant, "TCTP Impedance simulated with CST." Geneva: Presented at 17th October 2011 Impedance Meeting, CERN, October 2011.

[88] "`http://www.ansys.com/`."

[89] F. Carra, "Choice of material for the TCTP ferrite supports." Geneva: Presented at 1st October 2012 Meeting of the Collimator Working Group, CERN, October 2012.

[90] "TT2-111R data sheet available at `http://www.trans-techinc.com/products_detail.asp?ID=151`."

[91] M. Barnes, "Injection and Extraction Magnets," Magnets, CERN Accelerator School, 2009.

[92] H. Day, M. Barnes, F. Caspers, E. Métral, B. Salvant, C. Zannini, and R. Jones, "Coaxial wire measurements of ferrite kicker magnets," Tech. Rep. CERN-ATS-2011-275, Oct 2011.

[93] M. J. Barnes, F. Caspers, T. Kroyer, E. Métral, F. Roncarolo, and B. Salvant, "Measurement of the longitudinal and transverse impedance of kicker magnets using the coaxial wire method," Tech. Rep. CERN-ATS-2009-018, Jul 2009.

[94] M. J. Barnes, F. Caspers, K. Cornelis, L. Ducimetière, E. Mahner, G. Papotti, G. Rumolo, V. Senaj, and E. Shaposhnikova, "Measurement and analysis of SPS kicker magnet heating and outgassing with Different Bunch Spacing," Tech. Rep. CERN-ATS-2009-017, Jul 2009.

[95] C. Belver-Aguilar, A. Faus-Golfe, M. J. Barnes, F. Toral, and I. Podadera, "Beam impedance study of the stripline kicker for the CLIC damping ring," CERN, Geneva, Tech. Rep. CERN-ATS-2012-222, Aug 2012.

[96] B. Salvant, N. Mounet, C. Zannini, G. Arduini, O. Berrig, F. Caspers, A. Grudiev, E. Métral, G. Rumolo, E. Shaposhnikova, B. Zotter, M. Migliorati, and B. Spataro, "Update of the SPS Impedance Model," Tech. Rep. CERN-ATS-2010-077, Jun 2010.

[97] L. Ducimetière, N. Garrel, M. J. Barnes, and G. D. Wait, "The LHC injection kicker magnet," no. LHC-Project-Report-655. CERN-LHC-Project-Report-655, p. 4 p, Jun 2003.

[98] G. Arduini, T. Bohl, F. Caspers, E. H. Gaxiola, T. Kroyer, M. Timmins, L. Vos, and J. Uythoven, "Beam Induced Heating of the SPS Fast Pulsed Magnets," no. CERN-AB-2004-038, 2004, revised version submitted on 2004-09-29 09:29:30.

[99] L. Vos, "Beam Screens in the LHC Injection Kicker Magnets?" CERN, Geneva, Tech. Rep. LHC-Project-Note-131, Feb 1998.

[100] L. Ducimetière, U. Jansson, G. Schröder, E. B. Vossenberg, M. J. Barnes, and G. D. Wait, "Design of the injection kicker magnet system for CERN's 14 TeV proton collider LHC," CERN, Geneva, Tech. Rep. CERN-SL-95-80 BT. LHC-NOTE-337. TRI-PP-95-50. CERN-LHC-Note-337, Aug 1995.

[101] M. J. Barnes, F. Caspers, L. Ducimetière, N. Garrel, and T. Kroyer, "An Improved Beam Screen for the LHC Injection Kickers," Tech. Rep. LHC-PROJECT-Report-1029. CERN-LHC-PROJECT-Report-1029, 2007.

[102] F. Caspers, C. González, H. Tsutsui, and M. Dyachkov, "Impedance Measurements on the LHC Injection Kicker Prototype," CERN, Geneva, Tech. Rep. LHC-PROJECT-NOTE-219, Mar 2000, revised version number 1 submitted on 2000-03-17 14:16:47.

[103] F. Caspers and A. Mostacci, "Bench measurements of the LHC injection kicker low frequency impedance properties," CERN, Geneva, Tech. Rep. SL-Note-2002-030-AP, Oct 2002.

[104] M. Barnes, "MKI Vacuum and Temperature." Geneva: Presented at 25th October 2012 Meeting of the MKI Strategy Meeting, CERN, October 2012.

[105] B. Goddard, "MKI heating 2011 – more observations." Geneva: Presented at 2nd February 2012 Meeting of the MKI Strategy Meeting, CERN, February 2012.

[106] M. J. Barnes, L. Ducimetière, N. Garrel, B. Goddard, V. Mertens, and W. Weterings, "Analysis of ferrite heating of the LHC injection kickers and proposals for future reduction of temperature," CERN, Geneva, Tech. Rep. CERN-ATS-2012-211, Aug 2012.

[107] M. Garlasche, "MKI heating 2011 – more observations." Geneva: Presented at 2nd August 2012 Meeting of the MKI Strategy Meeting, CERN, August 2012.

[108] M. Barnes and P. Adrakata, "Electric Field on Surface of Ceramic and Cr2O3." Geneva: Presented at 31st October 2012 Meeting of the MKI Strategy Meeting, CERN, October 2012.

[109] M. Barnes, W. Weterings, and V. Namora, "MKI Tank#12, Inside, Emissivity." Geneva: Presented at 27th November 2012 Meeting of the MKI Strategy Meeting, CERN, November 2012.

[110] M. Garlasche, "MKI heating 2011 – more observations." Geneva: Presented at 12th November 2012 Meeting of the MKI Strategy Meeting, CERN, November 2012.

[111] M. Barnes and L. Ducimetière, "3rd MKI Strategy Discussion: 20/02/2012 Vacuum, Ferrite, Cooling, Beam Impedance and Pre-Scrubbing." Geneva: Presented at 20th February 2012 Meeting of the MKI Strategy Meeting, CERN, February 2012.

[112] M. Barnes and W. Weterings. Geneva: Presented at 11th May 2012 Meeting of the MKI Strategy Meeting, CERN, May 2012.

[113] M. Barnes and W. Weterings, "Emissivity of MKI Tank." Geneva: Presented at 16th March 2012 Meeting of the MKI Strategy Meeting, CERN, March 2012.

[114] M. Barnes, "8th MKI Strategy Meeting." Geneva: Presented at 11th July 2012 Meeting of the MKI Strategy Meeting, CERN, July 2012.

[115] M. Barnes. Geneva: Presented at 2nd August 2012 Meeting of the MKI Strategy Meeting, CERN, August 2012.

[116] M. Barnes, "Electric Field on Surface of Ceramic." Geneva: Presented at 15th November 2012 Meeting of the MKI Strategy Meeting, CERN, November 2012.

[117] O. Brüning, "Update of required beam characteristics at injection energy in LHC." Geneva: Presented at 30th March 2012 HL-LHC/LIU Joint Workshop, CERN, March 2012.

[118] M. Garlasche, "MKI Thermal Behaviour." Geneva: Presented at 27th November 2012 Meeting of the MKI Strategy Meeting, CERN, November 2012.

[119] M. Pivi, "Overview of HOM Damping at PEPII." Geneva: Presented at 18th April 2012 Meeting of the ICE section, CERN, April 2012.

[120] E. Métral, "Longitiudinal Beam Dynamics," Joint Universities Accelerator School, 2013.

[121] J. Le Duff, "Longitiudinal Beam Dynamics," Introductory CERN Accelerator School, 2010.

[122] F. Tecker, "Longitiudinal Beam Dynamics," Intermediate CERN Accelerator School, 2011.

[123] B. Holzer, "Transverse Beam Dynamics," Introductory CERN Accelerator School, 2010.

[124] D. Nagle, E. A. Knapp, and B. C. Knapp, "Coupled Resonator Model for Standing Wave Accelerator Tanks," *Review of Scientific Instruments*, vol. 38, no. 11, pp. 1583–1587, Nov.

[125] M. Garlasche and A. Bertarelli, "Dealing with ferrite heating: Figures of Merit and design guidelines." Geneva: Presented at 20/11/2012 LRRF Task Force Meeting. Available at `http://emetral.web.cern.ch/emetral/LRFF/LRFF20meetings.htm`, November 2012.

[126] C. Hargreaves, "Electromagnetic proximity effects and their consequences for radiative shielding." Eindhoven, Netherlands: Presented at the Fifth Internation Cryogenic Engineering Conference 1st January, 1975, January 1974.

[127] H. Tsutsui, "Resistive wall impedance of an LHC collimator," CERN, Geneva, Tech. Rep. LHC-PROJECT-NOTE-318, Jul 2003.

Appendix A

Beam Dynamics

In this appendix we shall introduce briefly the basics of transverse and longitudinal beam dynamics of charged particles in a synchrotron.

A.1 Longitudinal Beam Dynamics

In this section we shall define some key parameters of longitudinal motion to aid understanding of the effects of wakefields on particle beams. This text follows closely the introductions to longitudinal motion given by Métral [120] and Le Duff [121]. A significant parameter in the case of longitudinal dynamics and RF control is the parameter known as the momentum compaction factor. This is defined relating the variation in the closed orbit with momentum. For example, if we consider a nominal closed orbit in a circular accelerator of length C, defined for a particle of momentum p. For a particle with a momentum deviation Δp which gives a orbit length variation ΔC, they are related to one another by

$$\frac{\Delta C}{C} = \alpha_p \frac{\Delta p}{p} \tag{A.1}$$

assuming that the bending field B is constant. In this case $C = 2\pi R$ where R is the average radius of the closed orbit. This maybe related by infinitessimal changes to give

$$\alpha_p = \frac{\frac{dC}{C}}{\frac{dp}{p}} = \frac{\frac{dR}{R}}{\frac{dp}{p}} \tag{A.2}$$

and related to the dispersion of the optics and the bending radius ρ

$$\alpha_p = \frac{1}{C}\int_C \frac{D_x(s)}{\rho(s)} ds. \tag{A.3}$$

For most circular machines α_p is positive, i.e. higher momentum means longer circumference of the orbit. To relate the momentum compaction to the particle energy, it can be seen that

$$E = \frac{pc}{\beta} \rightarrow \frac{dE}{E} = \beta^2 \frac{dp}{p} \tag{A.4}$$

which substituting into Eqn. A.2 gives

$$\alpha_p = \beta^2 \frac{E}{R}\frac{dR}{dE}. \tag{A.5}$$

For a machine with a positive momentum compaction, there are two relationships:

1. a momentum larger than nominal results in an increased circumference of the orbit
2. a momentum larger than nominal results in an increase in velocity

If we consider what happens to the revolution frequency, we can see that at low energies, the velocity increases faster than C. At high energies, $v \approx c$ and remains almost constant, thus increases slower than C. There is an energy for which the velocity increase is compensated for by the increase in circumference, i.e. the revolution frequency doesn't change with increasing momentum. This is called the transition energy. Below this energy (below transition) increasing the energy of the particles results in a higher revolution frequency. Above the energy (above transition) increasing the energy of the particles results in a lower revolution frequency.

An additional useful factor to define is the slip factor η, defined as the revolution frequency spread per unit of momentum spread

$$\eta = \frac{\frac{df_{res}}{f_{res}}}{\frac{dp}{p}} = \frac{\frac{d\omega_{res}}{\omega_{res}}}{\frac{dp}{p}}. \tag{A.6}$$

Considering that $f_{res} = v/C$, if follows that

$$\frac{df}{f} = \frac{d\beta}{\beta} - \frac{dC}{C} \tag{A.7}$$

and similarly following from $p = \frac{mc\beta}{\sqrt{1-\beta^2}}$ is can be seen that

$$\frac{d\beta}{\beta} = \frac{1}{\gamma^2}\frac{dp}{p} \tag{A.8}$$

which when considering Eqn. A.2 leads to

$$\frac{df_{res}}{f_{res}} = \left(\frac{1}{\gamma^2} - \alpha_p\right)\frac{dp}{p} = \eta\frac{dp}{p}. \tag{A.9}$$

The transition energy is the energy for which $\eta = 0$, given by the relativistic γ factor at transition γ_{tr}

$$\gamma_{tr} = \sqrt{\frac{1}{\alpha_p}}. \tag{A.10}$$

Thus

$$\eta = \frac{1}{\gamma^2} - \frac{1}{\gamma_{tr}^2}. \tag{A.11}$$

It's thus seen that for particles above transition $\eta < 0$ and below transition $\eta > 0$.

A.1.1 Longitudinal Equations of Motion

Here shall be given a brief overview of the longitudinal equations of motion of a non-synchronous particle in an RF bucket. The momentum offset and the particles phase can be given by

$$\frac{d\left(\Delta p\right)}{dt} = A\left(sin\phi - sin\phi_s\right) \tag{A.12}$$

$$\frac{d\phi}{dt} = B\Delta p \tag{A.13}$$

where $A = (e\vec{V}_{rf})/(2\pi r_s)$ and $B = -(\eta h)/(p_s)(\beta_s c)/(r_s)$ where r is the particle orbit radius, $\vec{V}_{rf}$ is the peak RF voltage, h is the RF harmonic and the subscript s denotes the synchronous particle. Combining the above two equations we get to

$$\frac{d}{dt}\left(\frac{1}{B}\frac{d\phi}{dt}\right) - A\left(sin\phi - sin\phi_s\right) = 0. \tag{A.14}$$

If it is assumed that A and B change much more slowly than $\Delta\phi = \phi - \phi_s$, i.e. that significant acceleration occurs on a longer timescale than synchrotron oscillations, then this can be rewritten as

$$\frac{d^2\phi}{dt^2} + \frac{\Omega_s^2}{cos\phi_s}\left(sin\phi - sin\phi_s\right) = 0 \tag{A.15}$$

where

$$\frac{\Omega_s^2}{cos\phi_s} = -AB = \Omega_0^2 = \frac{e\vec{V}_{rf}\eta h c^2}{2\pi r_s^2 E_s}. \tag{A.16}$$

Subsequently we can make what is known as the small amplitude approximation, such that $\phi = \phi_s + \Delta\phi$. In this case it follows that

$$sin\phi = sin\left(\phi_s + \Delta\phi\right) \tag{A.17}$$

$$= sin\phi_s cos\Delta\phi + cos\phi_s sin\Delta\phi \tag{A.18}$$

$$\approx sin\phi_s + cos\phi_s\Delta\phi. \tag{A.19}$$

Similarly it can be seen that

$$\frac{d\phi}{dt} = 0 \Rightarrow \frac{d^2}{dt^2} = \frac{d^2}{dt^2}\left(\phi_s + \Delta\phi\right) = \frac{d^2\Delta\phi}{dt^2} \tag{A.20}$$

which subsequently leads to small amplitude approximation of Eqn. A.15

$$\frac{d^2\Delta\phi}{dt^2} + \Omega_s^2\Delta\phi = 0. \tag{A.21}$$

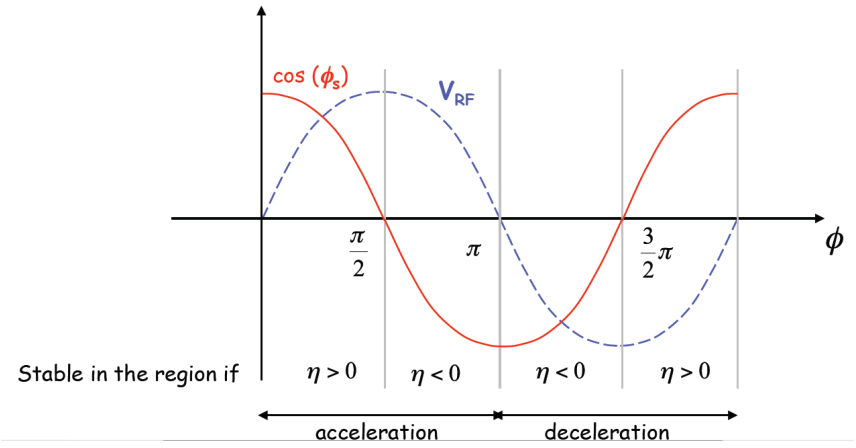

Figure A.1: The focusing synchronous phase positions for a particle below (P_1) and above (P_2) transition. The synchronous phase is chosen for a given particle energy and desired behaviour, and an off-momentum particle will be longitudinally focused to the synchronous phase by the RF system if the correct phase is chosen. This occurs due to balance of increased velocity with an increased size of orbit as a particle is accelerated by the RF electric field. Taken from [122].

Ω_s is known as the synchrotron frequency, in this case of the harmonic oscillator represented by the non-synchronous particle. For most accelerators, stability is obtained when $\Omega_s^2 > 0$. Ω_s^2 is given by

$$\Omega_s^2 = \frac{e\vec{V}_{rf}\eta hc^2}{2\pi r_s E_s} cos\phi_s \Rightarrow \Omega_s^2 > 0 \Leftrightarrow \eta cos\phi_s > 0. \tag{A.22}$$

This condition is due to an effect known as phase stability, wherein the stable phase of a particle relative to the RF phase is dependent on whether it is above or below transition. The stability of the particle oscillations relative to the RF phase are shown in Fig. A.1. It is interesting to note that when the particles cross the transition energy the stable phase changes drastically. In this case complex RF gymnastics are required to cross transition and remain stable.

A.1.2 RF Acceptance and Longitudinal Emittance

To examine longitudinal motion of bunches it is often easier to work with the conserved longitudinal quantities, as is the case with the transverse plane. This is given by the

mutiplying Eqn. A.15 by $\frac{d\phi}{dt}$ and then integrating with respect to ϕ. This gives

$$\frac{1}{2}\left(\frac{d\phi}{dt}\right)^2 - \frac{\Omega_s^2}{cos\phi_s}\left(cos\phi_\phi sin\phi_s\right) = constant. \tag{A.23}$$

This equation defines a constant of motion in longitudinal dynamics known as the longitudinal emittance. In addition there is a limited area of stability of an non-synchronous particle within the phase space, the boundary referred to as the seperatrix. The area of this seperatrix is dependent on the synchronous phase ϕ_s. This area is largest when $\phi_s = 0$ or $\pm\pi$, i.e. when there is no acceleration of the particles. This is normally the case during injection or extraction of beam to capture as much of the beam as possible during transfer. As acceleration is made stronger and stronger the stable phase space is reduced until reaching a minimum (area of 0) when $\phi_s = \pi/2$. An example above transition is shown in Fig. A.2.

A.2 Linear Transverse Dynamics

Here we shall introduce the basics of linear transverse beam dynamics. This introduction follows the formalism introduced in [123]. If we consider a charged particle of mass m and charge e moving with velocity v along the ideal orbit under the effect of the magnetic field B we can see that the Lorentz force ($F_L = qvB$) and the centrifugal force ($F_{cen} = \frac{\gamma m v^2}{\rho}$) are equal, leading to the relation

$$\frac{p}{e} = B\rho \tag{A.24}$$

where p is the particles momentum. $B\rho$ is referred to as the beam rigidity, denoting the constant term necessary to keep a particle on the ideal orbit.

If we consider the motion of a particle transversally displaced from the ideal orbit particle with a position (x, y) we must consider the variation of the magnetic field in the transverse directions. If we consider first just the horizontal motion, we can carry out a Taylor expansion of the field which gives us

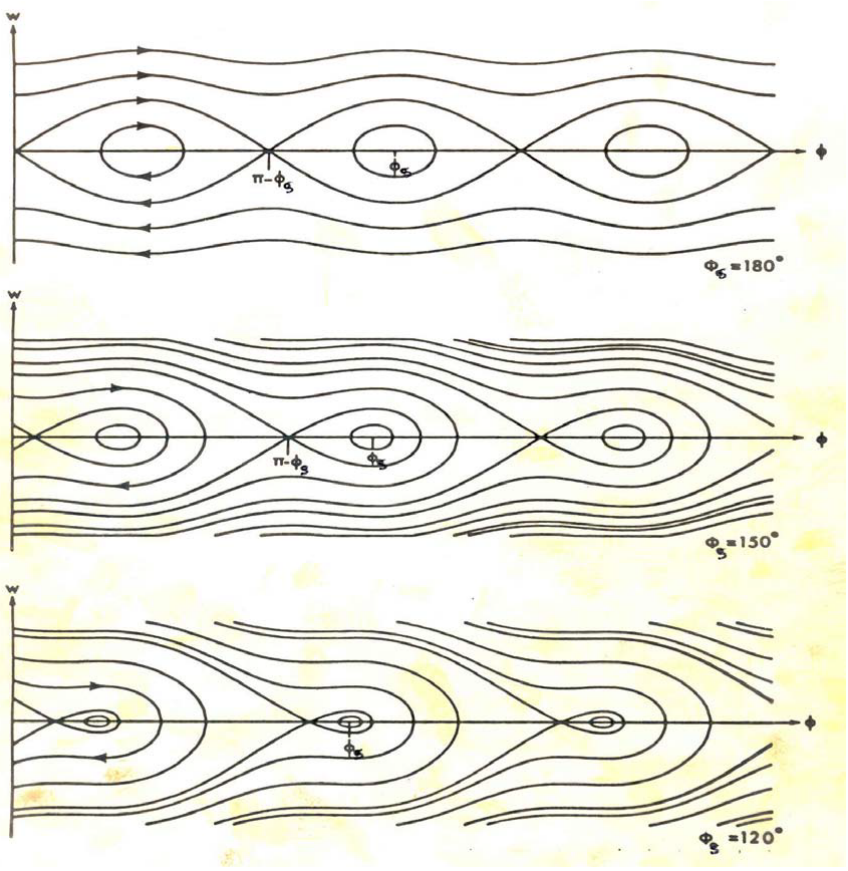

Figure A.2: The seperatrix for different synchronous phase values. Note that the acceptance decreases as $\phi_s \to \pi/2$. Taken from [121].

$$B_y(x) = B_{y0} + \frac{dB_y}{dx}x + \frac{1}{2!}\frac{d^2B_y}{dx^2}x^2 + \frac{1}{3!}\frac{d^3B_y}{dx^3}x^3 + ... \tag{A.25}$$

which is then normalised by p/e

$$\frac{B_y(x)}{p/e} = \frac{B_{y0}}{B_{y0}\rho} + \frac{1}{p/e}\frac{dB_y}{dx}x + \frac{1}{p/e}\frac{1}{2!}\frac{d^2B_y}{dx^2}x^2 + \frac{1}{p/e}\frac{1}{3!}\frac{d^3B_y}{dx^3}x^3 + ... \tag{A.26}$$

For the time being we shall consider only small displacements in x and y, thus shall consider only the linear terms, giving

$$\frac{B_y(x)}{p/e} = \frac{1}{\rho} + \frac{1}{p/e}\frac{dB_y}{dx}x \tag{A.27}$$

$$\frac{B_y(x)}{p/e} = \frac{1}{\rho} + k_f x \tag{A.28}$$

where $k_f = \frac{g}{p/e}$, g is the gradient of a quadrupole magnet (a magnet which has a magnetic field strength linearly proportional to displacement). This indicates that seperation of the function of magnets is a valid method of controlling the particles, using dipole and quadrupole fields. Next, to derive the equations of motion we shall consider the equation for radial acceleration a_r for a particle undergoing rotational acceleration in the defined coordinate system

$$a_r = \frac{d^2\rho}{dt^2} - \rho\left(\frac{d\theta}{dt}\right)^2. \tag{A.29}$$

For the particle on the ideal orbit $\rho = constant$, so $\frac{d\rho}{dt} = 0$, leading to the accelerative force being derived to be

$$F_x = m\rho\left(\frac{d\theta}{dt}\right)^2 = m\rho\omega^2 = \frac{mv^2}{\rho} \tag{A.30}$$

For a general particle, $\rho \to \rho + x$, leading to

$$F_x = m\frac{d^2}{dt^2}(x+\rho) - \frac{mv^2}{x+\rho} = eB_y v. \tag{A.31}$$

As $\rho = constant$, $\frac{d^2}{dt^2}(x+\rho)$ becomes $\frac{d^2x}{dt^2}$. In addition we are dealing with displacements of $x \ll \rho$, so we may approximate $\frac{1}{x+\rho} \approx \frac{1}{\rho}(1-\frac{x}{\rho})$ from the Taylor expansion and taking linear terms in x. Thus we acquire the equation

$$m\frac{d^2x}{dt^2} - \frac{mv^2}{\rho}\left(1-\frac{x}{\rho}\right) = eB_y v. \tag{A.32}$$

Subsequently we subsitute the magnetic field $B_y = B_{y0} + \frac{dB_y}{dx}x$ and arrive at

$$m\frac{d^2x}{dt^2} - \frac{mv^2}{\rho}\left(1-\frac{x}{\rho}\right) = ev\left[B_{y0} + \frac{dB_y}{dx}x\right]. \tag{A.33}$$

By dividing throught by the mass m

$$\frac{d^2x}{dt^2} - \frac{v^2}{\rho}\left(1-\frac{x}{\rho}\right) = \frac{evB_{y0}}{m} + \frac{ev}{m}\frac{dB_y}{dx}x. \tag{A.34}$$

Next we transform the coordinate from $t \rightarrow z$, such that

$$\frac{d^2x}{dt^2} = \frac{d}{dt}\left(\frac{dx}{dz}\frac{dz}{dt}\right) = \frac{d}{dz}\left(\frac{dx}{dz}\frac{dz}{dt}\right)\frac{dz}{dt} = \frac{d^2x}{dz^2}\left(\frac{dz}{dt}\right)^2 + \frac{dx}{dz}\frac{d}{dz}\left(\frac{dz}{dt}\right)\frac{dz}{dt}. \tag{A.35}$$

It can be seen that $\frac{dz}{dt} = v$, which is kept constant in this treatment. Therefore

$$\frac{d^2x}{dt^2} = \frac{d^2x}{dz^2}v^2. \tag{A.36}$$

Thus we arrive at the equation

$$\frac{d^2x}{dz^2}v^2 - \frac{v^2}{\rho}\left(1-\frac{x}{\rho}\right) = \frac{evB_{y0}}{m} + \frac{ev}{m}\frac{dB_y}{dx}x. \tag{A.37}$$

We then subsequently normalise by momentum and rearrange slightly to acquire

$$\frac{d^2x}{dz^2} - \frac{1}{\rho} + \frac{x}{\rho^2} = \frac{B_{y0}}{p/e} + \frac{1}{p/e}\frac{dB_y}{dx}x. \tag{A.38}$$

We then remember the definition of the beam rigidity (see Eqn. A.24) and the definition of the quadrupolar field strength arriving at

$$\frac{d^2x}{dz^2} - \frac{1}{\rho} + \frac{x}{\rho^2} = -\frac{1}{\rho} + k_f x$$
$$\frac{d^2x}{dz^2} + \frac{x}{\rho^2} = k_f x$$
$$\frac{d^2x}{dz^2} + x\left(\frac{1}{\rho^2} - k_f\right) = 0. \tag{A.39}$$

For the vertical plane the equation is the same, except that the focusing term is negative and there is no ρ term, giving

$$\frac{d^2y}{dz^2} + k_f y = 0. \tag{A.40}$$

It is interesting to note that there is a focusing term due to the dipolar magnet term. Historically this is the weak focusing effect, as opposed to the strong focusing regime of using quadrupole magnets. It can be seen that these equations are simply the equations of motion of a pseudo-harmonic oscillator with spring constants $K_{x/y}$ given by

$$K_x = \frac{1}{\rho^2} - k_f$$
$$K_y = k_f$$

leading to a general solution

$$x/y\,(s) = a_1 cos\left(\sqrt{K_{x/y}}s\right) + a_2 sin\left(\sqrt{K_{x/y}}s\right). \tag{A.41}$$

For a modern particle accelerator using focusing and defocusing magnets arranged in a periodic lattice (i.e. so that $k(s)$ becomes a periodic function such that $k_f(s+L) = k_f(s)$ where L is the length of the period of the lattice), and applying initial conditions $x(0) = x_0, x^{'}(0) = x_0^{'}$ it is possible to finally arrive at the solution for the motion of a particle through a periodic lattice

$$x\,(s) = \sqrt{\epsilon}\sqrt{\beta\,(s)}cos\left(\psi\,(s) + \phi\right) \tag{A.42}$$

where ϵ and ϕ are integration constants determined by the initial conditions, $\beta(s)$ is a periodic function determined by the focusing properties of the lattice. $\psi(s)$ is the phase advance of the oscillation, again determined by the lattice design parameters. These parameters define beam parameters, ϵ being the beam emittance, the preserved quantity in transverse phase space, β the betatron function, which is a property of the lattice and determines the physical size of the beam. One key important figure acquired from this derivation is the tune (also called the betatron tune) of the accelerator, that is the number of betatron oscillations per turn, given by

$$Q_0 = \frac{1}{2\pi} \oint \frac{ds}{\beta\left(s\right)}. \tag{A.43}$$

Off-Momentum Particles

During the operation of a particle accelerator there is often have a spread of particle energies due to dynamics in the longitudinal plane [121]. This gives rise to a momentum spread $\Delta p/p$ in the particle momentum, where $\Delta p = p - p_0$, p_0 being the on-path momentum. When considered in Eqn. A.39 this gives rise to an inhomogenous differential equation of the form

$$\frac{d^2x}{dz^2} + x\left(\frac{1}{\rho^2} - k_f\right) = \frac{\Delta p}{p}\frac{1}{\rho} \tag{A.44}$$

which leads to a modified solution of the pseudo-harmonic oscillator equation characterised by the dispersion of the lattice $D(s)$, written as

$$x\left(s\right) = \sqrt{\epsilon}\sqrt{\beta\left(s\right)}cos\left(\psi\left(s\right) + \phi\right) + \frac{\Delta p}{p}D\left(s\right). \tag{A.45}$$

This can be seen as another closed orbit solution to the machine lattice. One side effect of this is the slight change in the tune due to the off momentum particles, characterised by a factor known as the chromaticity ζ, related by

$$\frac{\Delta Q}{Q_0} = \zeta\frac{\Delta p}{p} \tag{A.46}$$

where ΔQ is the tune shift from the lattice tune for an on momentum particle Q_0. The tune working point is an important factor in designing an accelerator, as crossing integer or low order tune fractions (half, third or quarter integer) allows the summation of kicks in the machine driving large oscillations which may ultimately lead to particle loss.

Appendix B

TCTP Eigenmode Simulations - No Ferrite

f (GHz)	Q	R/Q (Ω)	R_s (Ω)
1.023	500	0.00052	0.3
1.053	725	0.00419	3.0
1.070	609	0.00040	0.2
1.119	462	0.02717	12.6
1.127	658	0.00006	0.0
1.161	432	0.00291	1.3
1.181	436	0.00251	1.1
1.187	1070	0.00422	4.5
1.195	509	0.01165	5.9
1.235	377	0.01146	4.3
1.207	453	0.45465	205.8
1.268	500	0.00201	1.0
1.280	404	0.01590	6.4
1.282	717	0.02778	19.9
1.291	551	0.13380	73.7

f (GHz)	Q	R/Q (Ω)	R_s (Ω)
1.300	568	0.27971	158.9
1.304	434	0.26437	114.7
0.131	233	0.00017	0.0
1.313	390	0.19889	77.5
1.322	297	0.00566	1.7
1.325	282	0.00026	0.1
1.331	602	0.10319	62.1
1.341	188	0.00001	0.0
1.342	197	0.03311	6.5
1.346	111	0.00026	0.0
1.357	421	0.01681	7.1
1.363	516	0.51441	265.5
1.365	514	0.34623	178.1
1.378	772	0.00637	4.9
1.392	519	0.09893	51.4
1.396	553	0.00465	2.6
1.417	696	0.07621	53.0
1.424	679	0.06070	41.2
1.429	521	0.02521	13.1
1.445	567	0.00123	0.7
1.454	926	0.00029	0.3
1.459	572	0.00005	0.0
1.464	990	0.00001	0.0
1.476	1052	0.00006	0.1
1.479	1097	0.00002	0.0
1.487	669	0.00790	5.3
1.495	627	0.01068	6.7

f (GHz)	Q	R/Q (Ω)	R_s (Ω)
1.504	647	0.00006	0.0
1.522	597	0.00917	5.5
1.524	852	0.00020	0.2
1.554	535	0.00107	0.6
1.556	909	0.00044	0.4
1.559	931	0.00044	0.4
1.580	795	0.01642	13.0
1.587	909	0.00133	1.2
1.589	929	0.00101	0.9
1.607	716	0.00000	0.0
1.609	610	0.00448	2.7
1.612	747	0.00000	0.0
1.615	827	0.00062	0.5
1.624	646	0.00004	0.0
1.632	844	0.00000	0.0
1.636	914	0.00016	0.1
1.643	449	0.00006	0.0
1.649	845	0.00012	0.1
1.653	617	0.00347	2.1
1.680	928	0.00110	1.0
1.683	762	0.00027	0.2
1.690	593	0.00321	1.9
1.698	768	0.00002	0.0
1.709	1058	0.00000	0.0
1.711	1046	0.00810	8.5
1.716	829	0.00002	0.0
1.722	997	0.00000	0.0

f (GHz)	Q	R/Q (Ω)	R_s (Ω)
1.732	953	0.00001	0.0
1.734	760	0.00002	0.0
1.743	894	0.00018	0.2
1.744	860	0.00092	0.8
1.748	882	0.00062	0.5
1.759	773	0.00007	0.1
1.767	723	0.00021	0.2
1.780	802	0.00226	1.8
1.785	858	0.00094	0.8
1.789	942	0.00034	0.3
1.795	646	0.00301	1.9
1.800	719	0.00030	0.2
1.801	985	0.00109	1.1
1.816	670	0.00013	0.1
1.825	924	0.00019	0.2
1.829	650	0.00001	0.0
1.832	1061	0.00005	0.1
1.837	351	0.00071	0.2
1.842	367	0.00044	0.2
1.858	641	0.00249	1.6
1.869	961	0.00063	0.6
1.882	1202	0.00046	0.5
1.883	396	0.00121	0.5
1.888	857	0.00371	3.2
1.895	1100	0.00050	0.6
1.897	688	0.00570	3.9
1.903	1039	0.00007	0.1

f (GHz)	Q	R/Q (Ω)	R_s (Ω)
1.910	710	0.00000	0.0
1.920	968	0.00000	0.0
1.930	219	0.05093	11.2
1.932	189	0.09952	18.8
1.944	588	0.03731	21.9
1.948	1048	0.00053	0.6
1.952	1027	0.01573	16.2
1.959	597	0.00651	3.9
1.966	643	0.04869	31.3
1.974	724	0.00005	0.0
1.993	627	0.00039	0.2
0.200	162	0.00090	0.1
0.260	333	0.00051	0.2
0.305	250	0.00152	0.4
0.315	312	0.00002	0.0
0.383	542	0.00091	0.5
0.388	399	0.00088	0.4
0.425	214	0.00152	0.3
0.484	488	0.00308	1.5
0.514	461	0.00199	0.9
0.514	452	0.00188	0.8
0.532	232	0.00192	0.4
0.586	444	0.00004	0.0
0.614	424	0.04269	18.1
0.633	213	0.00168	0.4
0.636	249	0.00180	0.4
0.641	453	0.11620	52.7

f (GHz)	Q	R/Q (Ω)	R_s (Ω)
0.665	411	0.06443	26.5
0.715	357	0.14033	50.1
0.716	362	0.14259	51.7
0.726	292	0.03288	9.6
0.750	365	0.01933	7.1
0.753	515	0.00803	4.1
0.781	344	0.10722	36.9
0.824	661	0.00063	0.4
0.826	306	0.00198	0.6
0.829	665	0.00061	0.4
0.851	342	0.04860	16.6
0.859	478	0.04383	20.9
0.863	628	0.00014	0.1
0.874	433	0.00005	0.0
0.902	509	0.00124	0.6
0.930	406	0.00161	0.7
0.941	460	0.22196	102.1
0.945	318	0.00803	2.6
0.962	536	0.00003	0.0
0.983	360	0.02222	8.0

Appendix C

TCTP Eigenmode Simulations - With Ferrite

f (GHz)	Q	R/Q (Ω)	R_s (Ω)
1.008	7	0.14378	1.0
1.019	78	0.19377	15.2
1.027	100	0.07519	7.5
1.042	21	0.04155	0.9
1.052	306	0.00385	1.2
1.071	116	0.00176	0.2
1.074	111	0.00204	0.2
1.075	147	0.00742	1.1
1.085	92	0.03424	3.1
1.126	215	0.00021	0.0
1.133	31	0.03086	1.0
1.142	60	0.22597	13.5
1.175	67	0.00764	0.5
1.216	31	0.76573	23.6
1.227	62	0.04137	2.6

f (GHz)	Q	R/Q (Ω)	R_s (Ω)
1.240	188	0.15624	29.4
0.130	80	0.00003	0.0
1.300	126	0.23688	29.9
1.314	168	0.00333	0.6
1.371	78	0.47218	36.8
1.404	157	0.04230	6.6
1.476	33	0.00084	0.0
1.501	76	0.00781	0.6
1.507	92	0.00004	0.0
1.545	49	0.00978	0.5
1.550	105	0.01460	1.5
1.578	32	0.00014	0.0
1.613	37	0.00006	0.0
1.636	13	0.00539	0.1
1.675	65	0.00010	0.0
1.679	64	0.00006	0.0
1.715	160	0.00133	0.2
1.723	206	0.00028	0.1
1.734	116	0.00010	0.0
1.770	83	0.00143	0.1
1.782	137	0.00064	0.1
1.792	113	0.00103	0.1
1.796	110	0.00103	0.1
1.806	33	0.00003	0.0
1.840	69	0.00051	0.0
1.844	16	0.00665	0.1
1.862	51	0.00057	0.0

f (GHz)	Q	R/Q (Ω)	R_s (Ω)
1.895	113	0.00397	0.5
1.919	41	0.00341	0.1
1.926	164	0.04103	6.7
1.933	75	0.00397	0.3
1.937	123	0.00103	0.1
1.969	36	0.00131	0.0
1.973	35	0.00130	0.0
2.006	59	0.00241	0.1
0.227	1	0.00377	0.0
0.241	1	0.01920	0.0
0.251	1	0.00910	0.0
0.295	18	0.00354	0.1
0.320	11	0.00180	0.0
0.388	56	0.00293	0.2
0.405	2	0.12558	0.3
0.409	41	0.00228	0.1
0.416	1	0.11308	0.1
0.493	12	0.00335	0.0
0.504	4	0.19510	0.8
0.512	50	0.00053	0.0
0.512	50	0.00044	0.0
0.515	138	0.00727	1.0
0.547	2	0.06283	0.1
0.585	5	0.41263	2.1
0.589	5	0.45154	2.1
0.606	39	0.00195	0.1
0.625	18	0.09450	1.7

f (GHz)	Q	R/Q (Ω)	R_s (Ω)
0.636	223	0.01395	3.1
0.653	5	0.41565	2.1
0.657	2	0.12553	0.2
0.703	42	0.00036	0.0
0.750	29	0.01932	0.6
0.752	140	0.02023	2.8
0.761	5	0.38464	1.9
0.842	113	0.00376	0.4
0.855	90	0.06217	5.6
0.864	6	0.32443	1.9
0.889	2	0.14481	0.4
0.901	50	0.00105	0.1
0.924	83	0.00009	0.0
0.938	61	0.25099	15.4
0.959	14	0.13559	1.9

Appendix D

Cavity Parameters and the Calculation of Eigenmode Properties

For any cavity which possesses resonant modes, it is possible to describe it's impedance by using a set of physical parameters. Each mode may be characterised by its resonant frequency f_{res}, its quality factor Q, its shunt impedance R_s and the parameter R_s/Q. These parameters are dependent on the geometry of the structure, and the materials that make up the surfaces and volume spaces within it. It is generally possble to consider these parameters by either evaulating the fields within the structure, or by comparison to equivalent circuit model of the cavity (a simple example of which is shown in Fig. D.1. More complex circuit models exist for calculating coupled cavities [124] defined by a resistance R_s, a capacitance C and an inductance L.

The capacitance and inductance of the circuit representation are related to the resonant frequency by

$$2\pi f_{res} = \omega_{res} = \frac{1}{\sqrt{LC}}. \tag{D.1}$$

The quality factor Q is defined as

$$Q = \frac{\omega_{res} W}{P_{surf}} = R_s \sqrt{\frac{C}{L}} \tag{D.2}$$

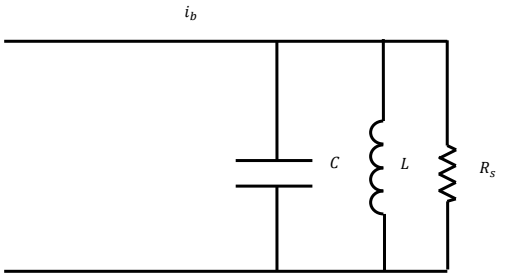

Figure D.1: The equivalent circuit model for a cavity mode with no coupling to neighbouring cavities.

considering the cavity parameters and circuit representation respectively. The shunt impedance R_s is defined as

$$R_s = \frac{V_{acc}^2}{P_{surf}} \tag{D.3}$$

where V_{acc} is the potential that a traversing particle experiences, given by

$$V_{acc} = \int_0^L E_z e^{j\omega z/c} dz. \tag{D.4}$$

A useful relationship to know regarding the quality factor is that due to the losses in the cavity being dependent on the conductivity of the wall material, for any given cavity the quality factor of a cavity made of material c, Q_c with a conductivity σ_c compared to the same cavity made from material d, with conductivity σ_d giving a quality factor Q_d, is given by

$$Q_c = \sqrt{\frac{\sigma_c}{\sigma_d}} Q_d \tag{D.5}$$

for the case where there is no significant quantity of lossy material in the structure. For cases of strong damping by the inclusion of lossy material this no longer holds true.

For any given eigenmode solution in an eigenmode solver in a computational electromagnetic solver (for instance Ansoft HFSS) the default results produced are the eigenfrequency f_{res} and the electromagnetic field pattern of the mode. Q is also given if a lossy material (either a finite conductvity or a material with dielectric or magnetic losses) is defined within the simulation volume. It is possible to calculate the R_s/Q of the resonance by evaluating the fields of the resonance, either using the internal calculator of the programme or by exporting the fields necessary and using an external script/code.

D.1 Longitudinal R_s/Q

For a structure, the longitudinal R_s/Q of the mode is defined by

$$\frac{R_s}{Q}_{\parallel} = \frac{V_{acc}^2}{\omega_{res} W} = \frac{\left| \int_{\infty}^{\infty} E_z\left(x,y,z\right) e^{j\omega_{res} z/(\beta c)} dz \right|^2}{\omega_{res} W}. \tag{D.6}$$

From HFSS we acquire a discrete field pattern due to the finite mesh, thus it is necessary to use a discrete integration method to calculate this from simulation results. The choice of algorithm for this is largely left to the user to decide.

It should be noted that the longitudinal R_s/Q is dependent on the beam displacement and path through the locale of the eigenmode, thus the beam path should be considered during the analysis, especially for devices where multiple possible beam paths exist.

D.2 Transverse R_s/Q

The transverse R_s/Q of an eigenmode can be calculated in two seperate ways. Using the similar definition of the longitudinal R_s/Q but for the transverse fields, the transverse R_s/Q for a particle displaced in the x direction (for the y-plane the field components are swapped $x \rightarrow y$, $y \rightarrow x$) is given by [34]

$$\frac{R_s}{Q}_{\perp} = \frac{c\left(\int_{\infty}^{\infty} \frac{\partial E_z(x,y,z)}{\partial z} e^{j\omega_{res} z/(\beta c)} dz \right)^2}{\omega_{res}^2 W} = \frac{\left(\int_{\infty}^{\infty} \left(E_x\left(x,y,z\right) + cB_y\left(x,y,z\right) \right) e^{j\omega_{res} z/(\beta c)} dz \right)^2}{cW}. \tag{D.7}$$

It can be seen that $(R_s/Q)_\perp$ is dependent on the transverse displacement of the beam as with $(R_s/Q)_\parallel$. For small displacements this dependence on the transverse position can be considered to be linear in non-extreme cases (i.e. far from any material boundaries/non-linear materials) and thus a transverse R/Q normalised to displacement used.

Appendix E

Ferrite Properties

There are a number of ferrites used for the damping of cavity modes in accelerator equipment, some of the details of which are given here. For the use of ferrite as a damping material, the important material properties to consider are the complex permeability $\mu_r = \mu^{'} - j\mu^{''}$, which determines the degree of damping of cavity modes, and the Curie temperature T_c which determines to which temperature the ferrite will remain effective as a damping material, important due to the significant power loss that may occur in the ferrite. Here we give examples of 3 ferrites commonly used for damping of cavity modes, and one additional ferrite that shows promise for use due to a high Curie temperature.

An additional figure of merit is the penetration depth of the ferrite. This figure determines how far the magnetic field penetrates into the ferrite, thus giving a guide as to how much ferrite is necessary to effectively damp any cavity modes. This is a frequency dependent value, given by

$$\delta(f) = \frac{c}{2\pi f} \frac{1}{\Re e\left[\sqrt{1 - \epsilon_r(f)\,\mu_r(f)}\right]}. \tag{E.1}$$

E.1 TT2-111R

TT2-111R is a ferrite made by Transtech. It is a variant of the TT2-111 ferrite with a slight conductivity to reduce the build up of electrostatic charge. TT2-111R is useful in

Table E.1: A selection of the physical properties of TT2-111R

$\epsilon^{'}$	12.5	
Conductivity	10^{-1}	S m^{-1}
T_c	375	^{oc}C

as it has a very high Curie temperature $T_c \approx 375°C$. Some material properties are shown in Tab. E.1. The complex permeability is shown in Fig. E.1(a) and the penetration depth in Fig. E.1(b).

E.2 4S60

4S60 is a ferrite made by Ferroxcube. It has a slight conductivity. Some material properties are shown in Tab. E.2. The complex permeability is shown in Fig. E.2(a) and the penetration depth in Fig. E.2(b).

E.3 4A4

4A4 is a NiZn ferrite made by Transtech. It has a mild conductivity to reduce electrostatic buildup. It is commonly used to damp cavity modes due to it's good vacuum performance. Some material properties are shown in Tab. E.3. The complex permeability is shown in Fig. E.3(a) and the penetration depth in Fig. E.3(b).

E.4 4E2

4E2 is a NiZn ferrite made by Ferroxcube. It has a mild conductivity to reduce electrostatic buildup, and holds promise as a ferrite for use for damping cavity modes where the power loss to the ferrite might be expected to cause it to heat significantly due to its high Curie temperature $T_c \geq 400°$C. Some material properties are shown in Tab. E.4. The complex permeability is shown in Fig. E.4(a) and the penetration depth in Fig. E.4(b).

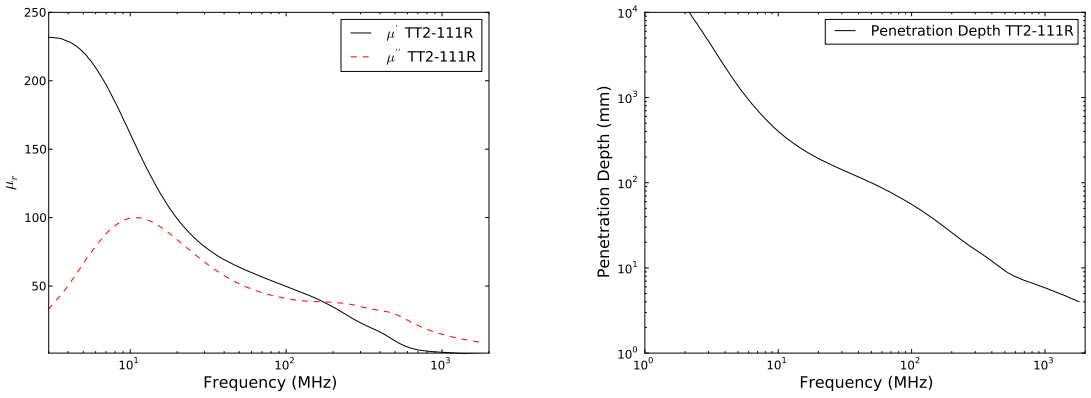

(a) (b)

Figure E.1: The permeability (a) and penetration depth (b) for TT2-111R.

Table E.2: A selection of the physical properties of 4S60

$\epsilon^{'}$	10	
Conductivity	10^{-5}	S m^{-1}
T_c	100	$^{o c}$C

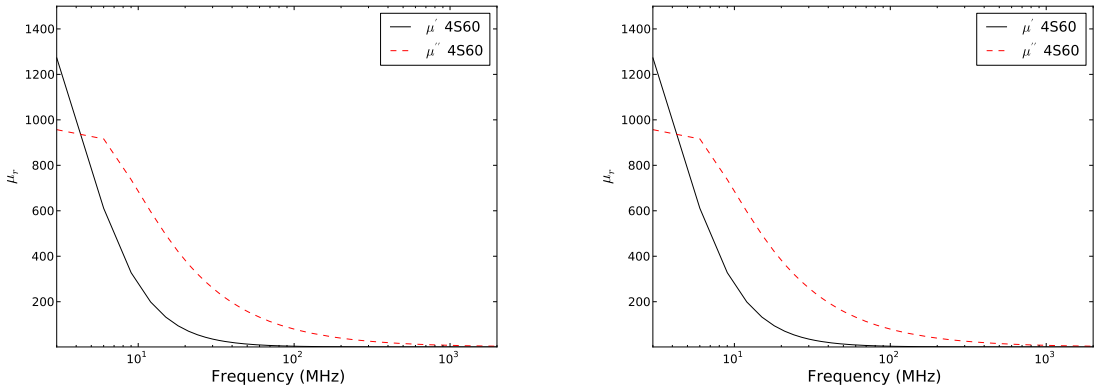

(a) (b)

Figure E.2: The permeability (a) and penetration depth (b) for 4S60.

Table E.3: A selection of the physical properties of 4A4

$\epsilon^{'}$	10	
Conductivity	10^{-6}	S m^{-1}
T_c	375	$^{o c}$C

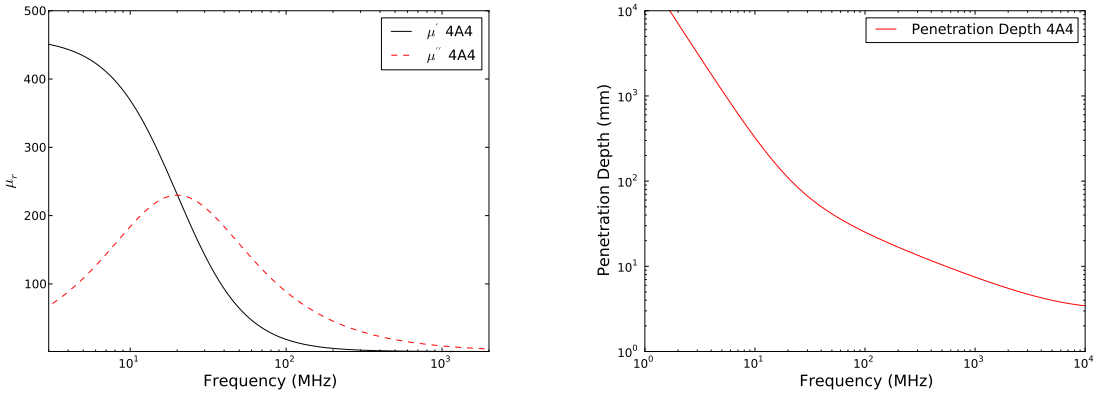

(a) (b)

Figure E.3: The permeability (a) and penetration depth (b) for 4A4.

Table E.4: A selection of the physical properties of 4E2

$\epsilon^{'}$	10	
Conductivity	10^{-5}	S m^{-1}
T_c	375	^{oc}C

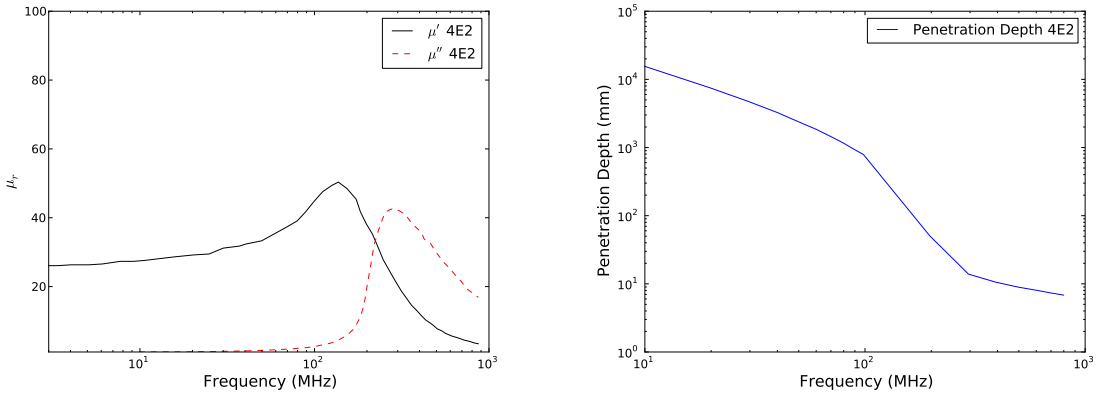

(a) (b)

Figure E.4: The permeability (a) and penetration depth (b) for 4E2.

Appendix F

Heat Transfer in Vacuum

An important factor in determining the temperatures reached within accelerator components is the rate of energy transfer from the internal components to the surrounding vacuum tank. In particular the high vacuum required in accelerator operation means that the transfer of energy becomes dominated by conduction and radiative transfer due to the absence of a medium for convection. Depending on the structure conduction of heat between components nominally in contact may not be well defined, and radiative transfer can be strongly affected by the surface emissivities of the components, particularly a concern due to the polishing of metallic surfaces for vacuum compatability which tends to leave the surfaces with a relatively low thermal emissivity ($\epsilon \approx 0.1$).

Here we shall briefly cover passive cooling within accelerator structures, discussing convection, conduction (including the case of near-field IR tunnelling) and radiative transfer.

F.1 Convection

The majority of accelerator components are under extremely high vacuum to support the circulating particle beam and thus there is little to any medium in which convection currents may flow. In this case the heat transfer by vacuum by means of convection is negligible.

F.2 Conduction

Conduction between components in an accelerator device varies by their degree of contact. Components that are afixed by some form of bonding (welding, brazing) have a well defined heat transfer by conduction due to the good physical bond between them. However components that are afixed by contact pressure (i.e. pushed by screw/nut, held by a casing/housing or just under the weight of gravity) may not have good or well-defined thermal contact with one another. This is due to the variation in the thermal conductivity between the two components depending on contact pressure, surface flatness, and the cleanliness of the surface (generally not a signficant factor in high vacuum quality finishes).

In particular some components may be highly sensitive to strongly exerted forces to improve contact pressure due to brittleness or mechanical weakness. In this case the heat transfer by conduction is not necessarily significant or simply represented.

F.3 Radiation

Radiation is very well defined in terms of heat radiation transfer within a vacuum. Two important factors in determining the thermal conductivity due to thermal radiation between two components are the thermal emissivity of the materials and the ratio of visible surface areas of the two materials. This effect is seen in Fig. F.1, in which is can be seen that the emissivity of the absorbing material is low (< 0.2), small changes in the emissivity can greatly increase or decrease the rate of power transfer. This is exacerbated the smaller the ratio of the surface areas between the emitting and absorbing components.

It can be seen that for components that may be exposed to dangerous heat loads (i.e. ferrites, thermal sensitive equipment), heat transfer by radiation may be improved by increasing the emissivity of surrounding components, and making sure it is thermally visible to a large surrounding area.

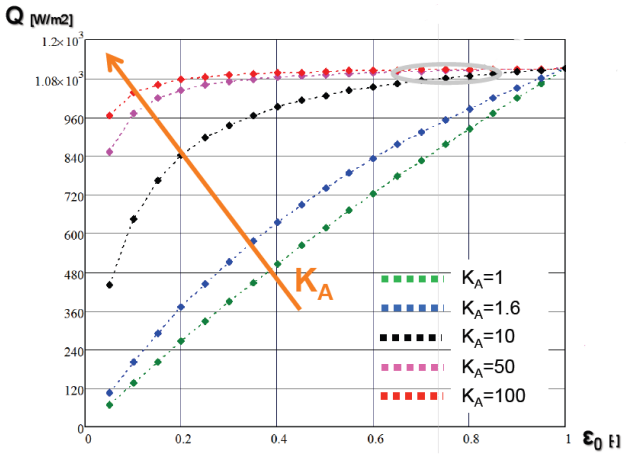

Figure F.1: The power transfer between two surfaces by radiative heat transfer as a function of emissitivity of the absorbing component and the ratio of the visible surface areas of the components. K_A is the ratio of the surface of the absorbing component and the emitting component. Figure produced by Garlasche et al [125].

F.3.1 Near-field radiation

In the case where two components are exceptionally close to one another a phenomena known as radiative tunnelling occurs. This effect on the thermal transfer is shown in Fig. F.2, where it can be seen that there is a region between the radiation dominated heat transfer and the conduction dominated transfer, as two objects are moved closer together, where the thermal conductivity greatly increases, but before the components are in physical contact. This is significant as it may be exceptionally beneficial to the heat evacuation in components that are in close proximity to surrounding components, but where the physical contact is not good, such as the case where ferrites are held in a casing, which due to their brittleness may not have a large physical force exerted on them.

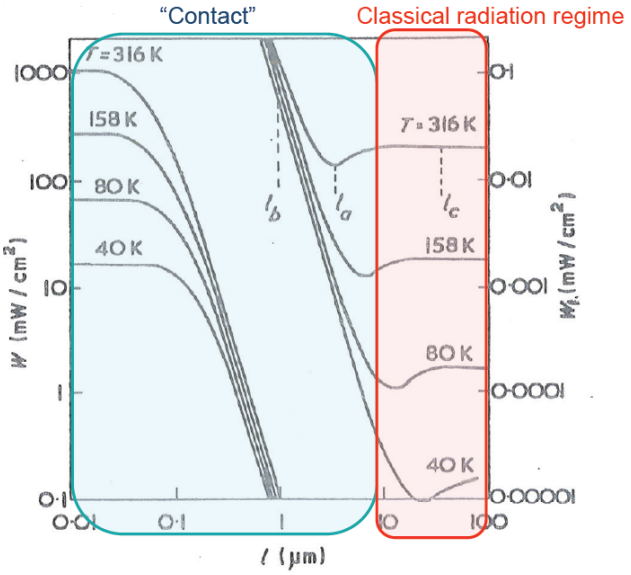

Figure F.2: An illustration of the change between the two regimes of thermal transfer by radiation and by conduction as the distance between two surfaces is reduced. It can be seen that there is a period between radiation and the beginning of transfer by contact where-in the rate of thermal transfer greatly increases. This is due to an effect known as radiative tunnelling [126].

Appendix G

Analytical Models of Resistive Wall Impedance

In this thesis a number of analytical models have been referenced, predominantly the Tsutsui model [26, 30, 61] and the Mounet model [17], representing two finite and infinite parallel plates respectively, and the Zannini mode [62] for C-core ferrite kickers (although valid for any material). In this appendix the methods used in deriving the impedances in these models, known as mode matching, will be briefly discussed.

G.1 Tsutsui Model

The Tsutsui model of resistive wall impedance defines the impedance for a geometry shown in Fig. G.1, whereby two finite parallel plates of width $2a$, distance b from the centre of the geometry of thickness d. For this model derivations for the longitudinal [26], dipolar transverse [30] and quadrupolar transverse [61] impedances exist. In addition the longitudinal and dipolar impedance for multi-layered walls has been dervied [127].

The model works as follows: waveguide modes in each volume (upper wall, vacuum and lower wall) are defined for their respective dimensions, material properties and the source current. In this case image currents are added at $(x, y) = (2na, 0)$ for $n = 0, \pm1, \pm2, ...$ to account for the perfect electrical boundary at $|x| = a$. These fields

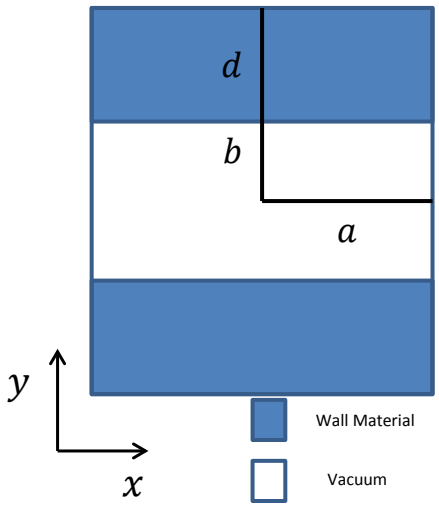

Figure G.1: The geometry treated by the Tsutsui model of resistive wall impedance.

are subsequently matched at the boundaries, and the impedance derived from the Fourier transform of the relevant fields (E_z for longitudinal impedance, $\mathbf{E}_\perp$ and $\mathbf{B}_\perp$ for the transverse impedances).

The impedance per unit length are subsequently given by

$$\frac{Z_\parallel(f)}{L} = j\frac{Z_0}{2a}\sum_{n=0}^{\infty} T_n(f) \tag{G.1}$$

for the longitudinal beam coupling impedance,

$$\frac{Z_x^{dip}(f)}{L} = j\frac{Z_0}{2a}\sum_{n=0}^{\infty} \frac{k_{xn}^2}{k} T_n(f) \tag{G.2}$$

for the horizontal dipolar beam coupling impedance,

$$\frac{Z_y^{dip}(f)}{L} = j\frac{Z_0}{2a}\sum_{n=0}^{\infty} \frac{k_{xn}^2}{k} T_n'(f) \tag{G.3}$$

for the vertical dipolar beam coupling impedance,

$$\frac{Z_x^{quad}(f)}{L} = -j\frac{Z_0}{2a}\sum_{n=0}^{\infty} \frac{k_{xn}^2}{k} T_n(f) \tag{G.4}$$

for the horizontal quadrupolar beam coupling impedance, and

$$\frac{Z_x^{quad}(f)}{L} = j\frac{Z_0}{2a}\sum_{n=0}^{\infty}\frac{k_{xn}^2}{k}T_n(f) \tag{G.5}$$

for the vertical quadrupolar beam coupling impedance, where

$$T_n(f) = \left[\frac{\frac{k_{xn}}{k(f)}\left(1+\mu_r(f)\,\epsilon_r(f)\right)shch + \frac{k_{yn}(f)}{k(f)}\left(\mu_r(f)\,sh^2tn(f) - \epsilon_r(f)\,ch^2ct(f)\right)}{\mu_r(f)\,\epsilon_r(f)-1} - \frac{k(f)}{k_{xn}}shch\right]^{-1} \tag{G.6}$$

$$T_n^{'}(f) = \left[\frac{\frac{k_{xn}}{k(f)}\left(1+\mu_r(f)\,\epsilon_r(f)\right)shch + \frac{k_{yn}(f)}{k(f)}\left(\mu_r(f)\,ch^2tn(f) - \epsilon_r(f)\,sh^2ct(f)\right)}{\mu_r(f)\,\epsilon_r(f)-1} - \frac{k(f)}{k_{xn}}shch\right]^{-1} \tag{G.7}$$

sh, ch, tn, ct are $sinh(K_{xn}b)$, $cosh(k_{xn}b)$, $tan(k_{yn}(b-d))$, $cot(k_{yn}(b-d))$ respectively, $k_{xn} = (2n+1)\pi/(2a)$, $k_{yn} = \sqrt{(\epsilon_r\mu_r - 1)k^2 - k_{xn}^2}$.

G.2 Zannini Model

The Zannini model is a model of resistive wall impedance designed to model the impedance of a C-core ferrite kicker, shown in Fig. G.2. As with the Tsutsui model, the fields are defined for the individual sections of the geometry (vacuum and ferrite) depending on a source current, and then the fields matched at the boundaries between media. In this case, the longitudinal fields of the porpogating TE and TM modes are field, and the transverse fields found by the use of Panofsky-Wenzel theorem.

The derivation in depth is given in [62].

G.3 Mounet Model

The Mounet model of resistive wall impedance represents the wall impedance of two infinite parallel walls, made of an arbitrary number of layers of material of any well defined (i.e. complex permitivitty/permeability is known for the frequency range of calculation)

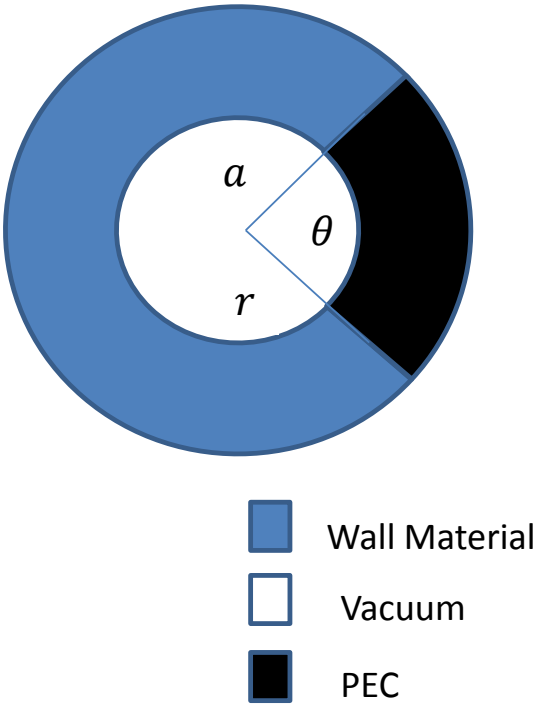

Figure G.2: The geometry treated by the Zannini model of resistive wall impedance.

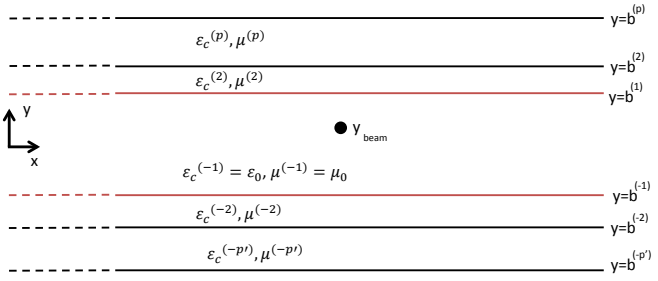

Figure G.3: The geometry treated by the Mounet model of resistive wall impedance.

material which do not necessarily have the same material composition on the top and bottom layers [17], for a particle of any relativistic factor β. This allows the prediction of the longitudinal, horizontal/vertical dipolar, horizontal/vertical quadrupolar and horizontal/vertical constant beam coupling impedances for almost any combination of materials. In particular for low frequency effects on multi-layer devices this is a useful analytical model.